A numerical investigation on augmented heat flux in non-standard variants of turbulent Rayleigh-Bénard Convection

A thesis submitted in
partial fulfillment of the requirements
for the degree of

Doctor of Philosophy

in

Mechanical Engineering

by

Krishan Chand

under the guidance of

Dr. Arnab Kumar De

Department of Mechanical Engineering,

Indian Institute of Technology Guwahati,

Guwahati - 781039,

Assam, India.

June 2023

Dedicated to my parents.

CERTIFICATE

This is to certify that the work presented in this thesis entitled "**A numerical investigation on augmented heat flux in non-standard variants of turbulent Rayleigh-Bénard Convection**" is carried out by **Krishan Chand** for the award of Doctor of Philosophy in the Department of Mechanical Engineering, Indian Institute of Technology Guwahati. The thesis embodies the results of original work and studies carried out by the student himself under my supervision and has not been submitted elsewhere for a degree.

Dr. Arnab Kr. De
Associate Professor,
Department of Mechanical Engineering,
IIT Guwahati, 781039, Assam.

Date: June, 2023
Place: Guwahati

Acknowledgement

First of all, I would like to express my deep sense of gratitude to my thesis supervisor, Dr. Arnab Kumar De, for his support and guidance. Throughout this journey, I have learnt a lot from him. I am also thankful for his inspiration and the trust he showed in me, which gave me a lot of confidence and helped me to establish an overall direction of research. I am deeply grateful for his valuable comments and suggestions. I acknowledge my fruitful collaboration with Dr. Pankaj Kumar Mishra. I thank him for sharing his rich experience in different fields and enlightening me on the physical aspects of turbulent flows. I express my sincere gratitude to my Doctoral Committee members, Prof. Anoop K. Das, Prof. Vinayak Kulkarni, and Dr. Partho Sarathi Gooh Pattader, for their invaluable suggestions. I would also like to acknowledge the infrastructure provided by the institute, especially the 'Param-Ishan' supercomputing facility, to accomplish my research successfully.

During my stay at IIT Guwahati, I came across several friends who made the journey very pleasant and colorful. I acknowledge all the love and cooperation that I have received from them at different stages of my PhD. I thank Deepak Kumar, Nitesh Kumar, Saurav Kumar, Shantanu, Akash Rana, Nitesh Singh, Mukesh Kumar, Debojyoti Nath, Naren, Arpita Shome, Jaishree Bharadwaj, Maitry yadav, and many other friends whose company I really cherished. My special thanks to Mukesh and Kuldeep for always showing their great interests to discuss several aspects of turbulent thermal convection and research ideas. I would also like to thank the Cricket club, which turned out to be a family at IITG.

Above everything, this PhD would not have been possible without the constant support, encouragement, blessings and good wishes of my family members. I am grateful to my parents for their continuous support and affection through this journey and beyond. I would always be

thankful for their enormous sacrifices made for me to transform my dream into reality.

Krishan Chand

Abstract

Rayleigh-Bénard Convection (RBC) is a buoyancy-driven flow in which the fluid is heated from the bottom. It is an ideal system for studying many complex fluid phenomena observed in nature and engineering applications. However, the actual flows do not possess the ideal boundary conditions. In fact, they encompass complex boundaries and forces which directly impact the flow dynamics, for instance, the presence of stabilizing/destabilizing forces like magnetic force and rotation, and asperities of surfaces underneath the flows, to name a few. To incorporate such flow-impacting factors, the standard RBC needs to be modified for a better understanding of the real fluid phenomena. In this thesis, we investigate the heat transport properties in two such variants of non-standard RBC, namely, the roughness-aided RBC and tilted RBC. In the former, the smooth isothermal surfaces are replaced by multi-scale roughness, whereas in the latter, buoyancy force acts at an angle to gravity. We consider rectangular (double-aspect ratio) and cubical (unit aspect ratio) geometries for $2D$ and $3D$ studies, respectively, over a Rayleigh number (Ra) range varying from 10^6 to 10^{10} with air chosen as the working fluid $(Pr = 0.7)$. In this thesis, quantitative and qualitative analysis of the coherent structures (boundary layer, thermal plumes and large-scale rolls), and the two response parameters: heat flux and flow strength, are used to understand the heat transport properties. Note that Nusselt number (Nu) and Reynolds number (Re) are a measure of heat flux and flow strength, respectively.

In the standard $2D$ RBC, thermal jet phenomenon occurs because of entrapment of thermal plumes due to the absence of one lateral dimension. The boundary layer thickness is computed using the so-called slope and 99% technique, which confirms the theoretical $Nu(Ra)$ scaling. In the boundary layer region, transport and dissipation terms of turbulent kinetic energy balance each other. On the other hand, buoyancy production balances dissipation in the bulk region.

Thermal plumes and background regions are quantified by the positive correlation between vertical velocity and temperature fluctuations. A higher threshold for the correlation yields faster convergence of plume and background share of dissipation. Exponential distribution of temperature fluctuations suggest the presence of hard turbulence at a very large Rayleigh number.

Compared to the standard RBC, heat flux increases significantly in the roughness cases beyond a critical Rayleigh number (Ra_c), which is marked as the onset of enhanced heat flux regime. This regime is observed to depend upon the roughness height, and the increment in heat flux occurs due to greater emission of thermal plumes from the rough surfaces. The morphological changes in plumes transform the state of large-scale rolls, i.e., a double-roll state to a multiple-roll state, at least in the taller roughness cases. The size of the rolls diminishes in the multiple-roll state, which has a higher tendency to evacuate the cavities and results in emission of more plumes. Also, the cascade of vortices in the taller roughness cases helps in evacuating the entrapped fluid. Owing to a larger number of plume emitting peaks, the maximum $Nu(Ra)$ scaling exponent is observed in the smallest roughness case, and it decreases with increase in roughness height. For the first time, we have quantified the boundary layer perturbation and explored its relation with the enhanced heat flux, which was previously assumed [1, 2].

In the tilted variant of RBC, we disentangle the dependence of $Nu - \phi$ trend on Ra, where ϕ represents the inclination angle. In the smooth case, inclined convection (IC) transports heat more efficiently for $Ra \leq 10^8$, whereas RBC does the same for $Ra > 10^8$. The $Nu - \phi$ trend yields a unimodal behavior up to $Ra = 10^8$ and a monotonically decreasing trend above it. In the unimodal trend, we obtain that $\phi = 75^\circ$ yields maximum Nu. The combined effect of roughness and tilt result in a large increment (25%) in heat flux. While increase in Ra delays the thermal stratification in the smooth case, roughness heights do the same in rough configurations. In the roughness cases, early onset of turbulence due to surface roughness limits the advantages of tilted convection to a lower Ra.

In $3D$ roughness-aided RBC, heat flux increases significantly $(\approx 50\%)$ compared to its smooth counterpart. However, it is found that roughness impacts the flow intensity weakly. In rough cases, a significantly higher volume fraction of thermal plumes ascertains their role in enhanced heat flux. While, in the smooth case, large-scale circulation (LSC) remains in one of the diagonal planes, the roughness asperities tend to lock it in a Cartesian plane and increase the longevity of thermal plumes in the bulk region. These arguments are further ascertained by computing the Reynolds number based on the angular velocity in Cartesian planes. Temperature fluctuations in the bulk region follow a clean $-7/5$ power-law in the inertial subrange for both

smooth and rough cases, indicating the Bolgiano scaling. It is observed that although roughness asperities do not influence the scaling law, they intensify the energy of eddies of all the length scales due to emission of intense thermal plumes.

Contents

Abbreviations

AB	Adams-Bashforth
BiCGSTAB	Bi-Conjugate Gradient Stabilized
BL	Boundary layer
CDS	Central difference scheme
CN	Crank-Nicolson
CV	Control volume
DNS	Direct numerical simulation
DRS	Double-roll state
FVM	Finite volume method
LES	Large-eddy simulation
LSC	Large-scale circulation
LSR	Large-scale roll
MRS	Multiple-roll state
PBiCGSTAB	Pre-conditioned Bi-Conjugate Gradient Stabilized
PDF	Probability density function
SIP	Strongly implicit procedure
SRS	Single-roll state
TBL	Thermal boundary layer
TKE	Turbulent kinetic energy
TRS	Triple-roll state

Symbols

α	Thermal diffusivity
β	Thermal expansion coefficient
ρ	Density of fluid
ν	Kinematic viscosity of fluid
μ	Dynamic viscosity
κ	Thermal conductivity
λ_θ	Thermal boundary layer thickness
λ_u	Viscous boundary layer thickness
ϵ_θ	Thermal dissipation rate
ϵ_u	Viscous dissipation rate
σ	Variance
η	Kolmogorov's length scale
ϕ	Inclination angle
θ	Non-dimensional temperature
p	Pressure
t	Time
g	Acceleration due to gravity
$\hat{k}$	Unit vector in vertical direction
S	Skewness
F	Flatness
q	Total heat flux
T_c	Temperature of cold surface

T_h	Temperature of hot surface
Δt	Time increment
ΔT	Temperature difference between hot and cold surfaces
x, y, z	Cartesian directions
u, v, w	Cartesian components of the velocity vector
R_1	Smallest roughness case
R_2	Intermediate roughness case
R_3	Tallest roughness case
S	Smooth case
U	Uniform roughness case
R	Irregular roughness case
HU	Half-uniform roughness case
HR	Half-irregular roughness case
H	Height of a convection cell
L	Length of a convection cell
Γ	Aspect ratio ($/H$)
Re	Reynolds number
Ra	Rayleigh number
Nu	Nusselt number
Pr	Prandtl number
$2D$	Two-dimensional
$3D$	Three-dimensional
$\langle \cdot\cdot \rangle_t$	Time averaging
$\langle \cdot\cdot \rangle_{V,t}$	Volume-time averaging
$\langle \cdot\cdot \rangle_{A,t}$	Area-time averaging

List of figures

List of tables

CHAPTER 1

Introduction

1.1 Natural convection

Natural convection is a heat transport phenomenon effected by fluid flow [3]. It is ubiquitous in nature and finds its application in various fields varying from atmospheric and geophysical flows to astronomical context. Figure 1.1 shows the application of thermal convection in the atmosphere, mantle of the Earth [4–6], and inside the Sun [7]. In the Earth's atmosphere, the north and south poles remain colder, while the equatorial region becomes warmer due to the Sun rays falling directly on it. The temperature difference between the two hemispheres induces a global flow circulation of air, where hot air moves towards the poles and cold air approaches the equator. Similarly, the heated surface due to sun rays during the daytime warms the air close to it, which starts rising upwards due to buoyancy effect and results in ocean currents. Convection plays a significant role in heat transfer from the core to the exterior of the Earth and Sun. The application of thermal convection is also found in industrial processes [8], engineering fields [9], and our daily life, such as heat exchangers, cooling of electronic devices, nuclear reactors, and in buildings [10].

Rayleigh-Bénard convection (RBC) is an ideal system to study thermal convection [14, 15]. It is a bottom-heated and top-cooled configuration, where the flow sets in due to thermoconvective instabilities [16, 17]. Figure 1.2 shows the schematic of a convection cell of height H and length L. The bottom surface of the cell is at a higher temperature (T_h), while the top surface

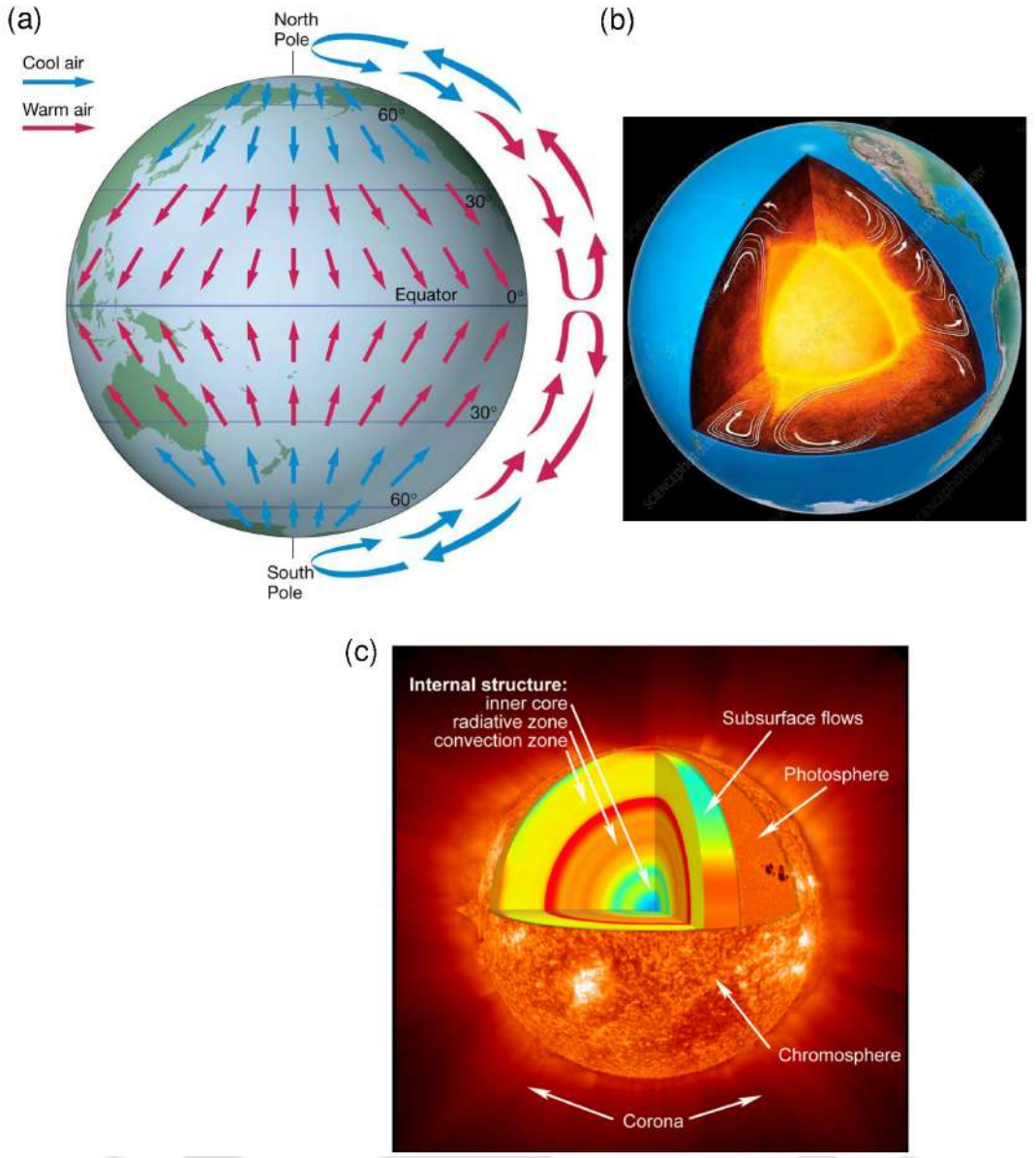

Figure 1.1: Examples of natural convection: (a) flow circulation in the atmosphere of the Earth [11], (b) convection rolls in the mantle of the Earth [12], and (c) inside the Sun [13].

is at a lower temperature (T_c). In the vicinity of the hot plate, thermal expansion of the working fluid occurs, which creates a density difference in the fluid. Due to thermal instability, the hot fluid rises upwards from the bottom thermal boundary layer (TBL), while the cold fluid simultaneously falls downwards from the top one. These hot and cold fluids are perceived as detached thermal boundary layers and termed as thermal plumes [18]. These plumes are responsible for heat transfer between the isothermal surfaces [19]. Note that while the buoyant force destabilizes the flow, the viscous force acts as a stabilizing agent. The ratio of buoyant force to viscous force is known as Rayleigh number $Ra = g\beta\Delta T H^3/(\nu\alpha)$, which represents the non-dimensional thermal forcing. Here, g is the acceleration due to gravity, β is the thermal expansion coefficient,

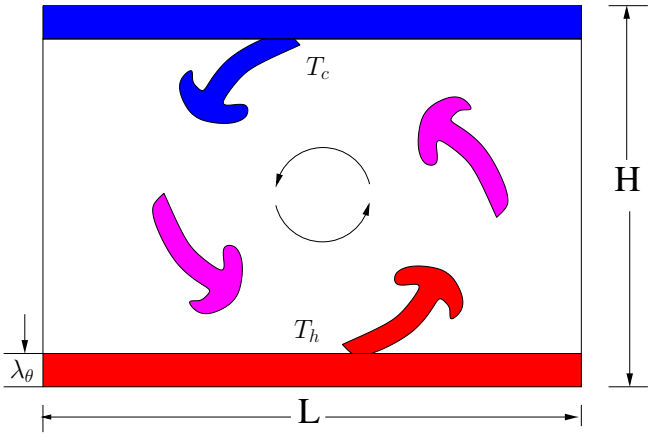

Figure 1.2: Schematic of Rayleigh Bénard convection, where red (blue) color represents the movement of hot (cold) plumes, and magenta color represents the diffused thermal plumes. Plumes are ejected from the thermal boundary layer, whose thickness is denoted by λ_θ.

$\Delta T(= T_h - T_c)$ is the temperature difference between the two isothermal plates, and ν and α are viscous and thermal diffusivities, respectively.

A smaller *Ra* signifies the dominating viscous effect, which results in a thermally stable flow. However, as *Ra* increases, the buoyant force competes with its viscous counterpart. As reported by Krishnamurthi & Howard [20], the buoyant force becomes sufficiently large to overcome the viscous resistance at $Ra = 1708$, irrespective of the fluid. With the further increase in *Ra*, the flow approaches a chaotic state, where it loses its temporal coherence [20]. Further, the loss of spatial coherence occurs at even larger *Ra*, where the flow becomes turbulent [21]. Other than the *Ra*, there are two control parameters: aspect ratio $(\Gamma = L/H)$ and Prandtl number $(Pr = \nu/\alpha)$. While aspect ratio is a geometric attribute of the convection cell, *Pr* is a property of a fluid, which signifies the ratio of momentum and thermal diffusion. In RBC, there are two key response parameters, namely, Nusselt number (*Nu*) and Reynolds number (*Re*). While the former is a measure of convective heat flux and is defined as the ratio of total heat flux to the conductive heat flux, the latter represents the flow intensity.

The study of thermal convection originates from the experimental study of Bénard [14] in 1901, who investigated the flow patterns in a system heated from the bottom, while the top one was open to the air. He observed a hexagonal pattern on the surface of the fluid, known as Bénard cells. Later, Rayleigh [15] investigated the Bénard's work theoretically and connected the onset of convection with Rayleigh number. To generalize the onset of the instability, Jeffreys [22, 23] studied different combinations of boundary conditions. In 1954, Malkus [24] proposed the marginal stability theory that relates the heat flux with Rayleigh number. According to the theory, thermal boundary layer remains stable up to the critical *Ra*. In the following years, a

number of theories were proposed [25–31] which are discussed in detail in Sec. 1.2.

Owing to the advancement in computational power and experimental tools, significant progress has been made in understanding the heat transport mechanism in turbulent Rayleigh-Bénard convection [28, 26, 27]. It has been adopted as a model to search for ways to enhance heat transfer [32–34]. Recently, the two non-standard variants of RBC have been used to enhance heat flux. First, the convection cell is facilitated with surface roughness, generally on the top and bottom plates. Second, the cell is tilted at a certain angle to break the flow symmetry. In the present work, we explore these two aspects with different types of irregular rough surfaces. A detailed discussion and literature review of these variants are provided in the subsequent sections.

1.2 Heat transport in turbulent thermal convection

In RBC, one of the key issue is the dependence of heat flux on Rayleigh number. After the Rayleigh's [15] theoretical investigation on the onset of convection, Prandtl [35] proposed a "free-fall" similarity theory which assumes free-fall velocity scale and the theory yields $Nu \sim Ra^{1/3}$. He considered an infinitely thick fluid layer heated from below. This theory failed for the finite height of the fluid layer. Later, in 1954, Malkus [24] and Priestley [25] independently proposed scaling theory of turbulent convection. Malkus [24] proposed the marginally stable theory wherein boundary layer remains marginally stable up to the critical Rayleigh number. On the other hand, Priestley [25] assumed that heat flux is independent of height of the convection cell, which implies decoupling of the top and bottom boundary layers. For $Nu \sim Ra^{a}$, the only scaling law for this theory is $a = 1/3$. Howard [26] further developed the marginal stability theory and proposed that temperature gradient is negligible outside the thermal boundary layer, while fluid remains stagnant inside it. Based on the theory of Malkus [24] and Howard [26], several researchers proposed "mean field theories" [36–39], which considered presence of several modes on top of the stable mean temperature field.

Later, Kraichnan [28] predicted the behavior of Nusselt number in the limit of higher Rayleigh number. He refined the similarity theory by considering a double boundary layer and proposed that the classical scaling exponent $1/3$ changes to $1/2$ at $Ra \approx 10^{18}$. This transition was attributed to the interaction between fluctuating horizontal wind and boundary layer. Spiegel [27] also studied for high Ra range and hypothesized that if the diffusivities are sufficiently small, then the rate of heat flux may be solely determined by the bulk dynamics. Such phenomenon occurs at very high Ra range, and this regime was termed as "ultimate scaling regime." In the

so-called ultimate regime, Chilla *et al.* [40] reported that thermal boundary layer and kinetic boundary layer do not play explicit role in heat transfer.

Castaing *et al.* [29] proposed the mixing layer theory, which yields $2/7$ scaling law ($Nu \sim Ra^{2/7}$). They characterized the *Ra* regime into soft ($Ra \leq 4\times10^7$) and hard ($Ra > 4\times10^7$) turbulence regime. The whole domain was demarcated into three layers based on different physical properties: A, B and C. Layer A is the boundary layer region near the top and bottom plate. The temperature difference of $\Delta T/2$ in this layer causes instability, which further generates plumes of size λ_θ which are expelled into layer B. Layer B is a mixing region of characteristic size greater than λ_θ but lesser than H. Thermal plumes accelerate in this region due to buoyancy effect and enter layer C. Central region of the cell with a characteristic size comparable to H is layer C. In this layer, thermal plumes are advected with almost constant velocity. This theory did not consider the large-scale roll and assumed that thermal plumes carry the heat from the hot to the cold plate. Later, Shraiman & Siggia [41] considered the role of mean flow in heat transport mechanism and prescribed the $2/7$ power law.

After a rigorous analysis, Grossmann and Lohse [30, 31] proposed a unifying scaling theory of *Nu* dependence on *Ra* and *Pr*. The key assumption of the theory lies in the observation that large-scale convection roll ("wind of turbulence") is responsible for the velocity and temperature fluctuations in the bulk region. $Ra - Pr$ phase space is divided into different regions as shown in Fig. 1.3. Four different regimes are characterized based on the domination of kinetic (ϵ_u) and thermal energy dissipation (ϵ_θ) inside the boundary layer (BL) and the bulk region (bulk). The scaling laws for different regimes are listed in Table 1.1. The four different regimes are:

1. both ϵ_u and ϵ_θ are dominated by their BL contributions
2. ϵ_θ is dominated by $\epsilon_{\theta,BL}$ and ϵ_u is dominated by $\epsilon_{u,bulk}$
3. ϵ_u is dominated by $\epsilon_{u,BL}$ and ϵ_θ is dominated by $\epsilon_{\theta,bulk}$
4. both ϵ_u and ϵ_θ are bulk-dominated.

Using $\Gamma = 2$, $Pr = 1$ and covering 6 decades of *Ra* up to 10^{14}, Zhu *et al.* [1] reported the transition to ultimate regime at $Ra = 10^{13}$. They observed logarithmic kinetic boundary layer profiles, which show their turbulent characteristics. Owing to these flow characteristics, they claimed the transition to the ultimate regime, though thermal boundary layer profiles were found locally logarithmic. They found that $Nu \sim Ra^{0.38}$ and suggested that plume ejecting

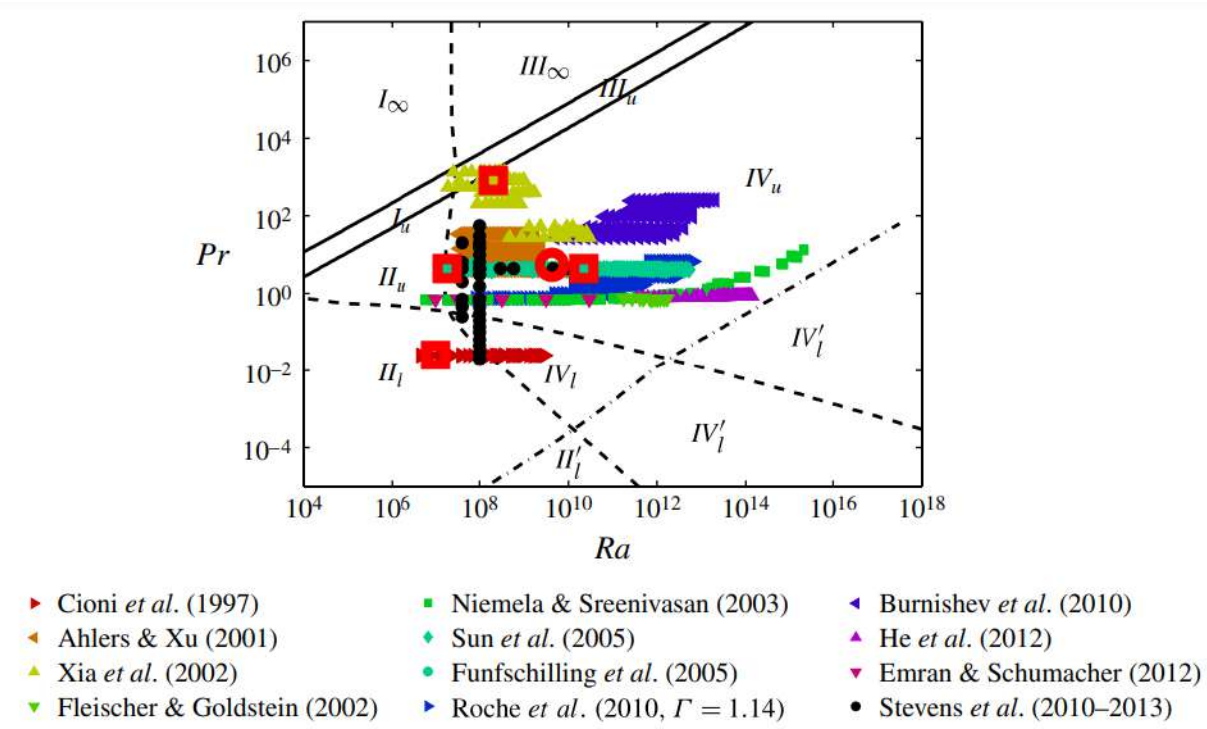

Figure 1.3: Different regimes in a $Pr - Ra$ phase diagram. Adopted from Stevens *et al.* [42].

Table 1.1: Power laws for $Nu(RaPr)$ including the prefactors which are adopted from experimental information.

Regime	Dominance of regime	BL	Nu
I_l	$\epsilon_{u,BL}$,$\epsilon_{\theta,BL}$	$\lambda_u < \lambda_\theta$	$0.27Ra^{1/4}Pr^{1/8}$
I_u		$\lambda_u > \lambda_\theta$	$0.33Ra^{1/4}Pr^{-1/12}$
II_l	$\epsilon_{u,bulk}$,$\epsilon_{\theta,BL}$	$\lambda_u < \lambda_\theta$	$0.97Ra^{1/5}Pr^{1/5}$
II_u		$\lambda_u > \lambda_\theta$	$(\sim Ra^{1/5})$
III_l	$\epsilon_{u,BL}$,$\epsilon_{\theta,bulk}$	$\lambda_u < \lambda_\theta$	$6.43 \times 10^{-6}Ra^{2/3}Pr^{1/3}$
III_u		$\lambda_u > \lambda_\theta$	$3.43 \times 10^{-3}Ra^{3/7}Pr^{-1/7}$
IV_l	$\epsilon_{u,bulk}$,$\epsilon_{\theta,bulk}$	$\lambda_u < \lambda_\theta$	$4.43 \times 10^{-4}Ra^{1/2}Pr^{1/2}$
IV_u		$\lambda_u > \lambda_\theta$	$0.038Ra^{1/3}$

region (hotspot) increases with Rayleigh number, which results in a steeper increase in Nu than the classical scaling regime. Further, Doering *et al.* [43] investigated the work of Zhu *et al.* [1] for even higher *Ra* and found a lack of evidence to claim the transition. In response, Zhu *et al.* [44] extended their work to even higher *Ra* (up to 4.64×10^{14}) and ascertained that the scaling exponent remains greater than $1/3$ beyond 10^{13}, which confirms the transition to the ultimate regime.

The dynamics and global features of the thermal convection system are highly influenced by the flow properties inside the boundary layers. The behavior of boundary layers has a strong connection with the scaling theories of heat transport in turbulent RBC. Ahlers *et al.* [18] proposed different methods to calculate thermal boundary layer thickness (λ_θ) using the average and variance temperature profiles. They observed the scaling behavior of thermal boundary layer as $\lambda_\theta \sim Ra^{-0.33\pm0.05}$. Grossmann and Lohse [45] reported the dependency of boundary layer thickness upon the aspect ratio as $\lambda_w/\lambda_p = \sqrt{4a}\Gamma^{-3/2}Re_w^{-1/2}$, where Re_w, λ_w and λ_p represent the wall Reynolds number, boundary layer thickness at the side walls and horizontal plates, respectively. Zhou *et al.* [46] studied the structure of velocity and temperature profiles near the horizontal plates at different positions in a 2D cell at $Ra = 10^8$ and proposed a dynamical boundary layer rescaling method. The rescaled instantaneous velocity and temperature profiles agree well with the classical Prandtl-Blasius boundary layer profiles. The method incorporated the time dependency by defining the relative vertical distance from the plates.

The role of dissipation rates and fluctuations in heat transfer is significant, and their study provides a deep insight into the heat transfer mechanism. Emran and Schumacher [47] studied statistics of thermal dissipation rate in a cylindrical cell of unit aspect ratio for $Pr = 0.7$ and *Ra* varying from 10^7 to 10^9. They observed a fat tail in the probability density function (PDF) of dissipation rates in the boundary layer region, indicating high intermittency near the wall regions. Moreover, the observed distributions were found to deviate from log-normal behavior. Zhang *et al.* [48] carried out the simulations in a wide range of Rayleigh number ($10^6 \leq Ra \leq 10^{10}$) and ascertained the power-law dependency of dissipation rates on *Ra* as $\langle\epsilon_u\rangle_{V,t} \sim Ra^{-0.18}$ and $\langle\epsilon_\theta\rangle_{V,t} \sim Ra^{-0.20}$. In the literature, statistics of temperature fluctuations have been studied to identify different flow regimes. Heslot *et al.* [49] observed that PDF of the fluctuations follows Gaussian distribution in the soft-turbulence regime but deviates from Gaussian in the hard-turbulence regime. They obtained the scaling exponent of the power-spectrum as $-7/5$. In another experimental study, Sano *et al.* [50] reported the existence of *Ra* dependency of power spectra between $10^8 \leq Ra \leq 10^{10}$. However, it shows more than one exponent for $Ra > 10^{11}$. Further, Zhang *et al.* [51] studied the behavior of the power spectra in a higher Ra range and used multifractal analysis to fit the high frequencies ($Ra > 10^{11}$) in a single function.

1.3 Role of surface roughness in RBC

We have reviewed several numerical, experimental, and theoretical studies for smooth convection cells in the previous section. But nature has its own choice of facilitating roughness to every surface. For example, it can be found in the urban atmospheric boundary layer (BL), and in the deep oceans. In both the examples, surfaces under the flow have rough topographies. Such flows help in understanding the phenomena of various natural processes related to thermal convection. Also, note that the natural uneven surfaces are not simple but abstruse. While studying the coastal length of Britain, Mandelbrot [52] reported the fractal dimension of uneven curves. He proposed the self-similarity attribute of these curves, where all the appearing patterns remain similar at all the scales. Since roughness is an attribute of surfaces, flow dynamics in a convection cell facilitated with roughness becomes essential. Practically, all the surfaces underneath the flows are rough, and some of the examples are oceanic flow, flow over the earth's surface, cooling of the electronic devices. These applications suggest to consider the rough surfaces in natural convection, and thus, unveil the physical phenomena responsible for heat flux.

Enhanced heat transport is highly desirable from both the fundamental and application perspectives. Several studies asserted that enhanced heat flux could be attained at a lower *Ra* if rough surfaces are used in the convection cell [53, 2]. Using rough top and bottom walls in the experiment, Shen and Tong [54] reported that rough configurations enhance the heat flux if roughness heights are comparable to the thermal boundary layer thickness. In comparison to the smooth case, heat flux was found to enhance by 20% due to the emission of large size thermal plumes from the interstices of the roughness elements. These plumes further travel vertically into the bulk and make the velocity (only vertical) fluctuations anisotropic. In a theoretical study, Villermaux [55] obtained the dependency of increased heat transfer rate on the fractal dimension of the rough surfaces, given that enhancement in the heat flux is only due to increase in surface area. Later, Ciliberto and Laroche [56] suggested that random roughness can affect the scaling exponent if thermal boundary layer thickness (λ_θ) lies between the maximum (h_N) and minimum (h_1) roughness heights ($h_1 < \lambda < h_N$). The investigation over the different distribution of roughness scales revealed that flatter distribution improves the scaling exponent. However, no improvement in the scaling exponent was observed for the extreme roughness scales, i.e., $\lambda < h_1$ and $\lambda > h_N$, because these extreme uneven surfaces do not perturb the boundary layers.

Du *et al.* [57] investigated the mechanism of enhanced heat transfer in rough convection cells. Two different roughness of heights 9 mm and 3.4 mm were used with the same surface area, which is 41% higher as compared to the smooth case. Surprisingly, the heat flux was observed

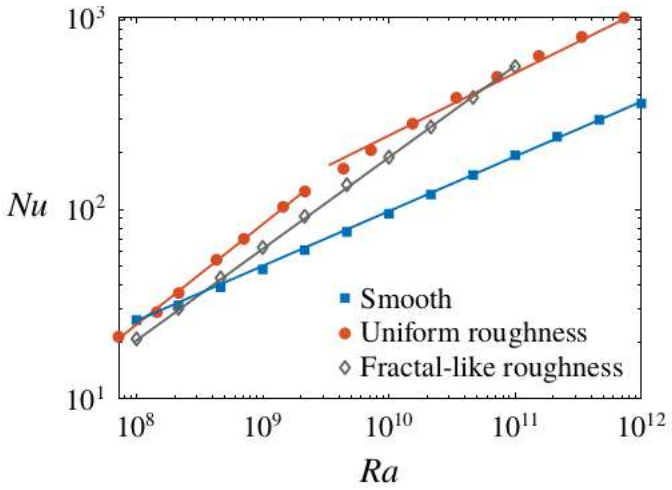

Figure 1.4: Comparison of $Nu(Ra)$ scaling regimes for the smooth case (square), mono-scale roughness (circle), and multi-scale roughness (diamond) heights. Usage of multi-scale roughness extended the enhanced exponent regime up to $Ra = 10^{11}$. Adapted from Zhu *et al.* [2].

to increase by 76% and 29% in the higher and lower roughnesses, respectively. Therefore, it suggests that enhancement in heat flux is due to the emission of extra thermal plumes and not because of the increase in the wetted area. Whenever the mean flow finds the peaks, it diverges like in the case of flow over a bluff body. Whereas, its interaction inside the grooves creates an adverse pressure gradient zone, which generates the secondary vortices in the valleys. Moreover, it was observed that taller roughness elements incite this mechanism at a lower *Ra*.

Later, Roche *et al.* [58] carried out an experiment using triangular grooved roughness and observed the $1/2$ scaling exponent. The enhanced scaling exponent was attributed to the laminar-turbulent transition inside the boundary layer. Also, they revealed that the inclusion of surface roughness incorporates the logarithmic correction in $Nu(Ra)$ scaling that occurs due to the variation of viscous sublayer with increasing *Ra*. Moreover, a weak $Nu(Pr)$ dependency was observed in the ultimate regime. In contrast to the above mechanism, Toppaladoddi *et al.* [53] attributed the observed ultimate regime to the increased interaction between the boundary layer and the bulk region. Using the optimum wavelength $(\lambda_{opt} = 0.1)$ of roughness element, for which *Nu* was found maximum, they observed the scaling exponent 0.483 and claimed it to be the highest then.

For the similar type of roughness elements (sinusoidal), Zhu *et al.* [59] explored the extent of higher exponent regime over a wider *Ra* range, $10^8 \leq Ra \leq 10^{12}$. They reported that the high exponent regime observed by Toppaladoddi *et al.* [53] stays temporarily only for a few decades of *Ra* and reverts to the classical scaling, see Fig. 1.4. Using different roughness configurations (characterized by their aspect ratio), Xie and Xia [60] suggested that enhanced heat flux strongly

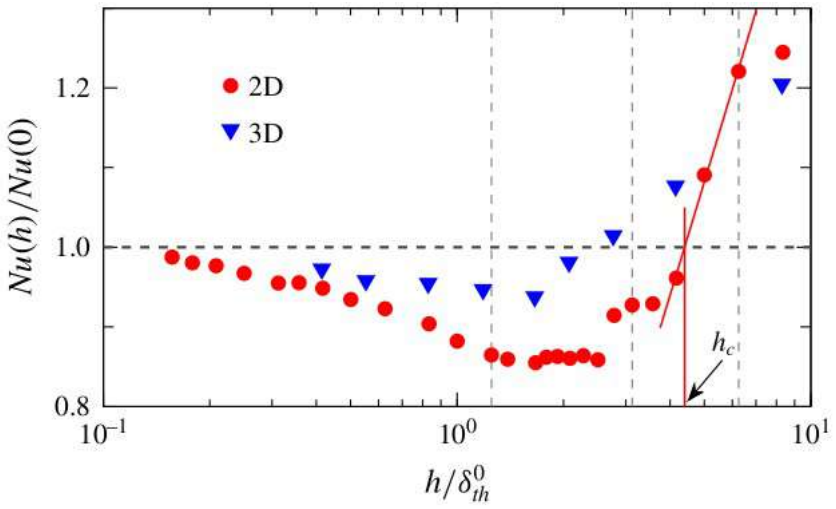

Figure 1.5: The normalized heat flux $(Nu(h)/Nu(0))$ as a function of roughness heights at $Ra = 10^8$. Note $Nu(0)$ and $\delta^0_{th}(= H/2Nu)$ refer to the heat flux and thermal boundary layer thickness computed from the smooth case for the same *Ra*, and h_c denotes the critical roughness height. Adapted from Zhang *et al.* [61].

depends upon the roughness geometry, and the $Nu(Ra)$ scaling exponent improved from 0.36 to 0.59 as aspect ratio increased from 0.5 to 4. However, rough surfaces influence not only the heat flux but also the local temperature fluctuations.

In addition to the wavelength, roughness height also plays a significant role in the flow dynamics [57]. A detailed investigation of critical height (h_c), where heights greater (smaller) than h_c yields the Nu enhanced (reduced) regime, is carried out by Zhang *et al.* [61], see Fig. 1.5. In the case of shorter roughness, the entrapped fluid inside the valleys yields a viscous dominated region and creates a thick boundary layer. However, for the taller roughness, induced secondary vortices inside these valleys enhance the mixing of the fluid. This enhanced mixing influences the boundary layer dynamics, which results in the enhanced heat flux regime. Further, it suggests that critical height decreases with increasing *Ra*. Based on the balance between viscous and buoyancy forces, the decrease in h_c was quantified as $h_c \sim Ra^{-0.6}$. This study paved the way for a combination of different roughness heights that can be used to explore the flow dynamics. Following this, Zhu *et al.* [2] introduced three different scales of roughness (sinusoidal) elements in the convection cell. They suggested that multi-scale roughness extends the local $1/2$ scaling regime up to 3 decades of *Ra* ranging from 10^8 to 10^{11}, which was wider than those in the previous cases, as shown in Fig. 1.4. This extension of the regime was attributed to the sustained plume-bulk interaction by the shorter roughness at higher *Ra*.

Tummers and Steunebrink [62] proposed a different mechanism for the enhanced heat flux

regime. Since LSC is responsible for carrying the thermal plumes from the boundary layer to bulk in a smooth cell, diffusion of thermal plumes is inevitable while traveling along the periphery. The square roughness used in the convection cell was found to break the LSC, which yielded a faster and direct interaction of hot (cold) plumes with the top (bottom) boundary layer. Consequently, the splashing of hot (cold) plumes in the top (bottom) boundary layer destabilize the flow near the walls, and a surge in plume emission causes higher heat flux. Besides, the fluid entrapped in the cavities creates more intense plumes with a longer life. Such a phenomenon exist not only in roughness facilitated convection cell, but also in the smooth cells, as reported by Lülff *et al.* [63]. The emission of such intense plumes was termed as thermal jet, but their insufficient intensity and the localized phenomenon resulted in a $2/7$ power law.

Wang *et al.* [64] also reported a similar mechanism for the enhanced heat flux. In a slender and rectangular tilted convection cell, they reported that a stable double-roll state reduces the heat flux, while the unstable triple roll or single roll state enhances it. These different roll structures were the consequence of the inclination provided to the cell. Thus, it shows that breaking of flow symmetry can lead to higher heat flux, which can be incited either using the roughness elements or by providing inclination to the convection cell.

1.4 Effect of inclination on heat transport properties

Flow inside an inclined convection cell is another variant of non-standard Rayleigh-Bénard convection. Since RBC is a buoyancy driven flow, tilting of the convection cell can influence the direction of buoyancy force and yield different flow structures. In inclined convection (IC), the effect of inclination angle (ϕ) on two aspects is of prime importance. Firstly, the global heat transport properties that encompass heat flux and turbulent intensity, and secondly, the evolution of flow structures. Since the flow structures influence the heat flux rate, the former aspect is discussed prior to the latter.

In RBC, three control parameters that govern the flow are Prandtl number (Pr), Rayleigh number (Ra), and aspect ratio (Γ) [18]. It is expected that these parameters also influence the variation of heat flux with inclination. First, we describe the effect of Pr and Ra on $Nu - \phi$ dependence, and subsequently, the effect of aspect ratio on it, which impacts through transforming the flow structures [64]. In what follows, we begin with the studies that address the effect of Pr on $Nu - \phi$ curve as shown in Fig. 1.6. In particular, it includes the studies of $Pr = 6.3, 480$, and 0.0096 by Guo *et al.* [65], Jiang *et al.* [66], and Khalilov *et al.* [67], respectively. While Guo

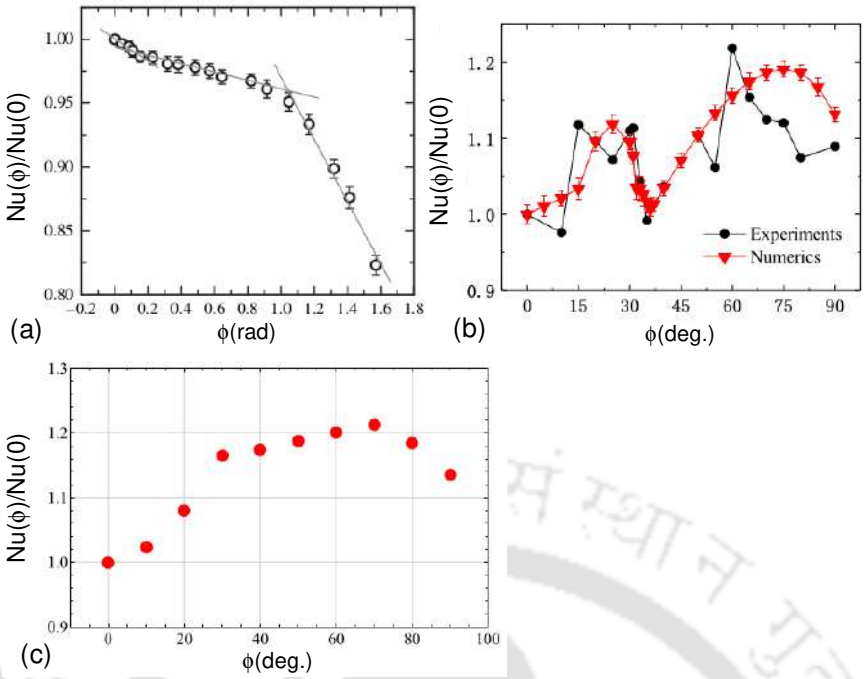

Figure 1.6: Characteristic of $Nu - \phi$ curves for three different fluids. (a) Monotonically decreasing curve for $Pr = 6.3$, adapted from Guo *et al.* [65]. (b) Bi-modal curve (double peak) for very high $Pr = 480$ from Jiang *et al.* [66]. (c) Unimodal (single peak) behavior for very low $Pr = 0.0096$, adapted from Khalilov *et al.* [67].

et al. [65] observed a monotonically decreasing trend (see frame a), Jiang *et al.* [66] obtained a bi-modal curve (see frame b), and Khalilov *et al.* [67] found a uni-modal behavior of $Nu - \phi$ curve (see frame c). Here bimodal (two peaks) and unimodal (single peak) refer to the number of peaks of local maximum heat flux obtained in the curve. In a quasi-2D cubic cell filled with water ($Pr = 6.3$), Guo *et al.* [65] reported a decreasing trend of Nu with three slopes the maximum being in the range of $60 - 90^{\circ}$, see Fig. 1.6(a). The maximum drop in Nu was found to be 18% for the vertical convection. In the same geometric configuration but with different parameters ($Ra = 6.8 \times 10^{10}$, $Pr \simeq 10$), Guo *et al.* [68] observed the similar decreasing trend in $Nu(\phi)$. Thus, inclination of the cell alters the heat transport mechanism which is reflected in Nu. They proposed that $Nu - \phi$ dependence does not depend upon the governing parameters like Ra and Pr. However, the small changes in the governing parameters should be noted, which may be the reason for similar trends in the two investigations. In water-filled cylindrical cell, Chilla *et al.* [69] investigated the effect of inclination on heat flux. They also observed a reduction in heat flux for weak inclination (up to 1.72°) and attributed it to the presence of two rolls state.

In a unit aspect ratio cylindrical cell, Shishkina *et al.* [70] studied the effect of tilt angle on Nusselt number and Reynolds number using four different Pr $(0.1, 1, 10, \text{and } 100)$ and at three

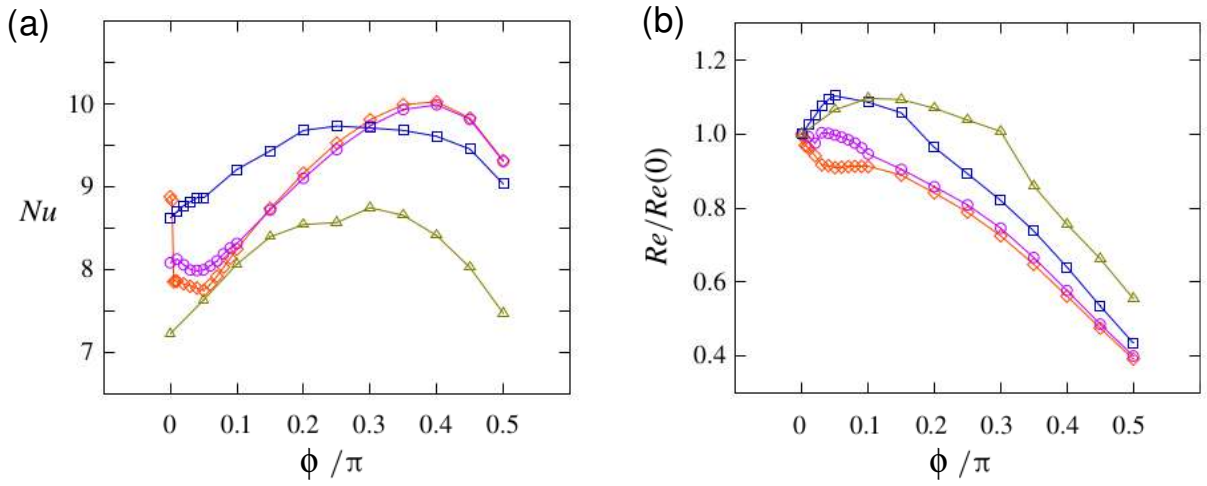

Figure 1.7: Effect of inclination angle on (a) *Nu* and (b) $Re/Re(0)$ of four different $Pr = 0.1$ (triangle), 1 (square), 10 (circle), and 100 (diamond) at $Ra = 10^6$. Note $Re(0)$ represents the Reynolds number in the horizontal case. The figure is adapted from Shishkina *et al.* [70].

$Ra = 10^6, 10^7$, and 10^8. In contrast to the previous observations where heat flux was found to decrease monotonically, they observed a complex $Nu - \phi$ dependency. Also, this dependency was found to vary with *Pr*, as shown in Fig. 1.7(a). The obtained *Nu* for different fluids agreed well with the hypothesis given by Verzicco and Camussi [19]. According to their proposition, LSC and thermal plumes act as heat engines for $Pr \leq 0.35$ and $Pr \geq 0.35$, respectively. The $Nu(\phi)$ curves were found nearly the same for both the higher *Pr* fluids except for $\phi \approx 0°$. This inconsistency at small inclination showed the transition of the heat carrier from thermal plumes to LSC. Moreover, LSC was shown to be the dominant flow structure at higher inclination angles, yielding the resemblance in the two curves. These curves first declined at smaller tilt and increased only to attain peaks close to the vertical convection. The peaks signified that LSC carries the heat more efficiently than the thermal plumes. For the two lower *Pr* fluids, the shape of the $Nu(\phi)$ curve remained the same. The heat flux was observed to increase with ϕ and attained a maximum in the intermediate inclination range, as shown in Fig. 1.7(a). In contrast to the higher *Pr* fluids, inclination enhanced the strength of the LSC for $\phi \approx 0°$, and thus, yielded higher heat flux. This study suggests that large (intermediate) inclination angles result in efficient heat transport in high (small) *Pr* cases. In contrast to the complex $Nu(\phi)$ dependency, $Re(\phi)$ curve followed a common trend except for $\phi \approx 0°$, see Fig. 1.7(b). Since LSC prevails at lower *Pr* fluids, slight inclination enhanced its velocity, which was reflected in higher Re. With the increasing inclination angle, Re first increased to attain a plateau and then dropped mono-

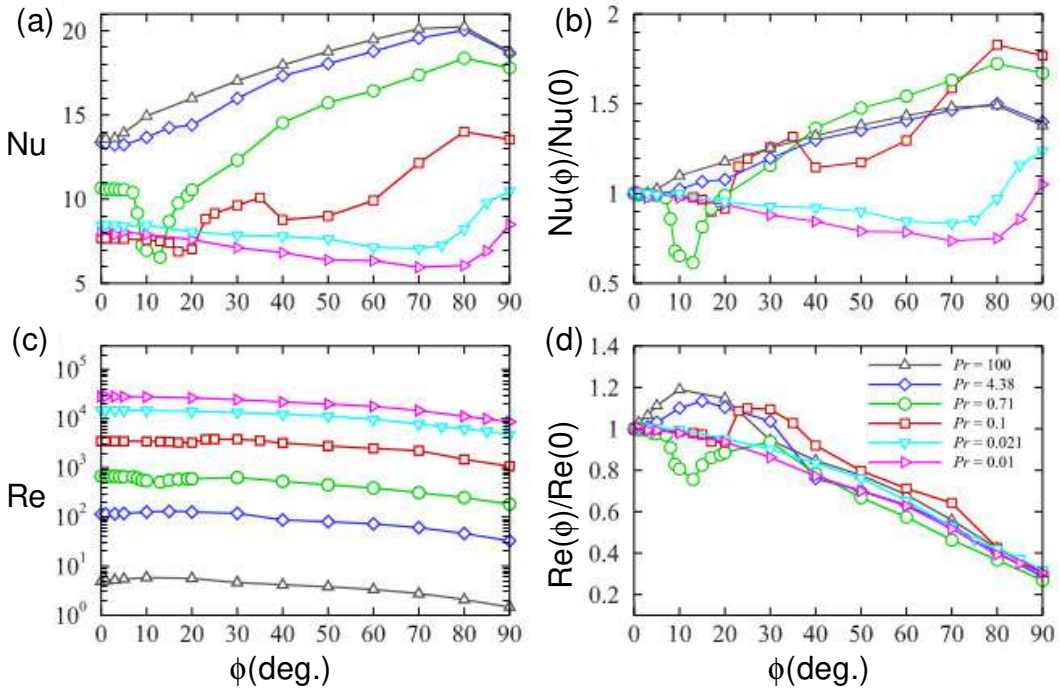

Figure 1.8: Effect of inclination angle on (a) *Nu*, (b) its normalized value $Nu(\phi)/Nu(0)$, (c) *Re* and (d) its normalized value $Re(\phi)/Re(0)$ in a wide range of *Pr* varying from 0.01 to 100 and at $Ra = 10^7$. The figure is adapted from Wang *et al.* [64].

tonically. The plateau signifies the transition of flow from a plume to LSC dominated in that inclination range, whereas the monotonic decrease indicated the attainment of stratified flow.

Interestingly, this study is in complete disagreement with the previous ones, perhaps, owing to different governing parameters. While Guo *et al.* [65, 68] argued that governing parameters do not influence the $Nu - \phi$ relationship, Shishkina & Horn [70] showed that the trend of heat flux with inclination depends upon them. It is important to note that Chilla *et al.* [69] and Guo *et al.* [65, 68] studied at a high *Ra*, whereas Shishkina & Horn [70] investigated in a low to moderate *Ra* range. Therefore, these arguments suggest that at higher *Ra*, $Nu - \phi$ drops monotonically [69, 65, 68]. On the other hand, it rises with ϕ and heat is transported more efficiently at greater inclinations when *Ra* is relatively lesser[70]. In the following studies, we further confirm these inferences related to the $Nu - \phi$ relationship.

In a $2D$ rectangular box of aspect ratio $1/2$ and $Ra = 10^7$, Wang *et al.* [64] studied the effect of *Pr* (ranging from $0.01 - 100$) on $Nu(\phi)$ and $Re(\phi)$ curves as shown in Fig. 1.8. At very low *Pr*, heat flux drops with rise in inclination up to $\phi = 80^\circ$, beyond which *Nu* starts increasing and becomes maximum at $\phi = 90^\circ$. On the other hand, at very high *Pr*, *Nu* increases with ϕ to attain a peak at $\phi = 80^\circ$ and drops subsequently. However, for the *Pr* varying between $0.1 - 1$,

Nu first decreases and attains a minimum around $\phi = 15°$. With further increase in inclination, it increases and follows the same trend as of high *Pr* cases. The *Re*(ϕ) dependence is found opposite to what Shishkina & Horn [70] observed in a unit aspect ratio cylindrical cell. The drop in *Nu* and *Re* corresponds to a double-roll state (DRS) or stable triple-roll state (STRS). They attributed these contrasting *Nu*$-\phi$ and *Re*$-\phi$ behavior to the transition in flow states due to a different geometry (aspect ratio) of convection cell. Recently, Jiang *et al.* [66] studied the flow at *Ra* $= 10^8$, and 5×10^8 for high *Pr* $= 480$ fluid in a two-dimensional confined inclined cell. In both the *Ra* cases, the variation of heat flux with inclination was found to follow a bi-modal behavior, wherein two peaks of *Nu* occur at $\phi = 25°$ and $75°$, as shown in Fig. 1.6(b). However, the Reynolds number increases with ϕ and attains a peak around $\phi = 10 \pm 2°$ before it drops. The peaks of *Nu* and Re at different inclinations indicate that the turbulent intensity does not always enhance the heat flux. However, a similar trend of *Nu* and LSC strength showed that the LSC was responsible for maximum heat flux. Indeed, LSC dominated the flow and carried the heat at intermediate and strong inclinations. Surprisingly, this coherent structure was previously reported to carry heat for lower *Pr* in level case ($\phi = 0°$).

Several studies have extensively used liquid sodium (*Pr* $= 0.0094$) as a working fluid for its high thermal diffusivity and industrial applications. As mentioned above, the heat transfer rate at a low *Pr* is found sensitive towards inclination. In a long cylinder of $1/5$ aspect ratio (D/H), Frick *et al.* [71] investigated the flow dynamics at four inclined angles, which are $0°$, $2°$, $45°$, and $90°$. Deviation of power spectra from Kolmogorov's $-5/3$ power-law indicated that turbulent intensity dropped with the increasing tilt angle. This study revealed that thermal plumes were responsible for carrying heat at small inclination angles, while LSC carried it at larger angles. The *Nu* obtained at $\phi = 90°$ was found greater than that in level case, which suggests that LSC carries the heat more efficiently than thermal plumes. The observed scaling law *Nu* $\sim Ra^{1/2}$ implied that the boundary layer did not influence the bulk flow in the long cavity cell. Using the same working fluid in a $1/20$ aspect ratio cylindrical cell, Vasilev *et al.* [72] obtained the maximum *Nu* at $\phi = 65°$ which confirms the arguments regarding the efficiency of LSC.

Since the evolved flow structures depend upon the cell geometry, aspect ratio becomes an important parameter in inclined RBC. To observe the effect of inclination on heat transfer, Khalilov *et al.* [67] investigated in a unit aspect ratio cylindrical cell using the same working fluid. Contrary to the long cylindrical cells, they observed a weak *Nu*(ϕ) dependency while the trend remained the same with the maximum heat flux at $\phi = 70°$, as shown in Fig. 1.6(c). Moreover, turbulent intensity and Re were found to behave similarly with the tilt angle. This variation sig-

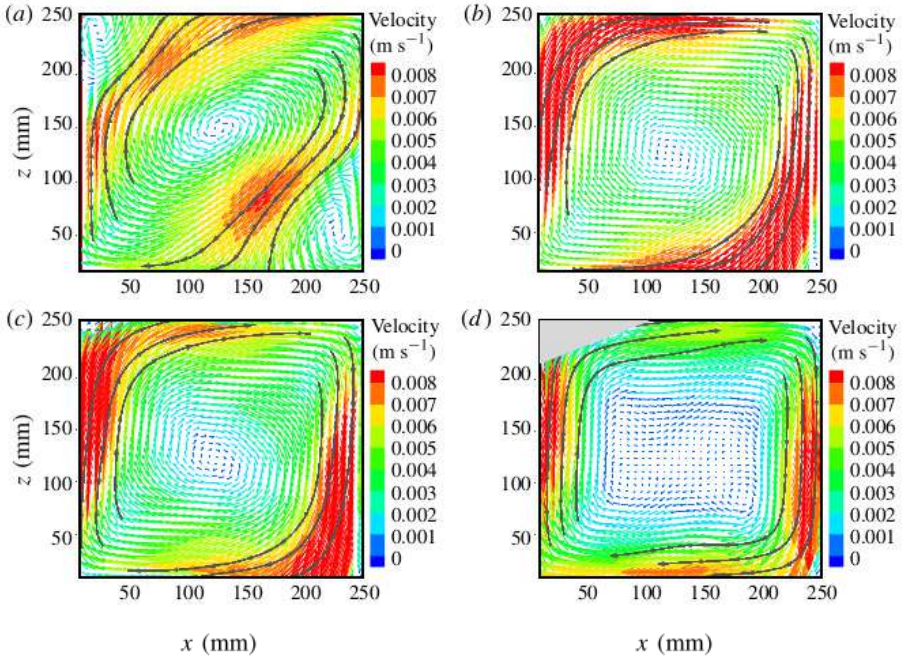

Figure 1.9: For $Ra = 4.42 \times 10^9$ and $Pr = 6.3$, time-averaged velocity field showing the transformation of an elliptic shaped cell at (a) $\phi = 0^\circ$ to a squarish one at (d) $\phi \approx 36^\circ$. Frame (b) and (c) shows the velocity field at the inclination angle of 8.59° and 13.17°, respectively. The figure is adopted from Guo *et al.* [65].

nifies the attainment of different flow states, which were characterized by the turbulent intensity. Based on the variation of turbulent intensity, three flow regimes were identified. The flow in the first regime remains highly turbulent and shows strong fluctuations, while the intensity drops in the second regime only to vanish entirely in the final regime.

The variation in heat flux with inclination occurs due to the transition in flow states. [71] observed similar flow states in both the horizontal and weakly inclined ($\phi = 2^\circ$) convection cells, implying that weak inclinations did not influence the flow structures. Further, Guo *et al.* [65] reported the transformation of the shape of LSC from elliptic to square-like in the range of inclination $0^\circ - 36^\circ$, see Fig. 1.9. Such transformation was previously reported as an effect of increasing *Ra* [73]. Moreover, the maximum velocity of the LSC was found at $\phi = 8.6^\circ$. As the inclination angle increased, the high-band velocity shifted towards the walls, which indicated the increasing span of LSC. Further, at $\phi \approx 67^\circ$, they observed that the fluid entering the bulk region returned to the horizontal plates in a tortuous manner, and it was termed as backflow.

Wang *et al.* [64] reported that the evolved flow states depend upon the initial inclination angle. For two different initial inclinations, one with the level case and the other with 20° inclined cell, flow developed into two different states. The investigation in a wide range of *Pr* revealed

that unstable triple roll state (UTRS) and single roll state (SRS) were responsible for the enhanced heat flux. However, it dropped in the presence of a double roll state (DRS). In addition to the roll structures, flow reversals also influence the flow dynamics and heat flux. Wang *et al.* [74] investigated the effect of tilt on flow reversals in two rectangular convection cells of aspect ratio 1 and 2. The study showed that tilt supported the reversals in the latter configuration and suppressed them in the former. A single corner roll triggered the reversals in a unit aspect ratio cell, while the simultaneous growth of the two corner rolls was responsible for their suppression in the other cell. Interestingly, the strength of DRS was found to be weakened during the reversals. On the contrary, improvement in the strength of triple and single roll was observed when the flow changed its direction.

1.5 Motivation and objectives

$Nu(Ra)$ scaling theories are well established for a smooth cell. However, it has been noticed that the transport mechanism in RBC can be significantly enhanced by introducing rough surfaces in the convection cell due to a flow transition from laminar to turbulent inside the boundary layer [58, 62]. Practically, all the surfaces underneath the flows are rough with a variety of roughness topology, height, and distribution. Owing to a number of factors, such as, increase in wetted area, inherent forcing of boundary layer instability and a greater trigger of plumes in the near-wall region, study of RBC over the rough surface has recently gained momentum. However, a single roughness scale has been used in almost all the studies that dealt with roughness-driven turbulent convection, except the studies carried out by Toppaladoddi *et al.* [75], Zhu *et al.* [2] and Ciliberto and Laroche [56].

Another variant of non-standard RBC is inclined convection (IC), which has yielded greater heat flux than RBC and vertical convection (VC) in many studies [71, 70, 66, 64]. As suggested by Shishkina & Horn [70], the dependence of heat flux on inclination angle (ϕ) is a complex function of three control parameters, Pr, Ra, and Γ. Although significant work has been carried out for inclined convection in both $2D$ and $3D$ cells, a unified view for the inclination angle that yields maximum heat flux remains elusive. Also, the combined effect of roughness and tilt on global heat transport properties has not been explored so far. These issues and gaps in the literature have motivated the present work to study the non-standard variants of RBC to obtain higher heat flux.

To incorporate a range of roughness scales (different height and wavelength), we have fo-

cused on irregular roughness set-ups in $2D$ and $3D$ cases. For $2D$, we use triangular elements of irregularly varying roughness heights and wavelengths, whereas for $3D$, conical roughness elements of varying heights are used, refer Sec. 2.3. Note that these irregular roughness geometries in both $2D$ and $3D$ typify improved multi-scale roughness, containing several roughness scales. For tilted convection, we use five inclination angles ($\phi = 0^\circ, 15^\circ, 45^\circ, 75^\circ$, and 90°), which span the entire range of inclination from RBC ($\phi = 0^\circ$) to vertical convection ($\phi = 90^\circ$). We have restricted this study only to $2D$ due to prohibitively high computational cost in $3D$ cells.

Based on the multi-scale roughness configurations and the tilted variants of RBC, the main objectives of the present work are as follows:

1. To investigate the heat transport properties and statistics of coherent structures in a $2D$ smooth convection cell.
2. To study the effect of irregular surface roughness on heat flux and flow structures.
3. To investigate the role of near-wall dynamics in heat flux enhancement for the irregular roughness configurations.
4. To study the effect of inclination angle on flow structures, and heat transport properties in smooth and roughness facilitated convection cells.
5. To explore the dependency of heat flux on different roughness set-ups in $3D$ cells.

1.6 Outline of the thesis

The remainder of the thesis is organized as follows. In chapter 2, we provide the details of mathematical modeling for both the level and inclined cases, grid generation and parallelization, diffuse interface immersed boundary method to identify the objects, and validation of the code. In chapter 3, we study the statistics of coherent structures for a smooth convection cell, where the coherent structures refer to the large-scale rolls, boundary layer, and thermal plumes. In addition, we study the turbulent kinetic energy budget and temporal statistics of temperature. This is followed by chapter 4, wherein we study the effect of surface roughness on global heat transport properties (Nu and Re), and identify the onset of enhanced heat flux regime, with different $Nu(Ra)$ scaling exponents.

In complement to the chapter 4, we show the significance of near-wall dynamics in heat flux enhancement in chapter 5. The enhanced heat flux regimes are found to have a connection with

boundary layer penetrating peaks. We investigate the role of secondary vortices near the rough surfaces, which help in evacuating the entrapped fluid, resulting in higher heat flux. We also study the cascade of secondary vortices in the cavity regions, yielding a thin thermal boundary layer and its perturbation, and multilayer characteristics of temperature profile in the near-wall region. Then we proceed to chapter 6, where we study the effect of inclination angle on *Nu* and *Re*. In particular, we unveil the effect of *Ra* on $Nu - \phi$ and $Re - \phi$ trends. For the smooth case, we identify the critical *Ra* below which inclined convection can be used to enhance the heat flux. Here, we identify the inclination angle that yields a maximum heat flux in both the smooth and rough cases. Further, the effect of roughness on $Nu - \phi$ and $Re - \phi$ trends are shown, and the roughness is found to delay the onset of thermal stratification.

In chapter 7, we study the effect of different roughness setups on heat flux through coherent structures in a 3D cubic cell. The heat transfer area for all the cases remains fixed for a systematic analysis. We investigate the statistics of thermal plumes and large-scale circulation to understand their connection with heat flux. In addition, we investigate the effect of roughness on small-scale statistics in the bulk region. The second-order vertical velocity and temperature structure functions are studied to understand the effect of roughness on strength of flow structures, which is also confirmed by power-spectra analysis and yields the Bolgiano $(BO59)$ scaling in the bulk region. Finally, we conclude the thesis and highlight some future works in chapter 8.

CHAPTER 2

Numerical details

This chapter contains the mathematical modeling of Rayleigh-Bénard convection and all the numerical details required for simulations. The discussion begins with the governing equations followed by the methodology of generating grids, and parallelization techniques. Further, a detailed discussion on the construction of surface roughness and diffuse interface immersed boundary method to handle them is provided. Finally, we validate the numerical setup for rough surfaces and show that different flow realizations do not impact the global heat transport properties.

2.1 Mathematical modeling and solver details

Rayleigh-Bénard convection is an incompressible buoyancy-driven flow governed by the continuity, momentum, and energy equations. The governing equations can be written in non-dimensionalized form, using the Boussinesq approximation, as

$$\frac{\partial u_i}{\partial x_i} = 0 \tag{2.1}$$

$$\frac{\partial u_i}{\partial t} + \frac{\partial (u_i u_j)}{\partial x_j} = -\frac{\partial p}{\partial x_i} + \sqrt{\frac{Pr}{Ra}} \frac{\partial^2 u_i}{\partial x_j \partial x_j} + \theta \delta_{iy} \tag{2.2}$$

$$\frac{\partial \theta}{\partial t} + \frac{\partial (u_j \theta)}{\partial x_j} = \frac{1}{\sqrt{PrRa}} \frac{\partial^2 \theta}{\partial x_j \partial x_j} \tag{2.3}$$

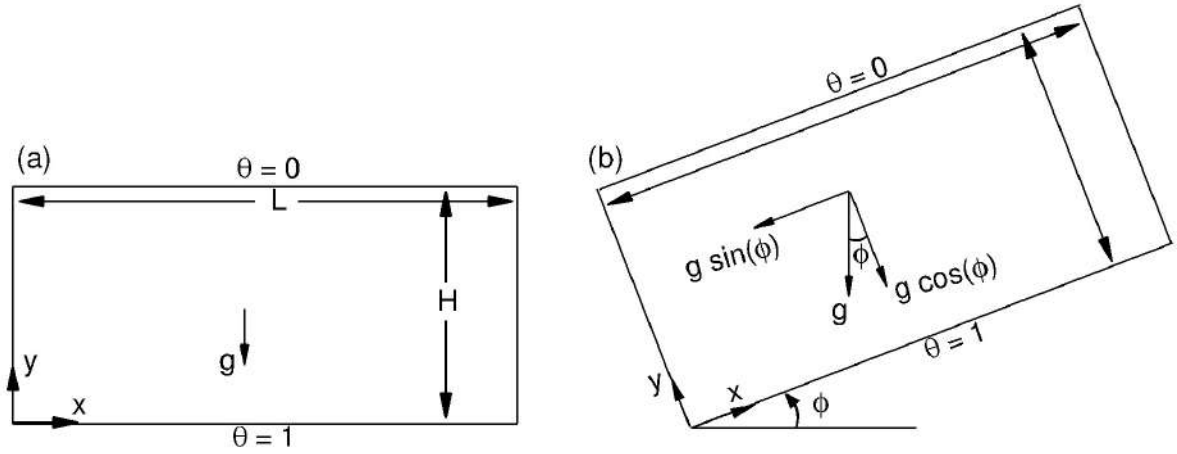

Figure 2.1: For a $2D$ cell, schematic of (a) the level or RBC case and (b) a tilted case showing the distribution of buoyant force along the isothermal plates and normal to them.

where $u_i = (u, v, w)$, $x_i = (x, y, z)$, and $\theta = (T - T_H)/(T_H - T_C)$ are non-dimensional velocity, Cartesian direction, and temperature, respectively. Here, the following reference scales are used to non-dimensionalize the governing equations: vertical spacing H between the isothermal walls, free fall velocity $\sqrt{g\beta\Delta T H}$ and temperature difference between the hot (T_H) and cold (T_C) plates $\Delta T = T_H - T_C$. Figure 2.1 shows the schematic of a level (frame a) and tilted convection cell, showing the distribution of thermal forcing along the isothermal walls and normal to them. In tilted RBC, thermal forcing acts in both the Cartesian directions, i.e., normal and along the isothermal surfaces, see Fig. 2.1b. The distribution of the thermal forcing is modeled by incorporating the inclination angle in the momentum equation through a body force. The resulting modified momentum equation becomes

$$\frac{\partial u_i}{\partial t} + \frac{\partial (u_i u_j)}{\partial x_j} = -\frac{\partial p}{\partial x_i} + \sqrt{\frac{Pr}{Ra}} \frac{\partial^2 u_i}{\partial x_j \partial x_j} + \theta \hat{e}_i \tag{2.4}$$

where $\hat{e}_i = (\sin\phi, \cos\phi)$. We consider the tilted RBC only for the two-dimensional case. Note that inclined case approaches the level case (RBC) as ϕ decreases.

The 2D simulations have been carried out in a rectangular cell of aspect ratio $\Gamma = 2$, while 3D flows are studied in a cubic box. For the investigation, air $(Pr = 0.7)$ is considered as the working fluid. In this thesis, we use $10^6 \leq Ra \leq 10^{10}$ and $Ra = 10^8$ for $2D$ and $3D$, respectively, to reveal the characteristics of turbulent thermal convection. For $2D$, the selected Ra range encompasses the turbulent flow features, and it is also suitable for identifying the onset of enhanced heat flux regimes in rough cases [53, 2]. For $3D$, the prime objective is to study the effect of different roughness configurations on the coherent structures (thermal plumes, and LSC). Thus, we have selected a fixed $Ra = 10^8$, which shows prominent plume structures and

LSC. Since vertical height between the isothermal surfaces changes due to roughness, we compute the effective height (h_{eff}) by assuming the same volume of fluid in smooth and rough cases [2]. Based upon this height, we calculate the effective *Ra*, which is defined as

$$Ra_{\text{eff}} = Ra\left(\frac{h_{\text{eff}}}{H}\right)^3 \tag{2.5}$$

A non-staggered finite volume method is used to solve the above set of governing equations 2.1-2.3. While the non-linear convective terms are handled using 2^{nd}-order Adams-Bashforth scheme, the diffusive and buoyancy terms are treated implicitly using the 2^{nd}-order Crank-Nicolson technique to retain the stability and robustness of the time marching procedure. All the resulting sparse linear systems are solved using the BiCGSTAB technique preconditioned by a highly scalable block diagonal version of the SIP procedure. The solver is parallelized using the standard MPI libraries to speed up the calculations. Time increment (Δt) for a stable time marching is selected based on the analytically obtained Kolmogorov time scale, $\tau_\eta = \sqrt{Pr/(Nu-1)}$, to ensure adequate temporal resolution which results in a maximum Courant number of 0.3. On the other hand, spatial resolution for all the cases reported here are chosen based on the Kolmogorov length scale, $\Delta x_{max}/\eta, \Delta y_{max}/\eta < 1$ and at least 8 grid points (N_{BL}) are ensured inside the thermal boundary layer estimated as $\lambda_\theta \sim H/(2Nu)$ [76].

2.2 Grid generation and parallelization

In the present work, we have used structured and non-uniform grid. The mesh is stretched in the vertical direction with a strong refinement near the isothermal surfaces, see Fig. 2.2. This setting yields the coarsest and the most refined grid spacing at the center of the domain and close to the isothermal surfaces, respectively. If x is a coordinate in a particular direction, where the domain spans up to the length L with N_x number of grid points, then the $(i+1)^{th}$ coordinate is given by [77]

$$x_{i+1} = L\frac{(\beta+2\alpha)(\frac{\beta+1}{\beta-1})^{\frac{\eta-\alpha}{1-\alpha}} - \beta + 2\alpha}{(1+2\alpha)(1+\frac{\beta+1}{\beta-1})^{\frac{\eta-\alpha}{1-\alpha}}} \tag{2.6}$$

Here, while $\eta((i-1)/(N_x-1))$ corresponds to the uniform grid, α and β are the grid refinement parameters. Note that $\beta(\geq 1)$ signifies the level of refinement; higher (lower) β indicates weaker (stronger) refinement. The other parameter (α) indicates the region of refinement. For $\alpha = 0$, the mesh is refined only near $x = L$, whereas, $\alpha = 0.5$ equally refines the mesh near both $x = 0$ and L. While we have used relatively heavy stretching for the roughness cases, a uniform mesh is used in most smooth cases. For $Ra \leq 10^8$, a smaller $\beta(= 1.1)$ is used for stronger refinement

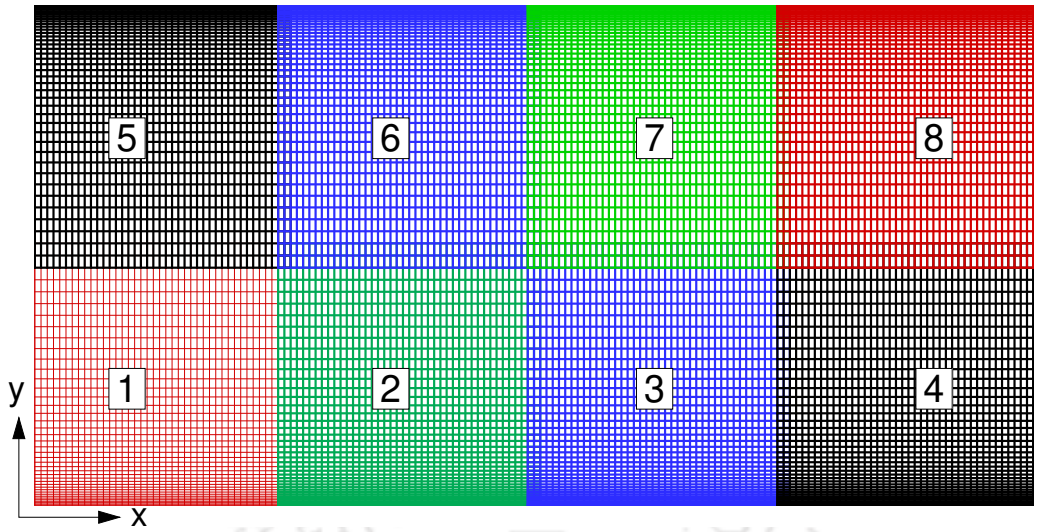

Figure 2.2: For a 2D cell, schematic showing decomposition of non-uniform mesh into 8 sub-domains for parallelization. The mesh is coarsest in the bulk, whereas it is refined close to the top and bottom walls.

near the walls. On the other hand, the grid refinement is relatively relaxed ($\beta = 1.4$) at higher $Ra > 10^8$. This setting of β is due to lesser grid points used for lower *Ra* cases, which demands a larger number of cells to resolve the roughness elements. The refined grid allows us to resolve the smallest length scale (Kolmogorov length scale) [78] and boundary layers [76]. In turbulent thermal convection, a flow is considered as well-resolved if the above-mentioned conditions are satisfied.

2.3 Construction of rough surfaces

Recently, rough surfaces have been used to obtain augmented heat flux [75, 79, 80]. However, in most of the previous studies, uniform roughness (mono-scale) configurations were used. To incorporate a range of roughness scales (different height and wavelength), we have used three irregular rough surfaces named as R_1, R_2, and R_3 for $2D$ (chapters 4-6) and conical roughness elements for $3D$ (chapter 7), as shown in Figs. 2.3 and 2.4, respectively. For $2D$, we have used triangular elements of irregularly varying heights and wavelengths. The roughness configurations are characterized by their maximum height, i.e., 5%, 10% and 20% of the cell height (H) for R_1, R_2, and R_3 cases, respectively. For $3D$ cases, as shown in Fig. 2.4, we use four different roughness set-ups: uniform (U), irregular (R), half-uniform (HU), and half-irregular (HR). In the uniform cases, the roughness height remains fixed $(h = H/10)$, whereas in the irregular cases, the height varies from $10-50\%$ of the maximum roughness height. In the half-variants of

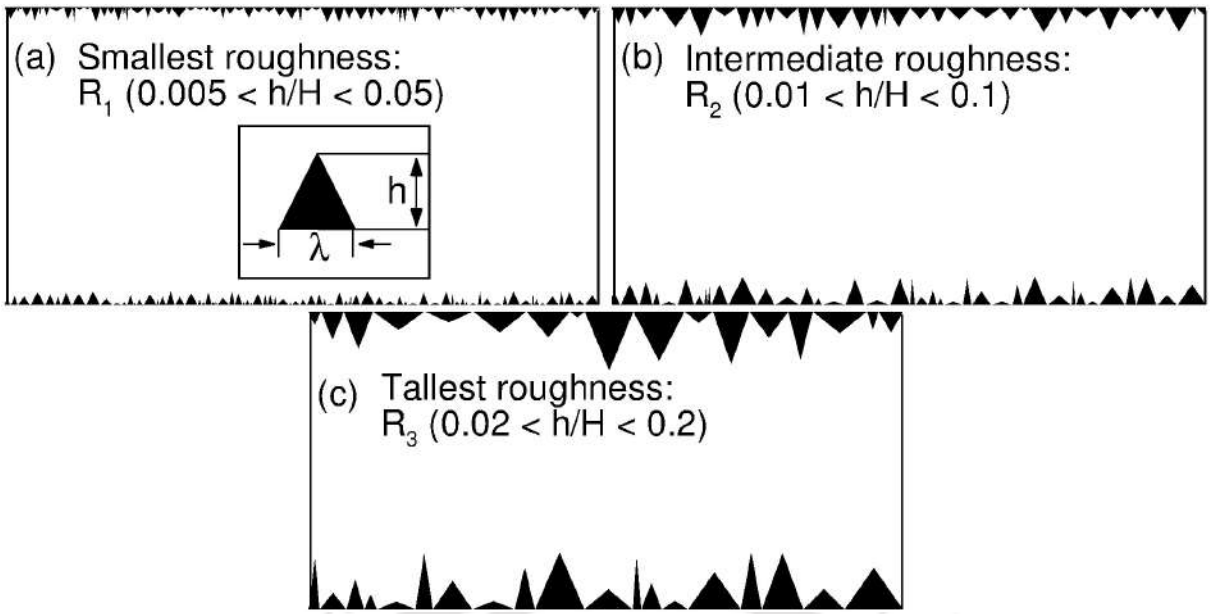

Figure 2.3: Schematic diagram of three random roughness set-ups for $2D$ cases, (a) R_1, (b) R_2, and (c) R_3, which are characterized by their maximum roughness heights. Inset shows the wavelength (λ) and height (h) of a roughness element.

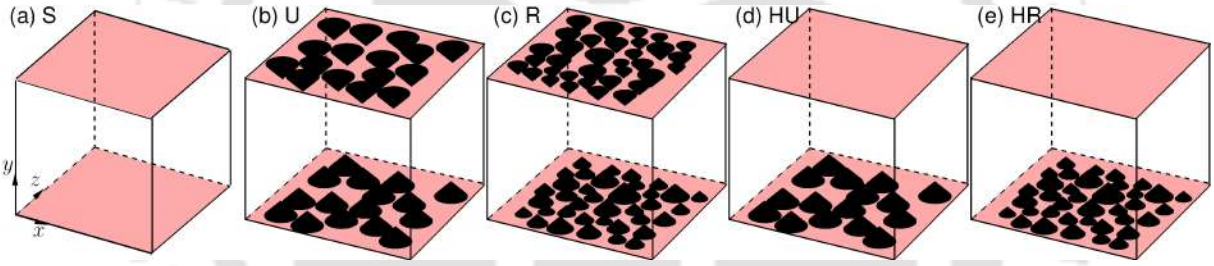

Figure 2.4: Schematic of the (a) smooth, (b) uniform, and (c) irregular, (d) half-uniform, and (e) half-irregular cases for $3D$ RBC. Temperature of all the bottom and top roughness elements are kept at $\theta = 1$, and 0, respectively.

U and R, roughness elements are placed only on the bottom surface. These irregular roughness geometries in both $2D$ and $3D$ typify improved multi-scale roughness, containing several roughness scales. The reason for selecting the roughness height and range is to instigate the boundary layer perturbation. Theoretically, boundary layer thickness and *Nu* are related as $\lambda_\theta = H/(2Nu)$, and $Nu \sim Ra^m$ [81]. These relations yield an inverse relation between λ_θ and *Ra*. The selected range of heights are appropriate to perturb the boundary layers.

To construct these surfaces, we employ a standard random number generator with normal distribution to generate amplitude and wavelength of the individual roughness elements. As h and λ are allowed to vary independently, a variety of triangular or conical-shaped elements fill the horizontal plates. It is to be noted that range of a truly random distribution is likely to

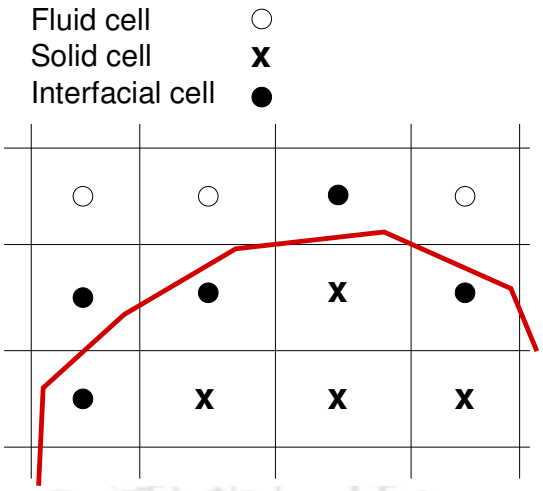

Figure 2.5: Schematic showing the fluid, solid, and interfacial cells for a $2D$ sample grid. The thick line (red) shows the linearized object boundary.

contain all possible heights and bases. However, since a finite horizontal span of the cell is used, only a finite number of such elements can be placed on the horizontal surfaces. Thus, in spite of choosing an element arbitrarily, finite number of them limits the possibility of the (λ, h) combinations. The present set-up is clearly an improved multi-scale roughness which contains a number of roughness scales. Note that since *Nu* is directly proportional to the heat transfer area, we have fixed the area in R_1, R_2, and R_3 cases. In $3D$, the following control parameters govern the heat transport properties: variation of roughness height and radius, heat transfer area (HTA), number of roughness elements (N), and spacing between them. In such scenarios, deciding a control parameter is very difficult due to their dependencies on each other. Since increase in heat transfer area (ΔHTA) is linked with all the other control parameters, we choose ΔHTA to construct the rough configurations, which is mathematically defined as

$$\Delta HTA_i = \frac{HTA_i - HTA_S}{HTA_S} \tag{2.7}$$

where $i =$ (U, R, HU and HR) and S represent the rough and smooth cases. In U and R cases, ΔHTA is 40%, whereas it is 20% for their half-variants. The increment of 40% in ΔHTA yields sufficient roughness elements to perturb the boundary layer. In HU and HR cases, the increment reduces to half due to presence of roughness elements only at the bottom plate.

2.4 Diffuse interface immersed boundary method

To handle the rough surface, we have used the diffuse interface immersed boundary method (DIIBM) [82, 83]. This method categorizes computational cells into fluid, solid, and interfacial

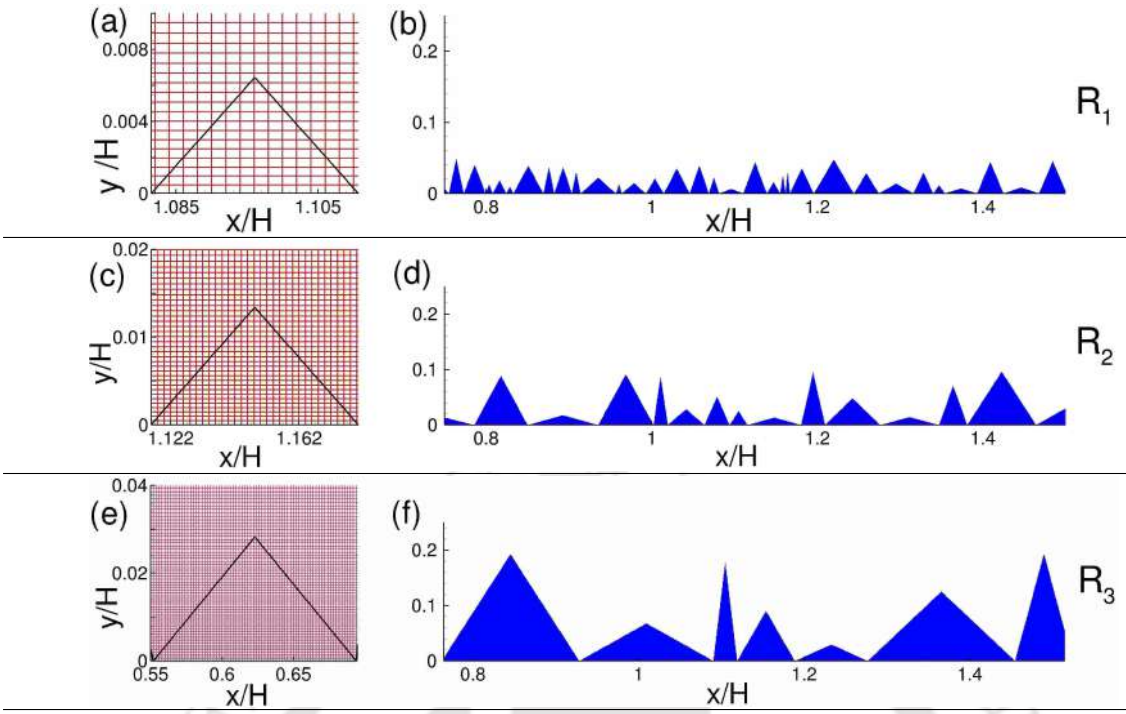

Figure 2.6: For the smallest $Ra = 10^6$, representation of mesh overlaid by linearized smallest roughness element (a, c, e), and the zero-level set representation (b, d, f) of a part of the linearized rough surfaces in R_1, R_2, and R_3 configurations. The roughness elements are shown in a zoomed view for better visualization.

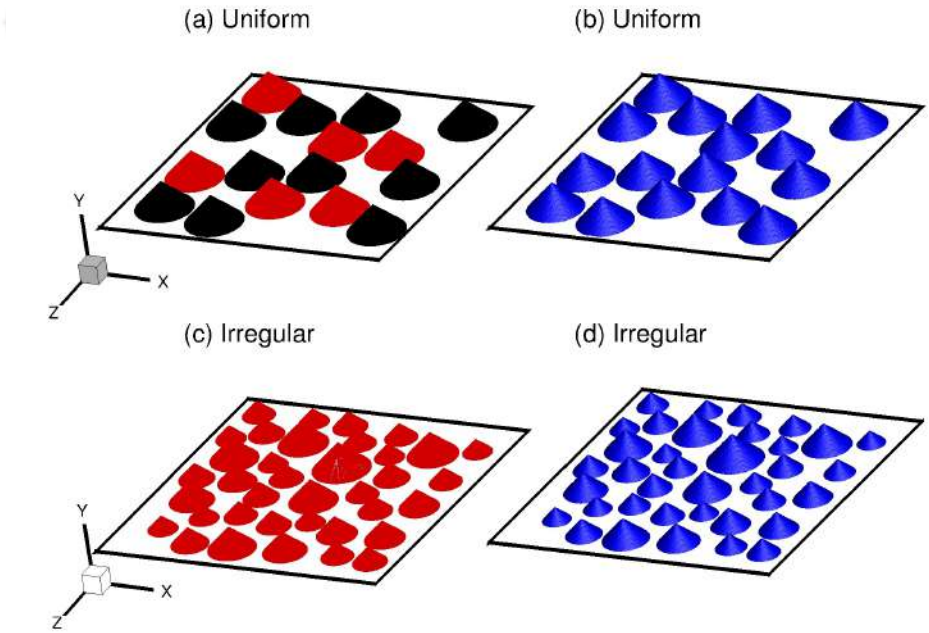

Figure 2.7: Representation of triangulated surface (a and c) and their zero-level set representation (b and d) for uniform (a and b) and irregular (c and d) cases. For better visualization, we show only the bottom surface and the roughness elements with different colors in the uniform case (frame a).

cells as shown in Fig. 2.5. They are identified by the volume fraction ($\phi = V_s/V_p$) criterion, which is defined as the ratio of volume of the body (V_s) present inside a computing cell (V_p). Note that for fluid, solid, and interfacial cells, $\phi = 0$, $\phi = 1$ and $0 < \phi < 1$, respectively. Thus, the body volume can be reconstructed whose volume is calculated by

$$V_{body} = \sum_{cell} \phi_i V_{pi}$$

and they are represented by the zero-level set function. Through the volume fraction, equation of conservation of momentum and motion of a rigid body are combined to construct a global equation which is solved in the entire domain. Boundary conditions are not directly imposed but enforced through the global equations, which can be written (after time-integration) as follows:

$$\sum_f F_f^{n+1} = 0 \tag{2.8}$$

$$(1-\phi_B)[\frac{u_{i,P}^{n+1} - u_{i,P}^{n}}{\Delta t} V_P + \aleph(\frac{\partial (u_i u_j)}{\partial x_j}) + \aleph(\frac{\partial p}{\partial x_i}) - \sqrt{\frac{Pr}{Ra}}\aleph(\frac{\partial^2 u_i}{\partial x_j \partial x_j}) - \aleph(\theta \delta_{i,y})] - \phi_B \frac{u_{i,P}^{n+1} - u_{i,B}}{\Delta t} V_P = 0 \tag{2.9}$$

$$(1-\phi_B)[\frac{\theta_P^{n+1} - \theta_P^{n}}{\Delta t} V_P + \aleph(\frac{\partial (u_i \theta)}{\partial x_j}) - \frac{1}{\sqrt{PrRa}}\aleph(\frac{\partial^2 \theta}{\partial x_j \partial x_j})] - \phi_B \frac{\theta_P^{n+1} - \theta_B}{\Delta t} V_P = 0 \tag{2.10}$$

where $\aleph$ is the numerical approximation, $n+1$ is the intended time step index, and P is the finite volume cell index. The global equations yield no-slip condition when $\phi = 1$, i.e., $u_{i,P} = u_{i,B}$ and $\theta_P = \theta_B$. Note that the scope of the boundary condition is limited to a computational cell. Thus, for reasonably well-resolved simulations, results are nearly identical to the sharp interface method. For more details, refer to De [82, 83].

Accuracy of the rendered volume is the key in the reconstruction of body surfaces, which depends upon the mesh size. Therefore, a sufficiently refined mesh in the wall-normal direction is employed to resolve the roughness adequately. In Fig. 2.6, for the three roughness cases, we show the grid resolution of the smallest roughness element (a, c, and e), and the zero-level set representation of a part of the linearized rough surface (b, d, and f). Note that we have shown the smallest roughness element at the smallest $Ra = 10^6$ because mesh refinement at higher Ra further improves the body resolution. The presence of sufficient grid points inside the roughness elements and nearly the exact representation of the rendered zero-level set function confirm the body resolution. The rendered volume of the object yields an error of 0.08% for $Ra = 10^6$, which is the smallest Ra case studied in this thesis. For the 3D case, we show the triangulated uniform and irregular surfaces and their zero-level set representation in Fig. 2.7.

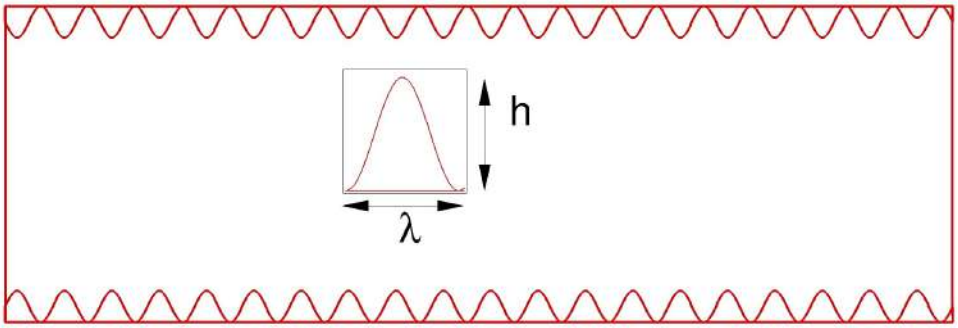

Figure 2.8: Schematic of the uniform sinusoidal roughness used by Zhu *et al.* [59]. Here both the wavelength (λ) and amplitude (h) are equal to 10% of the height of the convection cell.

For a grid size of $300 \times 300 \times 300$ (stretched in the vertical direction near the isothermal walls), the rendered volume of the object yields a maximum error of 0.085% and 0.4% for uniform and irregular cases, respectively. Considering these deviations in volume rendering as insignificant, we use the present numerical setup for further investigations. Note that this numerical setup is previously used for solving both stationary [84–86] and moving boundary problems [87].

2.5 Validation of the numerical setup

In this section, we establish the correctness of the diffuse interface immersed boundary method for roughness-aided convection by reproducing the previous results. Since conical roughness configuration has never been used earlier, we have restricted the validation test to $2D$ cases. Using sinusoidal roughness, Zhu *et al.* [59] investigated for optimum roughness geometry (wavelength to thickness ratio) in $2D$ RBC ($\Gamma = 2$). They found that $\lambda/h = 1$ yields highest heat flux. Here, the correctness of the current numerical setup is established by reproducing the results reported by Zhu *et al.* [59]. In Fig. 2.8, we show the reproduced sinusoidal roughness geometry for the validation. Owing to the higher computational cost, this test is restricted up to $Ra = 10^{10}$.

For a robust test, we select a global quantity (Nu) and vertical profiles of mean temperature. Figure 2.9 shows a direct comparison of the two above-mentioned quantities. For Nu, we observe the maximum and average difference of 7% and 3%, respectively. It is observed that deviation in Nu is minimal (less than 3% in most cases) except for a few cases. Also, the deviation nearly vanishes (see panel a) at higher Ra. Such small deviations are expected due to the implementation of boundary conditions, different numerical methods, complexity of the problem, and time sampling. We show comparison of the time-averaged vertical temperature profiles at two different Ra (in panels b and c). As expected, overlapping of the mean profiles at two different Ra

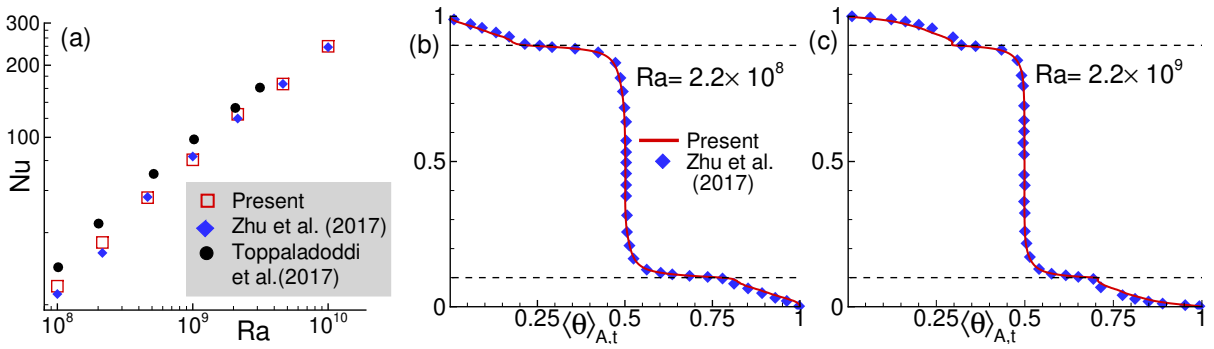

Figure 2.9: Comparison of (a) $Nu(Ra)$ and (b, c) time-averaged vertical temperature profile between the present data, Zhu *et al.* [59], and Toppaladoddi *et al.* [53] for sinusoidal roughness geometry. The horizontal dashed lines denote height of the roughness geometry.

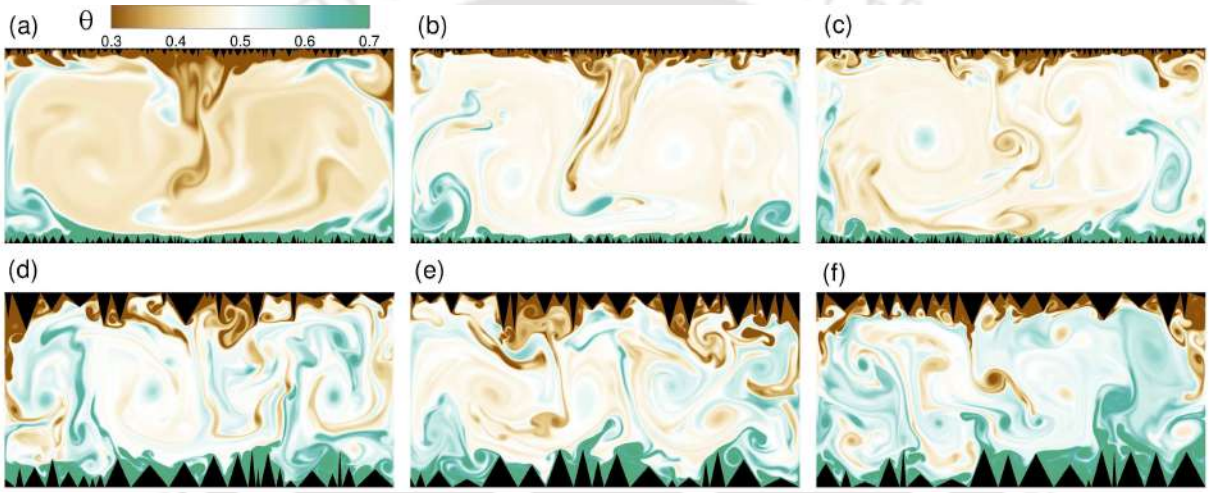

Figure 2.10: Instantaneous temperature field in different flow realizations for the smallest (a-c) and the tallest (d-f) roughness setups. The roughness boundaries are different, but the range of variation of their height and wavelength is same as that of R_1 and R_3 cases.

shows the accuracy of the present numerical setup.

2.6 Different flow realizations

In this thesis, we have selected three irregular (random) rough surfaces for $2D$ whose pattern does not repeat. Reason for selecting such complex geometries is to include a variety of roughness scale. To elucidate the dependence of heat flux and other transport properties on the arrangement of roughness elements, we investigate for three different flow realizations for both R_1 and R_3 in $2D$. On the other hand, for $3D$ cases, we have selected the most complex case, i.e., irregular (R), and use three different roughness geometries. This analysis also refers to the convergence of *Nu* for different flow realizations obtained in different roughness geometries. Geometric char-

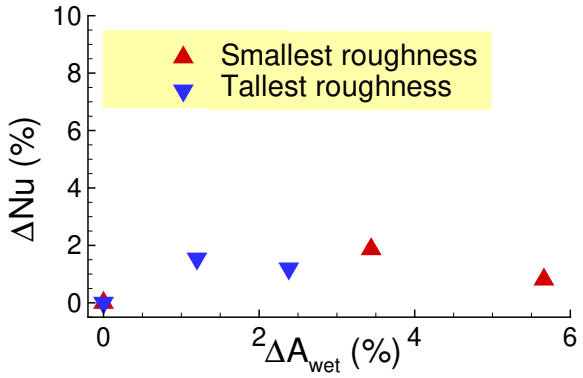

Figure 2.11: Variation of change (with respect to the first realization) in *Nu* with wetted area (ΔA_{wet}) of different flow realizations shown in Fig. 2.10. The filled triangle (red) and inverted one (blue) represent the smallest and tallest roughness geometries, respectively.

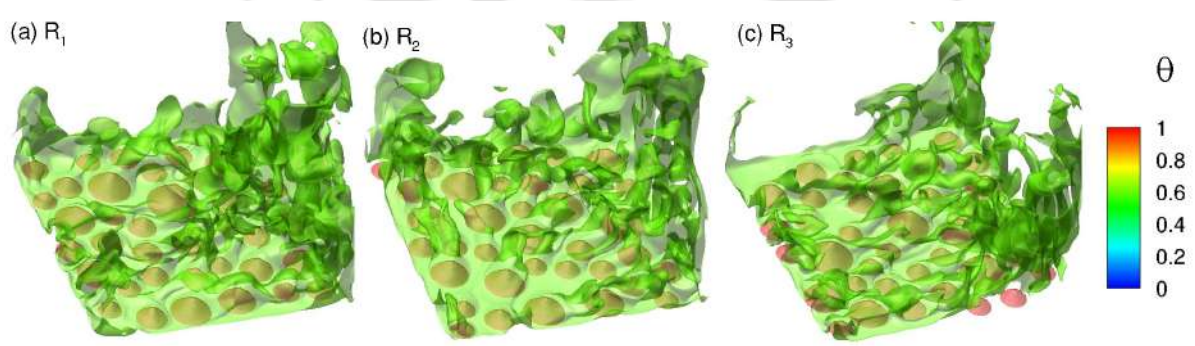

Figure 2.12: Instantaneous temperature iso-surfaces for different flow realizations in (a) R_1, (b) R_2 and (c) R_3. The roughness configurations are different, but the range of variation of their radius and height are same.

acteristics (height and wavelength) of these cases vary in the range of $0.005 \leq h/H \leq 0.05$ ($0.02 \leq h/H \leq 0.2$) for the smallest (tallest) roughness case.

In Fig. 2.10, instantaneous temperature field for three different realizations shows global flow structures. In R_1 (a-c) case, a double-roll state is evident in all the three realizations, whereas multiple-smaller rolls are evident in R_3 (d-f) case. The heat flux remains nearly same for the comparable wetted area, as shown in Fig. 2.11. We have calculated the change in heat flux (ΔNu) and wetted area (ΔA_{wet}) with respect to the first realization of both the smallest and tallest roughness cases. It is observed that the maximum variation in *Nu* (A_{wet}) remains less than 2% (6%), which is sufficiently small to show the independence of heat flux on the distribution of roughness height and wavelength. For $3D$ cases, we have considered three different realizations, $R_i (i = 1 - 3)$. Figure 2.12 shows the instantaneous temperature iso-surfaces for the three realizations. A similar large-scale circulation is evident in all the cases. Further, we have selected

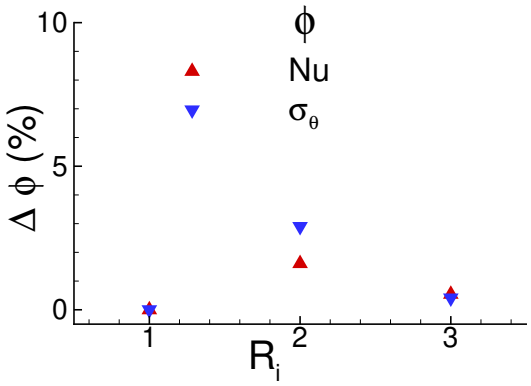

Figure 2.13: Variation of change in *Nu* and temperature variance with respect to the first realization for $3D$ cases $\mathrm{R}_i(i = 1 - 3)$.

two parameters for the comparison, change in *Nu* (ΔNu) and variance of temperature $(\Delta\sigma_\theta)$. As shown in Fig. 2.13, with respect to the first realization, a maximum deviation of 1.6% and 2.90% are observed in *Nu* and σ_θ. These results again ascertain the independence of heat transport properties on arrangement of roughness elements in $3D$ cases.

CHAPTER 3

Statistics of coherent structures in standard RBC

In this chapter, we have characterized the coherent structures in turbulent Rayleigh-Bénard convection using statistical measures. Absence of one lateral dimension leads to entrapment of plumes which are consequently released in the form of thermal jets. Axial non-uniformity in thermal boundary layers is eliminated at high Rayleigh numbers. The so-called slope and 99% *method produce identical boundary layer thickness whose power law variation confirms theoretical inverse-*Nu *scaling. Turbulent kinetic energy budget unveils a transport-dissipation balance near the walls, whereas buoyancy production nearly sustains turbulent fluctuations in the bulk region. Higher threshold for the correlation between vertical velocity and temperature results in faster convergence of plume and background share of dissipation while decay in volume fraction of plume region continues. Exponential distribution of temperature fluctuations suggests presence of hard turbulence at very large Rayleigh number. Changes in plume emission and its subsequent motion not only influence boundary layer instabilities but also causes departure from the -5/3 law in the frequency spectra.*

3.1 Introduction

In RBC, heat transfer rate is one of the main global characteristics, which can be expressed in terms of the Nusselt number (*Nu*) defined as the ratio of total to conductive heat flux, $Nu = qH/k\Delta T$ where q is the total heat flux and k the thermal conductivity of the fluid. In RBC, the heat is transferred from one plate to another through three coherent structures: boundary

layer, thermal plumes, and large-scale circulation, which have been considered as the basis of the $Nu(Ra)$ scaling laws. Malkus [24] studied fully turbulent convection and proposed the classical scaling, $Nu \sim Ra^{1/3}$. This theory was based on the marginal stability of the boundary layer. Later, Castaing *et al.* [29] experimentally proposed $2/7$ scaling law in the hard turbulence regime, $Ra > 4 \times 10^7$, where thermal plumes were considered as the heat carriers. In the limit of high *Ra*, Kraichnan [28] and Spiegel [88] found the $1/2$ scaling law, $Nu \sim (RaPr)^{1/2}$, which later became an evidence of the ultimate regime.

Later, Grossmann and Lohse [30] proposed a unifying scaling theory of *Nu* as a function of *Ra* and *Pr* based on the assumption that large-scale convection roll ("wind of turbulence") is responsible for the velocity and temperature fluctuations in the bulk region. The $Ra - Pr$ phase space was divided into four different regimes based on the domination of viscous (ϵ_u) and thermal dissipation (ϵ_θ) rates inside the boundary layer and bulk region. Zhu *et al.* [1] numerically studied two-dimensional (2D) RBC for six decades of Rayleigh number up to $Ra = 10^{14}$ and confirmed the transition to ultimate regime at $Ra = 10^{13}$, where both the kinematic and thermal boundary layer profiles are found to be logarithmic. The $Nu(Ra)$ scaling exponent (n) was observed as 0.38 which clearly shows the enhanced heat transport.

Boundary layer also plays an important role in understanding the dynamics and global features of RBC. Also, the behavior of thermal boundary layer has a strong connection with the scaling theories of heat transport. In a theoretical study, Grossmann and Lohse [45] showed the dependence of boundary layer thickness on aspect ratio. Ahlers *et al.* [18] reported that thermal boundary layer thickness follows a power-law dependence with *Ra*, viz., $\lambda_\theta \sim Ra^{-0.33\pm0.05}$. In a $2D$ square cell, Zhou *et al.* [46] proposed a dynamical boundary layer rescaling method. For more details, refer Sec. 1.2. Another important coherent structure is thermal plume, which is perceived as the detached thermal boundary layer and carries away the heat from the isothermal surfaces [31]. Emran & Schumacher [89] proposed a method to quantify the thermal plumes, which defines them by a positive correlation between vertical velocity and temperature fluctuations.

Identification of plumes from the background and their statistics in three-dimensional (3D) have been reported in a few previous articles [89, 90]. However in 2D, geometric constraints that result in morphological difference in emitted plumes affect the boundary layer which can cause a significant departure from the perceived behavior of coherent structures. In this chapter, we present a plume identification procedure that links to the thermal boundary layer structure. Scaling of global heat transport is viewed from the mechanisms that produce, transport or dis-

Table 3.1: Details of simulation parameters starting from the left: *Ra* is the Rayleigh number; Nu_c and Nu_{ref} are the Nusselt number obtained from the present simulation and Zhang *et al.* [48]; N_x and N_y are the number of grid points along the Cartesian directions; $\Delta x_{max}/\eta$ the ratio of max. grid spacing to the Kolmogorov length scale $\eta = HPr^{1/2}Ra^{-1/4}(Nu-1)^{-1/4}$; N_{BL} the number of points inside the thermal boundary layer estimated using $\lambda_\theta \sim H/(2Nu)$; $\Delta t/\tau_\eta$ ratio of time step to the Kolmogorov time scale; τ_{av} non-dimensional sampling time and the last two columns are ratios of numerical (ϵ^c) and analytical (ϵ^a) dissipation rates given by $\epsilon_u^c = \nu|\nabla \mathbf{u}|^2$, $\epsilon_\theta^c = \alpha|\nabla\theta|^2$, $\epsilon_u^a = \nu^3(Nu-1)RaPr^{-2}/H^4$ and $\epsilon_\theta^a = \alpha\Delta T^2 Nu/H^2$.

Ra	Nu_c	Nu_{ref}	$N_x \times N_y$	$\Delta x_{max}/\eta$	N_{BL}	$\Delta t/\tau_\eta$	τ_{av}	$\langle\epsilon_u^c\rangle/\langle\epsilon_u^a\rangle$	$\langle\epsilon_\theta^c\rangle/\langle\epsilon_\theta^a\rangle$
10^6	8.11	6.30	256×128	0.4678	11	0.0028	1000	0.99	1.00
3×10^6	9.77	7.64	320×160	0.5168	11	0.0031	1000	0.99	1.00
10^7	13.59	11.37	512×256	0.4821	12	0.0038	1000	0.99	1.00
3×10^7	17.54	16.50	640×320	0.5571	11	0.0047	1000	0.99	1.00
10^8	24.97	26.10	1024×512	0.5276	11	0.0030	1000	0.99	1.00
3×10^8	34.14	37.00	1360×680	0.5602	11	0.0014	1000	0.99	1.00
10^9	47.37	53.51	2048×1024	0.5472	12	0.0008	800	0.99	0.98
3×10^9	66.44	67.00	2400×1200	0.6669	8	0.0010	800	0.99	1.00
10^{10}	93.28	95.10	3200×1600	0.7376	9	0.0006	500	0.99	0.93

sipate turbulent kinetic energy. Thermal and viscous dissipation rates are analyzed in detail to establish a connection between the state of turbulence with fluctuating events that yield known shapes of distribution functions. Planar and temporal statistics are investigated to bring out key behavior in multiple layers where nature and effect of fluctuations are seemingly different. High resolution simulations carried out in this work have indicated a number of scaling laws that include heat transport, growth of boundary layers, structural contribution of plumes and global dissipation rates along four decades of Rayleigh numbers.

3.2 Numerical details

Incompressible buoyancy driven flows are governed by the continuity, momentum, and energy equations, see Sec. 2.1. All the simulations are carried out in a 2D rectangular cell of aspect ratio $\Gamma = 2$ with air ($Pr = 0.7$) being the working fluid, see Table 3.1. While no-slip condition is enforced for the velocity, isothermal condition is applied on the horizontal plates with the lateral

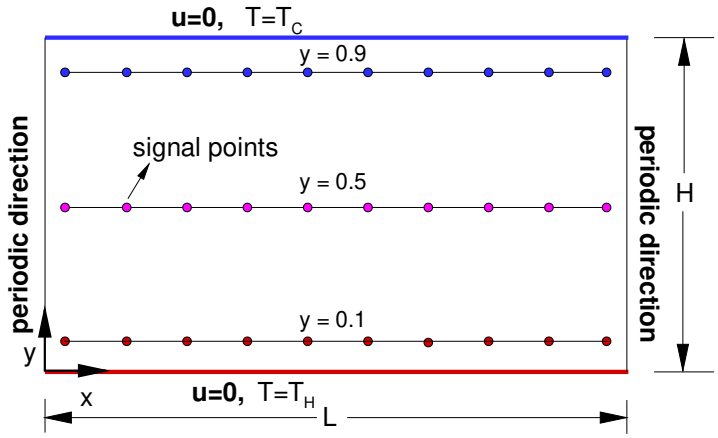

Figure 3.1: Schematic diagram of the physical set-up with geometric details and boundary conditions. To record time traces 10 equispaced stations are selected at three different heights as shown. Note, the flow is periodic in x-direction.

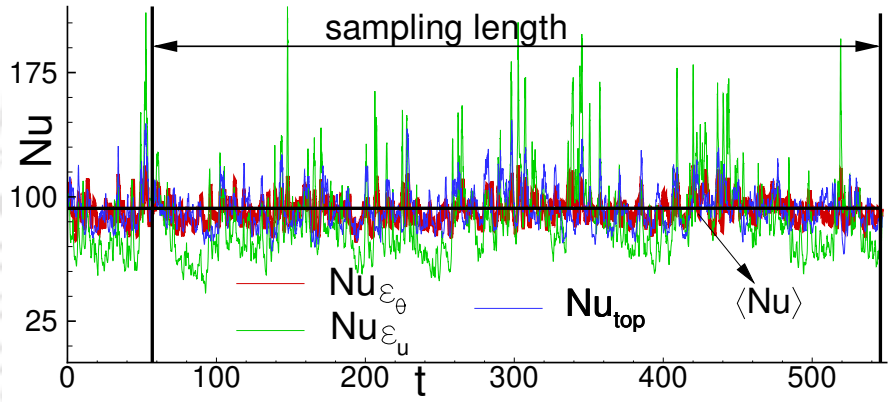

Figure 3.2: Sampling of Nusselt number based on thermal dissipation rate showing different flow states for the highest $Ra = 10^{10}$. Note that dash line representing its mean value, listed in Table 3.1.

walls taken as periodic boundaries. Ten equispaced signal stations are selected at three different heights to record time histories. Location of these numerical probes along with geometric features and boundary conditions are shown schematically in Fig. 3.1.

A small time increment (Δt) for a stable time marching is used to ensure adequate temporal resolution (maximum Courant number of 0.3). On the other hand, spatial resolution for all the cases reported here are chosen based on the Kolmogorov length scale, $\Delta x_{max}/\eta, \Delta y_{max}/\eta < 1$ and at least 8 grid points (N_{BL}) are ensured inside the thermal boundary layer estimated as $\lambda_\theta \sim H/(2Nu)$. Stevens et al. [91] suggested that for resolving small scale structures, ratio of numerically computed dissipation rates to the analytical estimates should remain close to

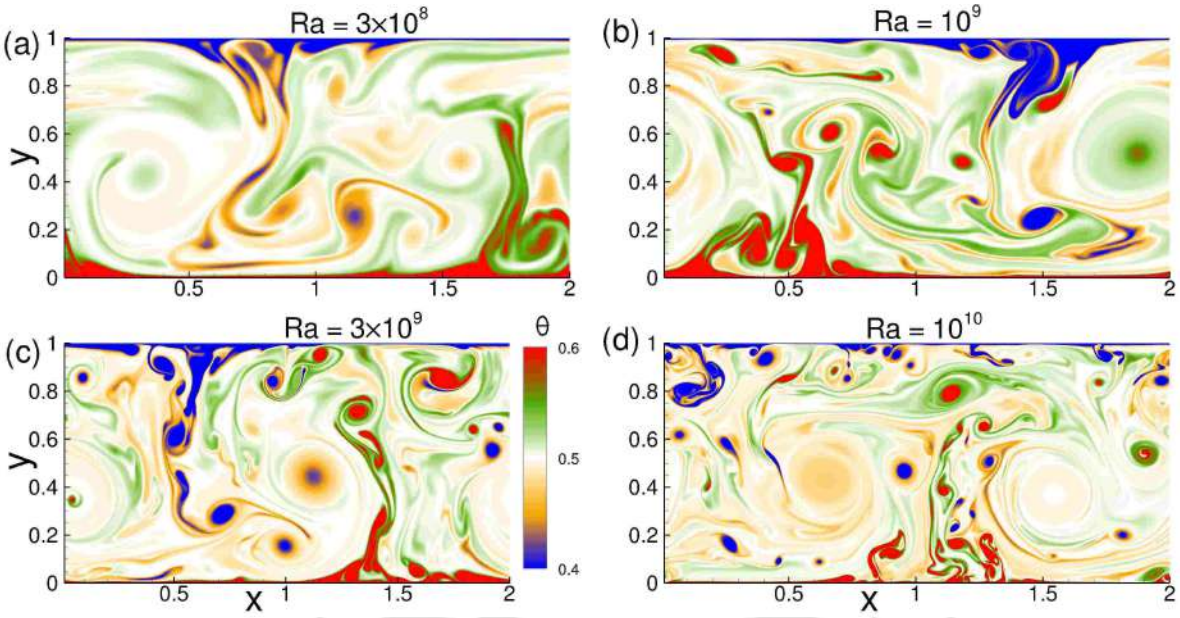

Figure 3.3: Snapshot of instantaneous temperature field for (a) $Ra = 3 \times 10^8$, (b) $Ra = 10^9$, (c) $Ra = 3 \times 10^9$, and (d) $Ra = 10^{10}$, showing evolution of small scale structures by breaking-up of large scale globules at high Rayleigh number.

unity. Further, volume-time average Nusselt number calculated using the thermal dissipation ($Nu_{\epsilon_\theta} = |\nabla\theta|^2$), viscous dissipation ($Nu_{\epsilon_u} = 1 + Pr|\nabla U|^2$) and on the horizontal surfaces ($\partial_y\theta$) are found to be consistent with maximum deviation of 5.59% occurring at the highest Rayleigh number. Convergence of these signals is used to identify the beginning of a statistically steady state, as shown in Fig. 3.2. All the numerical details along with the accuracy of computed dissipation rates are listed in Table 3.1. At the highest Rayleigh number, the most demanding case of all, one free fall time unit consumes approximately 4 hrs of CPU time on 24 computing cores. A simulation starts from the conduction state and once it enters a possible statistically stationary state long time sampling (τ_{av}) is carried out for converged statistical measurement.

3.3 Heat transport

Heat transport phenomenon is a key issue in turbulent Rayleigh-Bénard convection, where heat is carried by thermal plumes from boundary layers near the horizontal plates to the core region. These plumes are characterized as small scale structures of high temperature gradient. Further, large scale rolls (LSR) drive these thermal plumes into the core region. Snapshots of instantaneous temperature field at selected Rayleigh numbers are shown in Fig. 3.3 where two slow moving LSRs are noted embedded in a pool of small scale structures. Emergence of bright,

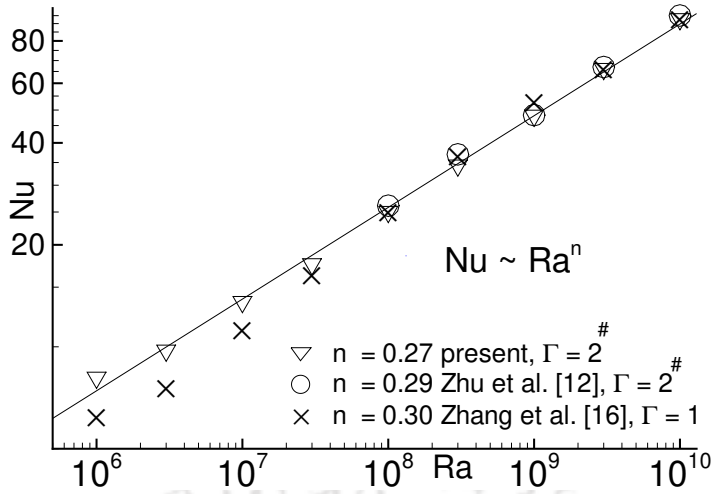

Figure 3.4: Scaling of *Nu* along four decades of *Ra*. Note that # indicates for periodic boundary conditions along the lateral walls.

Table 3.2: Columns from left to right represent *Ra*, vertically integrated shear production, buoyancy production and dissipation for all the cases.

Ra	$\int P_s dy$	$\int P_b dy$	$\int \epsilon dy$
10^6	-8.01×10^{-8}	8.49×10^{-3}	-8.51×10^{-3}
3×10^6	-6.11×10^{-8}	6.04×10^{-3}	-6.06×10^{-3}
10^7	-3.90×10^{-8}	4.75×10^{-3}	-4.76×10^{-3}
3×10^7	-1.07×10^{-8}	3.61×10^{-3}	-3.62×10^{-3}
10^8	-2.88×10^{-8}	2.87×10^{-3}	-2.87×10^{-3}
3×10^8	-5.21×10^{-7}	2.27×10^{-3}	-2.28×10^{-3}
10^9	1.07×10^{-6}	1.77×10^{-3}	-1.73×10^{-3}
3×10^9	5.87×10^{-6}	1.42×10^{-3}	-1.41×10^{-3}
10^{10}	-1.98×10^{-5}	1.09×10^{-3}	-1.01×10^{-3}

intense, highly localized small scale structures are observed with increase in *Ra* which indicates enhanced rate of heat transport. The two primary globules of hot and cold fluid seen at lower *Ra* (frames a,b) transform into thin jet-like structures at higher *Ra* (frames c,d) which can be attributed to the higher turbulent mixing. This formation of globules is not observed in 3D simulations as, unlike 2D, plumes are not restricted to a plane and they can have an extra lateral direction to escape. The entrapped fluid inter-mixed with its surrounding develops a strong vertical temperature gradient which subsequently shoots up in the form of a jet from the globules

into the bulk region. Effect of this phenomenon is also observed in planar statistics discussed in later section.

Instantaneous temperature field indicates enhancement in heat transfer owing to an increase in number of plumes with *Ra* and stronger turbulent mixing. This raises the important issue to quantify the enhancement of heat transfer rate with *Ra*. Since *Nu* is conceived as gradient of temperature $(\partial_y \theta)$, heat transfer rate can be expressed in terms of it which paves the way to establish a relation between heat transport and the imposed temperature difference (*Ra*). In Rayleigh-Bénard literature power-law behavior between *Nu* and *Ra* has long been established. The marginal stability theory proposed by Malkus [24] gave the resulting exponent $n = 1/3$ which is now referred to as the 'classical regime', and later, Kraichnan [28] predicted the behavior in the limit of higher Rayleigh number and proposed $1/2$ scaling law, $Nu \sim (RaPr)^{1/2}$, known as the 'ultimate regime'. Consequently, different regimes exist with different scaling exponent along the broad *Ra* spectrum. Hence, it is important to explore the transition between the classical and ultimate regime. Also, deviation in scaling exponent from the theoretical prediction $(Nu \sim Ra^{1/3})$ has been reported in a number of numerical and experimental studies with one such instance being Castaing *et al.* [29] where the scaling exponent was close to $2/7$. In the present work Nusselt number based on the thermal dissipation is averaged over the entire domain for the estimate, and for convenience *Nu* replaces $\langle Nu_{\epsilon_\theta} \rangle_{V,t}$ throughout the paper. A least-square fit of the data results in $Nu = 0.18\,Ra^{0.27}$ as shown in Fig. 3.4. The present exponent is in good agreement with the previous results [29, 92] where periodic horizontal directions were used, while marginal deviation is noticed with Zhang *et al.* [48] where lateral boundaries were treated as no-slip walls.

In shear flow turbulence approximate balance between shear production and dissipation leads to important scaling arguments. However, in turbulent convection, the flow is mainly sustained by a strong correlation between the vertical velocity and temperature. Moreover, while the near wall region is dominated by thermal instabilities that produce high gradient plumes, the bulk region is well mixed and homogeneous in nature. This indicates a different transport mechanism of turbulent kinetic energy at different parts of the domain. Dynamical equation for turbulent kinetic energy (TKE), $1/2\overline{u_i' u_i'}$, is obtained by contracting the equation for fluctuation and sub-

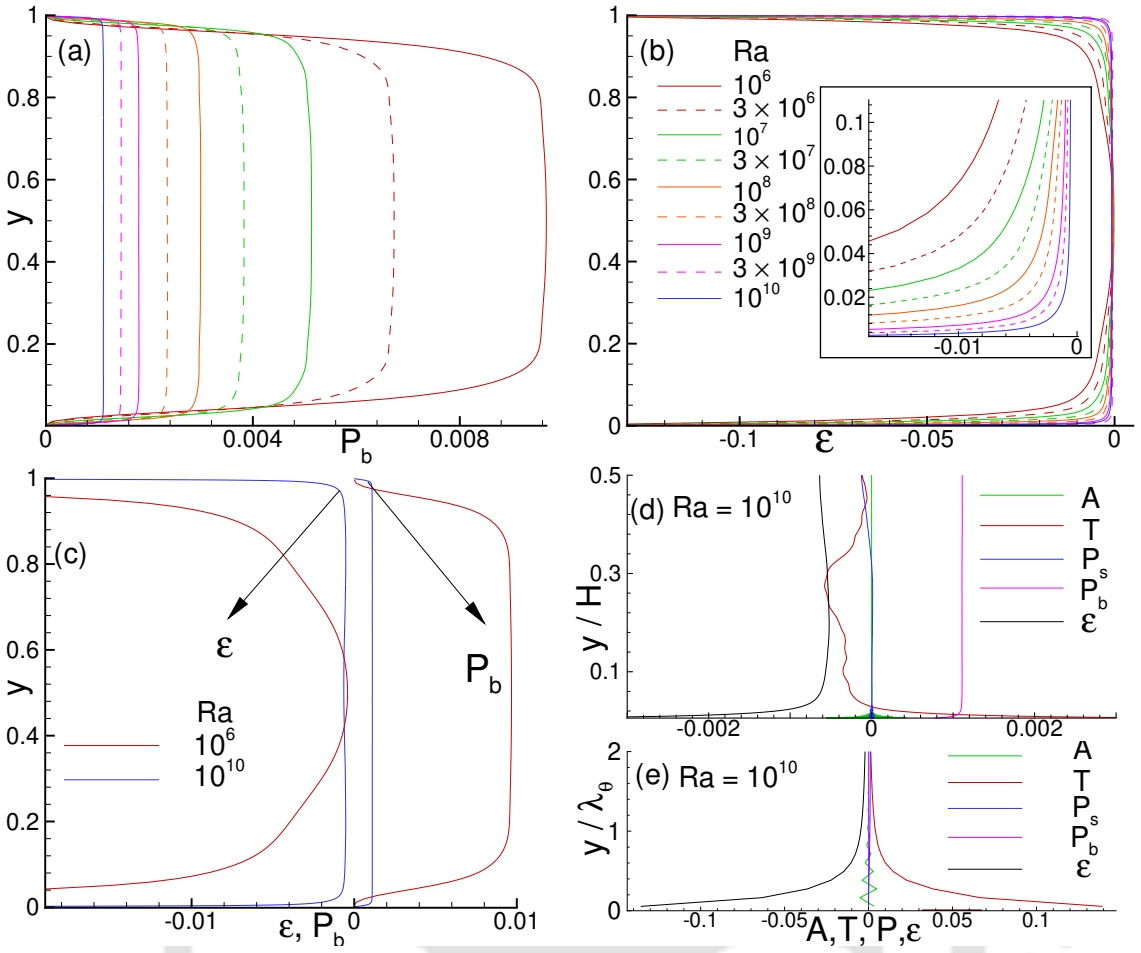

Figure 3.5: Turbulent Kinetic energy budget for $10^6 \leq Ra \leq 10^{10}$: (a) Buoyancy production ($v'T'$); (b) Dissipation rate (ϵ); (c) balance between dissipation and buoyancy production for the lowest and highest *Ra* simulations; (d) and (e) represents the kinetic energy budget in the core region and inside the thermal boundary layer for $Ra = 10^{10}$, respectively.

sequently effecting ensemble average ($\langle \ \ \rangle_{A,t}$) which results in

$$\underbrace{\partial_t(\frac{1}{2}\overline{u_i'u_i'}) + U_j\partial_j(\frac{1}{2}\overline{u_i'u_i'})}_{A} = \underbrace{-\overline{u_i'u_j'}S_{ij}}_{P_s} + \underbrace{g\beta\overline{u_i'\theta'}\delta_i y}_{P_b} \underbrace{-2\nu\overline{s_{ij}'s_{ij}'}}_{\epsilon} \underbrace{-\partial_j(\frac{1}{\rho}\overline{u_j'p'} + \frac{1}{2}\overline{u_i'u_i'u_j'} - 2\nu\overline{u_i's_{ij}'})}_{T} \tag{3.1}$$

where in the left-hand side temporal change and spatial transport combine to produce the advection (A). As the first term on the right-hand side can be cast into divergence form it is usually termed as transport (T) which being identically zero on the boundaries only redistributes the kinetic energy inside the physical region. The second and third terms are known as the shear (P_s) and buoyancy production (P_b) that feed energy to sustain turbulent fluctuations. The last term indicates dissipation (ϵ) of TKE which is known to occur primarily at small scales. P_b, P_s and

ϵ terms in the above equation are vertically integrated and listed in Table 3.2. While the buoyancy production and dissipation profiles are shown for all the Rayleigh numbers in Figs. 3.5(a) and 3.5(b), respectively, contribution of the principal terms for two extreme cases are shown in frame (c). In order to determine the relative importance of the transport and production of TKE near-boundary and the bulk regions are shown separately in frame (d) and (e).

Both buoyancy production (P_b) and dissipation (ϵ) increases sharply in the boundary layers. While P_b peaks outside the boundary layers, global maximum of ϵ can be used as a measure for boundary layer thickness. Though peak dissipation does not change with *Ra*, buoyancy production drops nearly ten manifolds across two extreme *Ra*. This indicates importance of shear production at increasing *Ra* and Table 3.2 confirms it, though the ratio P_s/P_b remains as small as 10^{-2}. With increase in *Ra* as the thermal plumes take the form of thin sheets to jets to high intensity spots their probability of occurrence improves at a given height that results in a lower area-averaged correlation $\langle v'\theta' \rangle$ while high velocity gradient of small scale structures favor a better correlation of the Reynolds stress and mean velocity gradient. Budget estimate at two extreme *Ra* (see frame c) indicates a slow changing bulk region with significant inhomogeneity transforms to a perfectly homogeneous mixture that starts right next to the boundary layers. When the vertical direction is scaled appropriately using the boundary layer thickness (λ_θ) near the wall and by the height (H) outside it, a multilayer behavior is noticed. Near the wall owing to stronger viscous effects velocity fluctuation is small which results in a smaller buoyancy production but viscous transport is significant which leads to an approximate balance rule $T \approx \epsilon$. Plumes that erupt from the boundary layer region moves out of it and continue towards the bulk region losing momentum slowly owing to greater heat exchange at the outer layers. As buoyancy production takes off decelerating plumes enter the bulk region when they lost their momentum leading to negligible transport and a different balance rule $P_b \approx \epsilon$ prevails. This multilayer behavior is only conceived at higher *Ra* owing to thinner wall layer, perfect homogeneous region, a greater probability of separation between them and high intensity small scale structures.

3.4 Plume statistics

Zhou and Xia [93] and Guo *et al.* [68] described thermal plumes as mushroom-like structures with a narrow cap of sharp temperature gradient and diffusive tail. These sharp temperature gradients are extreme fluctuating events of thermal dissipation rate and mostly found close to the isothermal walls. Thus, plumes can also be considered as permanently detached fragments

Table 3.3: Prefactor and the exponent of power-law fit ARa^m for volume fraction and dissipation of the plume and background regions defined by Eq. 3.2.

	volume fraction				dissipation			
δ (%)	A_{pl}	m_{pl}	A_{bg}	m_{bg}	A_{pl}	m_{pl}	A_{bg}	m_{bg}
0	0.72	−0.01	0.31	0.02	0.19	−0.21	0.23	−0.25
0.1	0.64	−0.01	0.38	0.01	0.37	−0.26	0.13	−0.20
1	0.80	−0.04	0.41	0.02	0.36	−0.27	0.20	−0.22
5	2.03	−0.13	0.47	0.02	0.07	−0.18	0.29	−0.24
10	3.52	−0.18	0.56	0.02	0.03	−0.13	0.29	−0.25

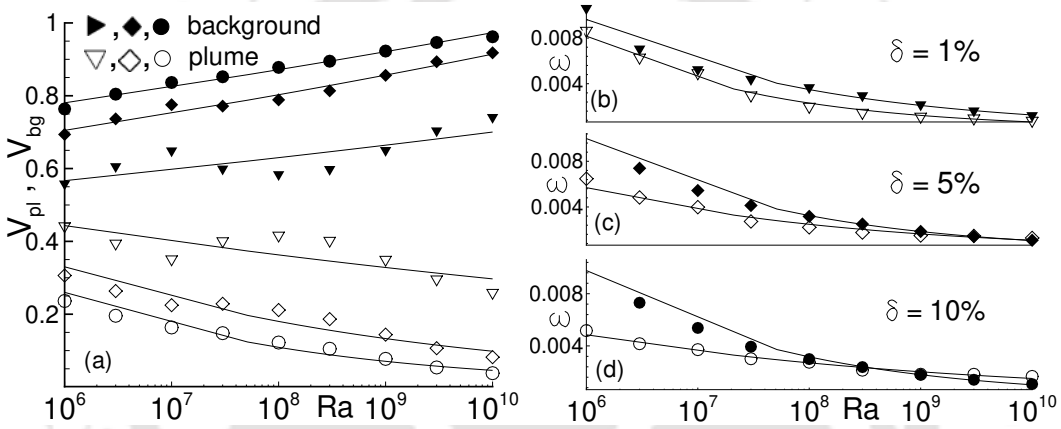

Figure 3.6: *Ra* and δ dependency of (a) volume fraction of plume (V_{pl}) and background (V_{bg}), variation of dissipation rates (ϵ_{pl} and ϵ_{bg}) for (b) $\delta = 1\%$, (c) $\delta = 5\%$, and (d) $\delta = 10\%$. Here V_{pl} and V_{bg} are computed using Eq. 3.2.

of thermal boundary layers that carry heat while they move into the bulk region [31]. Since heat is carried from the hot plate by the thermal plumes, subvolume V_{pl} was termed as “skeleton" by Emran and Schumacher [89]. In the present work, a positive correlation between vertical velocity and temperature fluctuations is used to quantify the plume dominated region. Domain of the cell (V) is decomposed [47, 89] into two disjoint subsets or subvolumes: plume-dominated region (V_{pl}) and turbulent background (V_{bg}) by using the following rule

$$\begin{aligned} V_{pl} &= \{\mathbf{x} \in V : v'\theta'/\Gamma > \delta\} \\ V_{bg} &= \{\mathbf{x} \in V : v'\theta'/\Gamma < \delta\} \end{aligned} \tag{3.2}$$

where Γ is the global instantaneous maximum of $v'\theta'$ and free parameter δ is the threshold which is varied as $0, 1\%, 5\%, 10\%$. Also mean thermal dissipation rate on both the subsets are defined

as

$$\epsilon_{pl} = \langle \epsilon_\theta \rangle_{V_{pl},t} = \Big\langle \frac{1}{V_{pl}} \int_{V_{pl}} \epsilon_\theta(\mathbf{x},t) dV \Big\rangle_t$$
$$\epsilon_{bg} = \langle \epsilon_\theta \rangle_{V_{bg},t} = \Big\langle \frac{1}{V_{bg}} \int_{V_{bg}} \epsilon_\theta(\mathbf{x},t) dV \Big\rangle_t \tag{3.3}$$

Power law fits for both volume fraction and dissipation rates are obtained in the least-square sense. All the exponents and prefactors of the scaling law at three different threshold are listed in Table 3.3. In order to bring out the scaling behavior, both volume fraction and dissipation are plotted with *Ra* in a log-log scale at three threshold values in Fig. 3.6. It is observed that Eq. 3.2 is not reliable for $\delta < 1\%$ as no consistent scaling rule emerges which does not support $3D$ results of Emran and Schumacher [89].

A falling trend of V_{pl}, seen in Fig. 3.6(a), indicates that boundary layer thickness decreases and consequently dissipation effect is subdued at higher *Ra*. Further, decreasing dissipation effect also points towards ultimate regime of thermal convection as according to Spiegel hypothesis [88] heat transport is independent of ν and α in the ultimate regime. On the contrary, increase in V_{bg} with *Ra* implies homogeneity is attained in a larger domain as *Ra* increases. This diverging trend in V_{pl} and V_{bg} becomes clearer at $\delta > 5\%$, while in $3D$ simulations a cleaner power law emerges at a δ as small as 1%. This points out a slower growth of fluctuations in $2D$ which finally settle to a state which does not reflect clear random behavior. Power law exponents for both volume fraction (0.02) and dissipation (0.25) for the background remains nearly same at all threshold. However, the same undergoes significant changes, -0.04 to -0.18 for V_{pl} and -0.27 to -0.13 for ϵ_{pl}, in the plume region. Thermal dissipation rate decays with increasing *Ra* for both plume and background dominated regions. It should be noted that background region, in contrast to plume region, is less sensitive to the threshold which is evident as V_{bg} grows almost linearly, and for a large *Ra*, $V_{bg} \approx V$. These trends are in complete agreement with the previous $3D$ results [89, 92].

3.5 Boundary layer

All the scaling theories of heat transport that predicts the functionality $Nu(Ra)$ have strong connections with the behavior of boundary layers. First such proposition was made by Malkus [24], widely known as the “Classical scaling theory", where decoupling of top and bottom boundary layers is reasoned for the heat transport that results into the classical scaling law,

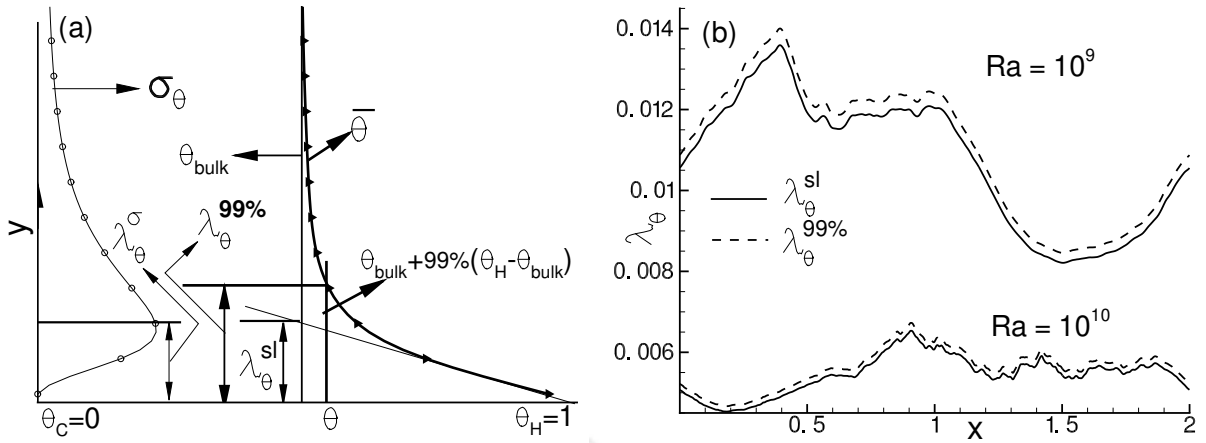

Figure 3.7: Geometric construction of boundary layer thickness computed from bulk temperature difference ($\lambda_\theta^{99\%}$), slope method (λ_θ^{sl}), and rms method (λ_θ^{σ}) is shown on the left (a) and on the right (b) λ_θ computed using the first two methods are seen identical at all *Ra*, though for clarity only two higher *Ra* are shown.

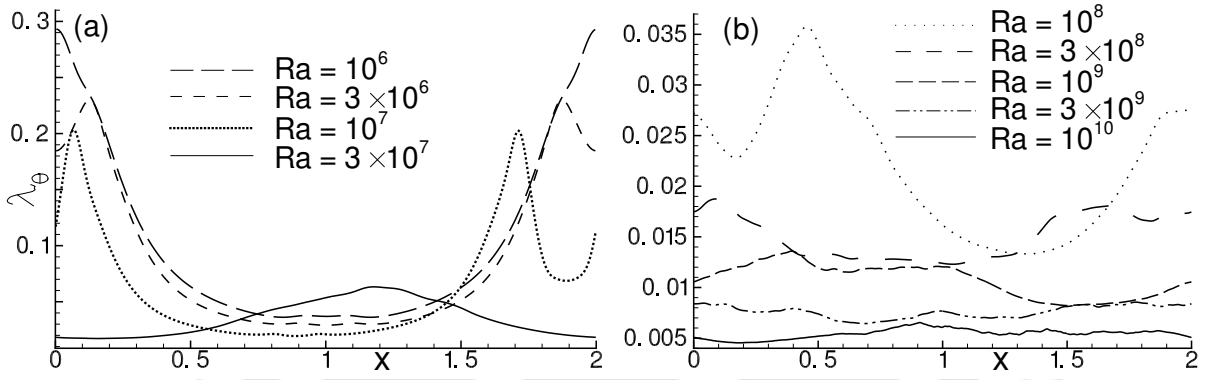

Figure 3.8: Thermal boundary layer thickness variation along horizontal direction near the bottom plate for (a) $Ra = 10^6, 3 \times 10^6, 10^7$ and 3×10^7 and (b) $Ra = 10^8, 3 \times 10^8, 10^9, 3 \times 10^9$, and 10^{10}.

$Nu \sim Ra^{0.3}$. Later, Spiegel [88] proposed that boundary layer does not play any explicit role in heat transport in the ultimate regime, known for the scaling exponent close to 1/2. After a rigorous analysis through a number of experiments and numerical simulations, Grossman and Lohse [30] proposed a unifying theory where laminar flow is predicted inside the boundary layer region for classical regime while existence of turbulent boundary layer is only argued in the ultimate regime. Afterwards Zhu *et al.* [1] confirmed the logarithmic velocity and temperature profiles in the transition to ultimate regime at $Ra = 10^{13}$ which paves the way to study the behavior of boundary layers at higher *Ra*.

In the present study boundary layer thickness is computed using three different techniques:

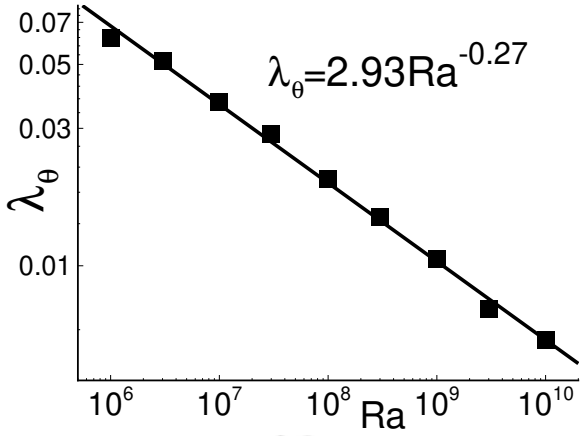

Figure 3.9: Scaling of the boundary layer thickness with *Ra* constructed using least square approximation.

vertical height from the horizontal plates to the point where linear extrapolation (tangent at the plate) of the average temperature $\langle\theta\rangle_{A,t}$ meets the bulk mean temperature termed as λ_θ^{sl}, and vertical distance from the plates where 99% of the temperature difference between the plate and bulk is recovered termed as $\lambda_\theta^{99\%}$, and vertical position of peak rms in the $\langle\theta'^2\rangle_{A,t}$ termed as λ_θ^{σ}. A schematic diagram depicting all the geometric construction is shown in Fig. 3.7(a). Variation of thermal boundary layer at the bottom plate along the horizontal direction for two highest *Ra* are shown in Fig. 3.7(b) which clearly demonstrates equivalence of the first two techniques explained above as they predict near identical boundary layer thickness.

Horizontal variation of the thermal boundary layer for different *Ra* is illustrated in Fig. 3.8. At low *Ra* presence of large scale rolls is strongly felt as λ_θ peaks near a uprising plume and remains almost constant away from it. Stronger horizontal motion of the rolls drive the flow in the intermediate region and boundary layer evidently has an integral effect with the core. With increase in *Ra* thermal boundary layers isolate themselves from the intermediate and bulk region as the uniform horizontal variation tends towards a nearly constant λ_θ. Thus, the boundary layer profile takes the shape of horizontal surface as it envelopes them which is reported to be an indication of the ultimate regime where heat transport is hardly affected by boundary layers and nearly the entire heated surface acts as a hotspot region. This transformation is attributed to the increase in number of small scale structures and decreasing effect of large scale rolls. Moreover, only at higher *Ra* signs of turbulent boundary layer is observed as smooth horizontal variation of λ_θ changes to locally oscillating one.

All the above arguments clearly show that characteristic of boundary layer changes with *Ra* and thus global heat transport. In order to study the effect of *Ra* on λ_θ, a relation is established

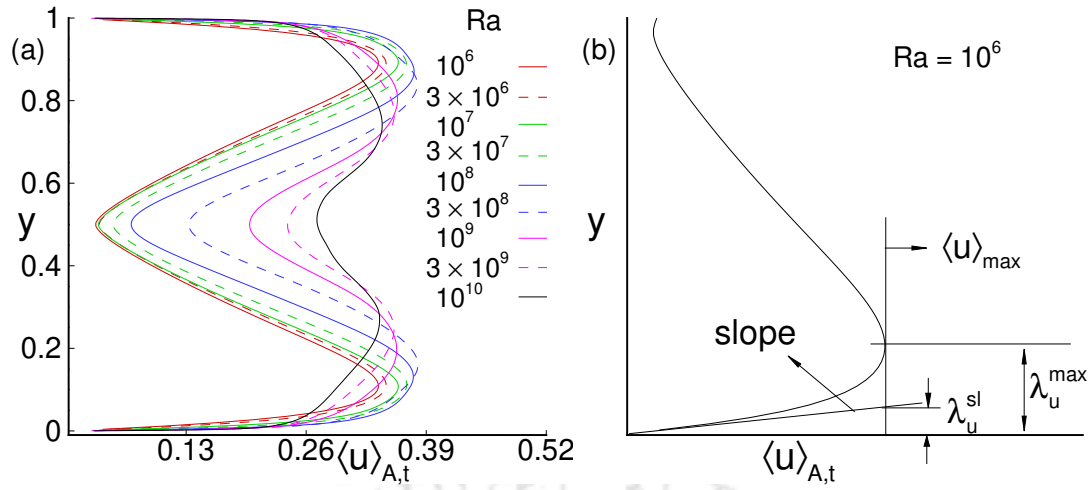

Figure 3.10: Vertical variation of area-time averaged absolute horizontal velocity $(|u|_{A,t})$ in frame (a), while a geometric representation of viscous boundary layer thickness computed using the slope (λ_u^{sl}) and maximum (λ_u^{max}) method in frame (b).

by computing the global thermal boundary layer thickness by effecting horizontal area-average $\langle\lambda_\theta\rangle_{A,t}$ for each *Ra*. A power-law behavior of $\lambda_\theta(Ra)$, in the least-square sense, reveals the scaling as $\lambda_\theta = 2.93\ Ra^{-0.27}$ as shown in Fig. 3.9. Overall conduction phenomenon is responsible for heat transport inside the thermal boundary layer, thus one can easily obtain a scaling relation $\lambda_\theta \sim (1/2)Nu^{-1}$ if λ_θ is used as the system height in the expression of *Nu* [94]. Moreover, $Nu \sim Ra^n$ scaling in Sec. 3.3 and $\lambda_\theta \sim Ra^{-n}$ here confirms the theoretical estimate $\lambda_\theta \approx Nu^{-1}$.

Next, viscous boundary layer causes maximum hindrance to heat transport and plays crucial role in its mechanism. Ahlers *et al.* [18] have proposed different methods to calculate viscous boundary layer thickness. For instance, time-average or area-time average of velocity and its fluctuation is used to compute the thickness. The first investigation of viscous boundary layer was carried out by Xin *et al.* [95], and Xin and Xia [96] using a light-scattering technique in a cylindrical cell and reported a weak *Ra* dependency as $\lambda_u^{sl}/L \sim Ra^{-0.16}$. Later, Sun *et al.* [97] computed the thickness in center of the domain above the bottom plate and obtained the dependency as $\lambda_u^{sl} \sim Ra^{-0.27\pm0.01}$ in a rectangular cell of unit aspect ratio and $Pr = 4.3$. The obtained scaling law is in good agreement with the Prandtl-Blasius relation. Furthermore, Verzicco and Camussi [19] ascertained the dependency as $\lambda_u^{sl} \sim 0.95Ra^{-0.23}$ using the area-time averaged profile in the same aspect ratio but for air $(Pr = 0.7)$ as a working fluid.

A comparative study of viscous boundary layer profiles computed from horizontal velocity and its variance has been carried out here. Time-averaged absolute horizontal velocity $|u|$ and

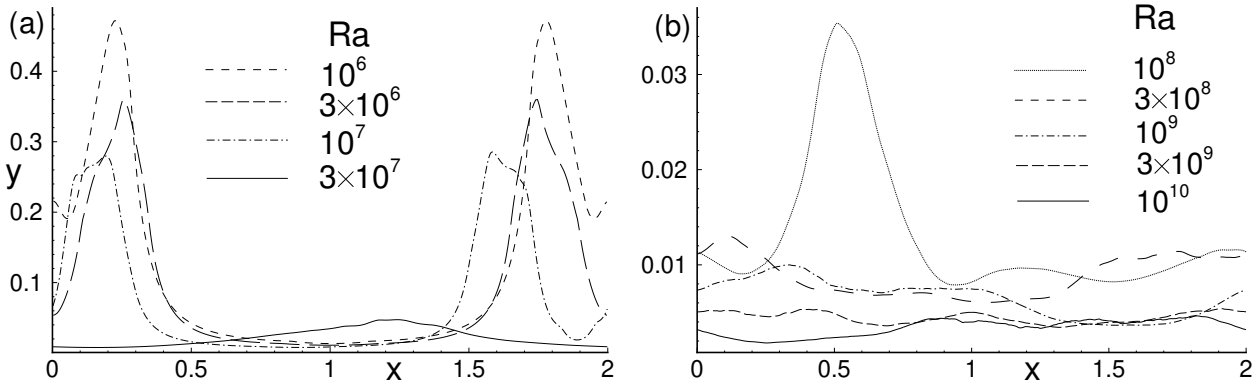

Figure 3.11: Viscous boundary layer thickness computed from absolute horizontal velocity for all *Ra* cases using the slope method.

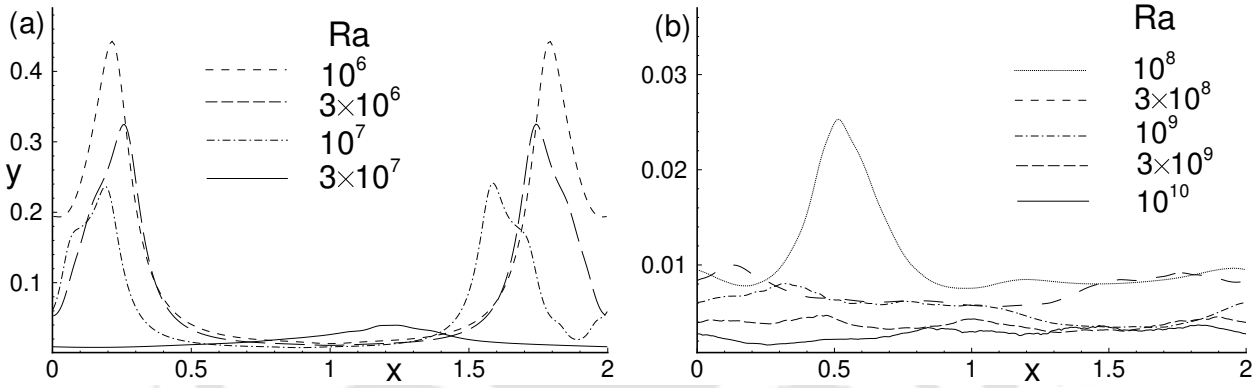

Figure 3.12: Viscous boundary layer computed from the variance of horizontal velocity using the slope method.

its variance $(u'^2)$are used to compute the boundary layer thickness. To establish *Ra* dependency, the time-averaged velocities are further averaged along the horizontal plane, and then used to compute the thickness. Figure 3.10 shows vertical variation of the absolute velocity profiles with Ra in frame (a), and a geometric representation of the boundary layer thickness in frame (b). The thickness is computed using two well-known techniques, namely, slope and maximum method. In slope method, vertical distance from the plate (top or bottom) where linear extrapolation (tangent drawn at the plate) of $|u|$ intersects local maxima/minima is termed as λ_u^{sl}. On the other hand, the vertical distance measured from the plate to the point where $|u|$ becomes maximum or minimum is represented as λ_u^{max}.

First, a comparison between the slope and maximum method follows. It is observed that only slope method gives physically consistent boundary layer, whereas the thickness computed using the other method increases with *Ra* which is inconsistent. Figure 3.10(a) shows the inconsistency where vertical height of the peak velocity increases with *Ra*. Therefore, the slope method is

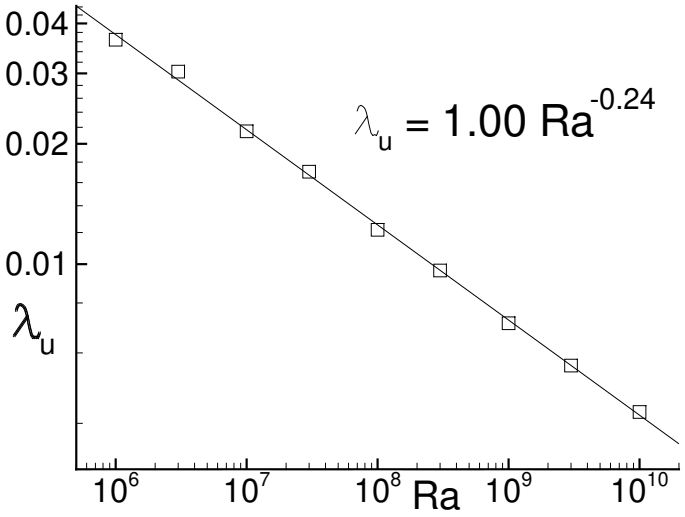

Figure 3.13: Rayleigh number dependency of viscous boundary layer thickness computed using slope technique.

employed for further comparison and physical description. Next, the profiles obtained using the above mentioned velocities are found similar as shown in Figs. 3.11, and 3.12. However, variance of the velocity gives inconsistent *Ra* dependency, while the scaling obtained from $|u|$, $\lambda_u^{sl} \sim Ra^{-0.24}$, is in good agreement with the previous studies [19] and theoretical estimate expected from Prandtl-Blasius expression.

The obtained viscous boundary layer profiles are similar to the thermal boundary layer. It is important to note that this similarity in the profiles is expected because value of the Prandtl number is 0.7 which is close to 1. Presence of LSRs has already been discussed in the previous sections, however, appearance of small scale structures increases with *Ra*. A clear effect of LSRs is evident from Fig. 3.11. Since the rolls are present in the center, the observed peaks for lower *Ra* near the walls are expected as shown in frame (a). On the other hand, nearly uniform profiles in frame (b) represent the reduced effect of those rolls. Thus, the proposition that near wall structures take the shape of the horizontal walls is supported by the viscous boundary layer profiles as well.

3.6 Statistics of dissipation rates

Next we present statistics of viscous (ϵ_u) and thermal dissipation (ϵ_θ) rates which play a crucial role in heat transport mechanism in turbulent RBC. Distribution of dissipation rate shows the role of extreme fluctuating events and its evolution with Rayleigh number. In Kolmogorov's refined

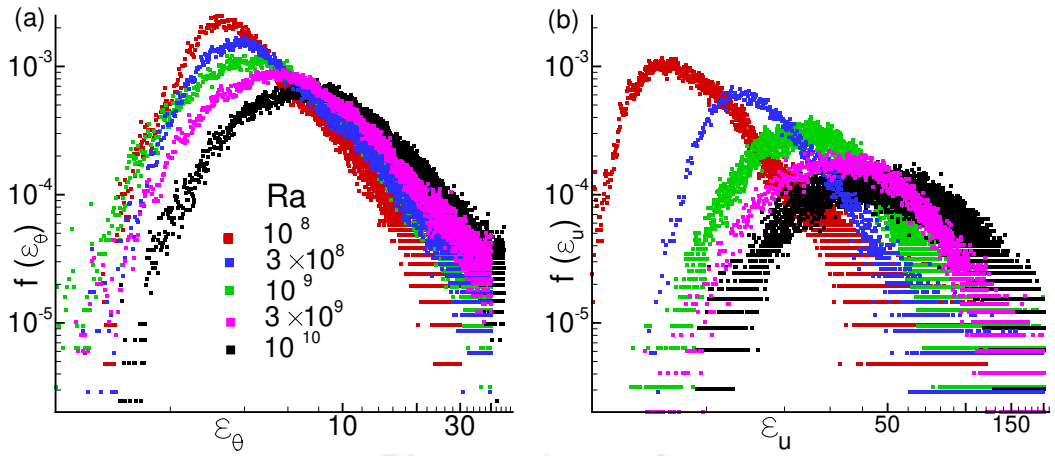

Figure 3.14: Spatial PDF of (a) thermal dissipation ϵ_θ and (b) viscous dissipation ϵ_u for Ra = 10^8, 3×10^8, $10^9, 3 \times 10^9$, and 10^{10}.

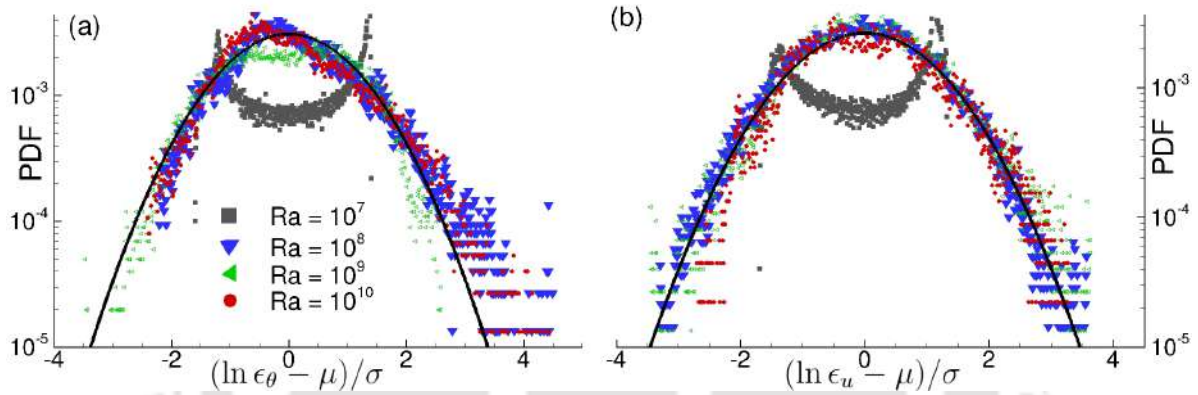

Figure 3.15: PDF of volume averaged (a) thermal dissipation rate (ϵ_θ) and (b) viscous dissipation rate (ϵ_u) computed from the normalized data where $\mu = \langle \ln \epsilon_\theta \rangle_V$ and σ are its mean and standard deviation. The thick black line represent the standard log-normal distribution for comparison.

similarity hypothesis for turbulent flows, dissipation fields are assumed to follow log-normal distribution [98]. Emran and Schumacher [47] investigated spatial distribution of thermal dissipation rate in two different subvolumes of the domain, boundary layer and the bulk region. In boundary layer region, they reported that the distribution deviates from the log-normal behavior near its tail, and found bumps in the core region. Zhang *et al.* [48] also observed deviations of dissipation rate from log-normal behavior. In the present study spatial distribution function of viscous and thermal dissipation rates are calculated by taking at least 250 instantaneous snapshots of the volume data. In non-dimensional form, the dissipation rates are written as

$$\epsilon_{\mathbf{u}} = \sqrt{\frac{Pr}{Ra}}(|\nabla \mathbf{u}|^2) \text{ and } \epsilon_\theta = \frac{1}{\sqrt{RaPr}}(|\nabla \theta|^2). \tag{3.4}$$

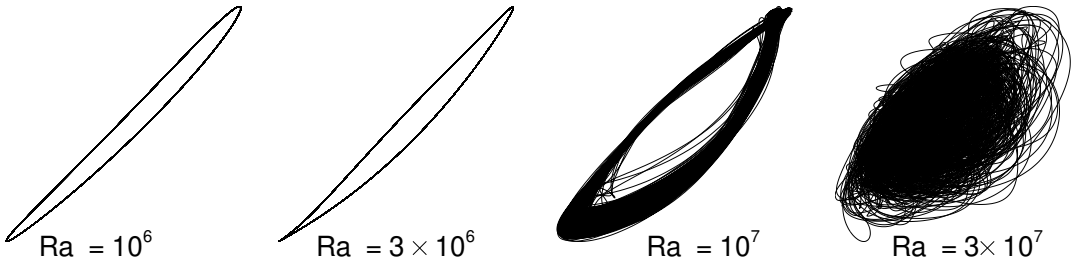

Figure 3.16: Phase diagram of volume averaged thermal dissipation rate (ϵ_θ) and viscous dissipation rate (ϵ_u) showing transition from periodic to turbulent state with increase in *Ra*.

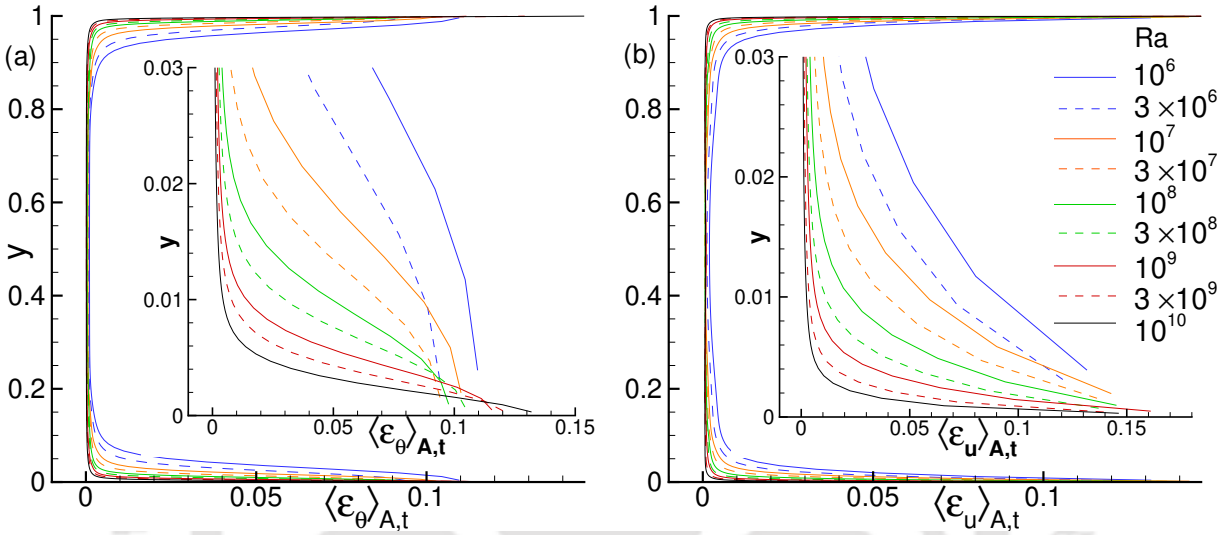

Figure 3.17: Area-time averaged vertical profiles of (a) thermal dissipation rate and (b) viscous dissipation rate where magnified view is shown in the inset in order to observe their behavior in the vicinity of horizontal walls.

Spatial distribution of both the dissipation rates, shown in Fig. 3.14, clearly show thick and scattered tail which signifies the intermittent local nature. Moreover, a long tail towards higher dissipation rate indicates the presence of extreme fluctuating events. The results are consistent with the previous studies[47, 48], although bumps near the core region are not observed here owing to computation of PDF in the whole domain rather than in subvolumes. A clear shift of peak towards higher dissipation rate with *Ra* can be attributed to sharp gradient due to a thin boundary layer. However, a drop in magnitude of both ϵ_u and ϵ_θ indicate greater homogeneity in the bulk at higher *Ra*.

Distribution functions of the normalized dissipation rates computed from time signals of volume averaged quantities with respect to standardized sample variable, $(\ln \epsilon - \mu)/\sigma$, are shown in Fig. 3.15 where μ and σ correspond to the mean and standard deviation, respectively. It is observed that for lower Rayleigh number $(\leq 10^7)$ distribution of both the dissipation rates show

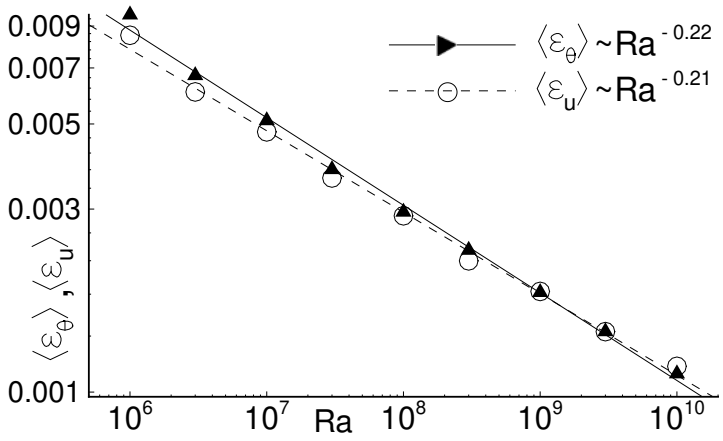

Figure 3.18: Scaling law of volume averaged dissipation rates with Rayleigh number where $\langle .. \rangle$ denotes the volume-time average.

two peak behavior which indicates a non-turbulent state. To clarify this point, phase diagram of dissipation rates are shown in Fig. 3.16 where a quasi-periodic nature emerges at lower *Ra* ($\leq 10^7$) while even at $Ra = 3\times10^7$, random nature of the flow is observed. Thus, two peak PDF observed at the indicated *Ra* clearly confirms that the flow is yet to attain a fully turbulent state. However, at higher *Ra* ($\geq 10^8$), PDF of both the dissipation rates show log-normal behavior in the core region, while the tails deviate with thick and scattered characteristics.

Further, vertical variation of $\langle \epsilon_u \rangle_{A,t}(y)$ and $\langle \epsilon_\theta \rangle_{A,t}(y)$ are investigated to ascertain the region of extreme fluctuations. In Fig. 3.17, both ϵ_u and ϵ_θ remain nearly constant in the bulk which indicates a well mixed homogeneous region. On the other hand, the dissipation rates increase rapidly and attain maximum values near the top and bottom plates which shows presence of extreme fluctuations in the boundary layer. It is observed that with increase in *Ra*, magnitude of dissipation rates decreases in the bulk, while it increases in the boundary layer which suggests thermal and viscous dissipation occur mainly in the vicinity of the horizontal plates. It is important to note that magnitude of $\langle \epsilon_u \rangle$ is greater than $\langle \epsilon_\theta \rangle$ near the walls which is also reflected in larger width of the PDF seen in Fig. 3.14(b). Both the quantities exhibit a similar decay characteristics, $\langle \epsilon \rangle \sim Ra^{-0.2}$, in least square sense shown in Fig. 3.18. However, exception in terms of marginal mismatch of the exponent is noticed only in the non-turbulent decade(s). The obtained power law behavior

$$\langle \epsilon_u \rangle_{V,t} = 0.14 Ra^{-0.21} \text{ and } \langle \epsilon_\theta \rangle_{V,t} = 0.20 Ra^{-0.22} \tag{3.5}$$

is in excellent agreement with the scaling reported by Zhang *et al.* [48].

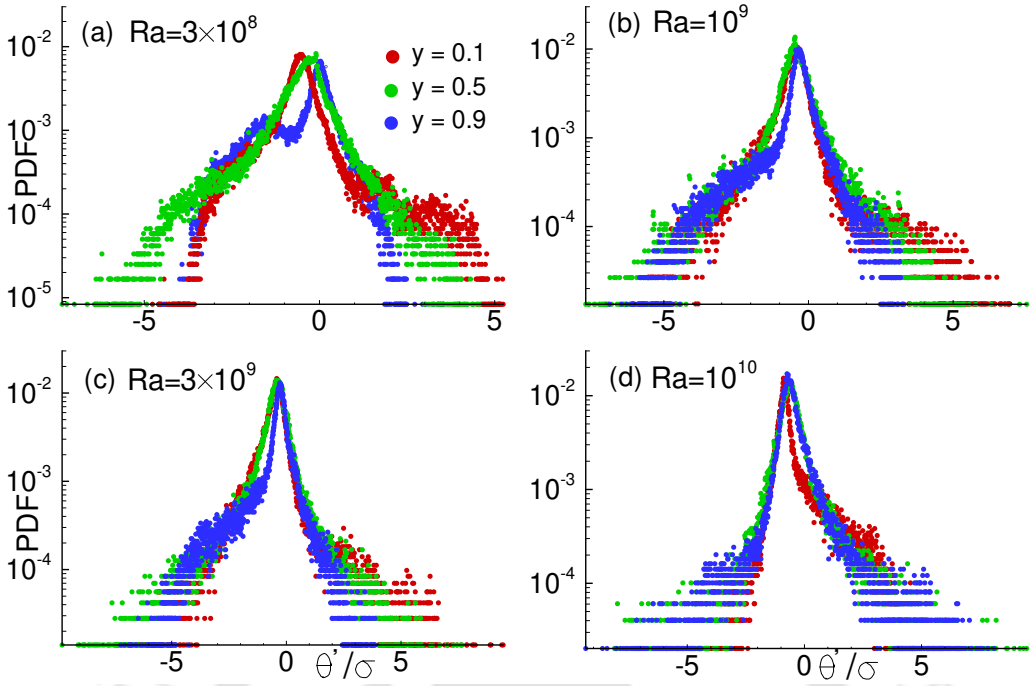

Figure 3.19: PDF of temperature fluctuations at a fixed location, $x/H = 1.1$, and at three different heights for (a) $Ra = 3 \times 10^8$, (b) $Ra = 10^9$, (c) $Ra = 3 \times 10^9$, and (d) $Ra = 10^{10}$.

3.7 Temporal statistics

In this section statistics of time signals are presented in three parts. First, PDF of temperature fluctuations, followed by calculation of correlation coefficients in both the near wall and bulk regions and finally power spectra of temperature is presented for the four higher *Ra* cases. Since the bulk and near wall regions pose different flow characteristics, signal stations are selected at three different heights of the domain in such a way that features of both the regions are captured adequately. They are located at three different heights near the mid-horizontal span, $x/H = 1$, as indicated in Fig. 3.1.

3.7.1 PDF of temperature fluctuations

Distribution of temperature fluctuations is expected to provide insight into different turbulent states across four decades of *Ra* considered in the present study. PDF of normalized (by standard deviation σ) temperature fluctuations, θ'/σ, is computed at three different heights and shown in Fig. 3.19. Heslot *et al.* [49] and Sano *et al.* [50] reported that distribution of temperature fluctuations transforms from Gaussian in soft turbulent regime to exponential distribution in hard turbulent regime, and this transformation represents attainment of a different turbulent state. It is evident from Fig. 3.19 that temperature fluctuations follow an exponential distribution near

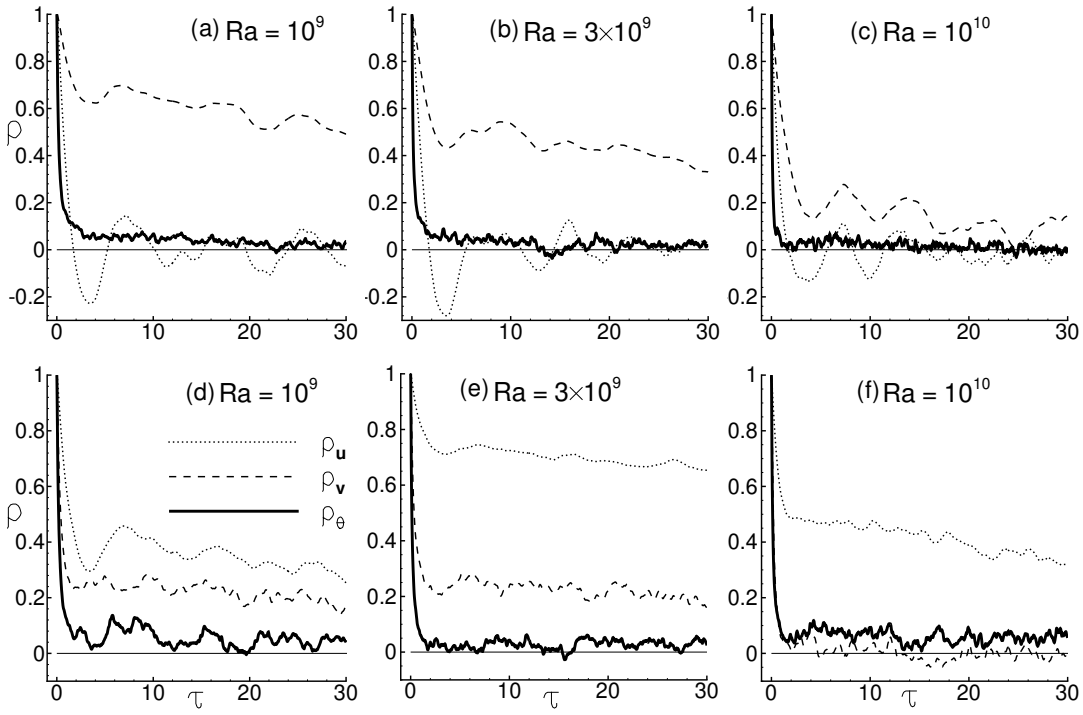

Figure 3.20: Auto-correlation coefficient $\rho(\tau)$ for the three higher *Ra* cases. Frames (a), (b), and (c) represent the correlation coefficient in the bulk region while (d), (e), and (f) near the bottom plate.

the peak of the PDF followed by a linear drop in the semi-log diagram which is consistent with Heslot *et al.* [49] and Sano *et al.* [50].

The mechanism of intermixing of hot and cold plumes causes instability in the boundary layers which results into detachment of thermal plumes [31]. Behavior of such detachments at higher *Ra* is indicated by the variation of peak and tail in the distribution of temperature fluctuations. It is observed that peak of the distribution rises with increase in *Ra*, and becomes thinner around its mean. This can be linked to large fluctuations in the flow which results from frequent emission of thermal plumes at higher *Ra*. Since plumes are considered as fragments of thermal boundary layer, frequent detachment of thermal plumes can be attributed to the observed higher peaks. On the other hand, larger width of distribution indicates rise in number of extreme fluctuations due to the intermixing of plumes. However, the scattered tails show the intermittent nature of these temperature fluctuations.

3.7.2 Correlation function

Autocorrelation function (ρ) is the simplest multi-time statistics which relates a random process with itself over time and thus it indicates how long the process sustains itself in its local

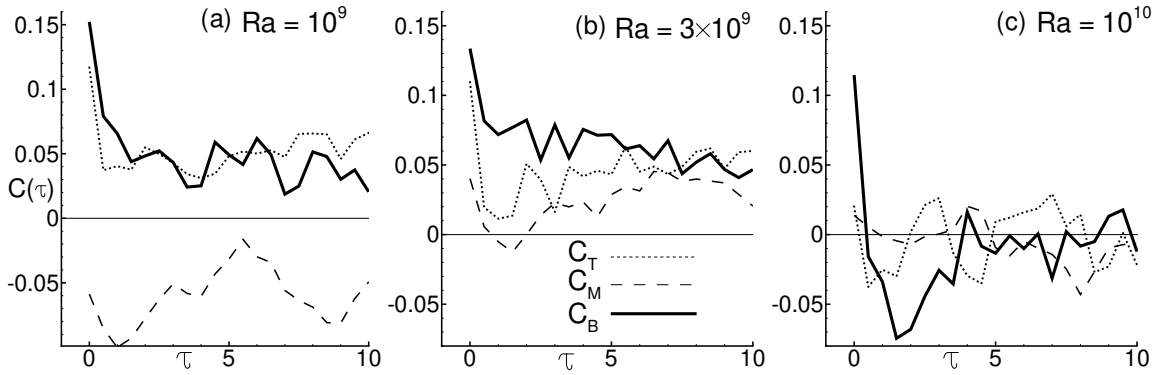

Figure 3.21: Cross-correlation coefficient between fluctuation of vertical velocity and temperature for (a) $Ra = 10^9$, (b) $Ra = 3 \times 10^9$, and (c) $Ra = 10^{10}$ at three different heights. Here, C_B, C_M and C_T represent locations near the bottom plate, central part and top plate, respectively.

neighborhood. For any process ϕ, autocorrelation coefficient is defined as

$$\rho_\phi(\tau) = \frac{\overline{\phi'(t)\,\phi'(t+\tau)}}{\sigma_\phi^2}, \tag{3.6}$$

where σ denotes standard deviation, computed as $\sigma_\phi^2 = \overline{\phi(t)^2} - (\overline{\phi})^2$, while τ and over bar represent delay time and temporal average, respectively. It is clear from the definition of ρ that ϕ is perfectly correlated at $\tau = 0$, i.e., $\rho(0) = 1$. A comparison of ρ_u, ρ_v and ρ_θ is presented for the three higher *Ra* cases in Fig. 3.20 where the top and bottom rows correspond to the bulk and region near the hot plate, respectively. Since flow behavior is similar near the top and bottom plate, correlation is shown only for the bottom plate.

In the bulk region, ρ_u drops quickly and oscillates about $\rho = 0$ which indicates the intermittent effect of two large scale rolls in the center of the domain. It is observed that the vertical velocity stays positively correlated indicating a persistent vertical motion in the center of the domain at lower Rayleigh number. All the autocorrelation coefficients decay faster at higher *Ra* which implies the loss of self-correlation due to increase in randomness in the flow. In the near wall region, ρ_u remains correlated for a longer period of time which indicates a persistent motion in the horizontal direction. The vertical velocity and temperature show similar decay behavior implying a positive correlation only near the wall region which gives rise to the buoyancy production that sustains turbulent fluctuations.

Cross-correlation (C_j) between fluctuation of vertical velocity and temperature, perceived as a measure to evaluate behavior of hot and cold plumes at different heights of the box, is defined as

$$C(\tau) = \frac{\overline{\phi_1'(t)\,\phi_2'(t+\tau)}}{\sigma_1\sigma_2}. \tag{3.7}$$

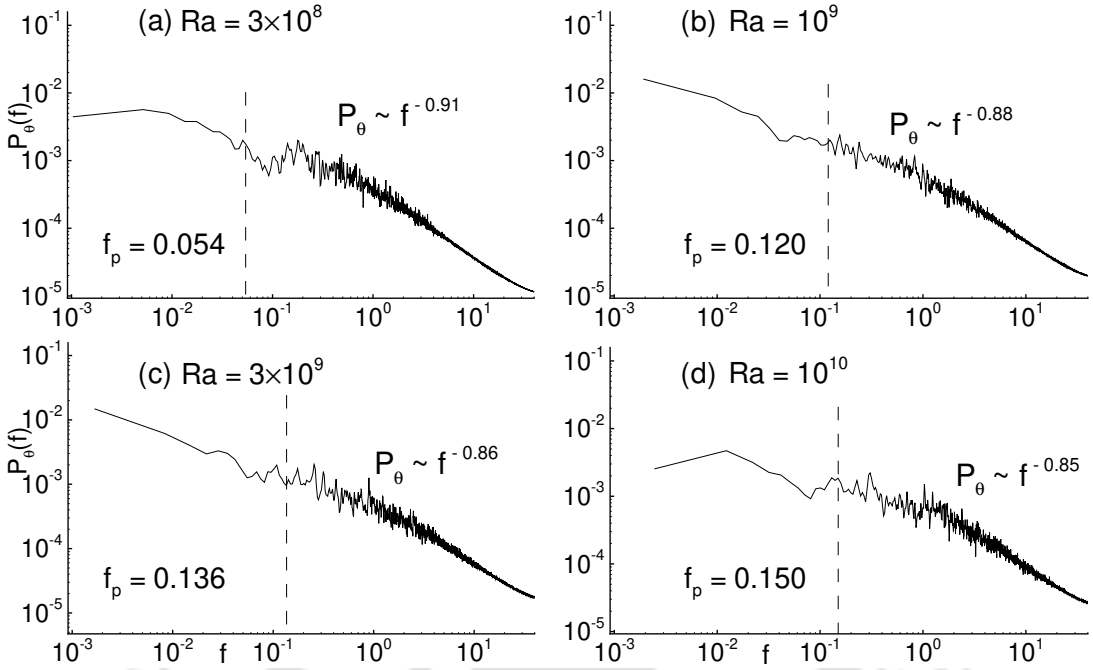

Figure 3.22: Power spectra of temperature fluctuation for (a) $Ra = 3 \times 10^8$, (b) $Ra = 10^9$, (c) $Ra = 3 \times 10^9$, and (d) $Ra = 10^{10}$ near the center of the domain, $x/H = 1.1, y/H = 0.5$. The dashed lines represent the cutoff frequency f_p.

Note, ϕ_1 and ϕ_2 represent temperature and vertical velocity, and prime, σ and τ represent their fluctuation, standard deviation and delay time, respectively. Here $j = B, M$ and T denotes location of probes near the bottom plate, central part and top plate, respectively. For instance, C_M represents the cross-correlation between v' and θ' in the bulk region.

High positive correlation in C_B and C_T, shown in Fig. 3.21, at zero delay time implies that the region near the top and bottom plates are dominated by plumes. Moreover, their faster decay with increase in *Ra* indicates frequent emission of plumes as a result of thermoconvective instabilities triggered by the splashing of cold/hot plumes on the opposite walls. On the other hand, negative or very small value (compared to C_B and C_T) of C_M indicates mixing of the hot and cold plumes which leads to a homogeneous bulk region. Intermittent appearance of cold and hot plumes near the top and bottom plates at $Ra = 10^{10}$ is indicated by their fluctuating positive and negative correlation about $C = 0$.

3.7.3 Power spectra

Power spectra (P_θ) of temperature fluctuations is computed by carrying out FFT of autocorrelation shown above in the center of the domain. Sano *et al.* [50] in their experiments observed

the power-law

$$P_\theta(f) = (\frac{f}{f_0})^{-s} exp(\frac{-f}{f_h}), \tag{3.8}$$

in the range $10^8 < Ra < 10^{11}$ where f is the frequency while f_0 and f_h are fitting parameters. The reported exponents were found to vary between 0.8 to 1.5 for different *Ra*. Later, Wu *et al.* [51] observed a single exponent up to $Ra = 10^{10}$ while for higher *Ra* they reported more than one exponent. Moreover, they also claimed that power-law doesn't exist at lower *Ra* $(< 10^8)$ due to the absence of inertial cascade. Note, the region of frequencies between the flat and sharp drop of power can be described as inertial cascade. In the present study, scaling of the spectra in the inertial subrange is highlighted in Fig. 3.22 which has a form

$$P_\theta(f) = (\frac{f}{f_c})^{-s}, \tag{3.9}$$

where f_c and s are fitting parameter and exponent, respectively. This power-law behavior is observed beyond a cutoff frequency (f_p) which describes the onset of turbulent fluctuations and shows the presence of inertial subrange which is absent in lower *Ra* cases. Cutoff frequency is quantified using the circulation time of the large-scale flow, described by rms of volume averaged horizontal velocity, $\langle u \rangle_V$[50, 48]. It is important to note that f_p increases with *Ra* which indicates the increased role of inertial cascade. It is also observed that the exponent changes with *Ra* showing clear departure from the $-5/3$ law which emphasizes the complex behavior of turbulence in 2D thermal convection. Due to the absence of one lateral dimension, plumes are entrapped inside the boundary layers and subsequently eject into the bulk as jet of plumes. This morphological change can be attributed as one of the principle reason behind the observed power-law departure. The obtained scaling exponent varies from 0.85 to 0.91 which is in the range reported by Sano *et al.* [50].

3.8 Planar statistics

Planar statistics of temperature is presented here to examine the flow characteristics in different regions of the domain. Four different measures of temperature fluctuations: the average temperature $\langle \theta \rangle_{A,t}$, variance σ_θ, skewness S_θ and flatness F_θ defined as

$$\sigma_\theta = \langle \theta'^2 \rangle, \;\; S_\theta = \frac{\langle \theta'^3 \rangle}{\langle \theta'^2 \rangle^{3/2}} \text{ and } F_\theta = \frac{\langle \theta'^4 \rangle}{\langle \theta'^2 \rangle^2}, \tag{3.10}$$

are shown in Fig. 3.23. Mean and variance provide a qualitative description of thermal boundary layer thickness while skewness being the third order moment, gives a measure of the asymmetry

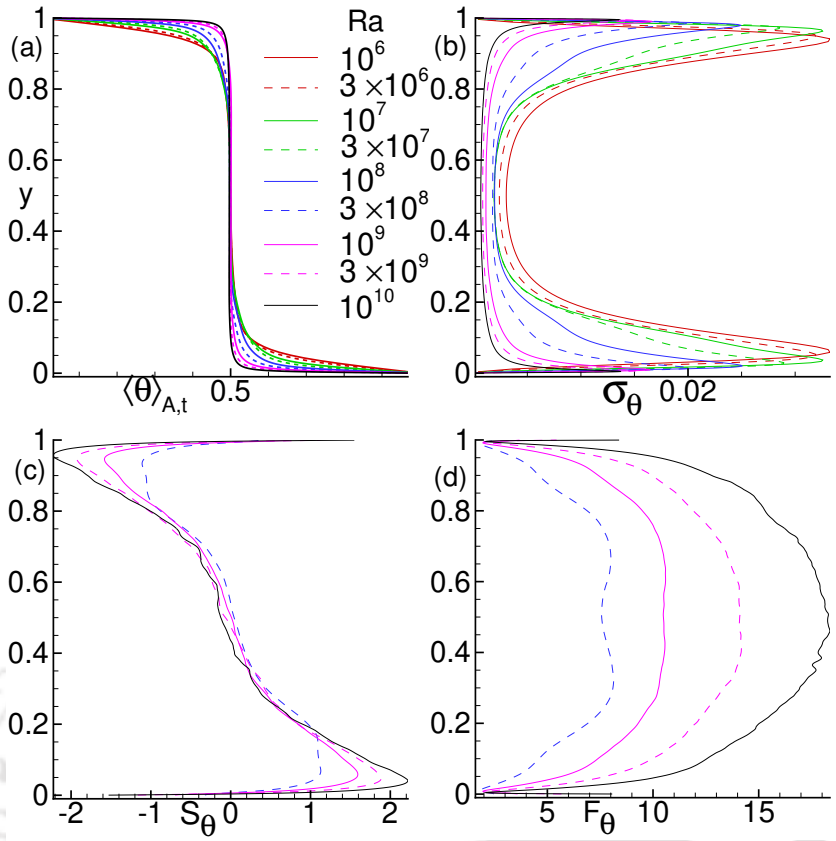

Figure 3.23: Area-time averaged vertical profiles of (a) mean temperature $(\langle\theta\rangle_{A,t}$, (b) variance σ_θ, (c) skewness S_θ, and (d) flatness F_θ.

in a distribution around its mean value. This aspect has been used to explain the asymmetric transport in turbulence by Wyngaard and Weil [99]. On the other hand, flatness measures the deviation in temperature fluctuations from Gaussian distribution.

Statistical convergence of the flow is evident from the symmetric profiles of mean and variance about the mid plane. They show sharp gradients near the plates due to high temperature fluctuations, and thus it represents the thermal boundary layers. Verzicco and Camussi [100], and Verzicco and Sreenivasan [101] quantified the thermal boundary layer thickness using peak value of the variance. It is observed that this peak drops as *Ra* increases which indicates the decrease in thermal boundary thickness. Nearly constant value of $\langle\theta\rangle_{A,t}$ and σ_θ indicates homogeneity in the bulk region. Wider bulk homogeneous region with increase in *Ra* is evident from shifting of the peaks towards the top and bottom plates.

The skewness profile starts from a negative (positive) value near the bottom (top) plate and attains a positive (negative) maximum (minimum) which subsequently assumes smaller values in the bulk. The peak value of S_θ represents magnitude of fluctuations near the thermal boundary layers. Moreover, its magnitude increases with *Ra* which indicates a highly unstable thermal

boundary layers leading to frequent emission of plumes. It is observed that the peak value of flatness increases from 8 at $Ra = 3 \times 10^8$ to 18 at $Ra = 10^{10}$ which is significantly higher than $F_\theta = 3$ reported for Gaussian distribution by Kerr[102] and De *et al.* [92] This indicates a highly non-Gaussian distribution of temperature emerges in 2D RBC. In Sec. 3.7.1, it was noted that the temperature distribution showed exponential behavior and attained sharp peaks for higher *Ra* cases. This deviation is quantified by the large value of F_θ (≥ 8) which justifies the observed departure in PDF of temperature fluctuations in Fig. 3.19. The obtained skewness and flatness profiles are not smooth due to entrapment of the fluid in the boundary layers. In connection to this observation, Lülff *et al.* [63] reported that vertical variation of higher order moments in 2D RBC are not smooth as compared to the three-dimensional cases.

3.9 Conclusions

In this chapter, we have studied turbulent Rayleigh-Bénard convection in a two dimensional rectangular cell of aspect ratio 2, in a wide range of Rayleigh number $10^6 \leq Ra \leq 10^{10}$, using air $(Pr = 0.7)$ as the working fluid, are carried out. Detailed study on local and global statistical properties of coherent structures are undertaken through scaling and ensemble measures of boundary layer, thermal plumes and heat transport. In absence of a lateral dimension in 2D, thermal plumes detached from boundary layers are entrapped while they take off which is reflected from intense hot or cold plumes near the top and bottom plates. Subsequently, they are emitted in the form of thermal jets into the bulk which is observed as thin, small bright structures. Strong agreement in $Nu(Ra)$ scaling with 3D data suggests the mechanism of formation of plume does not affect the global quantities. However, the resulting convection rolls carrying the plumes from the boundary layer to the bulk affect the structure of the boundary layers.

Boundary layer thickness, computed using the slope and 99% methods, yield similar profiles. Horizontal non-uniformity at low *Ra* apparently shows dominating effect of large scale rolls. On the other hand, a uniform profile at high *Ra* indicates that the entire horizontal surface behaves as a region of intense high/low temperature. The observed power-law, $\lambda_\theta = 2.93 Ra^{-0.27}$, provides the dependency of boundary layer thickness on Rayleigh number which agrees well with the theoretical estimate, $\lambda_\theta \sim Nu^{-1}$. A qualitative picture of boundary layer thickness is obtained by the presence of mean temperature gradient and variance near the wall region. Furthermore, turbulent kinetic energy budget indicates an approximate balance between transport and dissipation in the boundary layers, $T \approx D$, while buoyancy production is significant in the bulk region,

$P \approx D$, with advection (A) found insignificant along the entire height of the domain.

Thermal plumes, one of the essential coherent structures in RBC, are characterized by a positive correlation between fluctuations of vertical velocity and temperature. At any threshold, volume share of plumes drop with increase in *Ra* which is compensated by a rise in background. Smaller threshold produces uncertain data that reflects nearly similar contribution in dissipation, and only at larger threshold background share of dissipation far exceeds that of the plume. However, in the limit of high *Ra*, both these regions asymptotically produce same dissipation. Thus, relatively larger dissipation caused by plumes of less volume occupancy supports thin and brighter spots in global temperature map. While power exponents for plume fraction and dissipation are sensitive to the threshold, background region yields nearly same exponent. Similar nature of fluctuations of vertical velocity and temperature near the walls is further supported by the auto-correlation coefficients with higher $\langle v'\theta' \rangle$ supports the criterion adopted to identify the plumes and background regions.

Sharp peaks in PDFs of temperature fluctuations at higher *Ra* indicate frequent emission of plumes while increasingly wider tails seem to support extreme fluctuations. Exponential distribution of the same suggests attainment of a higher turbulent state which is quantified by the obtained flatness (≥ 8). The deviation in exponent from $-5/3$ in the frequency spectra indicates the complex nature of thermal convection in 2D and the morphological change of the entrapped plumes can be partly attributed to this observed departure. Vertical variation of skewness represents the behavior of frequent emission of plumes which is believed to affect the boundary layers as its peak value can be directly connected to the instability of the thermal boundary layers.

CHAPTER 4

Effect of rough boundaries on *Nu* and flow structures

This chapter reports a detailed investigation of the effect of rough boundaries on heat flux enhancement and flow structures in turbulent Rayleigh-Bénard convection. We consider three levels of roughness having maximum height as $5\%, 10\%$ and 20% of the cell height. Presence of rough surfaces induces a significant enhancement in heat flux beyond a critical Rayleigh number (Ra_c) the value of which strongly depends on the roughness height. The PDF of the temperature fluctuations exhibits the Bi-Gaussian distribution below Ra_c, while it shows exponential nature in the enhanced heat flux regime. Distinct nature of large-scale flow patterns is observed in this regime. While a stable double-roll state persists for the smallest roughness set-up, effect of corner rolls emerges in the intermediate level. Break down of the stable double-roll structure into multiple rolls is seen to be linked with higher heat flux owing to efficient washing out effect in the roughness grooves. A stronger horizontal motion elevates the shear production for the smallest roughness case. On the other hand, direct injection of plumes into the bulk improves the buoyancy production leading to larger heat flux for the tallest roughness. Roughness heights are seen not to have any discernible effect on the overall flow strength.

4.1 Introduction

In thermal convection, two questions are of paramount importance. First is the heat transfer rate, computed in terms of Nusselt number Nu, and second, the active mechanism responsible for it. Since both are interrelated, a deeper understanding of the mechanism helps in enhancing

the heat transfer rate. For instance, flow inside an inclined convection cell evolves differently than that in the horizontal cell, and thus, the induced flow states alter the heat flux [66, 64, 70]. Flow over rough surfaces is another such possibility that influences the flow dynamics and heat flux. The standard Rayleigh-Bénard convection is an ideal system to study the flow patterns and mechanism of heat transfer in natural convection. Thus, it is important to incorporate the surface roughness on the isothermal walls in RBC. For a detailed description, the reader is referred to chapter 1.

Several previous roughness aided-RBC studies reported a significant augmentation in heat flux due to enhanced $Nu(Ra)$ scaling exponent and prefactor [56, 58, 75], refer Sec. 1.3. For instance, Shen *et al.* [54] reported that *Nu* increases by 20% in rough cases, Du & Tong [57] observed a maximum of 76% increment, and Toppaladoddi *et al.* [53] obtained the highest scaling exponent (0.483). The enhanced exponent is attributed to two different mechanisms. First, roughness enhances the bulk-plume interaction, which disturbs the boundary layer [56, 57, 53]. Second, rough surfaces break the flow symmetry (LSC), which enhances the mixing of fluid [62]. It is important to note that the two mechanisms are related to the boundary layer dynamics. Invoking any of the two mechanisms using rough surfaces gives the enhanced exponent regime. But a vital prospect of these mechanisms still needs to be explored, i.e., how the heat flux and the scaling exponent respond if more than one mechanism in the convection cell is triggered. We attempt to answer this question using three irregular (random) roughness configurations in this chapter.

To the best of our knowledge, a single roughness scale has been used in almost all the studies that dealt with roughness driven turbulent convection, except the studies carried out by Zhu *et al.* [2] and Ciliberto and Laroche [56]. While Zhu *et al.* [2] used three roughness scales, Ciliberto and Laroche experimented over a wide range of glassy spherical roughness length scales. However, conical peaks have a higher tendency of nucleating thermal plumes than spherical surfaces, which makes it more suitable for the heat flux enhancement. In real-life problems, rough surfaces usually have several different length scales, and thus, it is essential to consider a number of roughness scales and investigate their combined effect on heat transfer and the scaling exponent. Indeed, random roughness becomes a natural choice that includes a wide range of scales and mimics the nature of complex uneven surfaces. We have focused on three levels of random roughness in the convection cell, as shown in Fig. 4.1. The main attribute of all the three roughness configurations lies in their randomly generated length scales, which are characterized by their range of heights. For more details about the roughness configurations, refer Sec. 2.3.

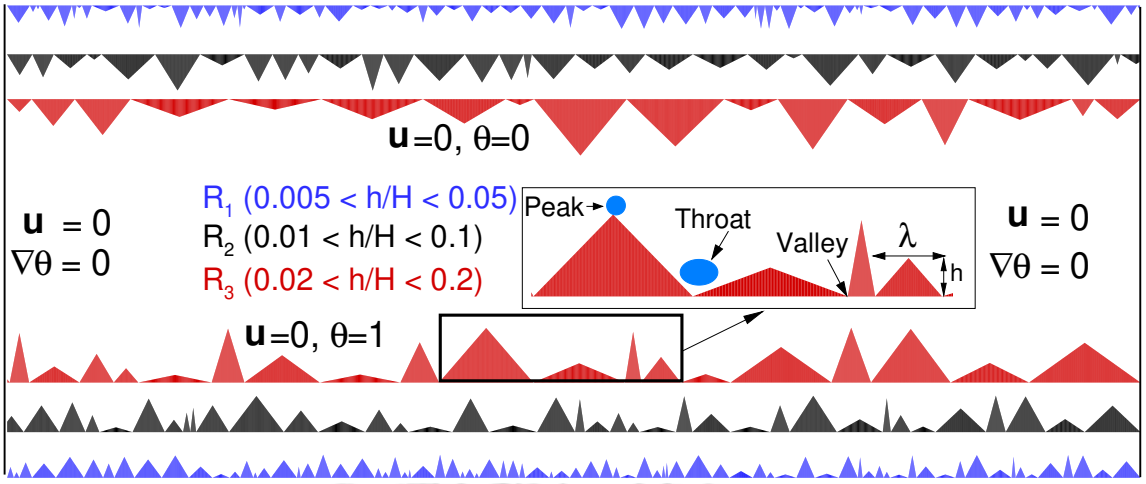

Figure 4.1: Schematic diagram of three random roughness configurations, R_1, R_2, and R_3, which are characterized by their maximum heights. Inset shows the zoomed view to indicate the peak, valley, and throat regions of a roughness element measured by its height (h), and base (λ).

To the best of our knowledge, this is the first attempt where several roughness scales are used to explore the mechanisms responsible for heat transport. Moreover, a comparison of *Nu* over the three roughness configurations may help in determining the type of roughness to be used for practical purposes.

4.2 Numerical details

The flow is simulated inside a two-dimensional rectangular box of aspect ratio $\Gamma = 2$ using air $(Pr = 0.7)$ as the working fluid, see Fig. 4.1. The top and bottom rough surfaces are kept at a fixed temperature, while adiabatic condition is used along the lateral walls. No-slip boundary condition is invoked for both the uneven surfaces and the lateral walls. Non-uniform mesh in the wall-normal direction is refined close to the rough surfaces. For adequate spatial resolution, the maximum grid spacing is kept smaller than the analytically estimated Kolmogorov length scale $(\eta = HPr^{1/2}Ra^{-1/4}(Nu-1)^{-1/4})$. It also satisfies the criterion of the minimum number of grid points inside the thermal boundary layer (TBL) [76]. In particular, 2560×1620 grid points are used in the horizontal and vertical direction, respectively, for the most demanding case, $Ra = 4.64 \times 10^9$. The non-dimensional heat flux (Nu) is computed using $Nu = \sqrt{RaPr}\langle v\theta\rangle_V - \langle \partial_z \theta\rangle_V$, where $\langle\cdot\rangle_V$ indicates the volume-averaged quantity. Statistical sampling is carried out for at least 200 free-fall time units once the flow attains dynamic stationary state. The numerical details of all the cases are listed in Table 4.1. For more details about the governing equations and surface

Table 4.1: Details of the simulation parameters for the three roughness configurations, R_1, R_2, and R_3. From left to right: *Ra* is the Rayleigh number; N_x and N_y are the number of grid points in x and y directions, respectively; N_{BL} is the number of grid points inside the thermal boundary layer calculated from the smooth case; Nu_{ref} is the reference Nusselt number taken from Zhu *et al.* [2] for multi-scale roughness; and Nu_{comp} is the computed Nusselt number in the present work. Here, underline, parenthesis, and overline mark the onset of enhanced heat flux regime in R_1, R_2, and R_3 cases, respectively.

Ra	$N_x \times N_y$ For R_i $(i = 1, 2, 3)$	N_{BL}	Nu_{ref} Zhu *et al.* [2]	Nu_{comp} R_1	R_2	R_3	Smooth
10^6	1000×600	87	–	6.84	6.06	5.08	07.35
2×10^6	1000×600	85	–	–	6.53	6.17	–
3×10^6	1000×600	75	–	8.49	7.07	6.89	09.01
6×10^6	1000×600	74	–	–	8.48	10.11	–
$\overline{10^7}$	1000×600	59	–	10.61	9.73	$\overline{12.00}$	12.44
3×10^7	1000×600	48	–	14.19	16.44	19.25	17.45
3.98×10^7	1000×600	43	–	15.31	18.39	22.08	–
(5.50×10^7)	1000×600	42	–	16.70	(20.97)	24.87	20.98
7.24×10^7	1000×600	29	–	18.28	23.44	28.68	–
10^8	1200×600	24	20.8	20.28	26.19	32.45	25.08
$\underline{2.15 \times 10^8}$	1200×700	19	30.1	$\underline{28.98}$	37.59	44.38	32.18
4.64×10^8	1400×800	16	43.6	44.34	53.69	61.81	40.93
10^9	2000×1000	13	63.1	64.05	76.02	86.67	51.50
2.15×10^9	2000×1400	13	92.2	88.88	105.60	117.48	60.49
4.64×10^9	2560×1620	11	130.3	132.72	145.73	158.29	74.92

roughness, refer chapter 2.

4.3 Enhanced heat flux regime

Rough surfaces in thermal convection cells have been extensively used for efficient heat transfer. Using pyramid roughness elements, Shen *et al.* [54] observed 20% enhancement in Nusselt number (Nu). While Ciliberto & Laroche [56] used spherical roughness, Du & Tong [57] used

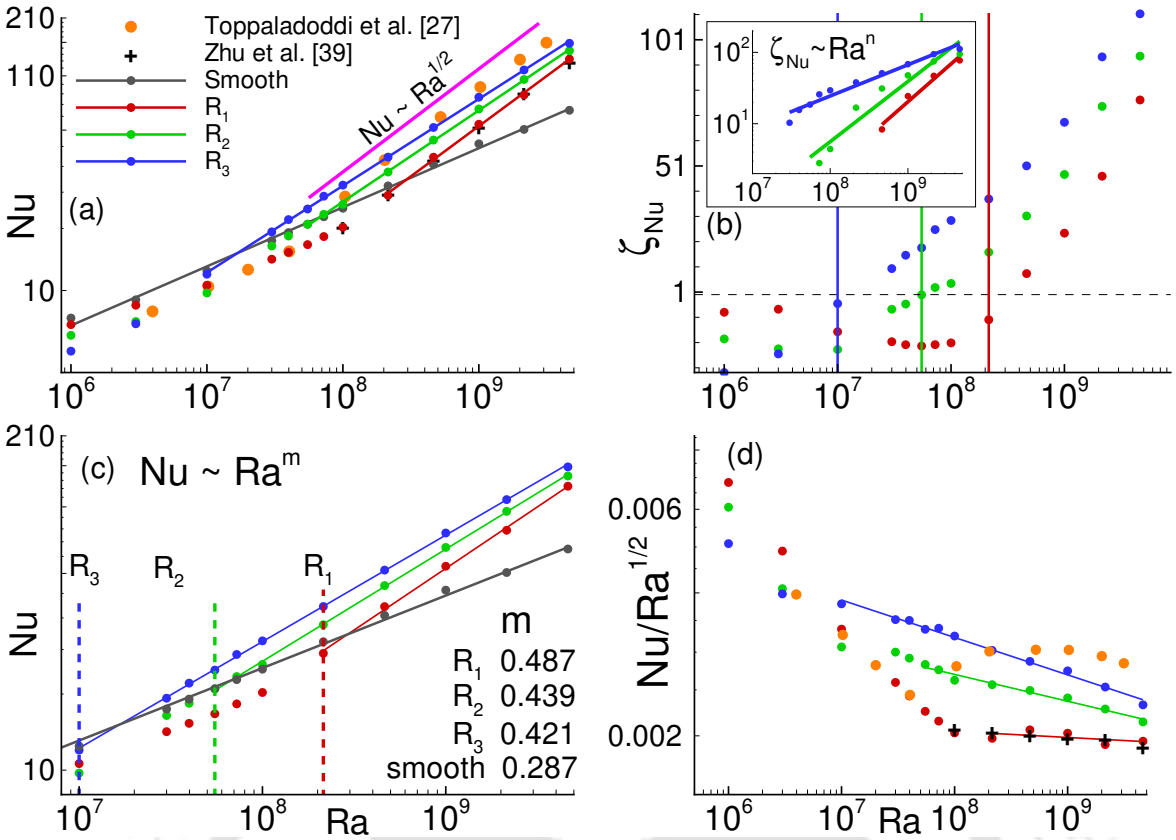

Figure 4.2: (a) Comparison of *Nu* for different roughness configurations. While Zhu *et al.* [2] used the periodic triple-scale roughness heights, Toppaladoddi *et al.* [53] used a uniform mono-scale configuration optimized for highest heat transfer. (b) Normalized heat flux $\zeta_{Nu} = (Nu - Nu_0)/Nu_0 \times 100$ as a function of *Ra* for the three random roughness configurations, where Nu_0 represents heat flux in the smooth case. The inset shows the power-law $\zeta_{Nu} \sim Ra^n$ where $n = 0.96, 0.84$, and 0.44 for R_1, R_2, and R_3 configurations, respectively. (c) The onset of enhanced exponent regime at the critical Rayleigh number, $Ra_c = 2.15 \times 10^8$, 5.50×10^7, and 1×10^7 for R_1, R_2, and R_3 setups, respectively. (d) A compensated plot $(Nu/Ra^{1/2})$ showing deviation from local $1/2$ scaling regime.

pyramids to enhance heat flux and found that scaling exponent (m) in $Nu \sim Ra^m$ changes when the roughness perturbs the thermal boundary layer. Since Nusselt number (Nu) is perceived as the measure of heat transfer rate from the underlying surface and the Rayleigh number (Ra) contains the applied thermal forcing, the exponent in $Nu \sim Ra^m$ scaling law acts as the key to heat transfer enhancement. Among a few others, roughened surfaces have been observed to push the classical Malkus [24] exponent of $1/3$ towards what Kraichnan [28] foresaw as the ultimate regime in thermal convection characterized by the "half-scaling" $(m = 1/2)$. It is a practice to refer to a *Ra* regime where the exponent improves from $1/3$ as the “enhanced exponent regime."

Recently, Toppaladoddi *et al.* [53] observed $m = 0.483$ in a lower *Ra* range varying from 10^8 to 4×10^9, and termed it as local $1/2$ scaling regime. The increased bulk-plume interaction was attributed to the improvement in the scaling exponent. Later, Zhu *et al.* [59] found the true extent of this regime, which sustains for only one and a half decades. However, with periodic triple-scale roughness configuration, Zhu *et al.* [2] observed the increased extent of the $1/2$ scaling regime due to persistent destabilized boundary layers up to a very high $Ra = 10^{11}$.

In what follows, we begin with the comparison of *Nu* for different roughness configurations. Figure 4.2(a) shows Nusselt number obtained for the mono-scale roughness by Toppaladoddi *et al.* [53], periodic triple-scale roughness by Zhu *et al.* [2], and the three present random roughness configurations and a smooth cell. Clearly, the random roughness shows higher *Nu* as compared to the other configurations, except for the mono-scale roughness where Toppaladoddi *et al.* [53] used optimum roughness height. Interestingly, the triple-scale and the smallest roughness configuration (R_1) used in the present work yield the same *Nu* beyond $Ra = 10^8$. Note that the triple-scale roughness in Zhu *et al.* [2] was termed as multi-scale roughness. However, presence of a range of roughness scales which have no preconceived order in the present work makes it close to reality, and also yields higher heat flux as compared to the previous roughness configurations.

Next, heat flux in the three roughness facilitated convection cells is compared. To exclude the effect of wetted area in *Nu*, we kept it nearly the same in the three roughness cases. Figure 4.2(b) shows the variation of normalized heat flux ($\zeta_{Nu} = Nu - Nu_0/Nu_0 \times 100$) as a function of *Ra* for the three configurations, where Nu_0 indicates heat flux for the smooth case. In order to highlight the differences in *Nu*, the enhanced heat flux regime is further represented by $\zeta_{Nu} > 0$. In this regime, the tallest roughness configuration (R_3) produces the maximum ζ_{Nu}, and it drops with the configurations characterized by their maximum roughness height. In the enhanced heat flux regime ($\zeta_{Nu} > 0$), it is observed that the normalized heat flux obeys a power-law behavior as $\zeta_{Nu} \sim Ra^n$, where n is the scaling exponent. As shown in the inset, least-square fit of the data yields $n = 0.96, 0.84$, and 0.44 for R_1, R_2, and R_3 configurations, respectively. Evidently, the exponent drops as the maximum roughness height increases. Surprisingly, effect of roughness height is not limited to an increase in heat flux. Larger the maximum height of roughness is greater is the heat flux enhancement. However, smaller the maximum height is higher is rate of increase of ζ_{Nu} with *Ra*. This indicates multifaceted behavior of the surface roughness. The one with the highest gain does not extend for the entire spectrum of *Ra*, as smaller roughness yields large rate of increase of *Nu* over Nu_0 at large *Ra*. On the other hand, $\zeta_{Nu}(Ra)$ behaves differently

when $\zeta_{Nu} < 0$ due to the geometric characteristics of the configurations. In R_1 case, the spacing between the roughness elements is too small to impact the flow behavior, and thus it behaves like the smooth case. On the contrary, in the other two configurations, a wider spacing between the roughness elements accumulate the flow, which resists the heat transport. Consequently, lower *Nu* is evident for these two configurations.

For uniform roughness heights varying in the range $0.05 \leq h/H \leq 0.15$, Zhu *et al.* [59] obtained similar results in the enhanced exponent regime, where *Nu* increases with roughness heights. Since nearly same wetted area is used for the three configurations, the three distinct curves perhaps indicate different heat transport mechanisms. The flow behavior at different roughness heights is described in greater detail in Sec. 4.4. Zhang *et al.* [61] observed that strong secondary vortices present near the rough surfaces wash the cavities, which enhances the heat flux. Though, they used mono-scale roughness elements, entrapment also persists in random configurations due to the formation of cavities between the elements. Varying the roughness heights may disrupt the entrapped fluid, effecting a greater mobility of the otherwise trapped fluid.

Before exploring the heat transport mechanism, $Nu(\sim Ra^m)$ scaling exponent in the enhanced heat flux regimes are studied. Figure 4.2(c) shows a least-square fit of the data, resulting in three different exponents as $m = 0.487$, 0.439, and 0.421 for R_1, R_2, and R_3 cases, respectively. Moreover, it also shows a different onset of the enhanced heat flux regime for the configurations, given by the critical Rayleigh number $Ra_c = 2.15\times10^8$, 5.50×10^7, and 10^7, respectively. Since taller heights have a higher tendency to penetrate the boundary layers, lower values of Ra_c in R_2, and R_3 are expected [59]. It is evident that the transition to the enhanced heat flux regime occurs at different *Ra*, which is in agreement with Zhu *et al.* [2].

Mathematical models proposed by Malkus [24] and Castaing *et al.* [29] indicate that the scaling exponent is linked with the heat transport mechanism. For uniform-sinusoidal roughness, Toppaladoddi *et al.* [53] reported the exponent $m = 0.483$, while Zhu *et al.* [2] obtained $m = 0.49$ for multi-scale roughness elements. They attributed these higher values of m to the increased bulk-plume interaction. Significant differences in the value of m for R_1, R_2, and R_3 configurations are also observed in the present study, as shown in Fig. 4.2(c). The cell with R_1 geometry yields the highest exponent $(m = 0.487)$, while it is least for the R_3 case $(m = 0.421)$. The value of m in R_1 configuration is close to that obtained by Toppaladoddi *et al.* [53], and Zhu *et al.* [2], which signifies the improved bulk-plume interaction by increasing the intense plume-emitting spots. On the other hand, breaking of large-scale rolls into smaller ones is responsible

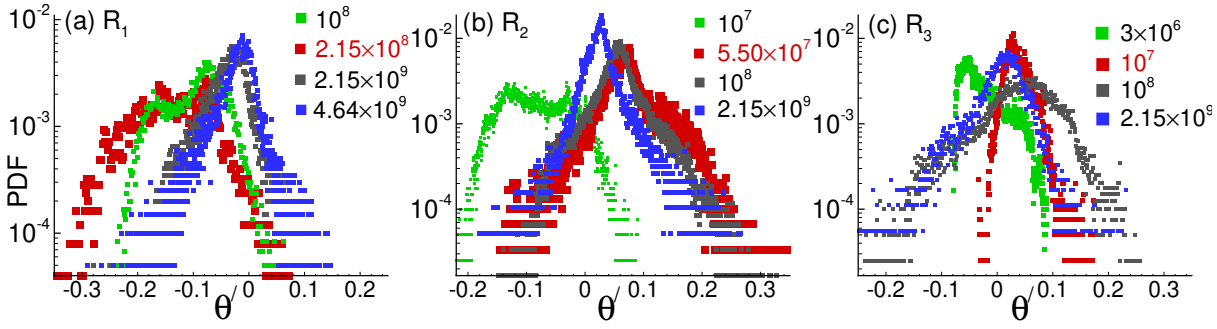

Figure 4.3: PDF of temperature fluctuations (θ') in the bulk (center of the domain), showing the transition from two peaks to a single peak distribution in (a) R_1, (b) R_2, and (c) R_3 configurations. The critical Rayleigh number (Ra_c) in the three configurations are represented by red color.

for the enhanced exponent in R_2 and R_3 cases. Such a phenomenon was previously reported in the inclined convection cell. The random roughness used in the present work shows the same without any inclination. A detailed discussion on heat transport mechanism is provided in the next section.

Further, consistency of the data in the enhanced scaling regimes is investigated through a compensated plot $(Nu/Ra^{1/2})$, as shown in Fig. 4.2(d). Evidently, R_2, and R_3 deviate from the local $1/2$ scaling regime, whereas R_1 yields a stable scaling with $m \approx 1/2$. Moreover, the same scaling parameters, both the exponent and prefactor, in R_1 and triple-scale roughness used by Zhu *et al.* [2] indicate the same heat transport mechanism. In this plot, a higher prefactor for the optimum roughness geometry used by Toppaladoddi *et al.* [53] is evident. The higher value clarifies why higher heat flux is obtained in this configuration as compared to the random roughness in Fig. 4.2(a).

Finally, to identify the transition to the enhanced *Nu* regime (Ra_c), we have investigated the PDF of temperature fluctuations (θ') in the bulk region (center of the convection cell). The PDF is computed for at least two hundred free-fall time units of sampling length. Figure 4.3(a-c) shows the PDF of temperature fluctuations in R_1, R_2 and R_3 cases, respectively. It should be noted that transition in the distribution of temperature fluctuations has been used to demarcate different turbulent states [50]. In a recent study, Chand *et al.* [103] have described the transition to a single peak distribution as the sign of attainment of a highly turbulent state which modifies the temperature statistics. With increasing *Ra*, Castaing *et al.* [29] found that PDF of θ' changes from a Gaussian to an exponential distribution, showing the transition to the hard-turbulent regime. Salort *et al.* [104] showed the change in histogram from Gaussian to a single-peak shape, when the probe was moved from the boundary layer region to the bulk. In the current

study, a clear transition from two peak behavior to a single peak is evident in all the three configurations at the critical Rayleigh numbers (Ra_c): 2.15×10^8, 5.50×10^7, and 10^7, respectively, for R_1, R_2, and R_3. This transition confirms the attainment of higher turbulent state and identifies the onset of enhanced *Nu* regime. However, since such an onset occurs early (smaller *Ra*) for taller roughness, distribution function having a single peak has a connection with uniform flatter profile with significant scatter and longer tails. On the other hand at small roughness, the onset occurs at a larger *Ra* when distribution has become polarized with sharp peak and virtually non-existent tails. Thus, onset of the enhanced heat flux regime occurs at relatively different flow states which clearly indicates role of average height of the roughness elements, though they do not appear in any specific pattern.

4.4 Heat transport mechanism

In natural convection, thermal plumes play a crucial role in the heat transfer phenomenon [19]. These plumes are detached boundary layer structures responsible for the $Nu(Ra)$ scaling law [29]. However, the heat transport mechanism in the rough configuration is different from the smooth case. In the latter, hot fluid gains sufficient energy to become unstable and rises from the boundary layers. On the contrary, roughness elements help to detach the hot fluid attached to them and thereby augment the heat transport properties. Note that the emission of thermal plumes and detachment are two different phenomena. Therefore, one way to influence the heat flux is by varying the plume emission process and their morphology. On the other hand, altering the large-scale rolls, which drives these plumes, is another way to enhance the heat flux [64]. While the former is responsible for enhanced heat flux in the roughness case, the latter has been observed for the tilted cells [64]. Surprisingly, in the present work, both the phenomena have been observed to modify the scaling laws.

In an experimental study, Shen *et al.* [54] observed large-sized thermal plumes in the bulk region, which enhanced the heat flux. Later, Stringano *et al.* [105] found the edges of the roughness elements to be the most active plume emission spots, hence emitting the plumes more frequently. By varying the geometric properties of roughness elements, Wagner & Shishkina [106] found that wider grooves affect the large-scale flow structures and strengthen the induced secondary vortices. These vortices wash-out the cavities and weaken the boundary layer perturbation to make the transport phenomenon similar to that in the smooth case. On the contrary, lack of ventilation in the cavities results in intermittent interaction between large-scale rolls and the fluid

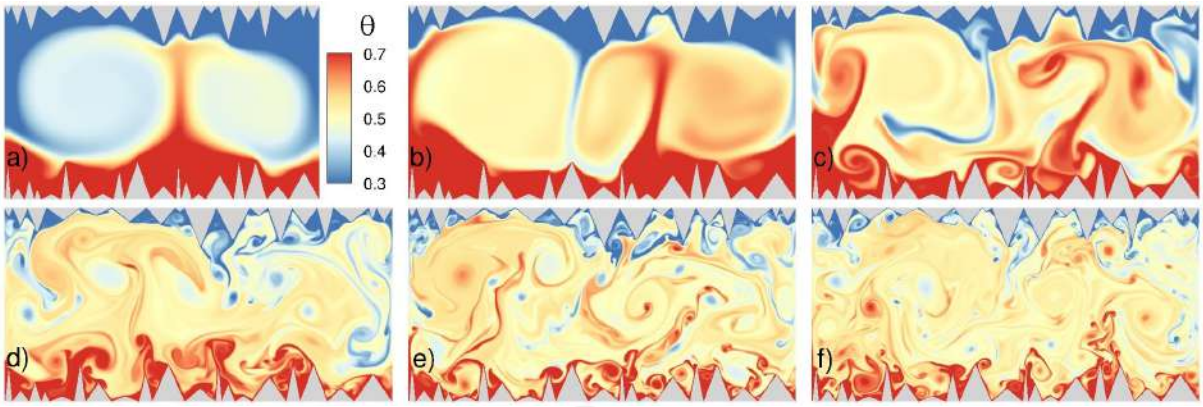

Figure 4.4: For R_3 configuration, instantaneous temperature field for *Ra* (a) 10^6, (b) 10^7, (c) 10^8, (d) 10^9, (e) 2.15×10^9, and (f) 4.64×10^9. At $Ra_c = 10^7$, the double-roll state transforms into a triple-roll state.

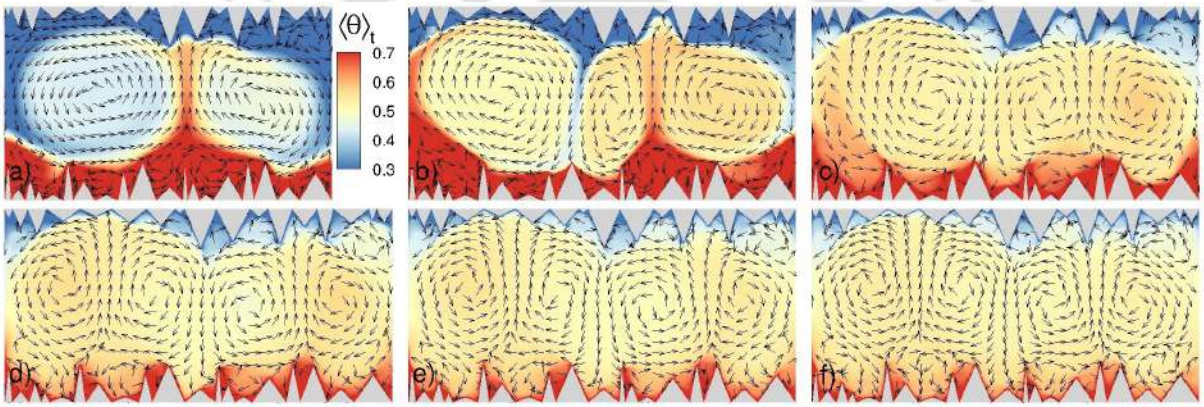

Figure 4.5: Time-averaged temperature field superimposed with velocity vectors showing the stable multiple-rolls for the same cases as in Fig. 4.4. The double-roll state transforms into a multiple-roll state beyond the $Ra_c = 10^7$.

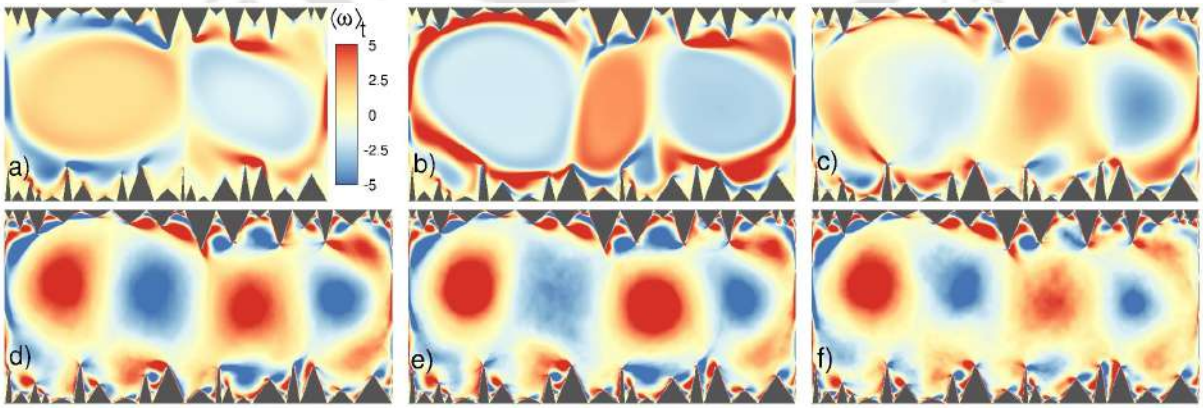

Figure 4.6: Time-averaged angular velocity field showing the stable multiple-rolls for the same cases as in Fig. 4.4. The triple-roll state further transforms into a complex four-roll state at the highest *Ra*.

resting in the cavities. This interaction sustains the perturbation of the boundary layers. Later, Toppaladoddi *et al.* [53] and Zhu *et al.* [2] attributed the enhanced heat flux and scaling exponent to the increased bulk-plume interaction. Since all of these investigations dealt with the uniform roughness, it is interesting to see how the process of plume emission and its interaction with the bulk respond to random roughness configurations.

To understand what triggers the enhanced heat flux regime, we look into the large-scale flow structures. Beginning with the tallest roughness (R_3), Fig.4.4 shows the instantaneous temperature field at six different *Ra*, covering the entire range of simulated cases. Interestingly, the double-roll state at a lower *Ra* ($< 10^7$) transforms into a triple-roll state at the critical $Ra_c = 10^7$, as shown in Fig. 4.4(b). These rolls further break-down into multiple-rolls at the highest *Ra*, see Figs. 4.5(d-f). Since instantaneous field is obscured by the turbulent fluctuations, to identify the stable rolls time-averaged temperature field overlaid by velocity vectors and angular velocity field are shown in Figs. 4.5 and 4.6, respectively. Apparently, smaller rolls have a higher tendency to wash out the cavities than the bigger ones due to their ability to enter the narrow spaces between the roughness elements. Also, the effect of large-scale rolls is evident in the detached large-sized thermal plumes, as shown in Fig. 4.4(c-e). The boundary layer under the influence of these strong rolls tends to leave the surface early, resulting in an emission of arbitrarily shaped thermal plumes. Therefore, breaking of large-scale rolls into smaller ones explains how the so-called bulk-plume interaction increases in this random configuration and incites the onset of enhanced heat flux regime. The features mentioned above are also reflected in the time-averaged angular velocity field, where pair of counter-rotating rolls are evident (see Fig. 4.6). As *Ra* increases, these rolls break down into a multiple-roll state. The figure also provides a clear visualization of secondary vortices near the roughness elements. A similar phenomenon of enhanced heat flux has been observed by Wang *et al.* [64], where a stable double-roll state transforms into an unstable triple-roll state in an inclined convection cell.

Next, the heat transport mechanism responsible for the higher heat flux in R_2 configuration is revealed using flow structures. While Fig. 4.7 shows the instantaneous temperature contours at six Rayleigh numbers, Figs. 4.8 and 4.9 indicate the time-averaged velocity field and angular velocity field, respectively. The time-averaged fields are shown here to confirm the stable large-scale rolls. In contrast to R_3 configuration, where a transition from double-roll state to multiple-roll state was observed, two primary rolls persist for the entire simulated *Ra* regime here. Nevertheless, the striking feature in this configuration is the contribution of corner rolls. At lower *Ra* ($< Ra_c$), weak corner rolls are observed, as shown in Fig. 4.8(a). However, with

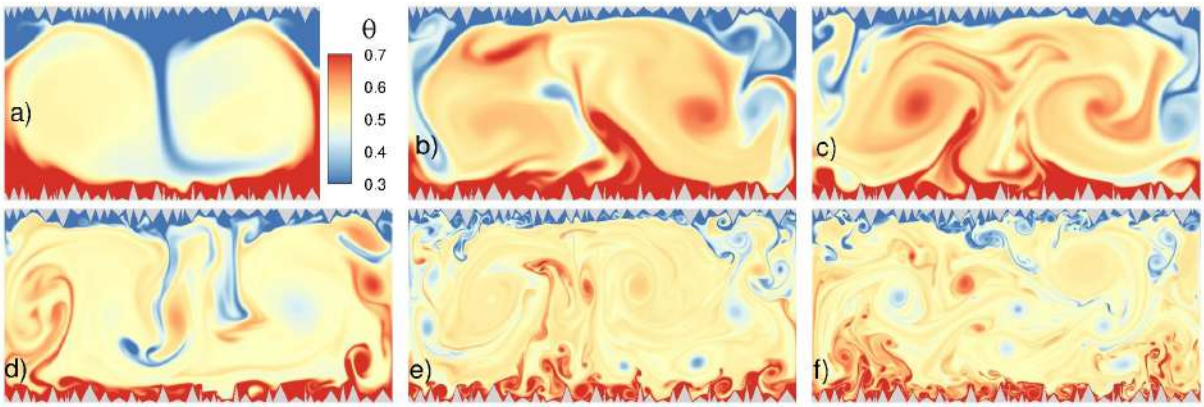

Figure 4.7: For R_2 configuration, instantaneous temperature field for *Ra* (a) 10^7, (b) 5.50×10^7, (c) 10^8, (d) 4.64×10^8, (e) 2.15×10^9, and (f) 4.64×10^9. Transition from a double-roll state to a complex multiple-roll state occurs at $Ra_c = 5.50 \times 10^7$.

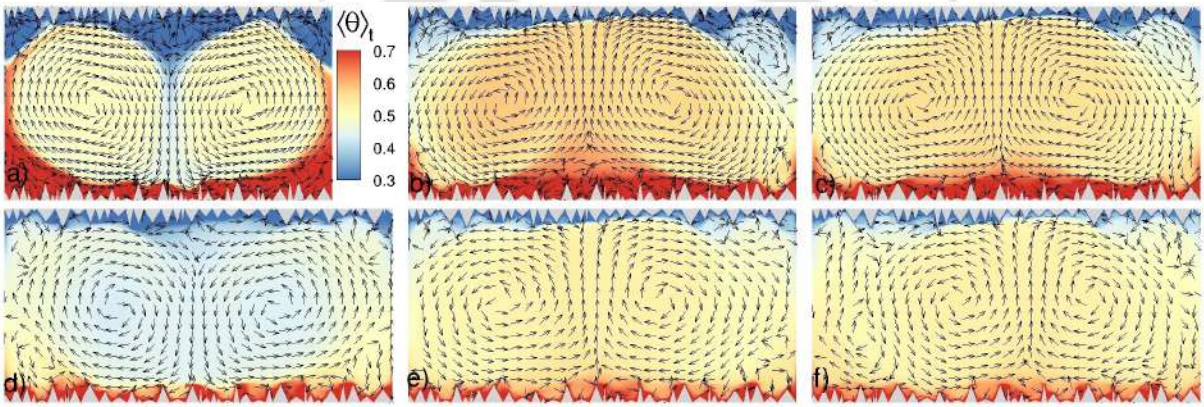

Figure 4.8: Time-averaged temperature field overlaid by velocity vectors showing the stable multiple-rolls for the same cases as in Fig. 4.7. Beyond $Ra_c = 5.50 \times 10^7$, the corner rolls become strong enough to drive the thermal plumes to the opposite boundary layer, which becomes prominent in the most demanding case.

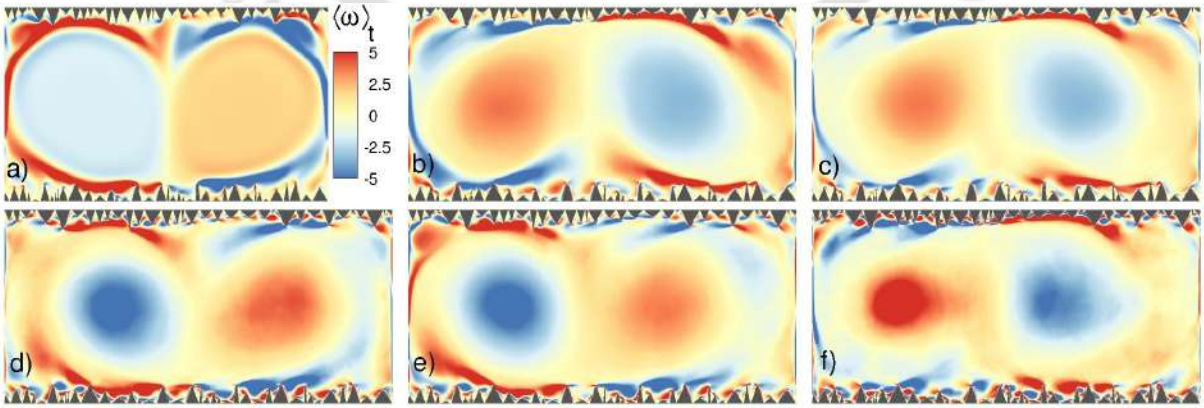

Figure 4.9: Time-averaged angular velocity field showing the stable multiple-rolls for the same cases as in Fig. 4.7. The strength of the two primary rolls increases with *Ra*, although, their size is controlled due to growing corner rolls.

increasing *Ra*, the strength and size of the corner rolls increase and become significant to wash out the cavities near the lateral walls. Figure 4.8(b) shows that the corner rolls near the right-lateral wall approach towards each other. The primary rolls near the corner rolls drive thermal plumes from one corner roll to another. In this way, the detached thermal plumes destabilize the opposite boundary layers to enhance the plume emission process. In the most demanding case, the emerging corner rolls are sufficiently large to drive the thermal plumes to the opposite boundary layer on their own, seen in frame (f). Note that the growth of the corner rolls also affects the size of the two primary rolls, which correspondingly approach cavities more efficiently and wash them out to enhance the heat flux, as seen in Fig. 4.8(d-f). Therefore, it is inferred that growing corner rolls as *Ra* increases triggers the enhanced *Nu* regime.

For the smallest roughness (R_1) configuration, similar to the R_2 case, a double-roll state persists for the entire regime, although the corner rolls do not grow with *Ra* anymore (see Figs. 4.10-4.13). The instantaneous temperature field shows the movement of thermal plumes along the lateral walls, while the time-averaged linear and angular velocity fields indicate the stable double-roll state. This double-roll state resembles the smooth case, where the large-scale rolls carry the thermal plumes to the opposite boundary layers. Therefore, a different mechanism than the complex multiple roll state and growing corner rolls cause the enhancement in both the heat flux and the scaling exponent in R_1 case. To investigate the mechanism, we observe the instantaneous temperature field in the vicinity of the rough surfaces. As shown in Fig. 4.13, instantaneous temperature contours are observed at the highest *Ra* case due to a more pronounced appearance of the flow structures. Temperature field at R_2, and R_3 configurations show that not only the peaks but also the slant edges emit thermal plumes. Zhu *et al.* [59] observed this increased plume emitting hotspots at a *Ra* close to 10^{12}. Interestingly, random roughness shows such characteristics at much lesser *Ra*, which makes it more preferable to its uniform counterpart. It is important to note that the plumes emitted from the slopes diffuse in the nearby surroundings to strengthen the secondary vortices, while the peaks emit intense plumes that enter the bulk directly. Evidently, very few secondary vortices and a significantly higher number of active peaks are present in R_1 configuration. Such thermal plume emitting regions, both the peaks and slopes, are termed as active spots (active peaks or active slopes).

At lower Ra ($< Ra_c$), insufficient active peaks allow the induced horizontal shear flow to create a smooth boundary layer over the rough surfaces filled with stagnant fluid. Such occurrence is similar to that in the smooth case where fluid residing in the cavities resist heat transfer resulting in a lower heat flux below Ra_c. However, as *Ra* increases, the thermal boundary layer

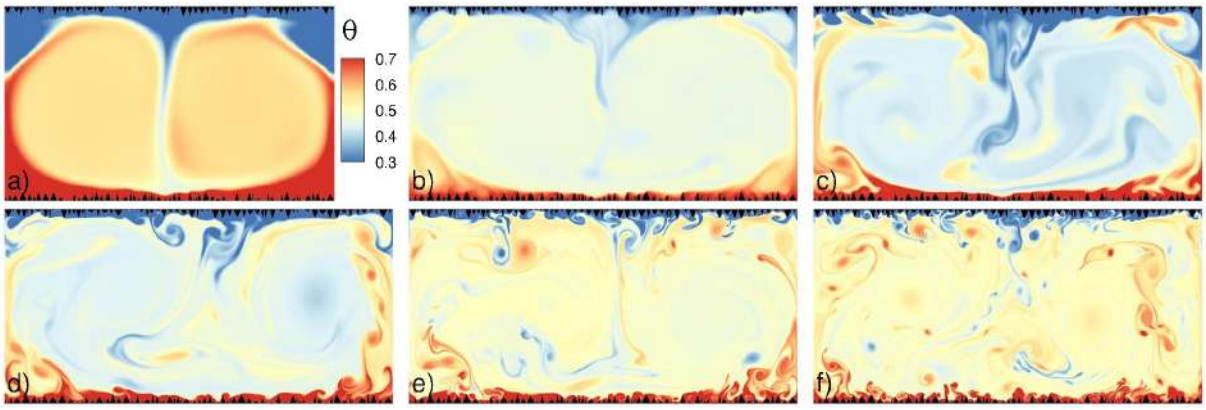

Figure 4.10: For R_1 configuration, instantaneous temperature field at *Ra* (a) 10^7, (b) 10^8, (c) 2.15×10^8, (d) 4.64×10^8, (e) 2.15×10^9, and (f) 4.64×10^9. A double-roll state persists in the entire range of simulated *Ra* cases.

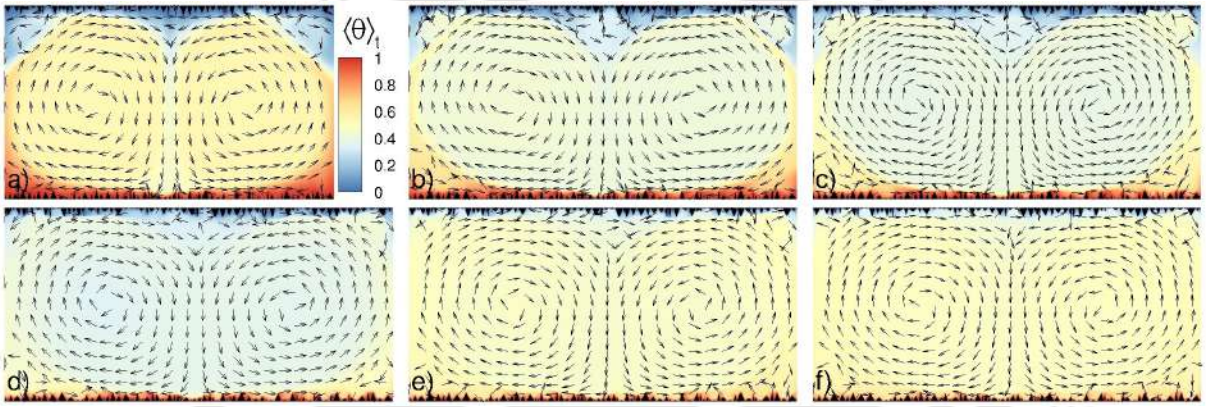

Figure 4.11: Time-averaged temperature field overlaid by velocity vectors showing the persistent and stable double-roll state for the same cases as in Fig. 4.10.

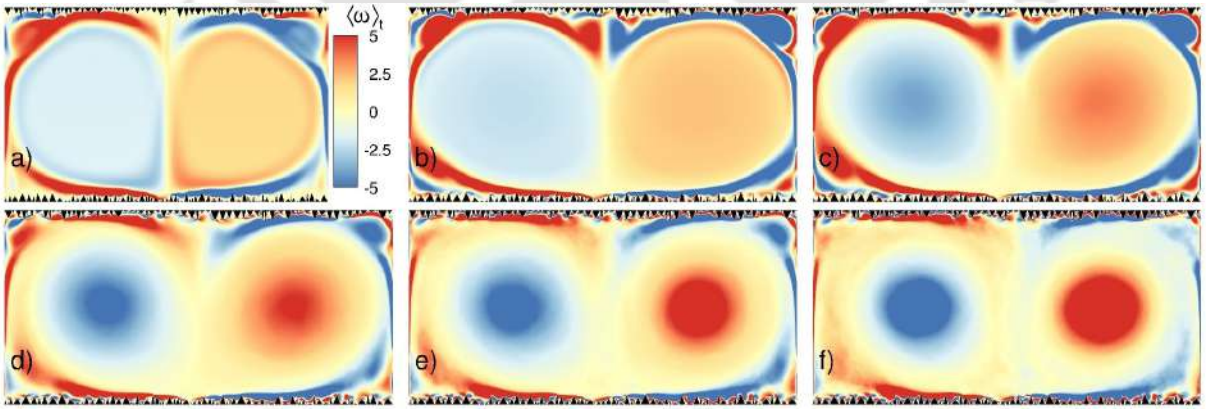

Figure 4.12: Time-averaged angular velocity field indicating the evidence of a double-roll state throughout the simulated *Ra* range. The angular velocity field is presented for the same cases as in Fig. 4.10 to show the entire *Ra* range.

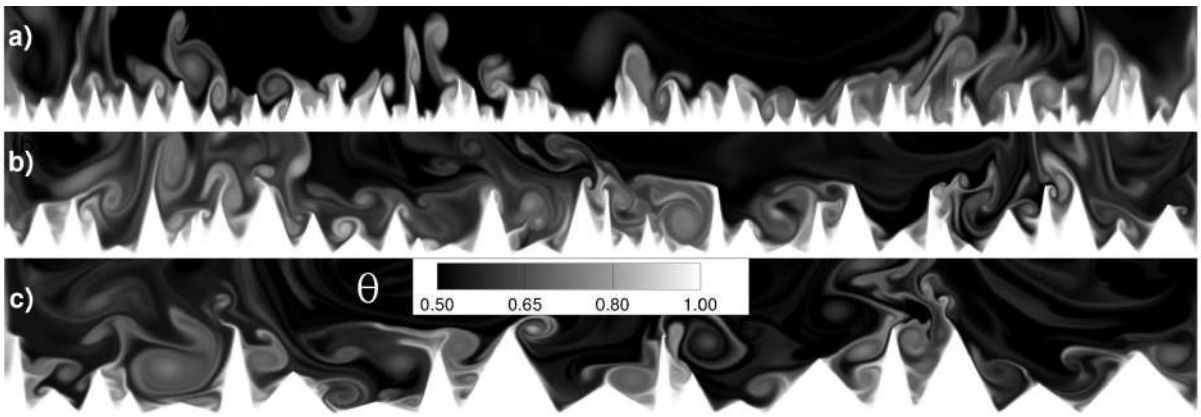

Figure 4.13: For $Ra = 4.64 \times 10^9$, snapshots of the instantaneous temperature field close to the bottom plate in (a) R_1, (b) R_2, and (c) R_3 configurations. A significantly higher number of peaks become active in R_1 case, which emits the thermal plumes in large quantities to enhance the so-called bulk-plume interaction.

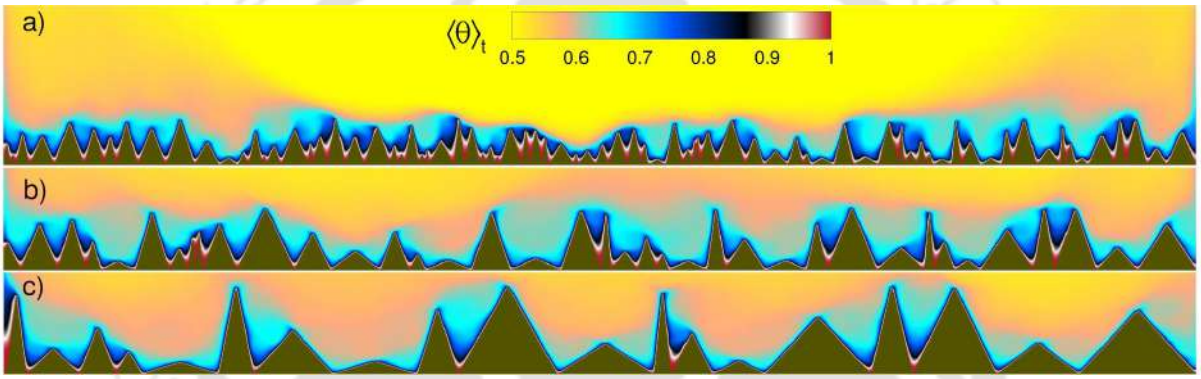

Figure 4.14: Time-averaged temperature field close to the bottom plate for (a) R_1, (b) R_2, and (c) R_3 configurations for the highest $Ra = 4.64 \times 10^9$. The approach of the bulk-mean temperature increases with overall heights of roughness elements. A thin covering of isothermal layer on the roughness elements disappears at R_1 making it more prone to greater boundary layer perturbations.

becomes thinner, and hence, exposes more peaks to the bulk fluid. Beyond the critical Ra_c, a sufficient number of peaks become active, and the boundary layer is perturbed throughout the surface. Thermal plumes emitted from these peaks enter the bulk directly to enhance the so-called bulk-plume interaction. Therefore, the increased bulk-plume interaction increases the heat flux and $Nu(Ra)$ scaling exponent. A note on the variation of this exponent with the roughness configurations is relevant here. The secondary vortices are either weak or absent in the R_1 configuration due to too many roughness elements creating smaller throat regions. However, in the other two configurations, the wider throat region causes strong secondary vortices. Since

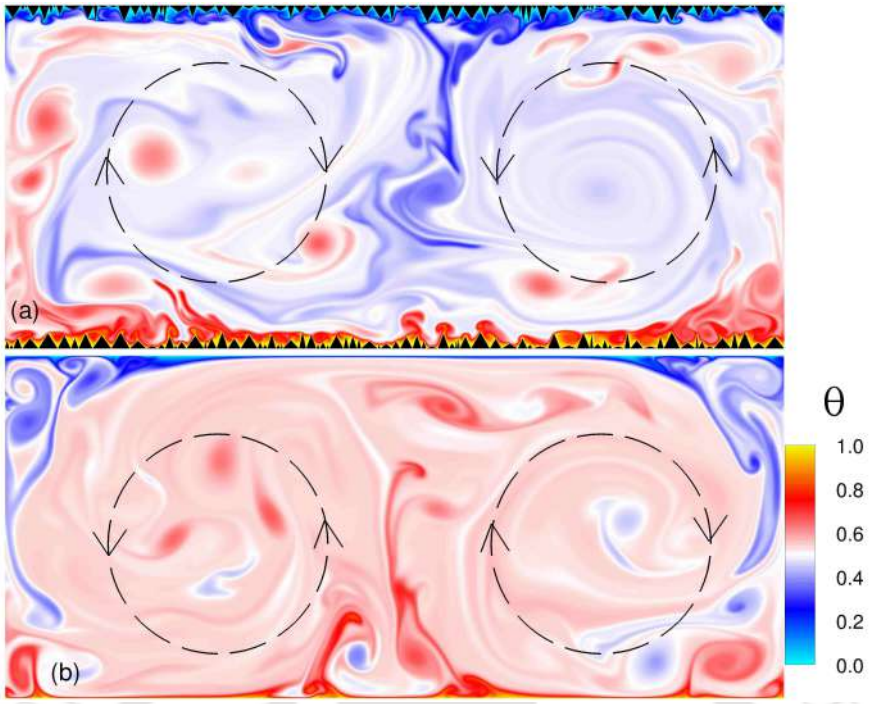

Figure 4.15: Instantaneous temperature field at $Ra = 10^9$ for (a) R_1, and (b) smooth case showing that the two large-scale rolls carry the thermal plumes to the opposite surfaces. Contrary to the other configurations, thermal plumes do not enter the bulk directly and move along the lateral walls and at the confluence of the large-scale rolls in these two convection cells.

the increased turbulence in the cavities reduces the perturbation of the boundary layer, a drop in the scaling exponent becomes obvious as it behaves similar to the smooth case in the cavities. These arguments agree well with the previous studies [106], where the wider throat region was found to strengthen the secondary vortices but reduce the $Nu(Ra)$ scaling exponent. Therefore, the present study suggests that the scaling exponent depends on the width of the throat region.

Further, with the help of a time-averaged temperature field in the vicinity of rough surfaces, perturbation of thermal boundary layers can be detected. As shown in Fig. 4.14, the large temperature gradient is confined to a thin layer near the roughness elements and covers the entire surface in R_3, except for the places where space between the roughness elements is minimal. Qualitatively, this smooth covering of the surface shows the absence of the perturbed boundary layers. Also, the presence of the bulk-mean temperature is apparent at most of the surface in this configuration. On the other hand, the boundary layer is more perturbed in R_2, while a strongly perturbed boundary layer is evident in the R_1 configuration. In the latter, the bulk-mean temperature of the flow hardly approaches the cavity fluid. Clearly, a narrow spacing between the roughness elements in R_1 case resists the bulk-mean temperature to reach the cavities, and thus,

supports the boundary layer perturbation. On the other hand, a wider spacing helps in a thorough mixing of the cavity fluid that allows the bulk-mean temperature to approach the cavities, as seen in the R_3 case. These results support the above arguments related to the high turbulent intensity, which modifies the scaling exponent in the three configurations. Furthermore, using a schematic diagram, Zhu *et al.* [2] showed the boundary layer perturbation near the rough surface. The schematic is found consistent with the present tallest roughness case (R_3), where the perturbation nearly vanishes. However, the perturbation is clearly observed in the other two cases. This study shows that spacing between the roughness elements controls the boundary layer perturbation. Also, the geometric characteristics of random roughness reveal a complex interaction between the bulk-mean and near-wall temperature, which was absent in the previous studies.

In order to study the role of plume emitting peaks, we further investigate two important components of turbulent kinetic energy (TKE) budget, buoyancy (P_b) and shear production (P_s). Mathematically, they are computed as

$$P_s = -\overline{u_i' u_j'} S_{ij} \qquad \text{and} \qquad P_b = g\beta \overline{u_i' \theta'} \delta_i y$$

where prime and S_{ij} represent the fluctuation and mean strain rate, respectively. While buoyancy production signifies production of turbulent fluctuations by thermal plumes, shear production indicates the energy interaction between mean flow and turbulent fluctuations. As shown in Fig. 4.16 and 4.17, we present the variation of P_b and P_s in the horizontal direction just above the maximum roughness height ($H/100$ unit distance above the maximum roughness height). It is evident that below the critical *Ra*, magnitude of the two components of TKE is insignificant. However, as *Ra* increases, their magnitude, and variation in the horizontal direction increases. Since P_b is a direct measure of thermal plume, a sudden rise in peaks confirms the idea of activation of numerous peaks beyond the critical *Ra*. A similar observation is quite apparent in R_2 and R_3 cases. However, magnitude of buoyancy production is higher in the two taller configurations. This happens due to frequent washing-out of the cavities by the smaller rolls present in two taller roughness cases and direct emission of thermal plumes in the bulk. The transformation of large-scale rolls into smaller ones provides them greater access to the cavities, which further supports why R_3 results in higher heat flux than the other configurations.

In terms of magnitude, shear production shows the opposite trend to P_b. In R_1 case, shear production is significantly greater as compared to R_2 and R_3. Note that higher P_s indicates transfer of energy from mean flow to turbulent fluctuations. It is observed that a double-roll state remains intact in the R_1 case, which incites a strong lateral movement of fluid. Interaction between the mean flow and surface roughness increases with *Ra*, resulting in stronger velocity

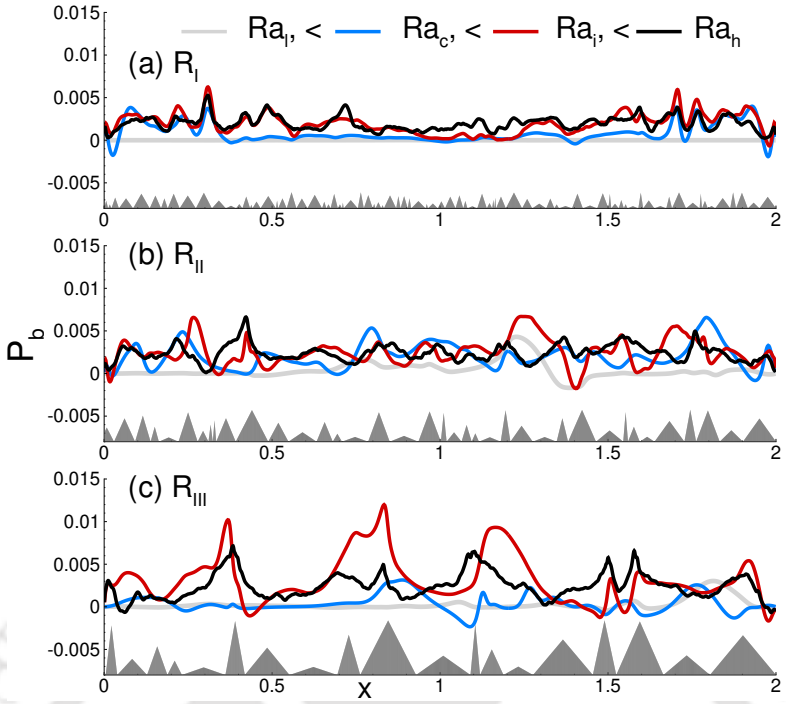

Figure 4.16: Buoyancy production in (a) R_1, (b) R_2, and (c) R_3 before, at and above the critical Rayleigh number (Ra_c). Ra_l indicates the Ra case lesser than Ra_c $(Ra = 3\times10^6)$, while Ra_i, and Ra_h show the intermediate (4.64×10^8) and highest Rayleigh cases (4.64×10^9), respectively. Note that the symbol "$<$" shows the increasing order of Ra from Ra_l to Ra_h.

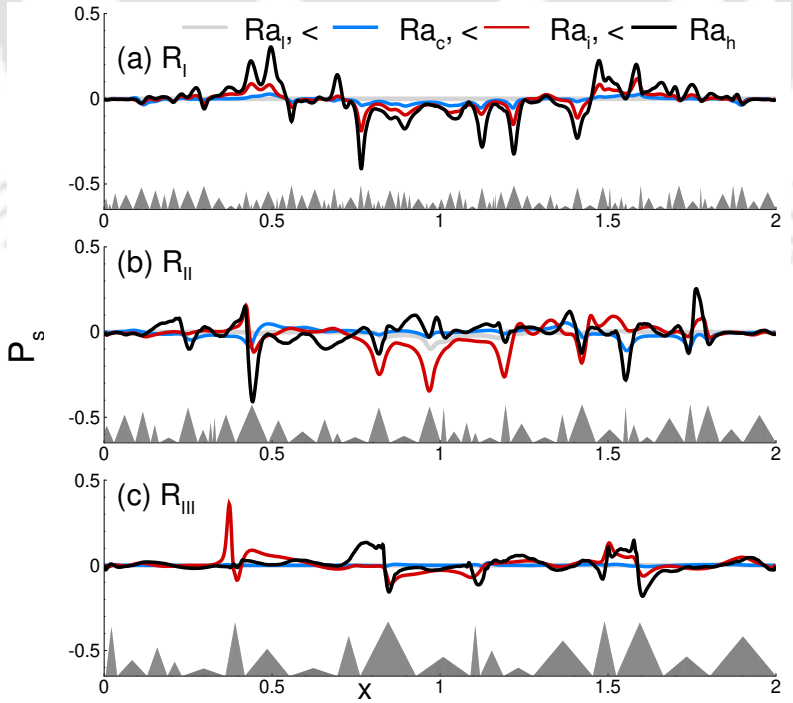

Figure 4.17: Shear production in (a) R_1, (b) R_2, and (c) R_3 before, at and after the critical Rayleigh number (Ra_c). The labels are same as in Fig. 4.16.

fluctuations. However, it seems obvious that multiple large-scale rolls hinder their motion, resulting in a flow that supports the vertical movement of thermal plumes more than the horizontal one. Thus, the two components of TKE ascertain the significance of active peaks and unveils the strongly induced horizontal movement of fluid in the R_1 case.

The previous investigations have suggested that the so-called bulk-plume interaction can be improved by increasing the number of active spots (plume emitting spots) [53, 59, 2]. However, the current study reveals that there can be three ways to enhance this interaction. First, by a breakdown of large-scale rolls into smaller ones, which can enter the cavities more efficiently and sweep the boundary layer, as in R_3 set-up. These smaller rolls enhance the mixing of fluid in the cavity regions to emit intense thermal plumes more frequently. Second, the growing strength and size of the corner rolls evacuate the cavities near the lateral walls and reduce the size of the primary rolls. Third, by increasing the number of active peaks, which emits more thermal plumes, as in R_1. Surprisingly, R_2, and R_3 also possess attributes of the higher active spots. These results suggest that not only the tilt of the cell but rough surfaces also induce complex roll states or distorted structures, which results in increased heat flux.

Thus far, in terms of large-scale rolls, we have argued that the heat transport phenomenon in R_1 case is similar to that in the smooth case. Figure 4.15 shows flow visualization in the two convection cells at $Ra = 10^9$. Clearly, two rolls of nearly the same size are evident in both the cases, as shown by the dashed lines. Moreover, Fig. 4.11 also shows the persistent double-roll state in the entire simulated *Ra* range. The induced shear flow near the isothermal surfaces destabilizes the boundary layers, resulting in the emission of thermal plumes. These plumes are further carried away by the large-scale rolls along their periphery and do not allow the thermal plumes to enter the bulk directly. It occurs due to strong large-scale rolls. The detached thermal plumes reach the opposite boundary layers and destabilize them. However, under the influence of stronger rolls, some plumes are directed towards the bulk region. The presence of these plumes is evident in the bulk region in both the cases.

Despite the similar heat transport mechanism in these two convection cells, different *Nu* and scaling exponent have been observed (see Sec. 4.3). In the smooth case, the emission of thermal plumes is localized to the confluence of two large-scale rolls and near the lateral walls. However, in the roughness case, several plumes emitting peaks cause significant differences in heat flux. Figure 4.15(a) shows numerous hotspots which emit intense thermal plumes. A homogeneous bulk region is also observed in the roughness case, while a marginally high temperature dominates the bulk region otherwise. We also note that greater emission of thermal plumes

also increases turbulent intensity in the bulk region. Therefore, the heat transport process in the two cases responds differently, suggesting that the enhanced emission of thermal plumes in the roughness case influences the transport properties without impacting the large-scale flow structures. These arguments explain how enhanced heat flux and scaling exponent was observed in the previous studies despite persistent double-roll state in roughened thermal convection cell of $\Gamma = 2$ [2, 53, 59].

4.5 Dissipation rates

Dissipation of energy is a natural phenomenon that occurs in all turbulent flows. Since RBC is a thermo-convective flow, both thermal (ϵ_θ) and kinetic energy (ϵ_u) dissipation rates become relevant. ϵ_θ and ϵ_u are quantified by temperature and velocity gradients, respectively. Mathematically, they are written in nondimensionalized form as

$$\epsilon_{\mathbf{u}} = \sqrt{\frac{Pr}{Ra}}(|\nabla \mathbf{u}|^2) \text{ and } \epsilon_\theta = \frac{1}{\sqrt{RaPr}}(|\nabla \theta|^2). \tag{4.1}$$

In RBC, all the $Nu(Ra)$ scaling theories assume the effect of boundary layers, which are associated with high thermal and kinetic energy dissipation rates. It occurs due to the dissipation of most of the thermal plumes (also known as detached boundary layer) in the near-wall region before being carried away by large-scale circulation (LSC). Previous sections reveal that roughness elements alter the nucleation of thermal plumes and heat transport mechanism. Thus, their effect on dissipation rates is also expected.

In RBC, dissipation rates play a crucial role in determining the global heat transport properties. Based on the literature, the importance of dissipation rates in a smooth and rough convection cell are described as follows. In a smooth convection cell, based on the dominance of dissipation rates in boundary layer and bulk region, Grossmann & Lohse [30] proposed a unified scaling theory, which yields the dependency of *Nu* on *Ra* and *Pr*. According to their proposition, both ϵ_u and ϵ_θ dominate in the bulk region in the so-called ultimate regime. Further, they modified the theory by assuming the contribution of thermal plumes instead of boundary layer region [31]. Later, Verzicco & Camussi [100] reported that at high *Ra* both ϵ_u and ϵ_θ increase in the bulk while they drop in the boundary layer region. Similar results were also obtained by Shishkina & Wagner [107] for thermal dissipation rate. These studies suggest that bulk contribution, in terms of the dissipation rates, should dominate as *Ra* increases, indicating the attainment of the ultimate regime.

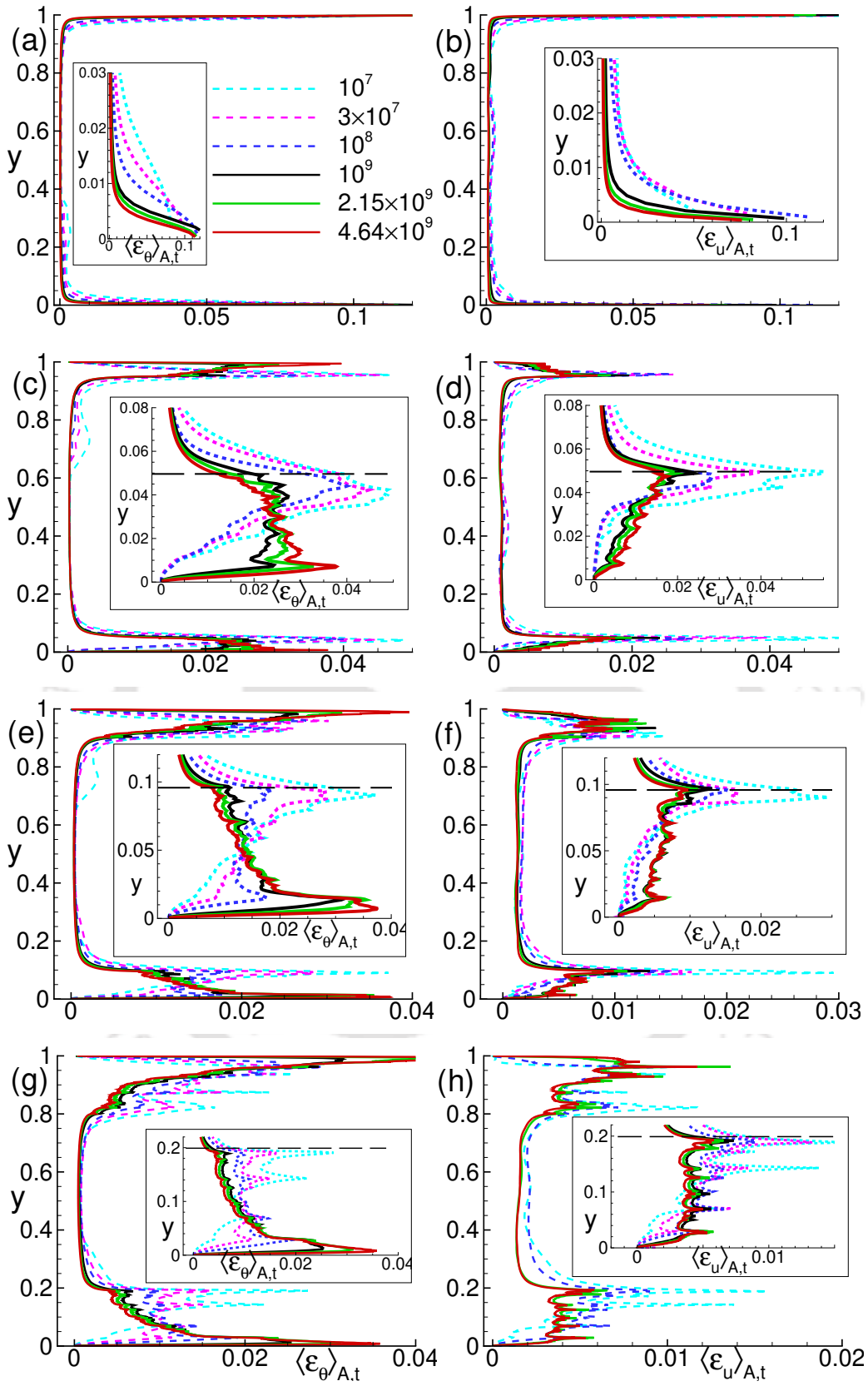

Figure 4.18: Vertical variation of thermal ϵ_θ (left panel) and kinetic ϵ_u (right panel) energy dissipation rates for the smooth (first row), R_1 (second row), R_2 (third row), and R_3 case (last row). The insets show the variation of dissipation rates near the bottom surface, and the long-dashed lines indicate the corresponding maximum roughness heights.

Stringano *et al.* [105] compared the global dissipation rate in a rough and smooth convection cell. With increasing *Ra*, the dissipation rates in the smooth case were observed to drop quickly compared to the rough case. Using a uniform roughness configuration, Zhu *et al.* [59] studied vertical profiles of thermal dissipation rate in the enhanced exponent regime and obtained saturation to the classical-regime that occurs due to formation of a thin boundary layer over the roughness elements at high *Ra*. In contrast to the smooth case, they observed that the dissipation rate increases in the cavity region with *Ra*, resulting in a boundary layer controlled regime. Thus, it appears that in roughness assisted convection, role of boundary layer and the bulk region reverses in the high-*Ra* regimes when viewed from the angle of dissipation rate. However, quantification of ϵ_θ in near-wall and bulk region unveils the true characteristics of enhanced exponent regime, which was absent in the previous study. Also, a thorough investigation of the dissipation rates in roughness facilitated convection cell is required in order to understand the global heat transport properties. Therefore, in the present work, firstly, vertical profiles of both ϵ_u and ϵ_θ are studied, and then the contribution of the dissipation rates from the near-wall and bulk regions are discussed. The dissipation rates computed from Eq. (4.1) are ensembled over time and horizontal area, represented by $\langle\phi\rangle_{A,t}$ for a quantity ϕ.

In what follows, we begin with the vertical profiles of the dissipation rates in the smooth convection cell, as shown in Fig. 4.18(a-b). The inset shows a magnified view of the profiles in the vicinity of the bottom plate. Both ϵ_u and ϵ_θ are nearly zero in the bulk region, indicating a well-mixed homogeneous region. The dissipation rates rise abruptly near the walls (see the insets), showing the boundary layer region. It is also evident that the extent of boundary layer region diminishes with increasing *Ra* as the homogeneous bulk region stretches towards the plate. Further, the dissipation profiles are presented for R_1, R_2, and R_3 cases in Fig. 4.18 (c-h), respectively. Marginal asymmetry in $\langle\epsilon_\theta\rangle_{A,t}$ at lower *Ra* can be attributed to the detachment of intense, large-sized thermal plumes from the roughness elements that directly enter and dissipate in the bulk region (see top panels of instantaneous temperature contours in Figs. 4.4, 4.7, and 4.10). However, the large-sized thermal plumes transform into small and fine-scale structures at higher *Ra*.

In the near-wall region, thermal dissipation rate increases with vertical height to attain a local maximum, followed by a decreasing trend to become nearly zero in the bulk region at a higher *Ra*. This observation is in contrast with the smooth case where dissipation rates are maximum close to the surface. This surge in ϵ_θ with y reflects the sudden change of flow behavior due to secondary vortices in the throat region. After reaching the maximum, it drops sharply above the

maximum roughness heights. On the other hand, at lower *Ra*, ϵ_θ increases in the throat region and becomes maximum at the tip of the tallest roughness height. This distinct feature is a direct effect of the confined fluid in the throat region, where fluid remains nearly stagnant at lower *Ra*. Insufficient strength of secondary vortices at lower *Ra* does not allow them to move out of the cavities, and hence the emitted plumes dissipate in the cavities. Furthermore, ϵ_θ in the throat region shows a smooth decline in R_3 case than the other configurations. In the tallest roughness case (R_3), the homogeneous-bulk flow has a higher tendency to enter the roughness cavities, which is reflected in smooth decline of ϵ_θ in the cavities. Note, owing to a lesser number of roughness elements, R_3 configuration is characterized by a wider throat region. Thus, it can be inferred from the observed smooth decline of ϵ_θ in R_3 that the dissipation rate is least affected by the roughness configurations having a wider throat region. Clearly, boundary layer dominated thermal dissipation can only be prescribed for high *Ra*. At lower *Ra*, ϵ_θ peaks close to the tip of the roughness.

Further, vertical profiles of kinetic energy dissipation rate are presented in the right panels of Fig. 4.18. In contrast to the variation of thermal dissipation rate with *Ra*, an increasing trend in $\epsilon_u(y)$ profile is observed for all *Ra* cases, and it becomes maximum at the tip of the tallest roughness heights. Interestingly, ϵ_u rises marginally up to a certain height, which qualitatively shows the viscous boundary layer inside the cavities. However, above the boundary layer, the presence of secondary vortices results in a sudden increase in the dissipation rate. This feature is more pronounced in lower *Ra* cases due to thick boundary layer. The above-mentioned effect of a wider throat region is also reflected in the vertical profiles of ϵ_u. Instead of continuously increasing up to the maximum roughness height, as seen in the previous two configurations, ϵ_u in R_3 remains nearly same inside the cavity. Thus, it is again confirmed that the wider throat region weakly affects the dissipation rates.

Thus far, it is observed that dissipation of kinetic and thermal energy varies in the cavities and bulk region, suggesting different flow behavior in these two regions. Therefore, it becomes crucial to investigate the contribution of dissipation rates from these two regions separately. However, it is important to note that the behavior of dissipation rates in the bulk region is nearly the same in both the rough and smooth cases. In the previous studies, boundary layer thickness computed from the well-known rms technique was used to demarcate the near-wall and bulk regions [107, 48]. However, in the current work, the dissipation rates in the cavities or near-wall (NW) region and the bulk region is studied. Note that instead of the boundary layer, the near-wall contribution is investigated here. Both ϵ_u and ϵ_θ are computed from the near-wall (NW)

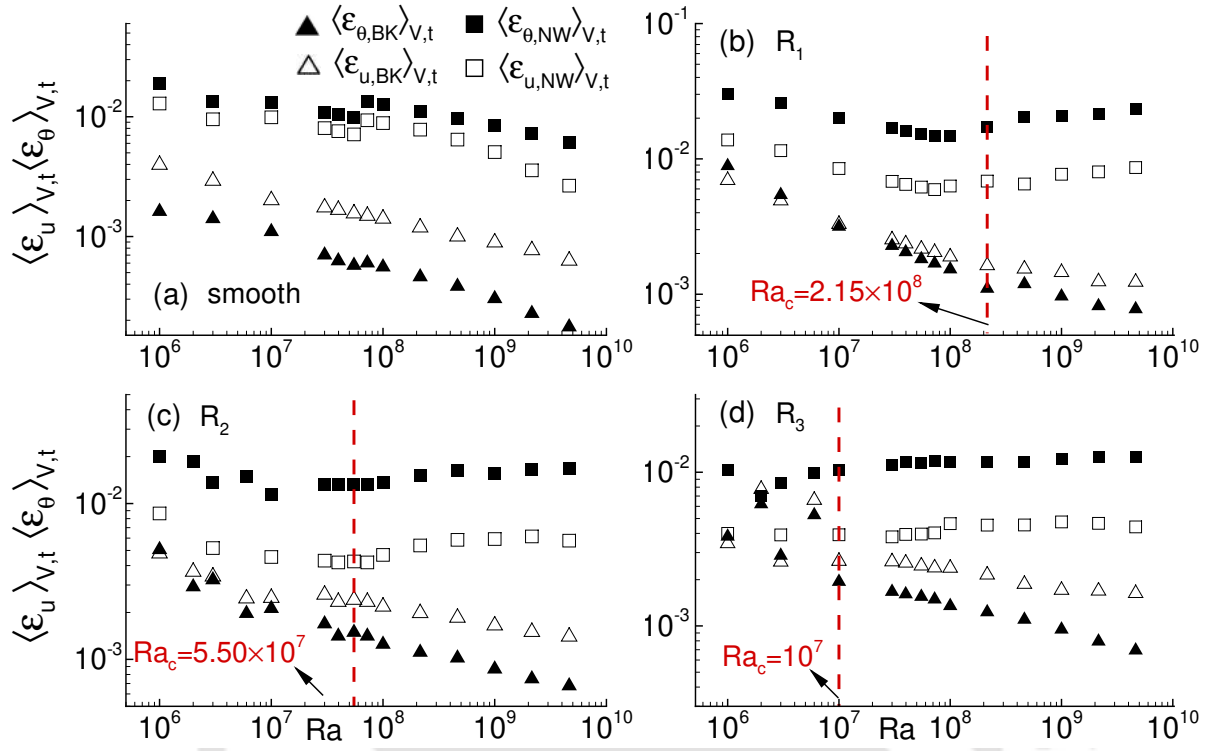

Figure 4.19: Locally-averaged thermal ϵ_θ (filled symbols) and kinetic ϵ_u (open symbols) energy dissipation rates for the near-wall (square) and bulk region (triangle) for the (a) smooth case, (b) R_1, (c) R_2, and (d) R_3 configurations. In the near-wall region, the dissipation rates indicate transition to the enhanced exponent regime in the three rough configurations. Vertical dashed-lines show the critical Ra_c beyond which the enhanced heat flux regime is obtained.

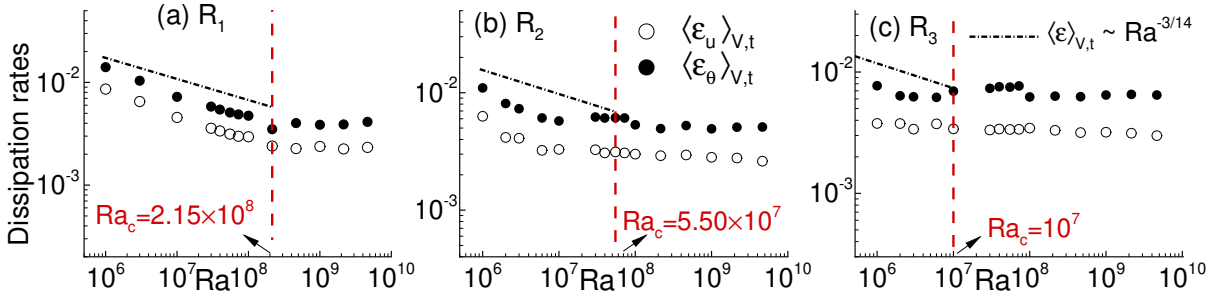

Figure 4.20: Variation of volume-averaged thermal (filled symbols) and kinetic (open symbols) energy dissipation rates with *Ra* in (a) R_1, (b) R_2, and (c) R_3 configurations. While the vertical dashed lines show the critical Ra_c beyond which the enhanced heat flux regime is obtained, the dash-dot lines indicate $\epsilon \sim Ra^{-3/14}$ which follows from the power-law $Nu \sim Ra^{2/7}$.

and bulk (BK) regions as

$$\langle \epsilon_{\theta,\mathrm{NW}} \rangle_{V,t} = \frac{1}{2}\left[\frac{1}{h_{max,b}}\int_0^{h_{max,b}} \langle \epsilon_\theta \rangle_{A,t}(y)dy + \frac{1}{h_{max,t}}\int_{H-h_{max,t}}^{H} \langle \epsilon_\theta \rangle_{A,t}(y)dy\right] \tag{4.2}$$

$$\langle \epsilon_{\theta,\mathrm{BK}} \rangle_{V,t} = \frac{1}{H-(h_{max,b}+h_{max,t})}\int_{h_{max,b}}^{H-h_{max,t}} \langle \epsilon_\theta \rangle_{A,t}(y)dy \tag{4.3}$$

$$\langle \epsilon_{\mathrm{u,NW}} \rangle_{V,t} = \frac{1}{2}\left[\frac{1}{h_{max,b}}\int_0^{h_{max,b}} \langle \epsilon_u \rangle_{A,t}(y)dy + \frac{1}{h_{max,t}}\int_{H-h_{max,t}}^{H} \langle \epsilon_u \rangle_{A,t}(y)dy\right] \tag{4.4}$$

$$\langle \epsilon_{u,\mathrm{BK}} \rangle_{V,t} = \frac{1}{H-(h_{max,b}+h_{max,t})}\int_{h_{max,b}}^{H-h_{max,t}} \langle \epsilon_u \rangle_{A,t}(y)dy \tag{4.5}$$

where $h_{max,b}$ and $h_{max,t}$ are the tallest roughness heights for bottom and top surfaces, respectively. Here, $\langle\phi\rangle$ and $\phi(y)$ refers to averaged and y dependent quantities. While $h_{max,b}$ for R_1, R_2, and R_3 configurations are 0.0496, 0.0958, and 0.1990, respectively, $h_{max,t}$ are 0.0491, 0.0958, and 0.1925, respectively. Note that it is obvious to observe differences in their values, as they are generated from a random number generator. The top and bottom surfaces are not simply inverted but created as two different objects with different limits, which results in the differences. Figure 4.19 shows the contribution from the bulk and near-wall regions for the smooth case and three roughness configurations. Note that near-wall and bulk region for the smooth case is identified by the peak value of the temperature variance [48].

For the smooth case, contribution of ϵ_u and ϵ_θ from both the bulk and near-wall region show monotonic drop for nearly four decades of *Ra*. The decreasing dissipation rates in the near-wall region indicate the thinning of boundary layers, while that in the bulk region shows the transformation of large-sized thermal plumes into small-scale plumes. Least-square fit suggests both of them drop at nearly the same rate. The obtained scaling laws for them are

$$\langle \epsilon_{\mathbf{u}} \rangle_{V,t} = 0.15Ra^{-0.22} \text{ and } \langle \epsilon_\theta \rangle_{V,t} = 0.82Ra^{-0.2} \tag{4.6}$$

which are in good agreement with the previous studies [103, 48].

In contrast to the smooth case, the decreasing trend of dissipation rate (for both the near-wall and bulk regions) with *Ra* ceases at the critical *Ra* in the roughness cases. Surprisingly, in the near-wall region, the dissipation rate becomes nearly independent of *Ra* in the enhanced exponent regime. The saturation in dissipation rates in the near-wall region indicate the increased active slopes, which is a slant surface of a roughness element that actively participate in thermal plume emission. Most of the thermal plumes erupting from these slopes diffuse in the cavity regions, as observed from the instantaneous contours in Fig. 4.13. Such enhanced eruption and subsequent diffusion of thermal plumes inside the cavities balance the assumed drop in the dissipation rates, resulting in nearly the same dissipation rates in the enhanced exponent regime.

On the other hand, both the dissipation rates continue to drop in the bulk region, though at a smaller rate. This supports our earlier observation about similar behavior of ϵ_θ in the bulk for the smooth and roughened cases. The splitting of global dissipation rates $\epsilon_\theta = \epsilon_{\theta,BK} + \epsilon_{\theta,NW}$, and $\epsilon_u = \epsilon_{u,BK} + \epsilon_{u,NW}$ turn out to be more accurate for roughness cases. Here the dominance of boundary layer at high *Ra* arrests the otherwise monotonic drop in $\epsilon_{\theta,NW}$ while the bulk contribution continues to fall.

We further show the dependence of global dissipation rates on *Ra* in Fig. 4.20. Instead of computing the dissipation rates in the bulk and boundary layer region separately, they are calculated by averaging over the whole domain. Both ϵ_u and ϵ_θ can be written in terms of the global heat transport properties as

$$\langle \epsilon_u \rangle_{V,t} = \sqrt{\frac{Pr}{Ra}}(Nu_{\epsilon_u} - 1) \qquad \text{and} \qquad \langle \epsilon_\theta \rangle_{V,t} = \frac{1}{\sqrt{PrRa}} Nu_{\epsilon_\theta} \tag{4.7}$$

where the respective *Nu* are calculated based on the dissipation of kinetic ($\langle |\nabla u| \rangle_{V,t}$) and thermal energy ($\langle |\nabla \theta| \rangle_{V,t}$). Beyond the Ra_c, global dissipation rates become nearly invariant of *Ra* in all the three roughness cases. With the $Nu \sim Ra^{1/2}$ scaling, ϵ becomes *Ra*-invariant which is clearly seen for $Ra > Ra_c$. On the other hand, an interesting feature emerges before the transition (below Ra_c) to the enhanced heat flux regime. Here, the dissipation rate drops with an exponent of $-3/14$, which can be theoretically obtained by assuming $Nu \sim Ra^{2/7}$ in Eqs. 4.7. Clearly, the best-fit of the data reveals that R_1 nearly follows the $2/7$ power-law, while it deviates as average roughness height increases. The prevailing $2/7$ law in R_1 case indicates the strong dominance of a double-roll state and ineffective roughness-flow interaction. In other words, the rough surface, in this case, is inactive due to a weak thermal forcing and the fluid close to the asperities behave as in the smooth case.

In conclusion, the vertical profiles of ϵ_θ and ϵ_u reveal the effect of a throat width on dissipation rates, where a wider throat region is found to influence them weakly. Contribution of the dissipation rates from the near-wall region ascertains the enhanced exponent regime through $\epsilon - Ra$ dependency, where the dissipation rates remain nearly the same throughout the enhanced exponent regime. It is proposed that the emission of thermal plumes from the slant surface and their subsequent diffusion in the cavity region alters the monotonically decreasing trend of dissipation rates with *Ra*. Moreover, the dominance of both the dissipation rates in the near-wall region indicates the boundary layer controlled regime, and the enhanced scaling exponent does not represent the so-called ultimate regime. Zhu *et al.* [59] also proposed that ϵ_θ in the cavities increases with *Ra*, signifying the boundary layer controlled regime. We have shown that such an argument holds only indirectly as increased plume emission from the slant faces make-up for

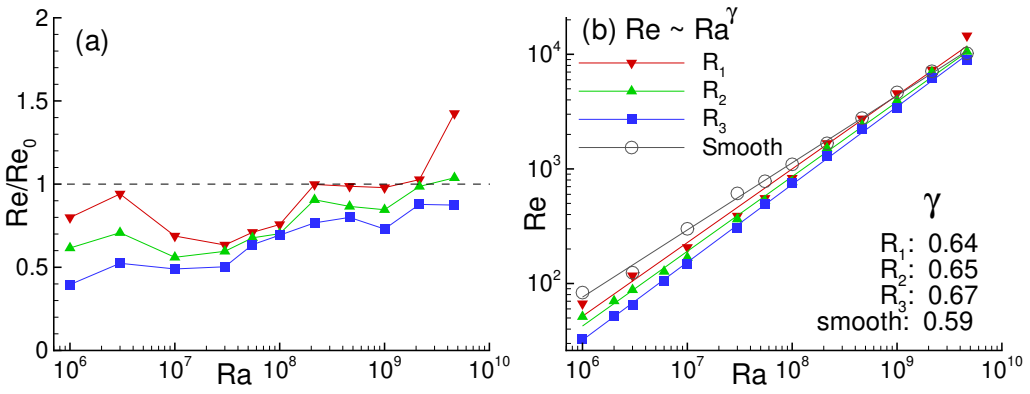

Figure 4.21: (a) Variation of normalized Reynolds number (Re/Re_0) with Ra for the three roughness cases. Note that Re_0 represents the Reynolds number for the smooth case. (b) $Re \sim Ra^{\gamma}$ scaling law shows marginal improvement in γ for roughness cases

the drop in ϵ_θ at higher Ra.

4.6 Effect of roughness on flow strength

In the previous section, we observed transformation of a double-roll state to a multiple-roll state in R_2 and R_3 configurations, whereas the former remained unaltered throughout the simulated Ra range for R_1 case. Here we study how stability of the DRS and its transformation impact the flow strength, which plays a crucial role in heat transport. In a previous investigation, Zhang *et al.*[48] quantified the strength of convection in terms of Reynolds number (Re) as

$$Re = \frac{UH}{\nu} \tag{4.8}$$

where $U = \sqrt{\langle \mathbf{u}.\mathbf{u} \rangle_{V,t}}$. They observed $Re \sim Ra^{0.59\pm0.02}$ which shows that flow strength in a 2D geometry is stronger than its 3D ($Re \sim Ra^{0.5}$) counterpart due to the absence of a lateral dimension which restricts the movement of plumes to escape in the third direction [108–110]. Consequently, the emitted thermal plumes drive the large-scale rolls and the corner rolls. Wang *et al.* [111] also used the same expression to quantify the strength of convection.

Figure 4.21(a) shows the variation of Re, normalized by the smooth case data (Re_0), with thermal forcing. Evidently, flow strength in the smooth convection cell is significantly greater than that in the roughness cases in the lower Ra range. Also, Re/Re_0 is the highest in R_1 and least in R_3, showing a consistent decreasing trend with increasing roughness height in the simulated Ra range. The lower flow strength in taller roughness cases indicates that multiple rolls hinder the flow strength. In lower Ra range, a slight improvement in Re signifies the mobility of entrapped

fluid. As *Ra* increases, roughness elements interrupt the flow which results in a drop in Re/Re_0 in the *Ra* range $3 \times 10^6 - 3 \times 10^7$. Subsequently, further increase in thermal forcing yields a monotonically increasing trend in $Re(Ra)/Re_0$. Interestingly, *Re* in R_1 case becomes comparable with the smooth case, $Re/Re_0 \approx 1$, in the enhanced heat flux regime. Eventually, it becomes greater than its smooth counterpart at the highest *Ra*. On the other hand, $Re/Re_0 < 1$ in the other two taller configurations indicates the reduced flow strength.

By recalling the enhanced heat flux due to roughness elements, we observe a contrasting role of roughness in impacting the flow strength. This contrasting behavior can be explained from the viewpoint of large-scale rolls. While MRS in R_2 and R_3 wash out the cavities efficiently, they impede the movement of flow. In other words, the taller roughness elements which directly emit thermal plumes in the bulk region also act as an obstacle for the large-scale rolls. In contrast, the smallest roughness case exhibits appreciable improvement in *Re*. In the enhanced heat flux regime in R_1 case, the tiny roughness elements become active and directly emit the thermal plumes in the bulk region, while below the Ra_c, contribution of these peaks in thermal plume emission is insignificant. Note that these active peaks impart a shearing effect on the large-scale rolls, which enhances the flow strength. This effect is seen in Fig. 4.17, where shear production in R_1 was significantly higher as compared to its taller roughness counterparts.

We further show the $Re \sim Ra^{\gamma}$ dependence for the three roughness configurations and smooth case in Fig. 4.21(b). For smooth case, it is observed that $Re \sim Ra^{0.59}$, which is same as reported by Zhang *et al.* [48]. However, the exponent is slightly higher in the roughness cases, although it is nearly equal for all of them, given by $0.64, 0.65$, and 0.67 for R_1, R_2, and R_3, respectively. Note that only a slight improvement in γ indicates the insignificant impact of roughness elements on $Re(Ra)$ scaling law. This analysis clearly shows that altering the flow structures can enhance the heat flux without improving the flow strength. Larger roughness has greater tendency to alter the stable DRS of low *Ra* range as compared to the smaller elements.

4.7 Conclusions

The present work has explored the effect of rough boundaries on both heat transport and flow dynamics in two-dimensional turbulent RBC. Though roughness elements of varying height and base are present, onset of enhanced heat flux regime, with different $Nu(Ra)$ scaling exponents, is triggered at different critical thermal forcing depending on the maximum roughness height. Such an onset is marked by a transformation from a double to a single peak in PDF of temperature

fluctuations in the bulk, and discontinuities in near-wall contribution of thermal dissipation rate. Unlike the smooth case, near-wall and global estimates of ϵ_θ become invariant of Ra in the enhanced heat flux regime. However, below the critical *Ra*, the $\epsilon - Ra$ dependence shows the evidence of the classical scaling. Thus, an increase in the $Nu(Ra)$ scaling with a near-constant near-wall contribution to thermal dissipation suggests a mixed view of the effect of boundary layer at high Ra.

The bulk-plume interaction which is seen to facilitate an enhanced scaling for all roughness heights, is achieved through different routes. For the tallest roughness heights, large-scale rolls breakdown into smaller ones which can enter the cavities more efficiently and sweep the boundary layer. These smaller rolls enhance the mixing of fluid in the cavity regions to emit intense thermal plumes more frequently. However, the growing strength and size of the corner rolls, at intermediate roughness heights, evacuate the cavities near the lateral walls and reduce the size of the primary rolls. On the other hand, owing to their ability to penetrate the boundary layer faster, smaller roughness set-up creates more plume emitting active spots. Thus, rough surfaces induce complex roll states or distorted structures which result in increased heat flux. Variation in buoyancy production just above the roughness peaks in the smallest roughness case confirms the idea of activation of plume emitting peaks. Moreover, the highest buoyancy production of turbulent kinetic energy in the tallest roughness case confirms the enhanced heat flux. However, the opposite trend in shear production indicates greater lateral movement for the smallest roughness set-up.

It is further found that random roughness plays an intricate role in influencing the two global transport properties, *Re* and *Nu*. In contrast to its effect on heat flux, flow strength (*Re*) drops in the two taller roughness configurations and improves for the smallest roughness case at $Ra = 4.64 \times 10^9$. Decrease in *Re* is attributed to the presence of a multiple-roll state which causes hindrance to the motion of large-scale rolls. Also, an insignificant change is observed in the $Re(Ra)$ scaling exponents showing a weak effect of roughness on flow strength.

CHAPTER 5

Significance of near-wall dynamics in enhanced *Nu*

This chapter complements the previous one, where enhanced heat flux was related to large-scale rolls. Here, we study near-wall dynamics for the same geometries and flow governing parameters. Three regimes are identified based on the number of roughness peaks penetrating the thermal boundary layer. In regime I heat flux drops marginally as only 50% *of the peaks emerge uncovered, followed by a nearly unaltered Nu in regime II. A sudden increase in Nu in regime III is noted with more than* 65% *penetrating peaks. In contrast to the previous observation, heat flux continues to increase even when all the peaks exceed the boundary layer. A significant improvement in fluid mixing inside the cavities is found due to the cascade of secondary vortices, which is connected to the improved heat flux in the tallest roughness set-up. A thin thermal boundary layer that envelopes the rough surface at higher Ra supports enhanced mixing of fluid inside the cavities. Greater perturbation of the thermal boundary layer for the smaller roughness set-up shows a consistent connection with the enhanced* $Nu(Ra)$ *scaling. Vertical distribution of mean temperature indicates the presence of multilayer characteristics with roughness-invariant near-wall region identified by a weakly non-linear profile. The variation of the mean temperature in the intermediate layer plays a crucial role in heat transfer enhancement as it reflects quality of ventilation of the entrapped fluid.*

5.1 Introduction

In the last chapter, we have observed that geometric features of a rough surface separate the bulk-mean flow from the cavity fluid. However, with increasing *Ra*, the flow inside these cavities, known as secondary vortices, becomes strong enough to move out and mix with the bulk-mean flow [105]. As discussed in Sec. 4.4, these secondary vortices further influence heat transport mechanism by altering the transport process, $Nu(Ra)$ scaling parameters, and the flow dynamics near the walls. Therefore, it is important to investigate the effect of near-wall dynamics on transport properties.

A triangular roughness element has two primary features, namely, the slope and tip (see Fig. 4.1). Although both help in emitting thermal plumes, they have significant differences in the emission phenomenon [2]. In the previous chapter, we have seen that multiscale roughness sustains the enhanced heat flux regimes. Zhu *et al.* [2] also reported that triple-scale roughness helps in sustaining the local $1/2$ scaling, which saturates for mono-scale configuration [53]. They also suggested that plumes emit only from the tips at lower *Ra*, whereas, at higher *Ra*, both the slope and tip emit thermal plumes, resulting in more plume emission spots. They attributed the increase in plume emission spots for the sustained $1/2$ regime.

For triangular roughness geometry, Zhang *et al.* [61] explored the effect of roughness height on heat flux in a unit aspect ratio cell for *Ra* varying from 10^7 to 10^{11}. They found that, for a fixed *Ra*, heat flux initially decreases with roughness height before it surges above critical height (h_c). They observed that heat flux increases for $h_c = 4.4 \times \lambda_\theta$, where λ_θ represents thermal boundary layer thickness. For $h < h_c$, fluid remains stagnant inside the cavities, which hinders the heat transport. They also revealed that the balance between viscous and inertia forces yield $h_c \sim Ra^0.6$. Later, Jiang *et al.* [112] used ratchet surfaces to explore the effect of roughness on heat flux. They found that interaction of blunt face of the ratchet with global flow circulation obstructs it and diminishes the heat flux.

Cavity region is another crucial geometric attribute in roughness-aided RBC. Note that width of cavity region is decided by the spacing between the roughness elements. Dong *et al.* [113] investigated the effect of five different roughness model for $10^6 \leq Ra \leq 10^9$ in a square geometry. The roughness models typically represent the different arrangements of roughness elements and also the cavity region. They observed that the models yield different critical *Ra*, beyond which enhanced heat flux can be obtained. They also reported that roughness influences the $Nu(Ra)$ and $Re(Ra)$ scaling, although the latter is impacted weakly.

Considering the importance of the near-wall dynamics (cavity spacing and roughness at-

tributes) and its role in enhanced heat flux, we investigate the significance of roughness peaks and cavity region in augmented heat flux. Furthermore, we study the effect of roughness on temporal statistics, temperature fluctuations and its probability density function (PDF) at roughness peak and inside a throat region. In addition, flow structures and cascade of vortices, perturbation of thermal boundary layers, and multilayer flow characteristics are also explored for a detailed investigation of flow dynamics in the near-wall region.

5.2 Significance of roughness peaks

In the previous chapter, it was shown that heat transport mechanism varies with roughness configurations, which poses difficulties for a unified view in the roughness driven thermal convection. Hence, a more generalized approach is required for random roughness configurations, as proposed in this section. It has already been established that enhanced $Nu(Ra)$ scaling exponent is related to thermal boundary layer thickness (λ_θ) [53]. For random roughness, Ciliberto & Laroche [56] reported that the exponent varies only when λ_θ lies between the shortest and tallest roughness heights. Beyond these extremities, the $Nu(Ra)$ dependency becomes similar to that of a smooth case. However, triangular-shaped roughness, used in the current study, favors plume emission than the spherical ones used by Ciliberto & Laroche [56]. In the present work, instead of the range of heights that vary with the roughness configurations, we have quantified the percentage of peaks required to penetrate the thermal boundary layer in order to influence the global transport properties.

Figure 5.1(a) shows variation of increment in heat flux (ΔNu) with the percentage of peaks (N_p) penetrating the reference thermal boundary layer (λ_{ref}). Note that the reference thermal boundary layer corresponds to the smooth case. The increment in heat flux and λ_{ref} are computed as

$$\Delta Nu = \frac{Nu - Nu_0}{Nu_0} \tag{5.1}$$

$$\lambda_{ref} \approx \frac{H}{2Nu_0} \tag{5.2}$$

where Nu_0 is Nusselt number for the smooth case. The dashed-dot lines indicate that 69.08%, 84.51%, and 83.33% of peaks must penetrate the boundary layer for transition to the enhanced heat flux regime in R_1, R_2, and R_3 cases, respectively. It is worthy to note that the difference in heat transport mechanism is also reflected in the percentage of peaks penetrating the thermal boundary layer. Moreover, it also suggests that a transport mechanism with multiple-roll states

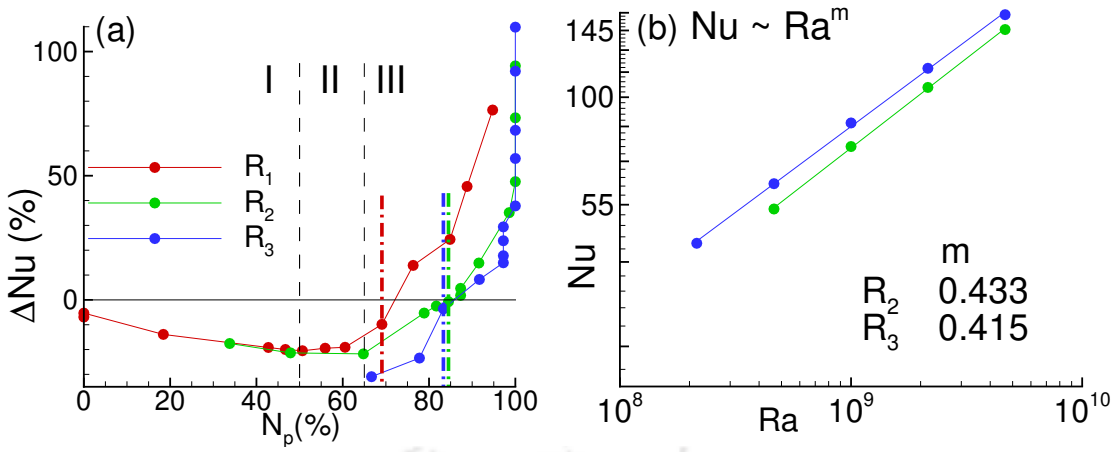

Figure 5.1: (a) Variation of increment in Nusselt number ΔNu, computed as $\Delta Nu = (Nu - Nu_0)/Nu_0$, with the percentage of peaks (N_p) penetrating the reference thermal boundary layer. Nu_0 and the reference thermal boundary layer are computed from the smooth case. While the dashed lines separate the three regimes, the dashed-dot lines represent the percentage of peaks required for the enhanced heat flux regime. (b) Persistence of the half-scaling in enhanced heat flux regime when all the peaks penetrate the boundary layer.

needs a higher number of these peaks, while the conventional double-roll state for $\Gamma = 2$ needs a fewer penetrating peak. As discussed in the previous section, the smaller rolls can accommodate themselves in the cavities, resulting in a weak perturbed boundary layer. Therefore, R_3 configuration needs a higher percentage of such penetrating peaks. In R_2 case, the emerging corner rolls behave in the same manner as the multiple-rolls. Since the corner rolls are smaller in size and are restricted to the vicinity of lateral walls, this configuration needs nearly same N_p as in R_3. Finally, in R_1 configuration, the thermal boundary layer is highly perturbed, and therefore, it needs the least percentage of penetrating peaks to achieve the enhanced scaling exponent.

It is further observed that beyond $Ra = 10^8$ (2.15×10^8), all the peaks penetrate the boundary layer in R_3 (R_2) case. As shown in Fig. 5.1(b), enhanced $Nu(Ra)$ scaling exponent regime is evident in this condition (with a slight reduction in the exponent), which completely contradicts Ciliberto & Laroche [56]. They asserted that the scaling exponent changes only when thermal boundary layer lies between the tallest and smallest roughness heights. However, the possible reason for the persistence of a higher exponent regime in the present work is the peak shaped roughness, which is suitable for the nucleation of thermal plumes compared to the glassy spherical roughness [56]. On the contrary, all roughness elements in R_1 configuration are not sufficiently tall to penetrate the boundary layer, and thus, this case is not shown here. Therefore,

this analysis suggests that a true multi-scale random roughness configuration in a convection cell results in the enhanced exponent regime even when all the peaks penetrate the boundary layer. However, these results need to be confirmed at a higher *Ra*, which is beyond the scope of the present work.

Next, the effect of these penetrating peaks is investigated on the increment in heat flux. As shown in Fig. 5.1(a), the $\Delta Nu(N_p)$ curve shows three regimes. Initially, it drops until 50% of the peaks penetrate the boundary layer, followed by a nearly constant value from 50% to 65%, and eventually, it monotonically increases beyond $N_p = 65\%$. The increment in heat flux reduces (or remains unchanged) in the first (second) regime due to fluid entrapment inside the cavities. The entrapped fluid remains nearly stagnant due to a weak thermal forcing, which tends to resist the heat transfer [61]. Once the cavity fluid becomes sufficiently strong, which is indicated by increasing *Ra* and boundary layer penetrating peaks, it moves out of the cavities to enhance the heat flux, as in R_3 case.

5.3 Temporal statistics in the near-wall region

Using V-shaped groove elements, Du & Tong [114] found that rough surface alters the temperature fluctuations in the near-wall region but not in the bulk region. However, in a cylindrical cell facilitated with groove-shaped roughness, Stringano *et al.* [105] observed that asperities on isothermal horizontal surfaces alter the temperature fluctuations in both the near-wall and bulk regions. Further, with square base pyramidal roughness, Salort *et al.* [104] found a destabilized boundary layer over top of the roughness elements. They also found that fluid inside the notches remains still, and statistics of temperature fluctuations change along the horizontal surface to show its non-homogeneous characteristics. Certainly, the above studies show that roughness geometry and its characteristics play an important role for the temperature fluctuations. The present roughness layout makes the situation even more complicated as the spacing between the roughness elements and their heights vary without any order over the horizontal surface. Thus, it is expected that randomly varying roughness spacing and heights, unlike previous studies, yield different flow behavior. We have selected two plume emitting spots located at two distinctly different relative regions of a roughness element. As shown in Fig. 4.1, these spots are geometric characteristics of roughness elements and are termed as the throat and peak. Owing to tiny roughness heights and narrow spacing between the elements, R_1 case is not included in this study as relative locations of peak and throat are not too different there.

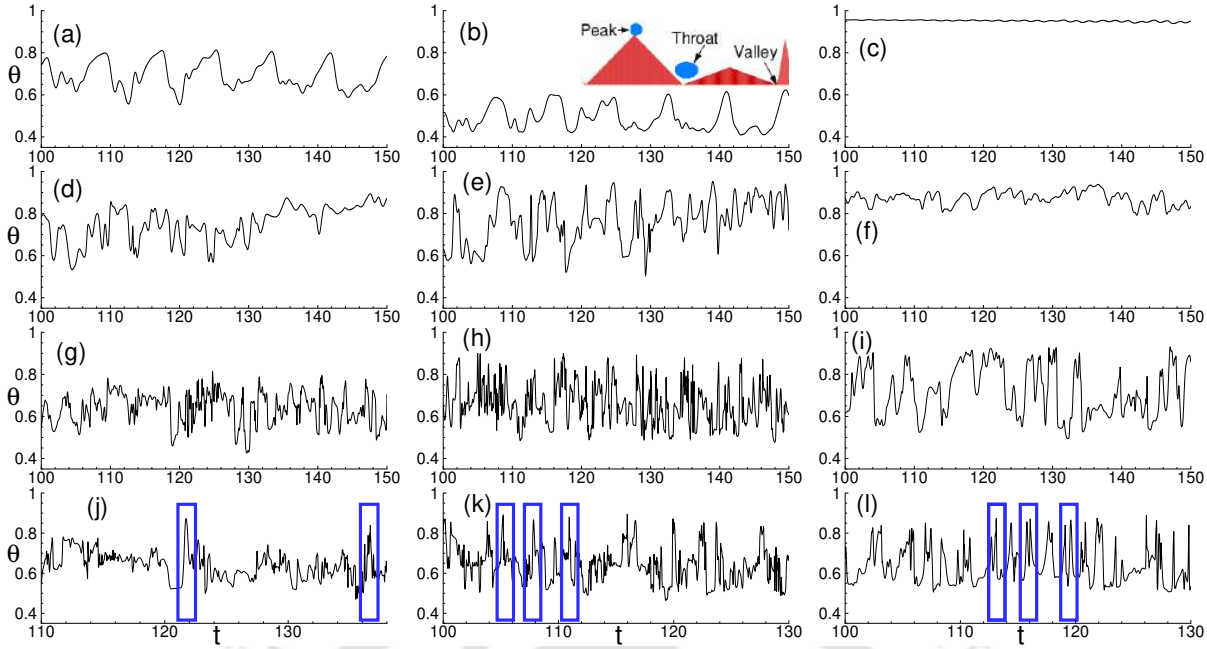

Figure 5.2: For R_2 configuration, time series of temperature recorded from the probes placed in the throat region (left column), at the tip of a peak (middle column), and inside bottom thermal boundary layer in smooth case (right column) for $Ra = 10^7$ (first row), 10^8 (second row), 10^9 (third row), and 4.64×10^9 (last row). The blue boxes indicate spikes in the time series.

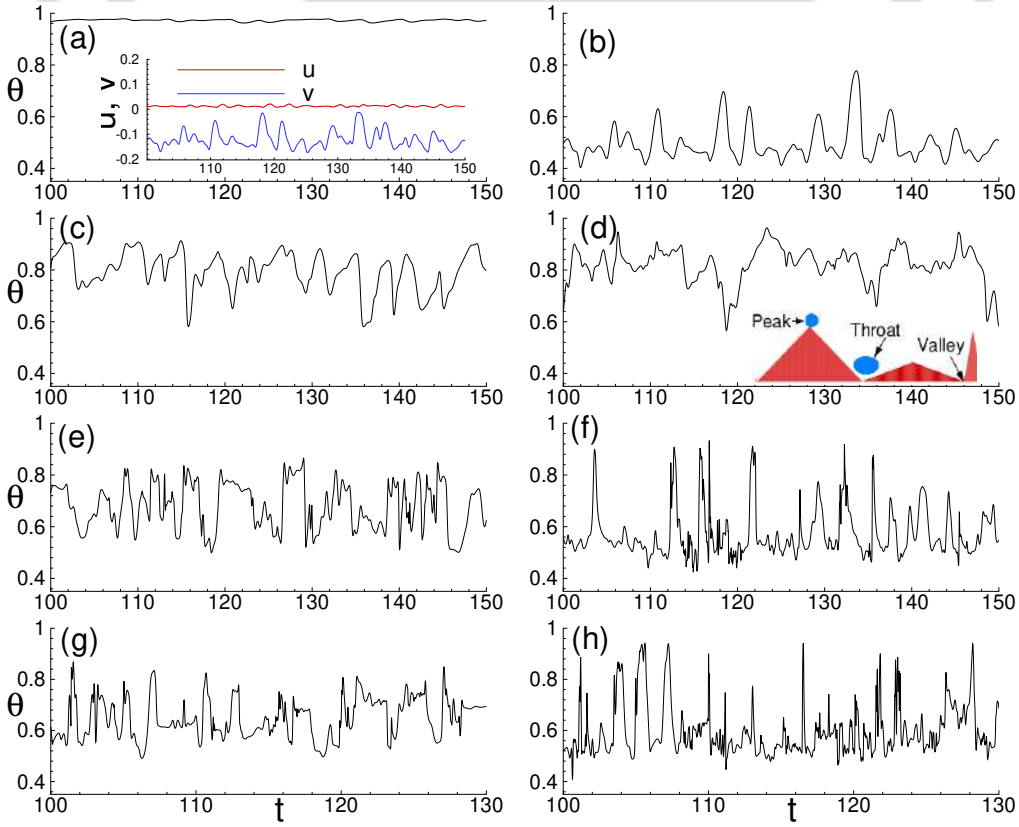

Figure 5.3: For R_3 configuration, time series of temperature recorded from the probes placed in the throat region (left column) and at the tip of a peak (right column) for $Ra = 10^7$ (first row), 10^8 (second row), 10^9 (third row), and 4.64×10^9 (last row). Inset in frame (a) shows time series of horizontal and vertical velocity obtained from the corresponding probe.

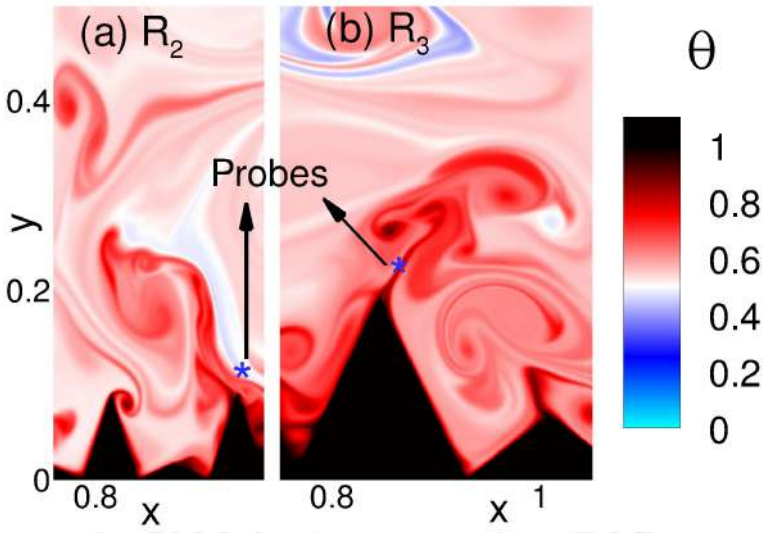

Figure 5.4: For the highest *Ra* case, an instantaneous snapshot of temperature contour near the peak region in (a) R_2, and (b) R_3 case at the instant of emission of thermal plumes. A robust thermal plume in R_3 case is short lived at a higher temperature state, whereas the emitted plumes are swept away by the large-scale rolls in R_2 configuration.

Figure 5.2 shows time series of temperature recorded from the probes for R_2 configuration placed in the throat, near the peak, and inside the bottom thermal boundary layer for the smooth case in left to right columns, respectively. Note the throat and peak region for a representative roughness element is shown in frame (b). At low *Ra* (10^7), mean temperature in the throat region is higher than that at the tip, indicating entrapment of fluid inside the cavities. However, a lesser mean temperature at the peak indicates that it has a better exchange with the bulk fluid ($\theta = 0.5$). Furthermore, two important features have been observed with increasing *Ra*. First, mean temperature of the throat region decreases and becomes nearly equal to that of the peaks. Second, the frequency of sharp spikes appearing in the time series increases at both the locations. These spikes are indicated in blue boxes which also reveal their frequency of occurrence. The former indicates increasing bulk-cavity flow interaction, while the latter shows frequent emission of intense thermal plumes. We also observe that peaks emit thermal plumes more frequently compared to the throat. Also, note greater extension of the maximum temperature in the time series which indicates emission of intense thermal plumes from the peaks than the throat. It occurs due to the continuous gain of thermal energy by the cavity fluid because of its inability to move out. Consequently, it results in a sudden burst of thermal plumes at any instant, yielding a sharp spike in temperature inside the throat region (shown with the rectangular boxes in the frame j), although, such events are not frequent. Time signature appears to be same for the throat

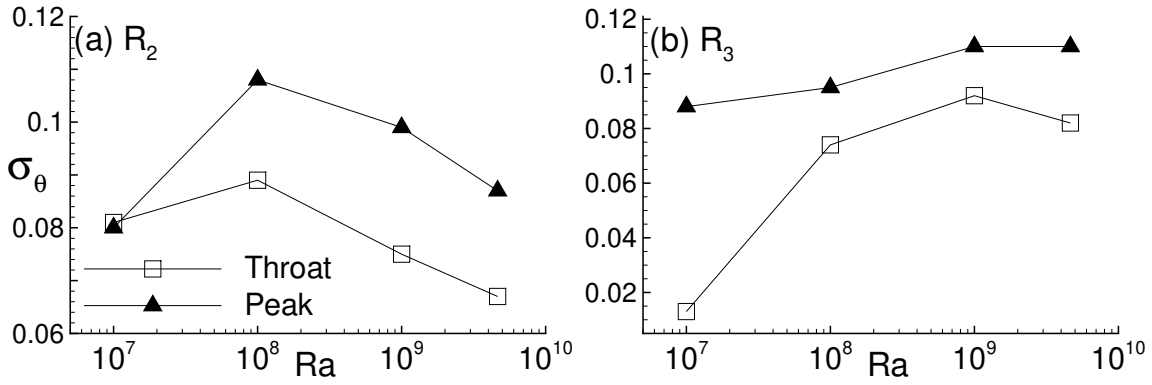

Figure 5.5: Effect of *Ra* on variance of temperature fluctuations (σ_θ) in the throat region and at the tip of a peak for (a) R_2, and (b) R_3 configurations.

and peak regions at smaller *Ra*. But with increase in *Ra* the peak region shows resemblance with boundary layer region of the smooth case (see frames k,l). Surprisingly, at higher *Ra*, the throat region shows controlled fluctuations with rare events of temperature spikes. This clearly indicates “washing-out" effect in the throat by the breakdown of stronger secondary vortices.

Temperature signal at the throat and peak for the R_3 set-up is shown in Fig. 5.3 which can be used to directly compare with R_2. At lower *Ra* (10^7), the behavior of temperature signal near the peak is similar in both the configurations. However, the throat region in R_3 is buried inside the thermal boundary layer which is evident due to absence of any temperature fluctuation, and hence, the absence of emission of thermal plumes. Note that the absence of temperature fluctuations do not signify the stagnant fluid. It can be seen from the velocity time series obtained from the same probe as shown in the inset of frame (a). Clearly, strong fluctuations in vertical velocity are evident, which support the above argument. Such a situation where hardly any temperature fluctuation is observed but velocity fluctuations are evident represent the boundary layer characteristics of the working fluid $(Pr = 0.7)$. Thermal plumes are emitted from the thermal boundary layer, which is thicker than its viscous counterpart. Therefore, it implies that the throat is lying underneath the corresponding thermal boundary layer. On the other hand, at higher *Ra*, a common feature appears at the peak and throat region in R_3 case, i.e., a short lived sharp spike at a higher temperature state before plummeting down to a lower one (or mean temperature state). Though a visible difference in temperature signal at the throat is obtained, peak region appears to be in the same state which confirms elevated levels of plume emission leading to an enhanced scaling of *Nu*. To understand the state of the emitted plumes, we study temperature contours near the probe location at the time of sharp spike, as shown in Fig. 5.4. The ephemeral dwelling at a higher temperature state shows the growing size of thermal plumes,

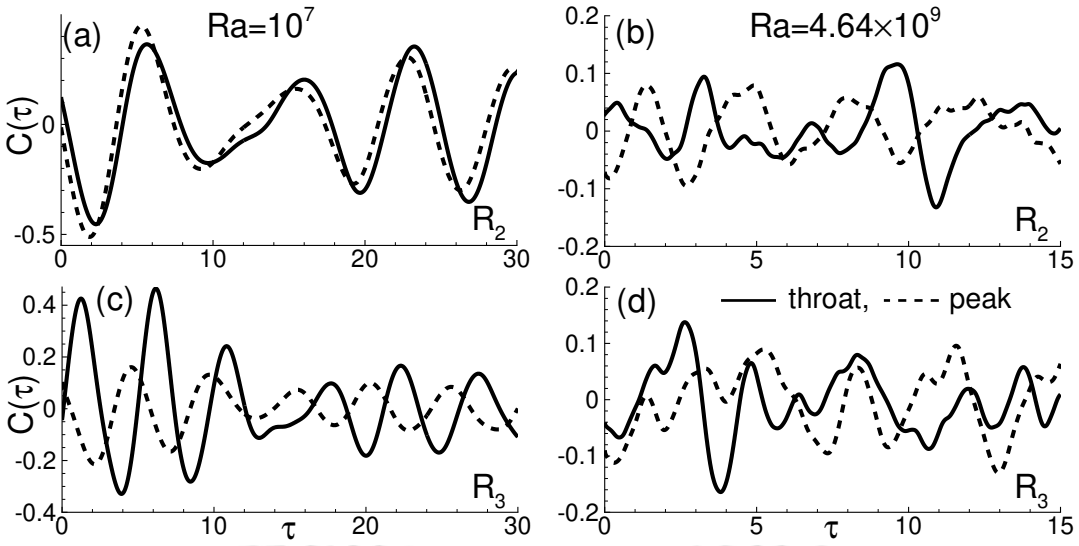

Figure 5.6: Correlation of temperature and *Nu* in the throat (dashed line) and at tip of peaks (solid line) for $Ra = 10^7$ (a and c), and 4.64×10^9 (b and d). The top row shows the correlation in R_2 case, while the bottom one represents that in R_3 case

which are reported in Sec. 4.4. Owing to their higher strength, the large-sized thermal plumes affect the bulk flow, which is indicated by the vertical extent of the emitted plume in frame (b). On the contrary, the emitted plumes are swept away under the influence of primary rolls in R_2 case (see frame a). Note that the temperature drops down to the bulk mean value as the plume emission is interrupted by the bulk fluid. Therefore, these observations suggest that the intense and large-sized thermal plumes are responsible for the transformation of the conventional double-roll state into a multiple-roll state in R_3.

A note on the frequency of plume emission in the smooth case as compared to the two specified locations is in order. A larger number of spikes, except for the highest *Ra*, in the rough cases as compared to the smooth case signify frequent emission of thermal plumes. Therefore, it suggests that roughness elements alter the emission of thermal plumes. For the highest *Ra* (4.64×10^9) case, frequency of plume emission in the smooth case becomes nearly equal to that at the tip for the rough cases. However, it does not imply that the number of emitting plumes becomes equal in the two cases. In the roughness cases, a significantly higher number of peaks and cavities emit thermal plumes in large quantities, as shown in the instantaneous contours in Fig. 4.15, while emission of the plumes in the smooth case is restricted to the confluence of two large-scale rolls and near the lateral walls (see Sec. 4.4).

The plume emission frequency at the two selected spots is further quantified by computing

variance of temperature fluctuations (σ_θ) as

$$\sigma_\theta = \langle \theta'^2 \rangle_t. \tag{5.3}$$

Figure 5.5 shows that variance at the peak is higher than that in the throat region, which again confirms the frequent emission of thermal plumes from the tips of the peaks. Also, note that the difference in the variance between the two spots remains nearly the same in the enhanced exponent regime. However, at $Ra = 10^7$, the difference is trivial in R_2 case and maximum in R_3 case. It occurs because both the spots are buried under the viscous dominated region in R_2 case. On the contrary, in R_3, owing to taller roughness heights, the peaks penetrate the viscous dominated region, but cavity fluid remains nearly stagnant due to insufficient buoyant forcing. Therefore, it implies that stagnant fluid in the cavities accounts for high thermal resistance, and hence, does not contribute to the emission of thermal plumes which is reflected in the distinctly low value of temperature variance. For R_3 case, the time series of the probe placed in the throat region has already shown the absence of temperature fluctuations at $Ra = 10^7$.

Further, the correlation (C) between temperature fluctuations (θ') and $\langle Nu \rangle_V$ is investigated at the tip of the peak and throat region due to a direct relationship between thermal plumes emission and heat flux. Mathematically, the correlation is computed as

$$C(\tau) = \frac{\overline{\phi_1'(t)\phi_2'(t+\tau)}}{\zeta_1 \zeta_2} \tag{5.4}$$

where ϕ_1, and ϕ_2 represent the $\langle Nu \rangle_V$ and θ, while the prime, ζ, and τ indicate their fluctuations, standard deviation, and delay time, respectively. The correlation is shown at a lower (10^7) and the highest Ra $(= 4.64 \times 10^9)$ for R_2, and R_3 configurations in Fig. 5.6. It is evident that $C(\tau)$ fluctuates around $C = 0$ in both the extreme Ra cases. The positive values indicate the thermal plume emission process, whereas negative ones signify the arrival of cold plumes in the plume shedding region. When the plumes emit and subsequently rise, causing positive temperature fluctuations, a positive correlation is expected. However, their downward movement yields a negative correlation. Once the cold plumes arrive at these locations, they trigger thermal instability, resulting in frequent emission of thermal plumes. At lower Ra, the correlation at both the peak and throat overlap in R_2. This overlapping confirms that the nature of the two plume emitting spots is same due to a viscous dominated near-wall region. However, in R_3 case, only the peak shows sustained thermal events as compared to an asymptotic decay in throat. These results confirm the differences (nearly same) in σ_θ at the tip and throat in R_3 (R_2). At higher Ra, nearly same decay of correlation at the tip and throat in R_2 indicates their equal contribution in plume emission. However, in R_3 case, a higher correlation at the tip shows that the peak

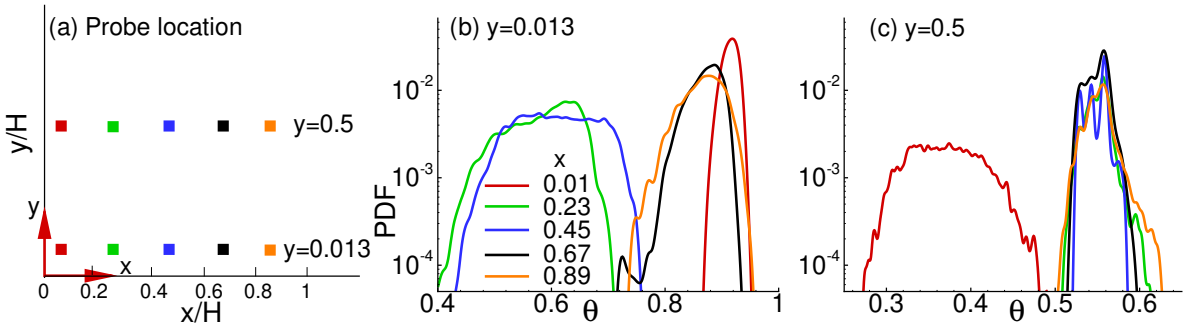

Figure 5.7: (a) Geometric location of the probes placed in a smooth thermal convection cell. For $Ra = 10^8$, the PDF of temperature in smooth case at two different heights, i.e., (b) $y = 0.013$, and (c) $y = 0.5$ at different horizontal locations.

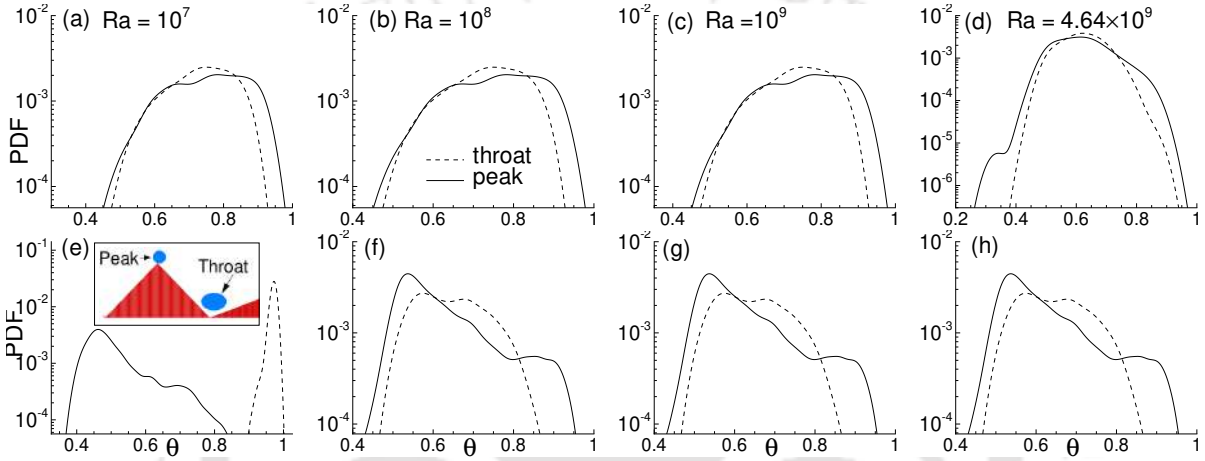

Figure 5.8: PDF of temperature in the throat and at the peak for (a,e) $Ra = 10^7$, (b,f) $Ra = 10^8$, (c,g) $Ra = 10^9$, and (d,h) $Ra = 4.64 \times 10^9$. The top panel shows the PDF for R_2 configuration while the bottom one indicates that of R_3 case.

contributes to enhanced heat flux more than the throat region.

5.4 Temporal PDF of temperature

In the last section, the time series obtained from the probes placed inside the throat region and near the tip of a roughness element indicated different tendency of plume emission. In this section, we further investigate the probability density function (PDF) of the temperature at these two spots in order to quantify it. However, before comparing the temperature distribution at the two locations, we first explain the flow behavior with the help of temperature distribution obtained from ten probes placed at different locations in the smooth case as shown in Fig. 5.7 (a). Note, owing to the symmetry, the probes are placed only in the left half of the cell.

In a cylindrical cell with triangular grooves, Stringano *et al.* [105] studied the PDF of temperature in the groove and roughness tips. They found a higher probability in the groove region, which indicates the frequent shedding of thermal plumes and also observed a smaller width of the distribution in the grooves. Moreover, a larger tail for the tips indicated the sweeping of hot fluid by the low-temperature bulk fluid. Investigating in a smooth convection cell, Salort *et al.* [104] obtained that temperature distribution transforms from Gaussian inside the thermal boundary layer to a skewed-inflexed distribution inside the bulk. Surprisingly, in the roughness facilitated convection cell, they observed that temperature distribution inside the notch transforms like that in the smooth case. However, above the roughness stud, a skewed-inflexed distribution was observed, which indicates flow above the studs is similar to the bulk flow. The above studies confirm that a rough surface alters the temperature distribution near the walls. Therefore, it is important to investigate the temperature distribution in the near-wall region to understand the modified flow dynamics in the presence of random roughness.

In the smooth case, Fig. 5.7(b) shows that temperature follows Gaussian distribution at all the five x locations near the horizontal wall ($y = 0.013$). However, the varying width and tail of the distribution indicate non-homogeneous character of the flow. Near the lateral walls, the distribution exhibits maximum temperature with narrow width. The presence of the lateral walls gives rise to corner rolls, which result in flow reversals. Since the fluid in the corner rolls remains close to the hot wall, it continuously gains thermal energy, as reflected in a higher mean temperature value. However, LSC influences the flow away from the lateral walls, yielding a wider distribution with a lesser mean value. Near the geometric center of the convection cell, accumulation of hot fluid results in a continuous emission of thermal plumes, well-known as thermal jet [103]. This feature is confirmed by the localized high mean temperature ($\theta \approx 1$). Note that owing to a symmetry about the vertical center line, distribution in the other half is not shown here. Further, nearly similar distribution curves at different x locations for $y = 0.5$ indicate a well-mixed homogeneous bulk region (see Fig. 5.7 c). However, a Gaussian distribution of temperature near the lateral wall ($x = 0.01$) indicates the boundary layer region.

For the roughness cases, Fig. 5.8 shows the temperature distribution for R_2 (top panel), and R_3 (bottom panel) configurations at four $Ra = 10^7$, 10^8, 10^9, and 4.64×10^9, to cover the entire range. In the former configuration, Gaussian distribution is observed at the two mentioned probe locations, inside the throat region and near the peak. However, width of the distribution increases with *Ra* at the tip of the roughness peak, showing a higher exposure of this location to colder fluid coming from the bulk. On the other hand, in R_3 configuration, Gaussian distribution is

observed only in the throat region, while a sharp narrow peak with an extended tail is evident for the other spot. The extended tail towards $\theta = 1$ indicates the emission of intense thermal plumes. However, such events are rare as reflected by a continuously decreasing probability as temperature approaches to the maximum value $\theta = 1$. Owing to larger roughness height, behavior at the peak and throat tends to differ as they are located differently in comparison to the boundary layer.

Clearly, the effect of roughness height is apparent in the temperature distribution in the two cases. While the distribution in the throat region is similar in both R_2 and R_3, a dissimilar distribution at the tip of the peak indicates the variation in the emission of thermal plume in the two roughness cases. Therefore, this analysis reveals how bulk fluid interact with different roughness heights to influence the emission of thermal plumes. Furthermore, in R_3 case, a narrow distribution at $\theta \approx 1$ is another striking feature in the throat region for the smallest *Ra* case, which again confirms the entrapment of fluid inside the throat region due to insufficient buoyant forcing.

5.5 Flow structures and cascade of vortices

Previous sections show significant differences in temperature statistics at the tip of the peak and the throat region. It happens because of the different flow structures present in the near-wall region, which will be discussed in the current section. A qualitative analysis to visualize the near-wall flow structures (secondary vortices) and the associated mechanism is described. In R_1 configuration, as discussed in Sec. 4.4, global flow structures remain nearly the same as in the smooth case. Nevertheless, it is natural that asperities present on the horizontal surface modify the local flow structures. Previous studies have also reported the modified flow structures in the presence of rough surface [105, 61]. Stringano *et al.* [105] observed the secondary recirculations inside the grooves at $Ra = 2 \times 10^{10}$, whereas no such structures were found at $Ra = 2 \times 10^{7}$. While investigating the effect of roughness heights on the heat flux, Zhang *et al.* [61] observed that the strong secondary vortices are responsible for washing out of the cavities, which further enhance the heat flux.

Flow structures in the near-wall region are shown by streamlines obtained from the time-averaged velocity field in the three roughness configurations. Owing to the similar flow structures near the top and bottom rough surfaces, we present only the latter. As shown in Fig. 5.9, smaller vortices between the roughness elements are apparent throughout the simulated *Ra* range

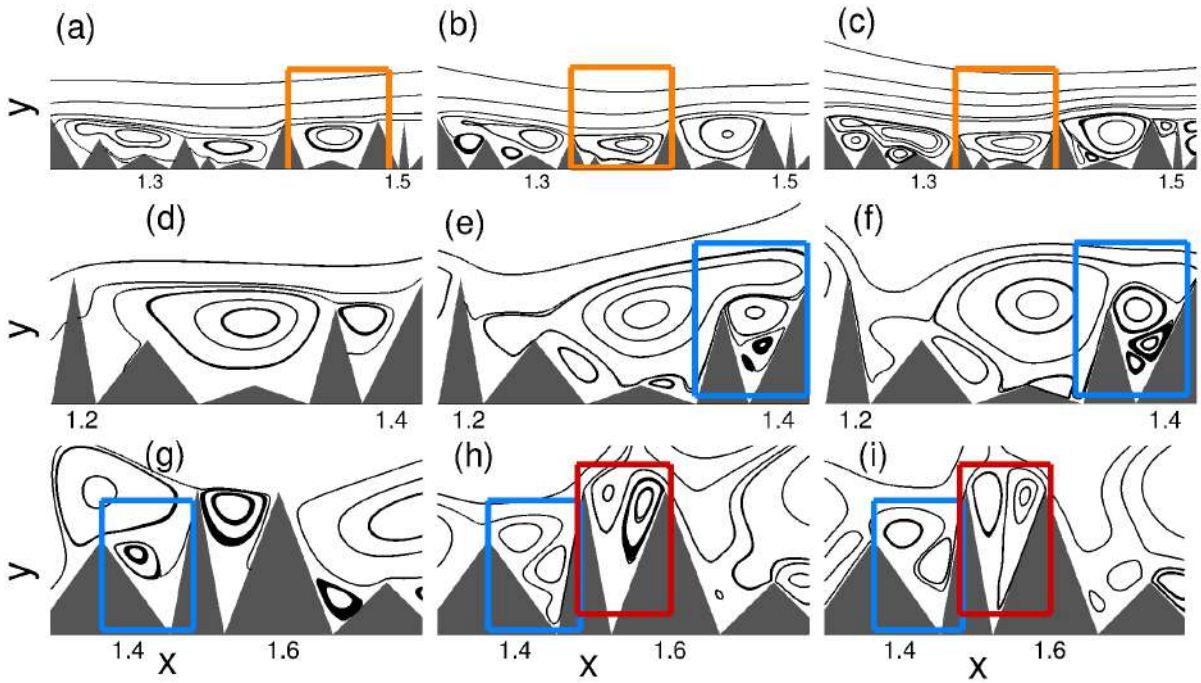

Figure 5.9: Streamlines obtained from the time-averaged velocity field showing the effect of *Ra* on local flow structures in R_1 (top row), R_2 (middle row), and R_3 (bottom row) configurations for $Ra = 10^7$ (left column), 10^9 (middle column), and 4.64×10^9 (right column). The orange boxes at the lowest *Ra* case indicate a valley consisting of smaller roughness elements between two significantly taller roughness heights. The blue boxes show the cascade of vortices in the vertical direction, while the red ones highlight the lateral alignment of two secondary vortices.

in all the three roughness configurations. These secondary vortices become stronger as *Ra* increases. The secondary circulations in the grooves were also found by Stringano *et al.* [105] at $Ra = 2 \times 10^{10}$. However, in the present random roughness configurations, such circulations are even evident at a very low $Ra = 10^7$. Since both the wavelength and height of roughness vary along the horizontal span, width of the throat region also varies along the horizontal direction. Consequently, the interaction of entrapped fluid in the throat region with the bulk fluid also varies. Such an arrangement of roughness elements creates a small valley region consisting of a few small roughness elements surrounded by two taller roughness heights as shown by the orange boxes in Fig. 5.9(a-c). The large-scale rolls solely drive the flow inside the valleys. Interestingly, even at the highest *Ra*, these vortices are found to remain weak such that they circulate only inside the cavities and do not influence the large-scale rolls.

It is interesting to observe the effect of *Ra* on the secondary vortices. As shown by the blue boxes in Fig. 5.9, it is observed that fluid entrapped inside the narrow cavities also responds to the large-scale rolls in R_2 and R_3 configurations. Initially, flow inside these narrow cavities remains

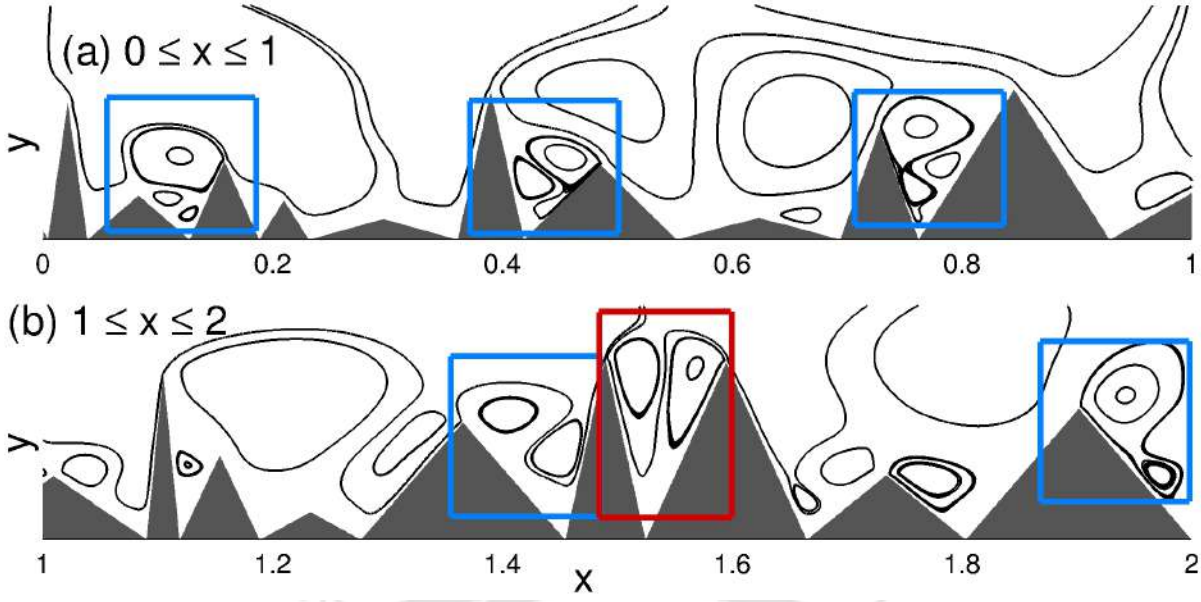

Figure 5.10: For R_3 configuration, streamlines obtained from the time-averaged velocity field for the highest $Ra = 4.64 \times 10^9$ showing the variation of local flow structures in the horizontal direction. While the top panel shows the structures in the first half of the domain $(0 \leq x \leq 1)$, the bottom one represents that in the other half $(1 \leq x \leq 2)$ of the domain. The meaning of colored boxes are same as in Fig. 5.9.

stagnant, although, a secondary flow sets in as *Ra* increases (see Fig. 5.9 e,f). With increasing *Ra*, this induced flow gains energy because of its inability to move out of the cavities. The induced vortices further incite the underlying fluid and create vortices of progressively smaller sizes. This phenomenon continues to invoke more such vortices which results in a cascade of secondary vortices. To identify what arrangement of roughness heights trigger this phenomenon, we observe the secondary vortices present near the bottom rough surface of R_3 case at $Ra = 4.64 \times 10^9$, shown as a blown-up view in Fig. 5.10, where these vortices are more pronounced. We observed that a narrow throat region is a favorable condition to obtain the cascade of vortices. These regions are represented inside the blue boxes.

Another striking feature emerges in R_3 case, where two laterally arranged vortices are evident and represented by the red boxes (see Fig. 5.10). It appears that both the roughness heights should be nearly equal with a narrow throat to promote such a layout of secondary vortices. It is caused by the presence of two counter-rotating rolls, which lies just above this roughness element (see Fig. 5.11 c). This phenomenon is observed only in R_3 configuration due to transformation of a double-roll state into a multiple-roll state. One may be intrigued by the case when such two adjacent roughness heights are unequal. The two possible cases are further discussed with the

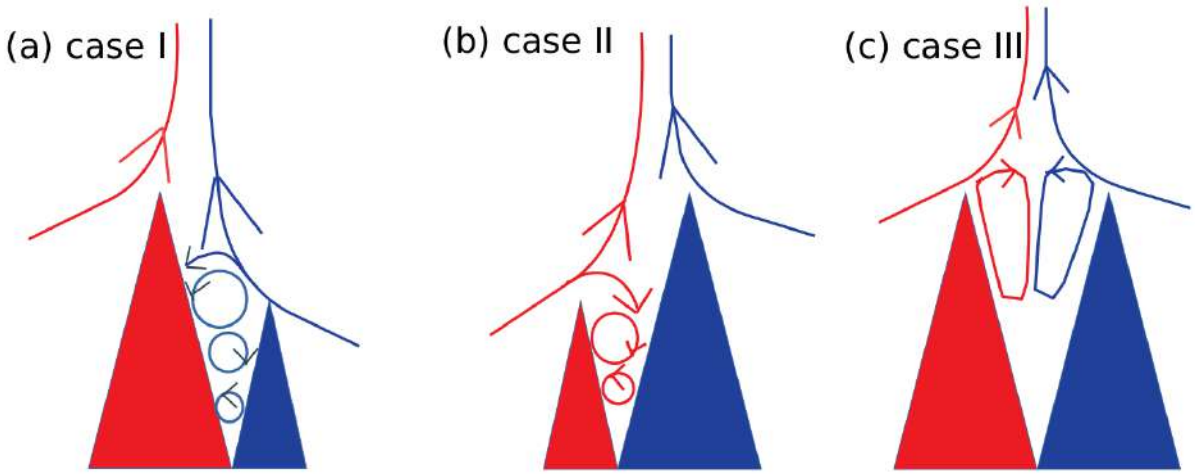

Figure 5.11: Schematic diagram showing the two possible cases in the situation of unequal roughness heights [(a) and (b)] and the lateral alignment of two counter-rotating secondary rolls (c). Flow inside the cavity is influenced by the corresponding large-scale roll of smaller roughness height.

schematic diagram in Fig. 5.11. Both the cases depict the same mechanism, which is governed by the large-scale roll corresponding to the smaller roughness height. Based on the above proposition, if one height is significantly smaller than the other, the shearing effect of large-scale roll above the smaller height influences the flow inside the cavity. Consequently, the induced flow further incites the underlying fluid to form the second vortex. Due to the absence of laterally induced flow, the cascade effect occurs down the valley and not laterally.

5.6 Thermal boundary layer

The previous section dealt with the local flow structures present near the rough surfaces and showed that the strength of the observed secondary vortices inside the cavities increases with *Ra*. Therefore, it is expected that the increased strength enhances the mixing of cavity fluid and thus, results in a thinner boundary layer, which conforms to the underlying surface. To ascertain it, we investigate thermal boundary layer (TBL) thickness near the bottom surface. Thermal boundary layer thickness (λ_θ) is calculated using a variant of the well-known rms technique [18]. In this modified technique, boundary layer thickness is defined as the vertical distance from the rough surface (instead of smooth surface in conventional RBC) to the location of the maximum rms of temperature fluctuation (σ_θ), as shown in Fig. 5.12. Recently, Chand *et al.* [103] have shown the effect of *Ra* on λ_θ, where large-scale rolls were found to influence the

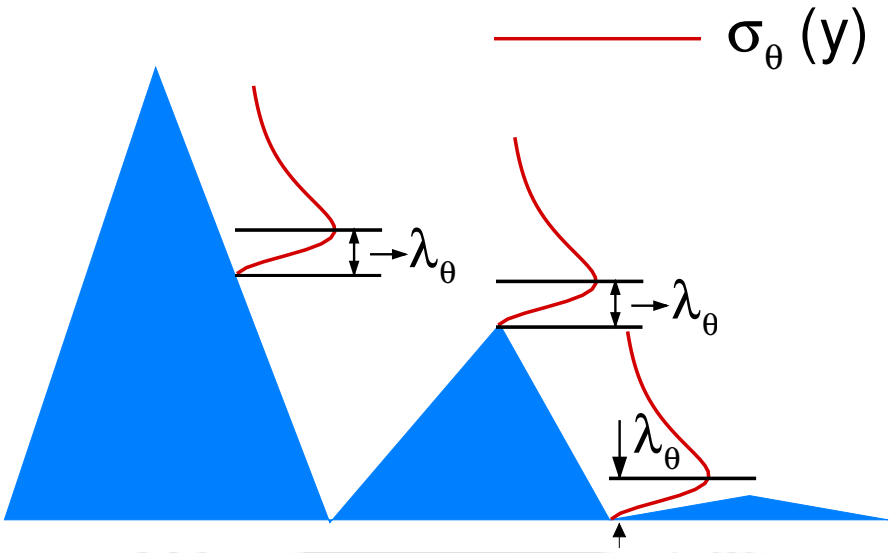

Figure 5.12: Schematic showing the construction of thermal boundary layer thickness (λ_θ) computed from the well-known rms technique in the presence of arbitrary roughness element.

boundary layer. Using a periodic triple-scale roughness, Zhu *et al.* [2] proposed that, at higher *Ra*, when a thin boundary layer covers the taller roughness heights, the smallest heights penetrate the boundary layer and enhance the extent of the $1/2$ scaling regime. However, the proposition was based on the expectations, and no evidence of a thinner boundary layer was reported. In the present work, the response of thermal boundary layer with the rough surface is quantified and presented as a horizontal variation of λ_θ to confirm the above proposition.

Figure 5.13 shows thermal boundary layer profiles for R_1, R_2, and R_3 configurations in the frames (a), (b), and (c), respectively. Firstly, the effect of *Ra* on thermal boundary layer is discussed, which is followed by a comparison of the boundary layer profile among the three roughness configurations. The profiles are shown for three different *Ra* cases, i.e., one before (or at the onset) the transition to the enhanced exponent regime and two cases after it. At lower *Ra*, a thicker thermal boundary layer is evident in all the three roughness configurations. It shows the viscous dominated flow near the rough surface, resulting in a thick λ_θ. However, with increasing *Ra*, λ_θ decreases and conform to the underlying rough surfaces due to strong secondary vortices. The regions where secondary vortices were seen to form a cascade of smaller vortices are indicated by the “red" and “blue" boxes whose meaning is same as in Figs. 5.9 and 5.10. It is clearly evident from the profile of TBL inside the highlighted cavities that strong secondary vortices mix the cavity fluid to result in a very thin boundary layer that nearly conforms to the cavity shape. Therefore, it suggests that cascade effect is an indication of a well mixed fluid

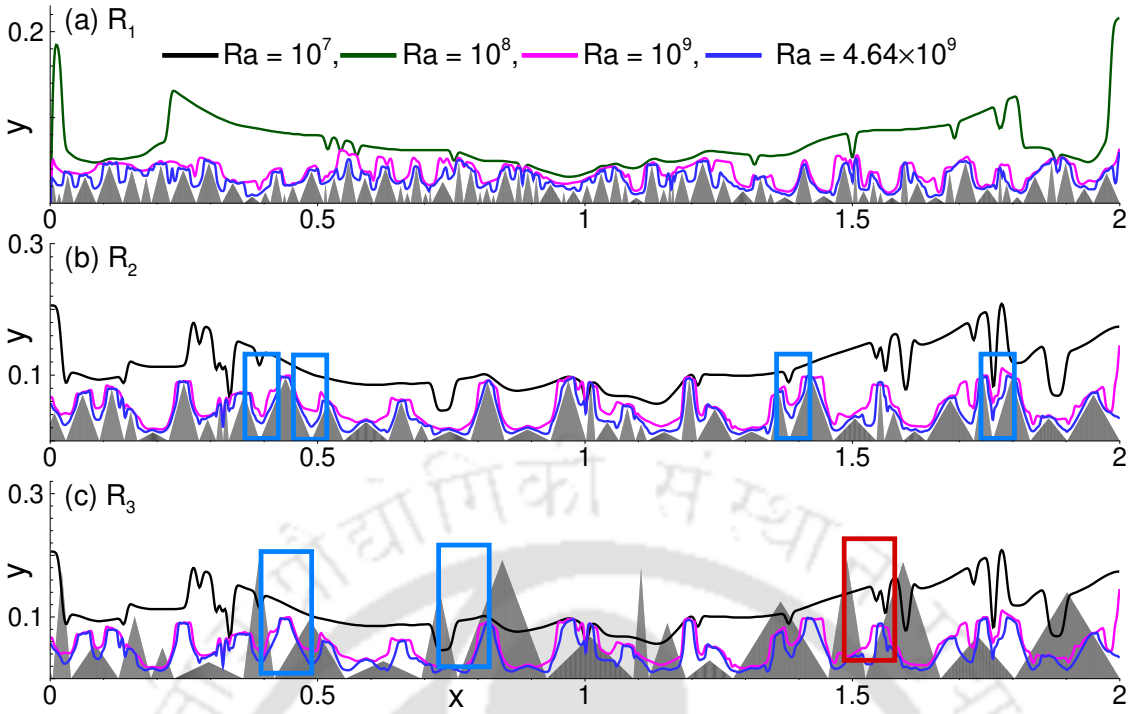

Figure 5.13: Thermal boundary layer thickness computed from rms technique at $Ra = 10^7$ (black), 10^8 (green), 10^9 (pink), and 4.64×10^9 (blue) in (a) R_1, (b) R_2, and (c) R_3 roughness cases. The profiles are shown at a lower and two higher *Ra* to show the coherent structure before and after the transition to the enhanced exponent regime. The meaning of the colored boxes are same as in Fig. 5.9.

which further helps in enhancing heat flux.

Further, we observe closely the thermal boundary layer profile for the highest *Ra* case for the three roughness configurations. Evidently, in R_1 configuration, the boundary layer profile does not follow the rough surface as it does in the other two configurations. It happens because of weaker secondary vortices in the near-wall region. On the other hand, strong vortices inside the cavities enhance the mixing of fluid, which yields a thin thermal boundary layer attached to the rough surface. As shown in the last frame of Fig. 5.13, the boundary layer has nearly reached the valleys, which can only be possible when secondary vortices wash out these cavities. Therefore, this study again confirms the phenomenon of the cascade of vortices in the two taller configurations. At the same time, in R_1, it clearly shows that bulk flow cannot invade the cavities. Such boundary layer profile where its thickness varies significantly in the valley, throat, and peak due to penetration of the roughness elements is termed as boundary layer perturbation. Normalized by its absolute maximum value, boundary layer perturbation (λ_P) can be quantified

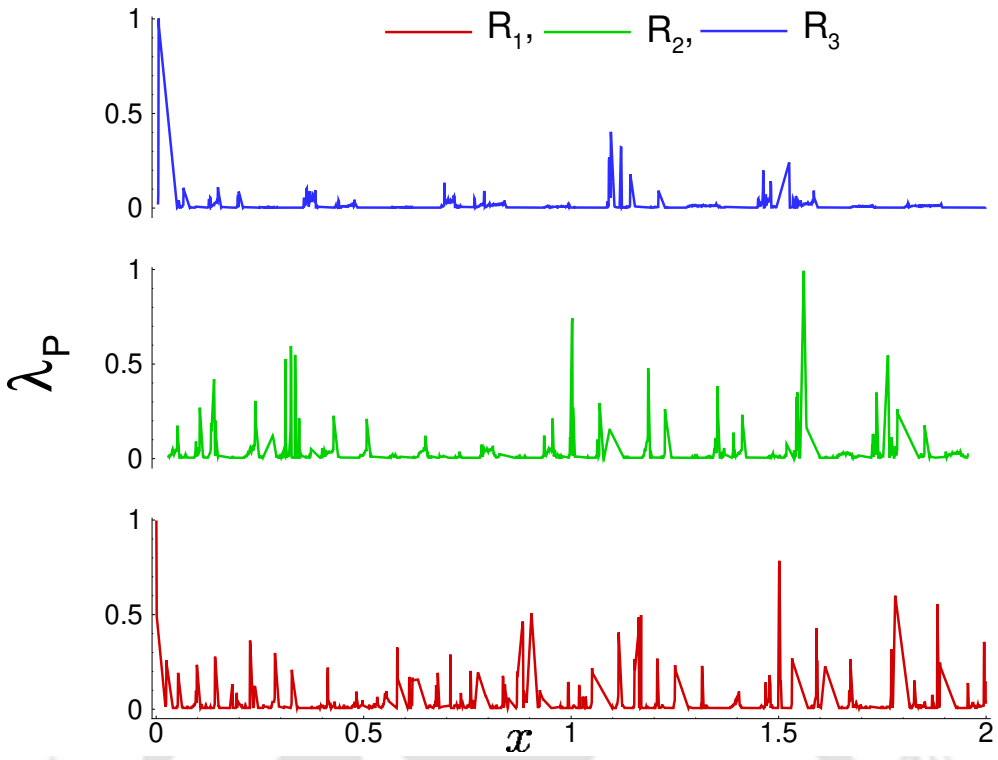

Figure 5.14: Perturbation of thermal boundary layer thickness computed as $|d\lambda_\theta/dx|$ and further normalized by its maximum value for the highest *Ra* case. The sharp emerging peaks show local perturbation of thermal boundary layer.

as

$$\lambda_P = \left|\frac{d\lambda_\theta}{dx}\right| \left|\frac{d\lambda_\theta}{dx}\right|^{-1}_{max}. \tag{5.5}$$

where only the absolute magnitude of $d\lambda_\theta/dx$ is considered. Figure 5.14 shows the perturbation of thermal boundary layer in R_1, R_2, and R_3 configurations for the highest *Ra* case. Note that nearly zero value and frequently appearing peaks indicate the locally unperturbed and perturbed boundary layer, respectively. A number of peaks representing the perturbation along the horizontal span are significantly higher in R_1 as compared to that in R_3. Therefore, the perturbation is maximum in the shortest roughness configuration (R_1) and minimum in the tallest (R_3). Strong secondary vortices enhance the turbulent intensity of the flow inside the cavities in the latter. Hence, the flow becomes nearly similar to that in the smooth case with increasing *Ra* and diminishes the perturbation of thermal boundary layer. We may recall here that R_3 set-up consistently yields higher *Nu*, though the $Nu \sim Ra^m$ exponent was found highest for the R_1 case. The process of cascade of secondary vortices, washing-out of the cavities and the resultant boundary layer perturbation are indeed interrelated. But they do not contribute in the same way

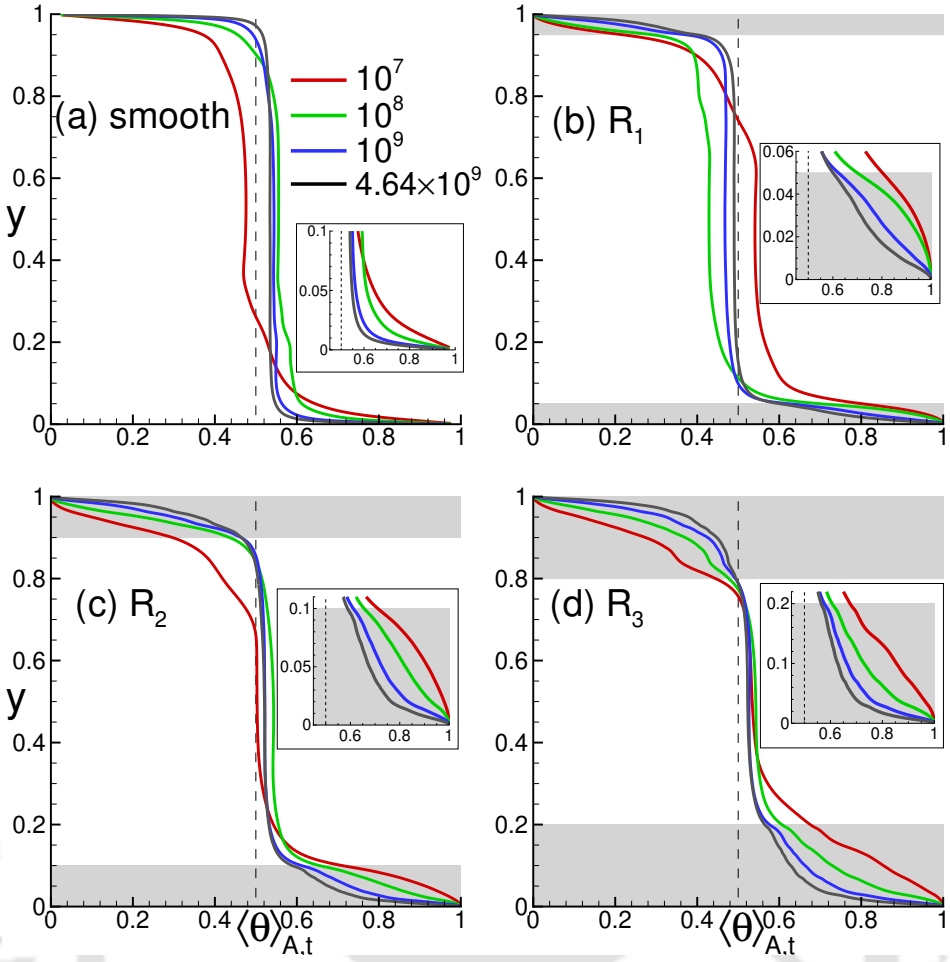

Figure 5.15: Vertical area-time averaged temperature profiles in (a) smooth, (b) R_1, (c) R_2, and (d) R_3 cases. Effect of *Ra*, ranging from 10^7 to 4.64×10^9, on flow characteristics is shown. The inset indicates the vertical profiles inside the cavity region.

in the heat transfer enhancement, as not all roughness heights promote thin covering of boundary layer, nor they respond uniformly to the boundary layer perturbation resulting in different levels of heat transfer enhancement.

5.7 Multilayer flow characteristics

Mean temperature profile along the vertical direction usually identifies two regions in the flow. First, nearly half of the total temperature drop occurs near the plate which results in *Nu* as the inverse of the thermal boundary layer thickness, $Nu \approx 1/2\lambda_\theta$. Once the major temperature drop has occurred near the plates, flow assumes a near homogeneous state in the central region termed as the bulk. It is expected that mean temperature profiles also reflect the characteristics of local flow structures. The mean temperature profile is calculated by area-time averaging of the

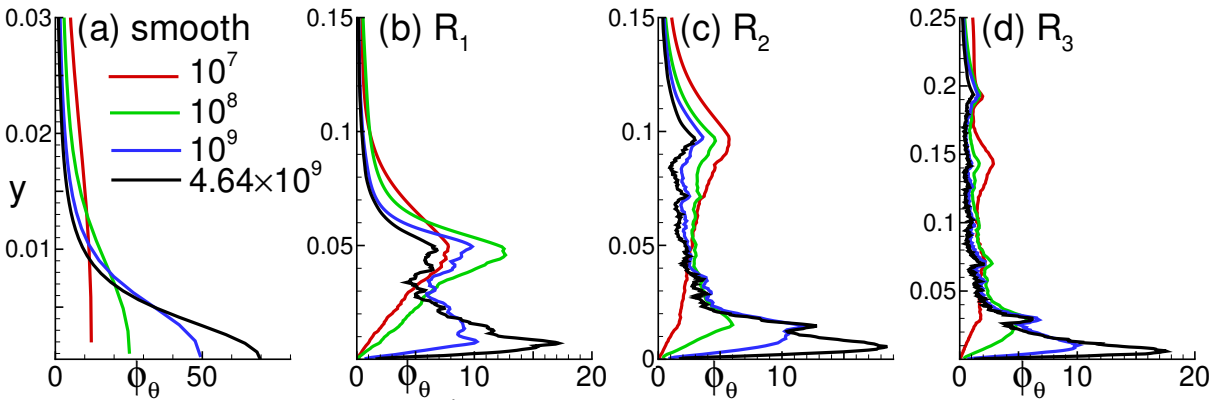

Figure 5.16: Vertical profile of absolute temperature gradient calculated as $|d\langle\theta\rangle_{A,t}/dy|$ in (a) smooth, (b) R_1, (c) R_2, and (d) R_3 cases.

temperature field represented by $\langle\theta\rangle_{A,t}$, where A and t stand for area and time, respectively. In general, these profiles identify the well-mixed homogeneous bulk region. However, in a roughness facilitated thermal convection, Zhu *et al.* [59] observed the effect of *Ra* on these profiles and proposed that the profiles become similar to that in the smooth case at higher *Ra*, which they argued as one indication of saturation of enhanced exponent regime to the classical one.

Figure 5.15 shows the vertical profiles of mean temperature in the smooth, R_1, R_2, and R_3 cases. As mentioned above, these profiles distinguish the flow characteristics as well-mixed homogeneous (in the bulk), and inhomogeneous (near the walls) regions. Interestingly, it is not the case at lower *Ra* where signs of inhomogeneity are clearly evident in the different mean temperature profiles. However, the mean value becomes close to $\langle\theta\rangle_{A,t} = 0.5$ due to increase in turbulent intensity with *Ra*. In the case of roughened convection cell, it is worth mentioning that a complex roll-state in R_3 set-up favors fluid mixing, which can be noted in the same mean temperature over a wide range of *Ra*. On the contrary, in smooth and R_1 cases, clearly different values of mean temperature at lower and higher *Ra* confirms the above proposition. Also, the deviation in the profiles indicates that bulk flow is more influenced by the rough surface at lower *Ra*. The inset shows the vertical profiles close to the rough surface, where the temperature profiles vary with roughness configurations to show the distinct flow characteristics. In R_1 case, the temperature drops slowly in a linear fashion, showing the viscous dominated region that affects the convection mode of heat transport. It is also reflected in a lesser heat flux value than the other configurations (see Fig. 4.2).

The profiles in the near-wall region indicate the temperature drop in three stages, which signifies the multilayer flow characteristics. Based on the temperature drop from the rough surface

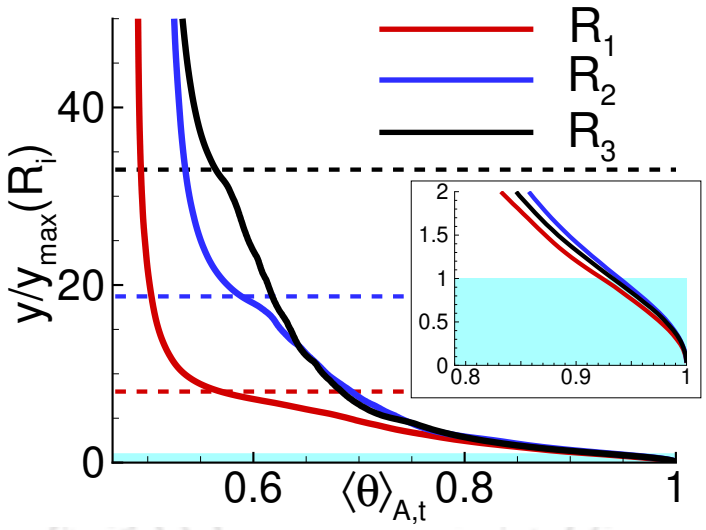

Figure 5.17: For the highest *Ra*, vertical variation of mean temperature profile with $y/y_{max}(R_i)$ where $y_{max}(R_i)$ is the location where ϕ_θ becomes maximum. The inset shows a blown-up view of the first layer where heat transfer occurs mainly by conduction.

to the bulk, the flow characteristics are distinguished into three layers. In the first layer (the closest to the wall), the flow remains nearly stagnant, and a sharp decrease in temperature due to thermal resistance in the valleys is observed. The second layer or intermediate layer shows a non-linear drop in temperature with a smaller temperature gradient. It is expected that this layer is controlled by secondary vortices present inside the cavities. The third layer represents the bulk flow, where large-scale rolls control the flow. Since strong secondary vortices and transition from a double-roll state to a triple-roll state occur in R_3 configuration, the second layer seems more prominent in this roughness set-up (see frame d).

As shown in Fig. 5.16, the above proposition is ascertained by calculating the absolute magnitude of temperature gradient (ϕ_θ) as

$$\phi_\theta = \left| \frac{d\langle\theta\rangle_{A,t}}{dy} \right|. \tag{5.6}$$

In the smooth case, the slope is maximum at the surface while it increases with y in roughened configuration to attain a maximum before dropping asymptotically to the bulk mean value. This dual characteristic of the temperature gradient confirms the multilayer flow characteristics. Interestingly, the first layer is evident in all three configurations and appears to be independent of the nature of rough surfaces. The profiles of mean temperature are further normalized by the vertical distance, denoted as $y_{max}(R_i)$, where i varies from 1 to 3, at which ϕ_θ attains an absolute maximum in the highest *Ra* case. Figure 5.17 clearly identifies the above-mentioned three regimes. The inset shows the enlarged view where the three profiles nearly collapse onto each

other in the first regime. It confirms that despite a huge difference in the roughness scales present in the three configurations, characteristics of the first layer (heat transport mainly occurs through the conduction) are independent of roughness geometry. The intermediate regime is separated from the third regime for the three configurations at their maximum roughness height by the corresponding dash lines. The secondary vortices control the flow behavior in the intermediate regime, which mimics the bulk flow and suddenly changes its behavior beyond the maximum roughness height. In R_3 case, the mean temperature profile in the intermediate regime continues to drop roughly in the same manner as it does in the third regime. The strong influence of secondary vortices improves the bulk-cavity flow interaction, which results in effective thermal convection inside the cavities. In the bulk flow controlled regime (third regime), the bulk fluid temperature remains same irrespective of the nature of rough surface.

Based on the vertical profiles of mean temperature in three levels of random roughness, we propose that the second regime plays a crucial role in enhancing the heat flux. Greater its resemblance with the bulk, higher the heat flux is, as it does in R_3. It also supports the prospect of washing-out of the cavities. Strong secondary vortices sweep the cavities appropriately to detach the thermal boundary layer, which is attached to the rough surfaces.

For better visualization of the flow near the cavities, streaks are generated by injecting massless particles from a number of carefully selected stations. Upon injection, they are tracked as they follow the local fluid motion using the Lagrangian description

$$\frac{d\overline{x}_p(t)}{dt} = \overline{u}(\overline{x}, t) \tag{5.7}$$

where $\overline{x}_p(t)$ is the particle coordinate which moves owing to the local fluid velocity $\overline{u}(\overline{x}, t)$. The time integration is carried out using the second-order Crank-Nicolson scheme. It must be pointed out that the location of the particles, more often than not, does not coincide with the cell centers. In order to determine velocity of the particles, thus, local reconstruction using second-order interpolation is required. The complexity of such local reconstruction for domain decomposition based parallelization is significant where a lot of bookkeeping is involved in addition to the “point-to-point" and “point-to-all" data communication. The overall effect is slowing down of the simulation as the number of injected particles keeps growing.

In the current work, we have selected 60 injection stations spread along the cavities. They are injected and subsequently tracked for almost 10 large-eddy turnover time. Figure 5.18 shows instantaneous streaklines at a number of instances indicated in the frames for the R_3 set-up. The top panel clearly shows that the shearing effect of large-scale rolls forms the secondary vortices which further triggers the underlying fluid to form another vortex down to the bottom of the

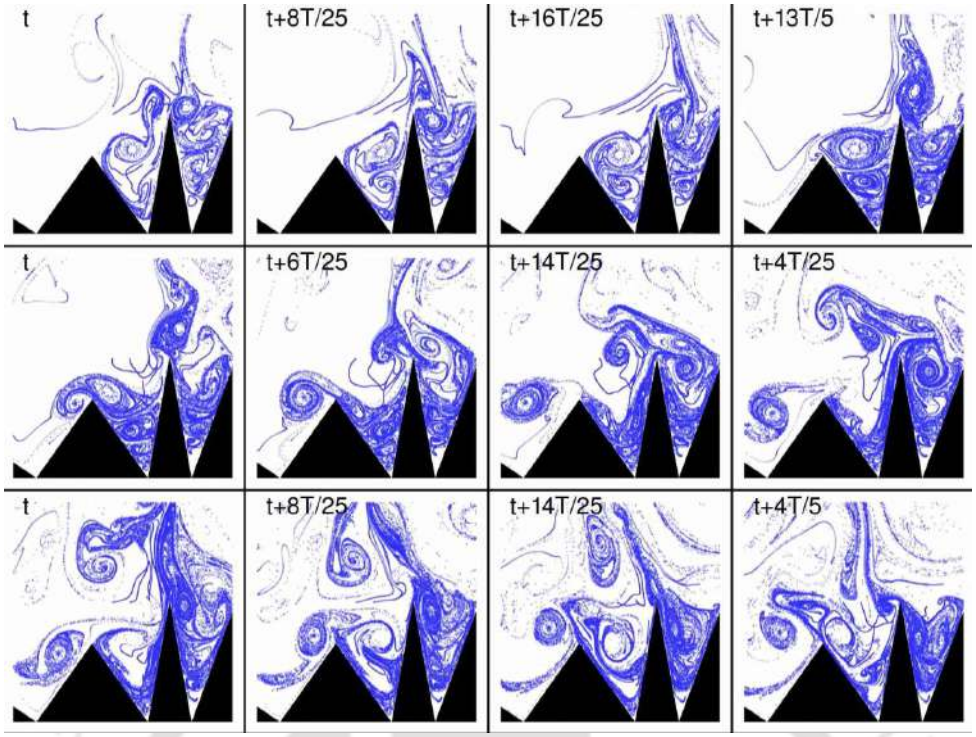

Figure 5.18: Streakline visualization at indicated instances (from left to right) near the roughness cavities in R_3 case at $Ra = 4.64 \times 10^9$. The top panel shows the formation of cascade of vortices and a stack of secondary vortices, while the middle one indicates the “washing-out" of the cavities. The last row represent the washed-out cavities which further forms the cascade of vortices.

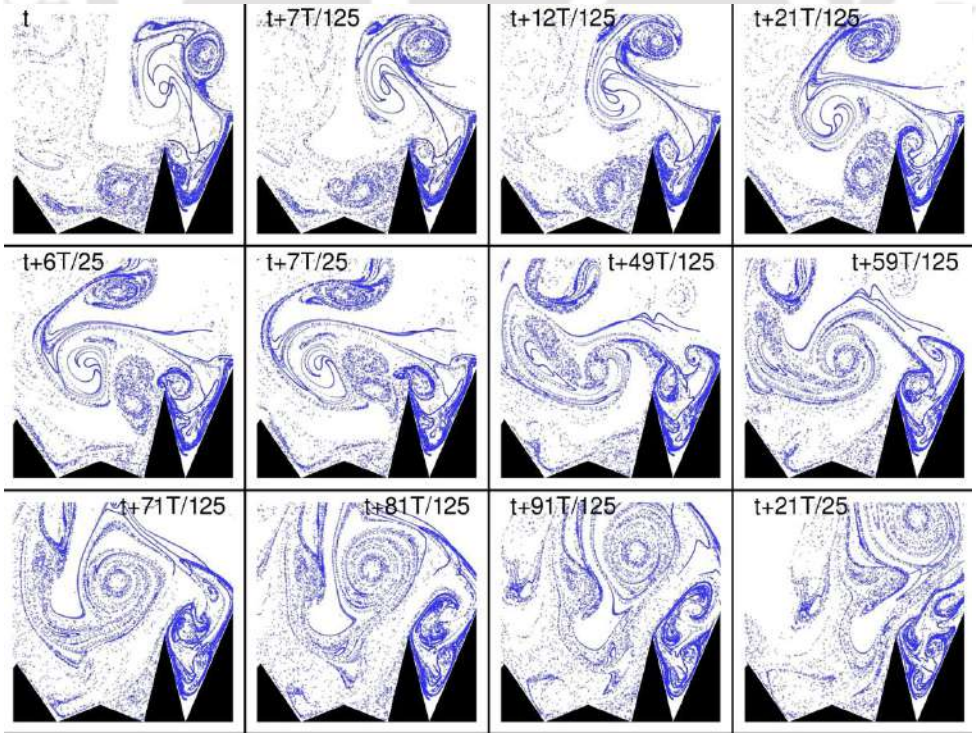

Figure 5.19: Streakline visualization at indicated instances (from left to right and top to bottom) near the roughness cavities in R_2 case at $Ra = 4.64 \times 10^9$. It shows the dynamical evolution of a mushroom-shaped thermal plume that washes away the nearby cavities.

cavities. It also reveals the growing size of the topmost vortex which attains enough strength to escape the cavity (middle row). Following the topmost vortex, the lower ones en route to the peaks along the slant surface mix with the bulk fluid (see bottom row).

Figure 5.19 shows instantaneous streaklines for the R_2 case obtained from 60 injection points placed inside the cavity regions. Similar to the R_3 case, secondary flow features like a stack of vortices are also evident here. However, the inability of the plumes to enter the nearby cavities is clearly seen to rise while it grows in size. Under the influence of the large-scale roll, its motion is inhibited. It subsequently sweeps the peak region but cannot penetrate the nearby smaller roughness throats keeping these regions nearly stagnant. Thus, the varying effect of roughness height is clearly observed where the path towards enhanced exponent regime is not necessarily the same. While the larger roughness favors washing out of the cavities, smaller ones are not equally effective in cleaning out the stagnant regions. Though the two configurations show the washing out of the cavities, it happens through different mechanisms. After attaining sufficient energy, secondary vortices escape the cavities in the taller heights. On the other hand, in intermediate roughness height, it occurs through the growing size of thermal plumes which under the influence of large-scale rolls enter the cavities to wash them out.

5.8 Conclusions

In this chapter, we have explored the significance of near-wall dynamics in enhancing the heat flux for the same roughness geometries and governing parameters used in the previous chapter. Based on the number of peaks penetrating the thermal boundary layer, three heat flux regimes are identified. Below 50% of penetrating peaks, heat flux marginally drops and remains unaffected within the range $50 - 65\%$. As it exceeds 65%, a sudden increase in heat flux occurs. It is observed that 69.08%, 84.51%, and 83.33% of penetrating peaks are required for the onset of enhanced heat flux regime with roughness height in increasing order. The investigation of near-wall dynamics has revealed the significance of secondary vortices present near the rough surfaces. The different response of throat and peak of a roughness element indicates a higher tendency of plume emission in the latter. The peaks emit more frequent and intense thermal plumes than the throat. The time series shows an ephemeral high temperature state in R_3, which reveals the emission of large-sized thermal plumes. It is also observed that the large-sized plumes affect the bulk-flow, and hence, they are responsible for transforming a double-roll state to a triple-roll state. The turbulent intensity computed from the temperature rms in the enhanced exponent

regime is found to be higher at the peaks, ascertaining their role in the enhancement. A sharp and narrow peak in probability density function of temperature at the tip in R_3 reveals the intermittent interaction of cold and hot plumes, while the Gaussian distribution in the throat indicates a boundary layer region. Surprisingly, both peak and throat are found to follow Gaussian distribution in R_2 case.

Further, weak secondary vortices present near the walls are attributed to a lesser heat flux in R_1. However, a cascade of secondary vortices representing a higher turbulent intensity in R_2 and R_3 wash out the cavities to increase *Nu*. Therefore, the cascade phenomenon is found to be very important to increase the heat flux. Not only the downward cascade but a lateral (lateral cascade) arrangement of two smaller rolls in a narrow cavity is also observed. Given the importance of cascade effect, this study reveals that a narrow throat region is a favorable site for a secondary vortex to undergo a progressive break down process leading to a well mixed fluid. These features are further confirmed by a thin thermal boundary layer (λ_θ) profile in very narrow cavities.

The quantification of thermal boundary layer and its perturbation confirms the concept of boundary layer perturbation to enhance the $Nu(Ra)$ scaling exponent, which was previously assumed. The maximum perturbation in R_1 yields the highest $Nu(Ra)$ scaling exponent, while the minimum perturbation in R_3 gives the lowest scaling exponent. The different level of perturbation in the three configurations reveals that tuning of the maximum roughness height is an important parameter to extend the enhanced exponent regime as proposed by Zhu *et al.* [2]. It also suggests that the perturbation vanishes even in a random roughness configuration, as seen in R_3. Vertical mean temperature profile near the rough surface shows evidence of multi-layer flow characteristics. A weakly non-linear profile closest to the wall exhibits collapse of data for all the roughness set-ups. We propose that the intermediate layer plays a crucial role in heat transfer enhancement. Greater its resemblance with the bulk, higher the heat flux is. Beyond the maximum roughness height flow asymptotically approaches the bulk through the outer layer.

CHAPTER 6

Effect of tilt on heat transport properties

In this chapter, two-dimensional $(2D)$ *tilted Rayleigh-Bénard convection is studied in both smooth and roughness facilitated convection cell of double-aspect-ratio* $(\Gamma = 2)$*. We investigate the effect of inclination angle* $(0^\circ \leq \phi \leq 90^\circ)$ *on heat flux* (Nu)*, Reynolds number* (Re)*, and flow structures. In a Rayleigh number range* $10^6 \leq Ra \leq 10^9$*, we address the* $Ra-$*dependence of* $Nu(\phi)$ *trend. In the smooth case, while greater tilt results in the highest heat flux below* $Ra = 10^8$*, Nu drops with* ϕ *monotonically above it (RBC transports heat most efficiently), which explains the different* $Nu(\phi)$ *trend observed in the previous studies due to* $Ra-$*dependence [65, 70, 67]. For the smooth case, we identify the control parameters* $(\phi = 75^\circ$ *and* $Ra = 10^7)$ *which yield maximum heat flux (an increment of* 18% *with respect to the level case). On the other hand, among the three roughness setups used in the present study, the tallest roughness configuration yields the maximum increment in heat flux* (25%) *in vertical convection* $(\phi = 90^\circ)$ *at* $Ra = 10^6$*. With increase in Ra, Re changes with* ϕ *marginally in the smooth case, whereas it shows notable changes in its roughness counterpart. We find that the weakening of thermal stratification is directly related to the height of roughness peaks. While Ra delays the onset of thermal stratification (in terms of inclination angle) in the smooth case, an increase in roughness height plays the same role in roughness facilitated convection cells.*

6.1 Introduction

In the previous chapters, we have focused mainly on $Nu(Ra)$ dependence and its associated heat transfer mechanism in roughness-aided RBC. Inclined convection is another variant of non-standard Rayleigh-Bénard convection, which is used to enhance the heat flux [115, 116]. However, the enhancement strictly depends upon the governing parameters, described later in detail. On account of buoyancy, inclination induces characteristics of shear flow. This setting of heat transfer enhancement has been studied extensively over the years in both two- and three-dimensional $(3D)$ geometries [117, 64, 118, 119].

In an experimental study, Dropkin & Somerscales [115] observed that the $Nu(Ra)$ scaling exponent does not change with ϕ and the variation in heat flux occurs due to different prefactors. Ahlers *et al.* [120] observed a drop in heat flux as the convection cell is tilted due to the attributes of large-scale rolls and transformation of flow states from a single-roll to a double-roll state. For very low-Prandtl-number fluid $(Pr = 0.0094)$, Frick *et al.* [71] suggested that thermal plumes carry heat at small inclination angles, while large-scale circulation (LSC) carries it at larger angles. For the same working fluid, Vasilev *et al.* [72] obtained the maximum Nu at $\phi = 65^\circ$ which confirms the higher efficiency of LSC. Shishkina & Horn [70] investigated the effect of Ra and Pr on $Nu(\phi)$ and $Re(\phi)$ in a range of Pr varying from 0.1 to 100 for $Ra = 10^6, 10^7$, and 10^8. They suggested that $Nu - \phi$ relationship is a non-monotonic function of Pr and Ra, and does not follow a simple power-law. In 2D RBC, Wang *et al.* [121] identified the range of aspect ratios in which tilted RBC can be used to enhance the heat flux. A brief review of the inclined convection is tabulated in Table 6.1, which highlights the principal findings and their reasons. However, the detailed literature for tilted RBC is provided in Sec. 1.4.

It is clear from the literature that IC yields greater heat flux than RBC and VC [71, 70, 66, 64]. However, a unified view for the inclination angle that yields maximum heat flux remains elusive, which was also suggested by Shishkina & Horn [70]. Therefore, this chapter aims to disentangle the Rayleigh number dependence of $Nu(\phi)$ for a low $Pr = 0.7$ and $\Gamma = 2$, which has not been studied extensively so far. In the Ra range $10^6 \leq Ra \leq 10^9$, we identify the control parameters (Ra and ϕ), which result in enhanced heat flux for IC. To the best of our knowledge, the scaling theories for $Nu(Ra)$ and $Re(Ra)$ power laws are available only for the two extreme inclined cases, i.e., RBC $(\phi = 0^\circ)$ [24, 29] and VC $(\phi = 90^\circ)$ [122–124]. However, in a recent study, Zhang *et al.* [119] extended the GL theory for horizontal buoyancy. Considering the unavailability of the above-mentioned power laws, we report the $Nu(Ra)$ and $Re(Ra)$ scaling exponents for each inclination angle. For the first time, we report the impact of surface roughness on $Nu(\phi)$ and

$Re(\phi)$ using three roughness setups used in the previous chapters, see Fig. 6.1. The physical argument for considering surface roughness is that it enhances the emission of thermal plumes and breaks the large-scale rolls into smaller ones, which influence the heat flux [125]. So it will be interesting to study the combined effect of roughness and tilt on global heat transport properties.

In most of the IC studies, confined geometries ($\Gamma \leq 1$) have been used to realize the idea of heat flux enhancement [69, 126, 120, 71, 72, 67, 70, 127, 65, 66, 64]. Since the flow in nature does not occur in confined geometries, studies dedicated to wider convection cells are of greater interest [121]. Moreover, Wang *et al.* [121] suggests that heat flux enhancement occurs only for $\Gamma \leq 8$. To avoid the effect of confinement due to lateral walls for ($\Gamma < 1$) and to achieve the enhanced heat flux, we have selected a relatively wider convection cell of $\Gamma = 2$. The present study is conducted at five tilt angles ($\phi = 0°$, $15°$, $45°$, $75°$, and $90°$) that cover the entire inclination range. We have considered $\phi = 15°$ and $75°$ to elucidate the competing transport mechanism between LSC and thermal plumes and identify the most efficient state of heat transport, respectively.

6.2 Numerical details

Under the Oberbeck–Boussinesq approximation, incompressible, tilted buoyancy-driven-flows are governed by the continuity, energy, and momentum equations, see Eqs. 2.1-2.4 in section 2.1. Figure 6.1 shows the schematic of a double-aspect-ratio tilted convection cell with boundary conditions and three same roughness setups, i.e., R_1, R_2, and R_3. We consider five inclination angles $\phi = 0°, 15°, 45°, 75°$, and $90°$, and a wide *Ra* range varying from $10^6 - 10^9$. The numerical details are tabulated in Table 6.2. With respect to the level case, the top and bottom surfaces are kept at isothermal temperature conditions, whereas the lateral walls are adiabatic. No-slip velocity boundary condition is enforced on all four walls (including rough surfaces). It is not intuitive to use horizontal and vertical terminology in a tilted cell to refer to the directions along the isothermal surface and normal to it. Thus, we indicate here onwards the direction along the isothermal surfaces as IS and normal to them as NIS.

In the present work, we compute the two response parameters, *Nu* and *Re*, as

$$Nu = 1 + \sqrt{RaPr}\langle v\theta \rangle_{V,t} \text{ and } Re = \sqrt{\frac{Ra}{Pr}}U \tag{6.1}$$

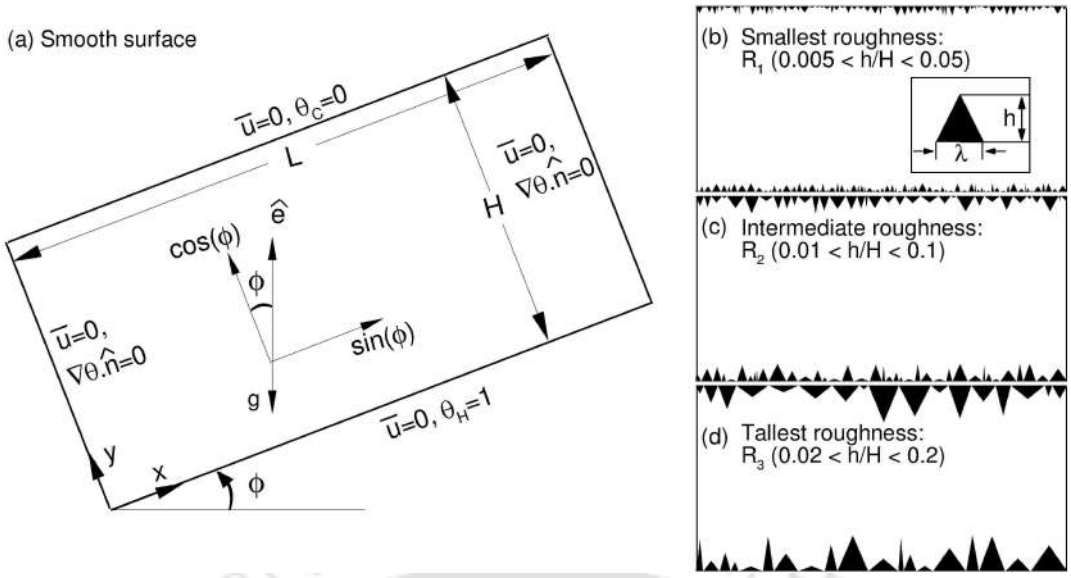

Figure 6.1: Schematic diagram of (a) the smooth tilted convection cell with boundary conditions and components of unit vector $(\hat{e})$ in x and y directions, the (b) smallest (R_1), (c) intermediate (R_2), (d) tallest (R_3) rough surfaces. Inset in frame (b) shows the wavelength (λ) and height (h) of a roughness element.

Table 6.1: A brief review of inclined thermal convection including the governing parameters (Γ, Pr, Ra), inclination range, the principal findings, the characteristic of $Nu(\phi)$ curves, and the inclination angle at which maximum heat flux is obtained. The studies are tabulated in the increasing order of Pr except for the last two investigations, which include a range of Pr.

References	Γ	Pr	Ra	Inclination range	$Nu(\phi)$ curve (max. at $\phi =$) principal findings
Frick *et al.* [71]	$1/5$	0.0094	$2 \times 10^6 - 10^7$	$0°, 2°, 45°, 90°$	unimodal ($45°$) Turbulent intensity decreases with ϕ
Vasilev *et al.* [72]	$1/20$	0.0094	2.4×10^6	$0° - 90°$	unimodal ($65°$) LSC is responsible for heat transfer
Khalilov *et al.* [67]	1	0.0094	1.47×10^7	$0° - 90°$	unimodal ($70°$) Small increase in $Nu(\phi)/Nu(0°)$
Shishkina *et al.* [70]	1	$0.1, 1$	$10^6 - 10^8$	$0° - 90°$	unimodal ($\approx 54°$) Intermediate ϕ yields efficient heat transfer
Chilla *et al.* [69]	$1/2$	2	$10^{11} - 10^{12}$	$0° - 1.72°$	monotonously decreasing DRS reduces Nu
Sun *et al.* [126]	$1/2$	4.3	$10^9 - 10^{11}$	$2°$	2% decrease in Nu due to locking of LSC

Ahlers *et al.* [120]	1	4.38	up to 10^{11}	$\approx 11^\circ$	0.5% reduction in *Nu* at $\phi = 10^\circ$
Weiss *et al.* [127]	1/2	4.38	1.8×10^{10} 7.2×10^{10}	$0 - 0.12rad$	*Nu* slightly increases with tilt
Guo *et al.* [65]	$\Gamma_x = 1$ $\Gamma_y = 1/4$	6.3	4.42×10^9	$0^\circ - 90^\circ$	monotonously decreasing Span of LSC increases with ϕ
Guo *et al.* [68]	$\Gamma_x = 1$ $\Gamma_y = 1/4$	≈ 10	6.8×10^{10}	$0^\circ - 90^\circ$	Characteristic of $Nu(\phi)$ depends upon Γ rather than *Ra* and *Pr*
Shishkina *et al.* [70]	1	10, 100	$10^6 - 10^8$	$0^\circ - 90^\circ$	complex (72°) Large ϕ yields efficient heat transfer
Jiang *et al.* [66]	1	480	$10^8, 5 \times 10^8$	$0^\circ - 90^\circ$	bi-modal (75°) LSC is responsible for peaks in $Nu(\phi)$ curve
Wang *et al.* [74]	1, 2	$0.05 - 5$	$10^7 - 10^8$	$0^\circ - 90^\circ$	ϕ supports reversals in $\Gamma = 2$, while it suppresses in $\Gamma = 1$
Wang *et al.* [64]	1/2	$0.1 - 100$	$10^6 - 10^9$	$0^\circ - 90^\circ$	UTRS and SRS enhance *Nu* while DRS reduces it

where $U = \sqrt{\langle \mathbf{u} \cdot \mathbf{u} \rangle_{V,t}}$ and $\langle \cdots \rangle_{V,t}$ indicates the volume-time average [48, 111]. It is important to note that *Nu* can also be defined on the basis of thermal ($Nu_{\epsilon_\theta} = \langle |\nabla \theta|^2 \rangle_{V,t}$) and viscous ($Nu_{\epsilon_u} = 1 + Pr\langle |\nabla \mathbf{u}|^2 \rangle_{V,t}$) dissipation rates. For smooth boundaries, Nu_{ϵ_θ} and Nu_{ϵ_u} are directly connected because of the mean vertical convection. On the other hand, they do not have a direct connection in the rough boundary case. While studying the bounds for convective heat transfer between the rough boundaries, Goluskin & Doering [128] used the background decomposition for temperature and suggested that Nu_{ϵ_θ}, normalized by $Nu(Ra = 0)$, quantifies the heat flux across the layers. However, owing to the intricacies associated with roughness facilitated tilted convection cells (where buoyancy acts in both directions) in the present work, we have defined Nusselt number as mentioned above in Eq. 6.1. For converged statistics, sampling of at least 200 free-fall time units is carried out in the statistically stationary state. Note that the conduction state ($\mathbf{u} = 0$, and $\theta = 1 - y$) is used as the initial condition.

6.3 Effect of inclination on flow structures

It is well-known that flow structures in RBC are sensitive to the inclination angle [74] and aspect ratio [121]. The sensitivity here refers to a change in the state of large-scale rolls. Figure 6.2

Table 6.2: Simulation details for the level case. From left to right: type of convection cell; Rayleigh number (Ra); number of grid cells in x and y directions ($N_x \times N_y$); ratio of maximum grid spacing to the Kolmogorov length scale $\eta = H\sqrt{Pr}Ra^{-1/4}(Nu-1)^{-1/4}$ in x ($\Delta x_{max}/\eta$) and y ($\Delta y_{max}/\eta$) directions, respectively; the number of points inside thermal boundary layer (N_{BL}). Note that reference Nusselt number for the smooth case is taken from Chand *et al.* [103], while for the roughness case, it is taken for the multi-scale roughness geometry [2]. Here, $*$ refers to the $\phi = 75^\circ$ cases only.

Case	Ra	$N_x \times N_y$	$\Delta x_{max}/\eta$	$\Delta y_{max}/\eta$	N_{BL}
Smooth	10^6	256×128	0.50	0.50	9
	$2.15 \times 10^6(*)$	512×256	0.31	0.31	9
	$4.64 \times 10^6(*)$	512×256	0.40	0.40	9
	10^7	512×256	0.50	0.50	10
	$2.15 \times 10^7(*)$	512×256	0.61	0.61	10
	$4.64 \times 10^7(*)$	600×300	0.67	0.67	9
	10^8	1024×512	0.53	0.53	11
	3×10^8	1200×600	0.65	0.65	9
	10^9	1440×720	0.78	0.78	9
R_1	10^6	1000×600	0.13	0.12	87
	3×10^6	1000×600	0.18	0.17	75
	10^7	1000×600	0.36	0.36	59
	3×10^7	1000×600	0.51	0.50	48
	10^8	1200×600	0.42	0.53	24
	2.15×10^8	1200×700	0.56	0.60	19
	4.64×10^8	1400×800	0.64	0.70	16
	10^9	2000×1000	0.61	0.76	13
R_2	10^6	1000×600	0.13	0.12	87
	3×10^6	1000×600	0.18	0.17	75
	10^7	1000×600	0.36	0.36	59
	3×10^7	1000×600	0.51	0.50	48
	10^8	1200×600	0.42	0.53	24
	2.15×10^8	1200×700	0.56	0.60	19
	4.64×10^8	1400×800	0.64	0.70	16
	10^9	2000×1000	0.61	0.76	13
R_3	10^6	1000×600	0.13	0.12	87
	3×10^6	1000×600	0.18	0.17	75
	10^7	1000×600	0.36	0.36	59
	3×10^7	1000×600	0.51	0.50	48
	10^8	1200×600	0.42	0.53	24
	2.15×10^8	1200×700	0.56	0.60	19
	4.64×10^8	1400×800	0.64	0.70	16
	10^9	2000×1000	0.61	0.76	13

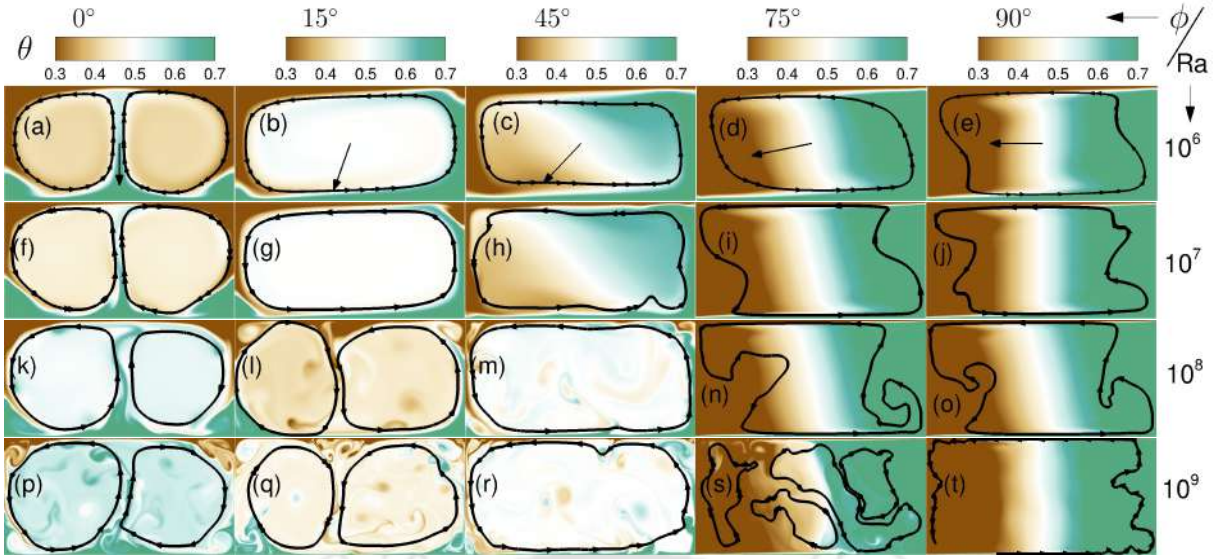

Figure 6.2: Instantaneous temperature field overlaid by streamlines showing the variation in large-scale rolls as inclination angle increases from $\phi = 0^\circ$ to 90° (left to right). While rows $(1-4)$ refer to $Ra = 10^6, 10^7, 10^8$, and 10^9, columns $(1-5)$ refer to $\phi = 0^\circ, 15^\circ, 45^\circ, \phi = 75^\circ$, and 90°. The arrows in the first row indicate the direction of gravity. For any specific tilt angle except $\phi = 0^\circ$, the flow states change with *Ra*.

shows the instantaneous temperature field for all the five tilt angles (left to right) and four *Ra* cases (top to bottom). The effect of inclination angle is evident in all the *Ra* cases, where flow structures transform from a double-roll state at $\phi = 0^\circ$ to a thermally stratified state at $\phi = 90^\circ$. While the former is a consequence of a double aspect ratio, the thermal stratification occurs due to a temperature gradient acting normal to the gravity in the latter. These states have already been identified in the previous studies [70, 124, 67]. Similar transformation of the flow states were observed by Wang *et al.* [74] for the same governing parameters. However, for $\Gamma = 1/2$, Wang *et al.* [64] observed an unstable triple-roll state at smaller tilt angles (close to the level case) and a single-roll state beyond $\phi \approx 10^\circ$.

At $Ra = 10^6$, it is observed that flow structures attain the shape of the cell at $\phi = 15^\circ$ (see frame b), where the direction of thermal plumes is aligned such that hot plumes move rightwards along the hot isothermal wall and cold plumes opposite to it. As a consequence, a large-scale circulation (LSC) forms instead of a double roll state (in the earlier studies, a large-scale roll is termed as LSC in a unit aspect ratio cell [70]). Therefore, inclination incites LSC that spans the entire cell, which is consistent with Guo *et al.* [68], though the flow state changes with further increase in inclination angle. At $(\phi = 45^\circ)$, movement of hot and cold fluid is restricted to the right and left part of the cell, respectively, indicating weak thermal stratification with the central

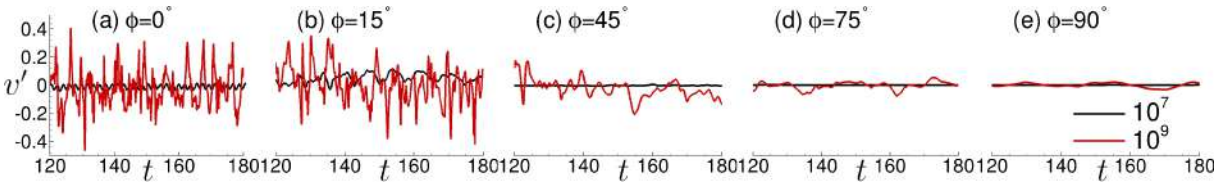

Figure 6.3: Time series of vertical velocity fluctuation ($v' = v - \langle v \rangle_t$) in the vicinity of geometric center of the convection cell ($x = 1.1, y = 0.5$) for *Ra* $= 10^7$ and 10^9 at all five inclination angles. With increase in inclination angle, intensity of fluctuations drops in both the *Ra* cases.

region showing fluid mixing. At $\phi = 75°$ and $90°$, flow structures are nearly same, and the flow becomes thermally stratified. Flow states at *Ra* $= 10^7$ remain same as in *Ra* $= 10^6$, and it is also consistent with the previous studies [74]. However, large-scale structures undergo significant changes beyond *Ra* $= 10^8$, see the last row of Fig. 6.2, where these effects are more pronounced for *Ra* $= 10^9$. It is clearly evident that a double roll state persists even at $\phi = 15°$ and the organization of corner rolls is similar to that in the level case. At $\phi = 45°$, signatures of thermal stratification are absent, and sudden detachment of thermal plumes from the smooth walls is observed at randomly located spots. Unlike the level case, in a tilted setup, thermal plumes (traveling along the isothermal surface) experience both buoyancy and induced shear. Therefore, it is quite apparent that both these forcing are competing with each other. While traveling along the hot surface, thermal plumes continuously gain heat. Once they attain sufficient energy to overcome the viscous resistance, they detach and move directly into the bulk, which impacts the heat flux to be described in Sec. 6.4. The observed weak thermal stratification suggests that an increase in *Ra* delays it, where the delay is in terms of inclination angle. This feature becomes more prominent for the highest *Ra* case, where evidence of relatively higher fluid mixing is seen even at $\phi = 75°$. In this case, a complex flow state is observed, where several circulation cells are evident in relatively smaller regions of the cell, which restrict the movement of fluid. Notably, we find that the transition to a single large-scale circulation shifts towards a greater inclination angle as *Ra* increases. This observation is in contrast to the results reported by Wang *et al.* [74]. They found that the above-mentioned shift first increases with inclination from 10^7 to 5×10^7 and eventually drops beyond 7×10^7.

To ascertain the weakening of turbulence with increasing inclination, we show time series of vertical velocity fluctuation (v') obtained from a probe placed near the geometric center of the cell ($x = 1.1, y = 0.5$) at *Ra* $= 10^7$ and 10^9 in Fig. 6.3. The vertical velocity is chosen because it signifies the rise of thermal plumes in the bulk region. At *Ra* $= 10^9$, in the level case, large fluctuations are evident in frame a. With increase in inclination angle, the fluctuations

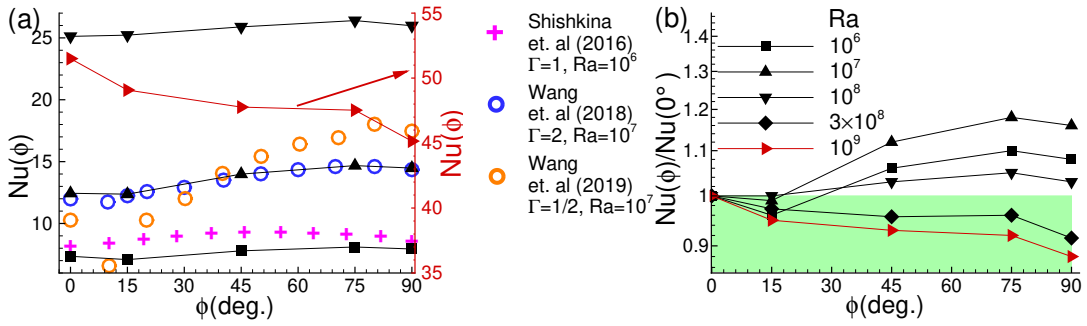

Figure 6.4: (a) Comparison of $Nu(\phi)$ curve obtained in the present work with Shishkina & Horn [70] ($Ra = 10^6$, $\Gamma = 1$ and $Pr = 1$), Wang *et al.* [74] ($Ra = 10^7$, $\Gamma = 2$ and $Pr = 0.71$), and Wang *et al.* [64] ($Ra = 10^7$, $\Gamma = 1/2$ and $Pr = 0.71$). Note that the arrow indicates the vertical axis (red color) for the highest *Ra* case. (b) Variation of normalized heat flux with inclination, where *Nu* data is normalized by that of level case $\phi = 0°$.

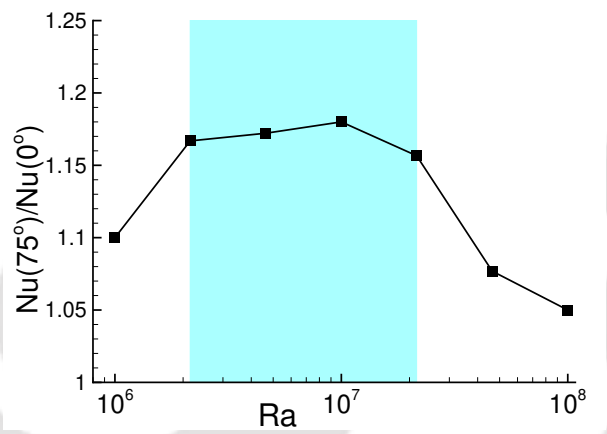

Figure 6.5: Identification of the *Ra* range where IC transports heat in the most efficient manner for $\phi = 75°$. The shaded region represents the *Ra* range $(2.15 \times 10^6 \leq Ra \leq 2.15 \times 10^7)$ where significant increment in heat flux is obtained.

drop and nearly vanish at $\phi = 90°$. The sharp fluctuations signify movement of thermal plumes at the geometric center. As shown in frames c-e, a weak fluctuating signal in intermediate and higher tilt angles shows the absence of vertical movement of thermal plumes in the bulk region. It indicates movement of the flow along the walls, and the diminishing effect of buoyancy in the transverse direction is responsible for such movement. In comparison to $Ra = 10^7$, evidence of fluctuations in vertical velocity at $Ra = 10^9$ are clearly seen at $\phi = 75°$, which confirms better mixing of fluid relative to the lower *Ra* case.

6.4 $Nu - \phi$ dependence

Nusselt number from the present study is compared with a few previously reported data in Fig. 6.4a. Our data agrees well with Wang *et al.* [74] for $Ra = 10^7$. Marginal difference is noted for $Ra = 10^6$ with Shishkina & Horn [70] who used $\Gamma = 1$. At small to moderate Ra ($\leq 10^8$), the $Nu(\phi)$ trend remains same, while it drops monotonically for $Ra = 10^9$ which is shown in a separate scale. To directly compare the $Nu - \phi$ dependence at different Ra, we show the normalized heat flux in Fig. 6.4b. For $Ra \leq 10^8$, a drop in Nu at $\phi = 15^\circ$ is evident in all the cases. With further increase in ϕ, it starts rising again to attain a maximum at 75°. Interestingly, the $Nu(\phi)$ trend becomes weaker with increasing Ra and drops monotonically beyond $Ra > 10^8$. In contrast to the present work, Wang *et al.* [64] obtained similar and robust $Nu(\phi)$ trend up to $Ra = 10^9$ in the convection cell of $\Gamma = 1/2$. This inconsistency can be attributed to the differences in the aspect ratio. For VC, the distance between the hot and cold plates in $\Gamma = 1/2$ is twice of that in $\Gamma = 2$, which favors thermal stratification and delays the onset of turbulence. Since greater tilt is effective in transporting heat due to laminar characteristics of the flow, Wang *et al.* [64] did not observe any variation in the $Nu(\phi)$ trend due to the dominating thermal stratification. They attributed the minimum Nu at smaller inclination angles to the double roll state at $Ra = 10^6$, and stable triple roll state at $Ra = 10^7$ and 10^8. On the other hand, as seen in Fig. 6.2(b,g,l,q), we observe that flow exhibits a single roll state in the two lower Ra cases and a double roll state in the other two higher ones. Contrary to the previous studies where the single roll state was found responsible for enhancing the heat flux [64], we find the same state to diminish it for $Ra \leq 10^7$. This shows that the $Nu(\phi)$ dependence is similar for $\Gamma = 1/2$ and 2 at lower Ra ($\leq 10^8$) despite different flow states.

Next, we identify the inclination angles which yield maximum heat flux for each Ra case. It is evident that IC with greater tilt ($\phi = 75^\circ$) transports heat most efficiently till $Ra = 10^8$, where $\phi = 75^\circ$ is seen as optimum inclination angle. However, beyond $Ra = 10^8$, RBC transports heat more efficiently. To observe the $Nu(Ra)$ trend for the optimum inclination angle, we further present the variation of normalized Nu by including four extra data points in Fig. 6.5. Heat flux initially rises with Ra to become maximum at $Ra = 10^7$ and drops monotonically beyond it. Interestingly, the optimum inclination becomes the most effective one at $Ra = 10^7$, with an increment of 18% in Nu. As shown by shaded region, we observe a Ra range $2.15 \times 10^6 \leq Ra \leq 2.15 \times 10^7$ where increment in heat flux is more than 15.7%. Below and above this range, a sudden drop in augmented heat flux is noted.

We further explore why the normalized heat flux drops with increasing Ra at $\phi = 75^\circ$. To

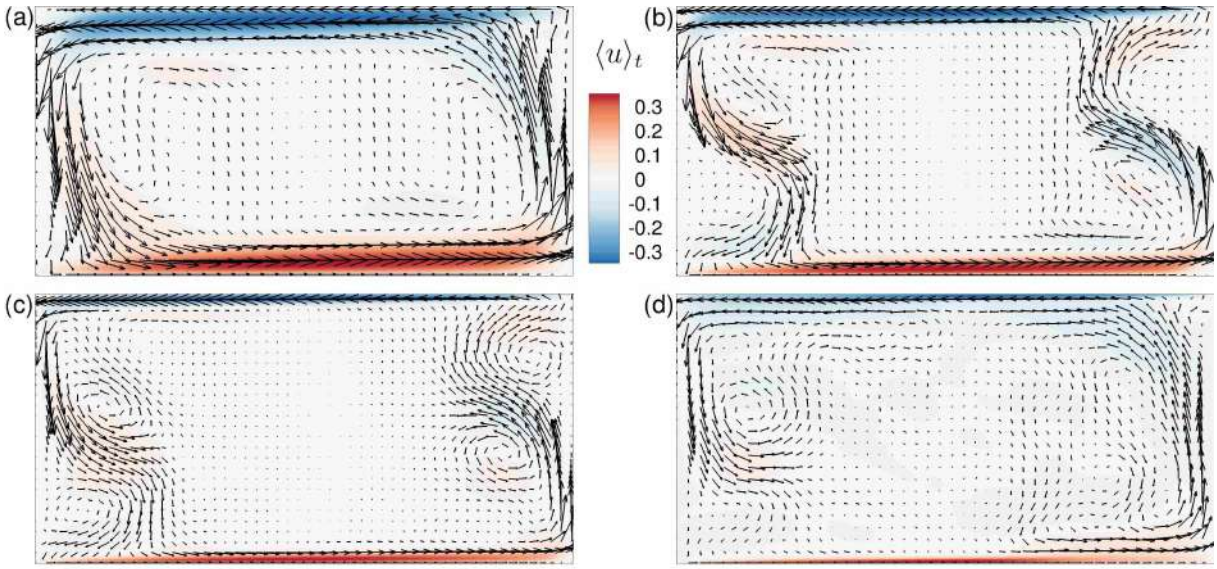

Figure 6.6: For $\phi = 75°$, component of time-averaged velocity field in the direction of IS overlaid by velocity vector at *Ra* = (a) 10^6, (b) 10^7, (c) 10^8, and (d) 10^9. With increase in *Ra*, the strength and region of velocity in the direction of IS diminish.

answer it, we show the time-averaged velocity field in the direction of IS overlaid by velocity vector in Fig. 6.6. It is noted that with increase in *Ra*, the intensity of the velocity drops near the isothermal walls. At the highest *Ra*, hot and cold fluid movement towards the opposite plates is obstructed due to the formation of several small-scale flow structures. These structures redirect the cold (hot) fluid towards the colder (hotter) region and restrict the fluid mixing. In other words, weakening of thermal convection in the direction of IS is responsible for the reduced heat flux at higher *Ra*. In Fig. 6.7, we quantify the drop in the velocity near the hot plate. $N(= 10)$ equispaced probes are placed at a distance of $y/H = 0.05$ to obtain the mean velocity in the direction of IS (u_p) and NIS (v_p), which are computed as

$$u_p = \frac{1}{N} \sum_{i=1}^{N} |\langle u_i \rangle_t| \tag{6.2}$$

$$v_p = \frac{1}{N} \sum_{i=1}^{N} |\langle v_i \rangle_t| \tag{6.3}$$

where i and $\langle \cdot\cdot \rangle_t$ represent the probe number and time-average. Clearly, u_p drops monotonically till $Ra = 10^8$ and becomes nearly constant beyond it, which shows weak convection in the direction of IS. However, v_p is insignificant compared to u_p, which is expected at such a greater tilt due to thermal stratification.

One reason to consider the three decades of *Ra* in the present study is to establish a $Nu(Ra)$ dependence for each inclination angle, which is described as follows. Figure 6.8a shows the

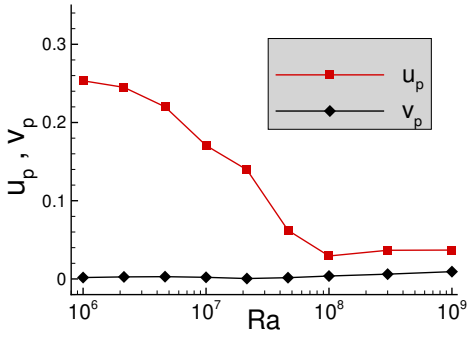

Figure 6.7: For $\phi = 75°$, strength of velocity in the direction of the IS and NIS as a function of *Ra*. The velocities are computed from probes placed at a distance of $y/H = 0.05$ unit away from the hot plate.

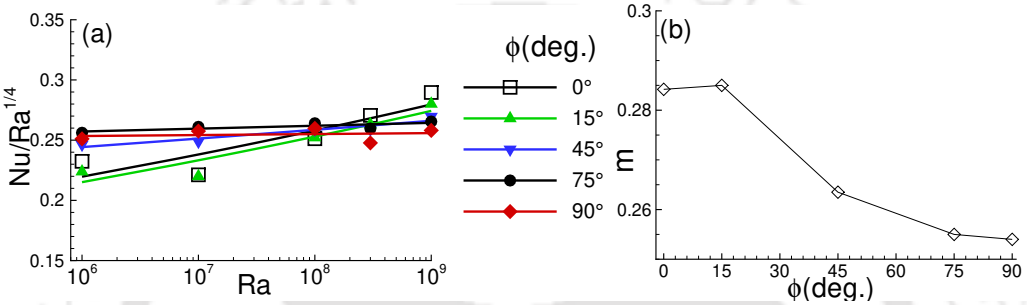

Figure 6.8: (a) The compensated Nusselt number showing the attainment of $1/4$ power-law as inclination increases from $\phi = 0°$ to $90°$. (b) Variation of the $Nu(Ra)$ scaling exponent with inclination angle.

compensated $Nu(Ra)$ scaling law in order to study the deviation from $Nu \sim Ra^{1/4}$. The greater tilt cases strictly follow the $1/4$ law, whereas a significant deviation is observed as ϕ approaches the level case. Further, in frame (b), we show the variation of $Nu(Ra)$ scaling exponent (m) with ϕ and found that a slight tilt does not alter the scaling exponent. On the other hand, it drops sharply as the cell is tilted beyond $\phi = 15°$. Evidently, the exponent becomes nearly invariant for $\phi \geq 75°$. It is evident that m is higher $(m = 0.284)$ in RBC than that in VC $(m = 0.254)$ due to which the $Nu(\phi)$ curve shifts downward with increasing *Ra*. Consequently, the most efficient heat transport state turns out to be the level case for $Ra > 10^8$.

6.5 $Re - \phi$ dependence

Reynolds number (Re) is another response parameter that depends upon *Ra* and inclination. It is a measure of turbulent intensity and computed as $Re = \sqrt{Ra/Pr}U$, where $U = \sqrt{\langle \mathbf{u} \cdot \mathbf{u} \rangle}$, see Eq. 6.1. In Fig. 6.9a, we show a comparison of absolute *Re* among the present study, Shishkina

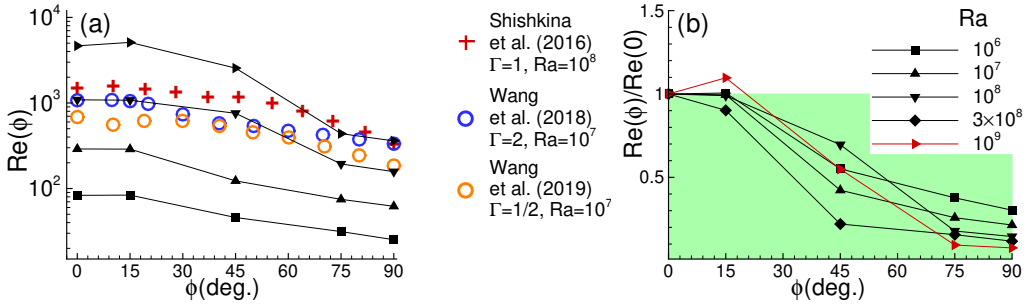

Figure 6.9: (a) Comparison of $Re(\phi)$ trend obtained in the present work with Shishkina & Horn [70] ($Ra = 10^8$, $\Gamma = 1$ and $Pr = 1$), Wang *et al.* [74] ($Ra = 10^7$, $\Gamma = 2$ and $Pr = 0.71$), and Wang *et al.* [64] ($Ra = 10^7$, $\Gamma = 1/2$ and $Pr = 0.71$). (b) Variation of normalized Reynolds number with inclination. Note that the normalization is carried out with respect to the level case ($\phi = 0°$). The shaded region highlights the drop in Reynolds number below the level case.

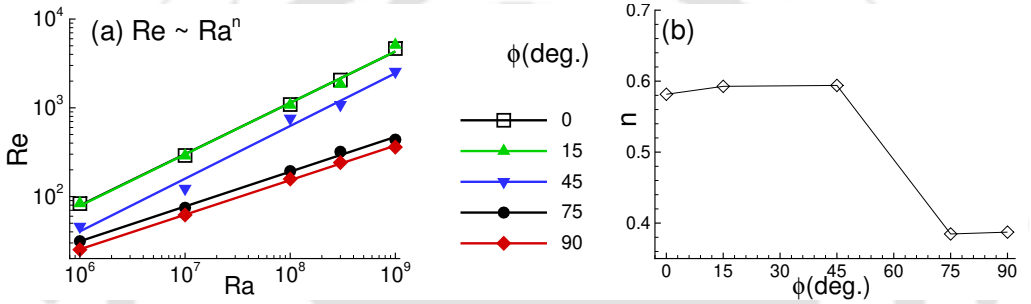

Figure 6.10: (a) Least square fit of the $Re(Ra)$ data for all the inclination angles. (b) Variation of the $Re(Ra)$ scaling exponent with inclination angle.

& Horn [70], Wang *et al.* [74], and Wang *et al.* [64]. We observe that the trend of *Re* in the present work agrees well with the above-mentioned studies. It is noted that with increasing ϕ, *Re* first remains nearly same up to $\phi = 15°$ and then drops monotonically. For a direct comparison of $Re(\phi)$ at different *Ra*, we present the normalized $Re(\phi)/Re(0)$ data in Fig. 6.9b, where the shaded region shows $Re < Re(0°)$. It is observed that *Re* remains unaltered till $\phi = 15°$ for $Ra \leq 10^8$, whereas it increases nearly by 10% in the highest simulated *Ra* case. For $Ra = 10^9$, $Nu(\phi)$ shows a reduction in heat flux for $\phi = 15°$, which is in contrast to the *Re* at the same inclination. Thus, in a double aspect ratio configuration, despite unaltered or a small increase in turbulent intensity, the drop in *Nu* indicates that the enhanced turbulent intensity does not necessarily improve the heat flux. Similar observation was made by Jiang *et al.* [66], who reported that instead of turbulent intensity, the strength of LSC enhances the *Nu*. However, the double roll state at $\phi = 15°$ in Fig. 6.2(q) seems to be responsible for the enhanced turbulent intensity at $Ra = 10^9$. With further increase in inclination angle, *Re* plummets sharply and decreases by more than 90% at $\phi = 90°$. The observed trend is different than what Wang *et al.* [64] found,

where *Re* first drops and then rises again before following the monotonically decreasing trend. Again, this inconsistency may be attributed to the differences in the aspect ratio, which plays a significant role in determining the turbulent intensity due to the gap between the two isothermal walls. This analysis also suggests that *Re* drops fastest in the intermediate inclination range and not near the vertical convection.

In Fig. 6.10, we show the least square fit of $Re(Ra)$ data. For $\phi = 0^\circ$, we observe that $Re \sim Ra^{0.59}$ which is in good agreement with the previous studies [129, 48, 130, 125]. In addition, we further study the $Re(Ra)$ dependence for other inclination angles, which have not been reported so far. The level case $\phi = 0^\circ$, and 15° follow nearly the same power law, $Re \sim Ra^{0.59}$. In these two cases, the collapse of $Re(Ra)$ curves indicates the insignificant effect of smaller inclination angle on turbulent intensity, which is also supported by the obtained flow states. With further increase in $\phi(= 45^\circ)$, we observe the same scaling exponent but with a significant drop in absolute *Re*. The observed drop may be attributed to the single-roll state. In comparison to a double-roll state, thermal plumes, driven by a single-roll, traverse a larger distance to reach the opposite plate. As a result, thermal plumes diffuse early, which diminishes the strength of the single large-scale roll. In the two highest ϕ cases, the $Re(Ra)$ nearly follow the same power-law and the least scaling exponent $n = 0.39$. Figure 6.10b shows the variation of n with ϕ, where the exponent remains nearly same till $\phi = 45^\circ$ and subsequently drops to a significantly lower value for the two highest inclination cases. The variation in the exponent signifies differences in the transport mechanism. While the higher exponent marks the presence of turbulence in the flow, its lower counterpart highlights the signature of laminar characteristics, which can also be seen from the stratified temperature field in Fig. 6.2.

6.6 Effect of inclination on flow structures in the rough cells

In Figs. 6.11(a-c), we present time-averaged temperature field overlaid by streamlines for R_1, R_2, and R_3 configurations, respectively, to identify the changes in flow state with Rayleigh number and tilt angle. The temperature fields are shown for increasing *Ra* (top to bottom) and ϕ (left to right). In R_1 case, flow features change from a double-roll state in the level case to the stratified flow in the VC ($\phi = 90^\circ$) for all *Ra* cases, where only central part of the cell shows a homogeneous mixing of hot and cold fluid. On the other hand, flow structures in the inclined cases $\phi = 15^\circ$, 45°, and 75° show transformation from the double-roll state to a single-roll state (except at $\phi = 75^\circ$ for the highest *Ra*), spanning the entire cell. In the lowest *Ra* case, the effect

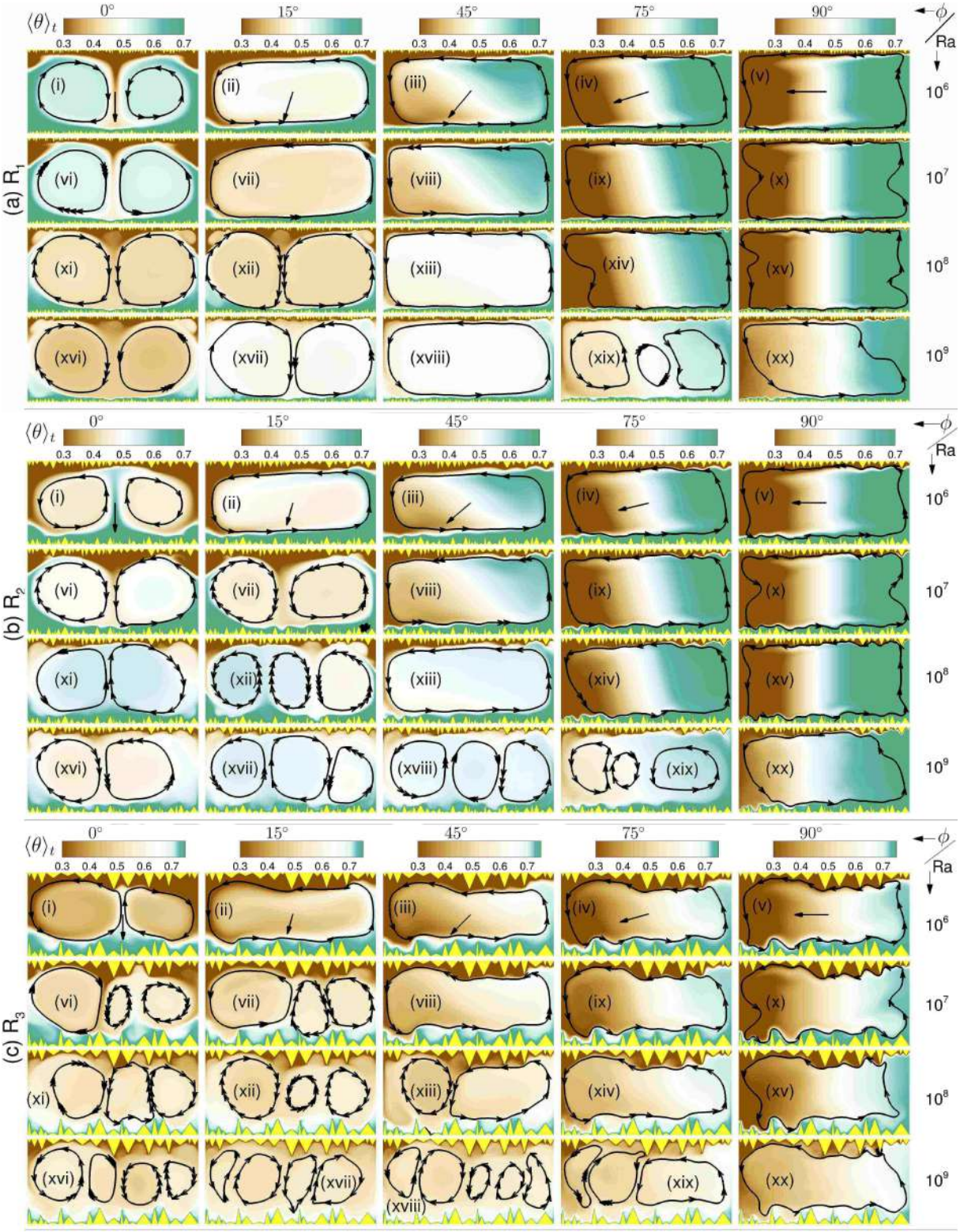

Figure 6.11: In (a) R_1, (b) R_2, and (c) R_3, time-averaged temperature field superimposed with streamlines for $Ra = 10^6$ (i-v), 10^7 (vi-x), 10^8 (xi-xv), and 10^9 (xvi-xx). Inclination angle varies from left to right in the order: $\phi = 0°$, $15°$, $45°$, $75°$, and $90°$. The arrows in the first row of each roughness case indicate the direction of gravity.

of inclination is significant as it brings the double-single roll state transformation at $\phi = 15^\circ$ and incites thermal stratification at $\phi = 45^\circ$. With increasing *Ra*, effect of inclination becomes weaker as the flow structures appear to be same at $\phi = 0^\circ$ and 15° for $Ra = 10^8$. Since thermal plumes shrink with increasing *Ra*, smaller-sized plumes, owing to their greater mobility at higher *Ra*, do not align themselves in a single-roll state at $\phi = 15^\circ$. Further, at $\phi = 75^\circ$, with respect to the smooth case, a weaker thermal stratification and relatively better fluid mixing is evident in the cell. As ϕ approaches 90°, thermal stratification is clearly seen where nearly still, cold and hot fluid are present in the vicinity of the cold and hot isothermal walls of the cell, respectively.

In the intermediate roughness configuration (R_2), a large-scale roll is attained at $\phi = 15^\circ$ for the lowest *Ra* case. For $Ra = 10^7$, we observe that the flow state remains same for $\phi = 0^\circ$ and 15°. Such a response of flow structures towards inclination is also observed in R_1 but at a higher $Ra = 10^8$. For $Ra = 10^8$, a triple-roll state is evident at $\phi = 15^\circ$, while for the highest *Ra* case, a triple-roll state is found for all the inclinations between $15^\circ \leq \phi \leq 75^\circ$. At $\phi = 75^\circ$, it appears that thermal stratification has vanished due to the presence of a multiple-roll state. On the other hand, it is still evident in VC, although a weaker one.

Features of the flow structures that appeared in the R_2 case become more pronounced in the tallest roughness configuration (R_3) as shown in Fig. 6.11c. The tendency of transformation of the flow state in the level case to higher tilt angles is found same for the lower *Ra* cases (up to $Ra = 10^7$) in R_2 and R_3 configurations. However, beyond $Ra = 10^7$, significant differences are observed in R_3 case. Increasing roughness height delays the emergence of a single large-scale roll that depends upon the inclination. In particular, this transition appears at $\phi = 75^\circ$ and 90° for $Ra = 10^8$ and 10^9, respectively. For the highest *Ra*, multiple smaller rolls persist at $\phi = 45^\circ$ and 75°, respectively. As observed for R_2 case, these rolls improve mixing of fluid in the cell. The most interesting feature appears in VC, where we observe that thermal stratification is nearly absent. It is evident that roughness delays thermal stratification due to its ability to break the large-scale rolls and emit thermal plumes directly into the bulk region. It can also be viewed as early onset of turbulence in greater tilt cases. Since increase in roughness height reduces the distance between isothermal walls, increase in turbulent intensity is obvious, which is reflected in delayed thermal stratification. This result elucidates why Wang *et al.* [64] observed greater heat flux at greater inclination even at $Ra = 10^9$.

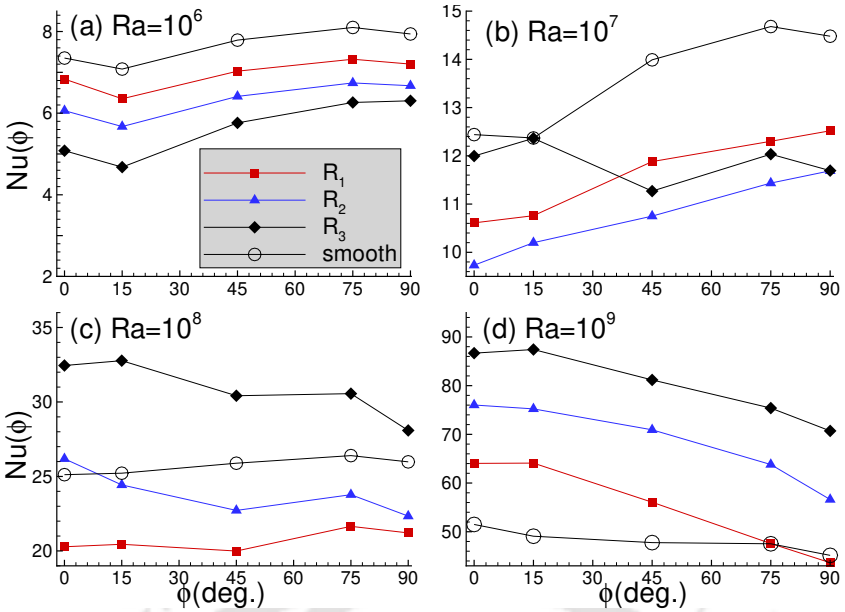

Figure 6.12: Dependence of heat flux on inclination angle for Ra = (a) 10^6, (b) 10^7, (c) 10^8, and (d) 10^9 in R_1, R_2, and R_3 configurations. The $Nu(\phi)$ curve does not change with roughness configurations at the lowest and highest Ra.

6.7 Effect of inclination on *Nu* in the presence of roughness

Figure 7.3 shows a comparison of $Nu(\phi)/Nu(0^\circ)$ among the smooth, R_1, R_2, and R_3 cases for the four Ra that covers the entire simulated Ra range. For the lowest Ra, the $Nu(\phi)/Nu(0^\circ)$ trend is same for all three roughness cases which is similar to the smooth case. It happens because of a weaker thermal forcing, due to which fluid remains inside the cavities [61, 131]. Also, all the roughness elements are buried under a thick thermal boundary layer. The stagnant fluid and the thicker boundary layer suppress the effect of roughness at lower Ra, yielding a $Nu(\phi)$ trend similar to that of the smooth case. We observe that the $Nu(\phi)$ drops till $\phi = 15^\circ$ and rise with further increase in inclination angle. In the smooth, R_1, and R_2 cases, the maximum heat is transported at $\phi = 75^\circ$. On the other hand, VC ($\phi = 90^\circ$) yields maximum heat flux in R_3. For any particular tilt angle, heat flux decreases as the configuration changes from the smooth to R_3 case. Since the cavity space increases from R_1 to R_3, volume of stagnant fluid inside them also increases. In such a scenario, heat is transferred only through the conduction. Therefore, for lower Ra, this study suggests that taller the roughness height is, lesser is the heat flux, which answers why the smooth case yields the highest heat flux and R_3 the least.

For $Ra = 10^7$ (see frame b), the normalized $Nu(\phi)$ curve in R_1, and R_2 is nearly similar except for $\phi = 15^\circ$, whereas a completely different trend is observed for R_3 case. Contrary to the smooth case, Nu increases monotonically in R_1 and R_2 cases to become maximum at 90°.

It suggests that small asperities on the isothermal walls make the vertical convection the most efficient heat transport system. In R_3, *Nu* is either higher or comparable to R_1, and R_2. It happens because roughness elements in R_3 become active at this $Ra(=10^7)$ and perturb thermal boundary layer to modify the flow structures by directly injecting thermal plumes in the bulk [131]. On the other hand, owing to their relatively shorter height with respect to thermal boundary layer, roughness elements in the other two cases remain buried inside it. Here active roughness refers to those elements which actively participate in emitting thermal plumes and are not buried inside the thermal boundary layer. The idea of activation is clearly seen from the nearly same $Nu(\phi)$ trend in the two smaller roughness cases.

For $Ra = 10^8$, the trend in all three configurations reverses completely due to differences in active roughness peaks. In this case, flow states in R_1 and R_2 are same beyond $\phi = 15°$, which is also reflected by similar $Nu(\phi)$ trend in Fig. 7.3(c). On the other hand, in R_3, the trend becomes nearly same beyond this *Ra*. This similarity is attributed to the early onset of transition to a multiple-roll state in R_3 through taller roughness peaks. Also, beyond this *Ra*, R_3 yields higher heat flux than smooth, R_1 and R_2 cases. The reason for the highest heat flux in R_3 is again multiple-rolls and boundary layer penetrating peaks. In Chand *et al.* [131], it was already noted for the level case that onset of enhanced heat flux regime occurs at $Ra = 2.15 \times 10^8$, 5.50×10^7, and 10^7 in R_1, R_2, and R_3 cases, respectively, which supports the above arguments.

For the highest $Ra(=10^9)$, maximum heat flux is produced by the tallest case (R_3) and minimum by the smooth case. Interestingly, the trend of increasing heat flux with roughness heights at the lowest *Ra* reverses at the highest one. The reason behind this change is presence of multiple-rolls (five large-scale rolls) in R_3, whereas a maximum of three and two rolls are present in R_2 and R_1 cases, respectively. Basically, a larger number of rolls improves the plume ejection spots, which enhance *Nu* [111]. Another physical argument that can be made here is widening of the cavities with increasing roughness height. Wider cavities have a higher tendency to get washed out more efficiently to enhance the emission of thermal plumes [61, 53].

For each inclination angle, we further show the variation of normalized heat flux with *Ra* in Fig. 7.5. Based on $Nu/Nu(0)$, we define enhanced, $Nu > Nu(0)$, and reduced, $Nu < Nu(0)$, heat flux regimes. Note that the *Ra* beyond which enhanced heat flux regime changes to the reduced one is termed as the critical Rayleigh number (Ra_c). For R_1, R_2, and R_3 cases, Ra_c is found as 10^8, 10^7, and 3×10^6, respectively. The width of the enhanced heat flux regime diminishes with increasing roughness height. In this regime, $Nu/Nu(0)$ increases with inclination, as shown by upward arrows. However, a contrasting effect of ϕ, represented by the downward arrows, is seen

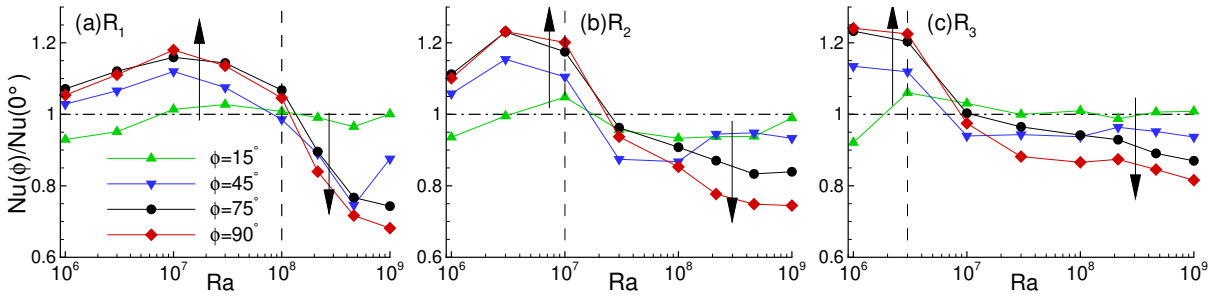

Figure 6.13: Variation of normalized heat flux, $Nu(\phi)/Nu(0)$, with Ra for (a) R_1, (b) R_2, and (c) R_3 configurations at four different inclinations. While the vertical dashed line demarcates the enhanced and reduced heat flux regimes, the horizontal dash-dotted line represents $Nu(\phi)/Nu(0^\circ) = 1$. The upward (downward) arrows indicate the increasing (decreasing) Nu with ϕ.

in the reduced heat flux regime. The transition in the $Nu(\phi)$ trend reflects the onset of turbulence, which again supports our observation that RBC transports heat more efficiently than IC at larger Ra. From R_1 to R_3, the decrease in Ra_c signifies early onset to turbulence due to a surge in plume emission [125]. In particular, we observe a maximum improvement of 18%, 24%, and 25% in heat flux for R_1, R_2, and R_3 cases, respectively. On the other hand, following the same order, a maximum reduction of 32%, 25%, and 17% in heat flux is observed in the reduced heat flux regime.

Next, we study the effect of tilt on $Nu(Ra)$ dependence by showing the least square fit of the Nu data in Fig. 6.14(a-e), and $m(\phi)$ behavior in frame (f). In R_1 case, note that deviation from the fitting at the highest Ra is observed up to $\phi = 45^\circ$, which indicates the late onset of turbulence (higher Ra_c). The deviation is also evident from the rising error bar in frame (a-c). However, as $\phi > 45^\circ$, the error bar nearly vanishes, which signifies the laminar heat transport throughout the simulated Ra range. This is apparent from the similar $m(\phi)$ trend in R_1 and the smooth case beyond $\phi = 45^\circ$. For these two cases, the exponent drops to $m \approx 1/4$ in VC, which is consistent with the previous results [123, 124]. On the other hand, the early onset of turbulence is responsible for the higher exponent in the two taller roughness configurations. A direct connection between the turbulent intensity and scaling exponent is evident as configuration changes from R_1 to R_3 in frame f. It is interesting to note that despite significant differences in roughness heights, the $m(\phi)$ trend remains nearly same in the three cases. Here, the effect of decreasing $m(\phi)$ corresponds to the drop in heat flux as Ra increases beyond Ra_c.

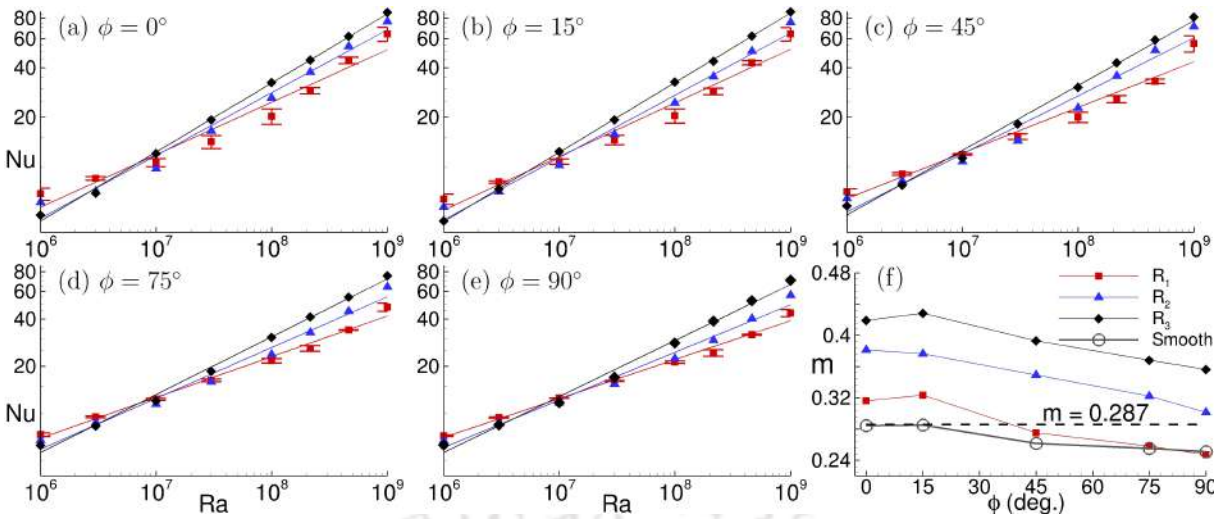

Figure 6.14: (a-e) Least-square fit of $Nu(Ra)$ at different inclination angles. (f) $Nu(Ra)$ scaling exponent (m) as a function of inclination angle for R_1, R_2, and R_3 cases. The dashed line in frame f represents $m = 0.287$ obtained for the smooth case at $\phi = 0°$. Note that $Nu(Ra)$ data is presented with the error bars in the R_1 case to show deviation from the least-square fit.

6.8 Effect of inclination on *Re* in the presence of roughness

Figure 6.15 shows the variation of Reynolds number with inclination at four *Ra* that covers the entire simulated *Ra* range. Similar to the smooth case, the $Re(\phi)$ curve shows a consistent trend where it remains nearly identical or changes slightly at small inclination $(\phi = 15°)$ and drops monotonically with further increase in ϕ in all the four *Ra* cases. However, roughness impacts the turbulent intensity, which is reflected in the deviation from the smooth case in $Re(\phi)$. At lower $Ra(\leq 10^7)$, roughness height suppresses the turbulent intensity, i.e., taller the roughness height is, lesser is the turbulent intensity. It happens due to the stagnant fluid residing in the cavities at lower *Ra*. It is also reflected from the nearly same *Re* in the smooth and R_1 case, where the flow structures are similar. Beyond $Ra = 10^8$, as expected, differences in *Re* in the three configurations reduce due to movement of fluid in the cavities (secondary vortices), which washes them out. The role of roughness heights is remarkable for a greater tilt at $Ra = 10^9$. Here, while the *Re* between $\phi = 75°$ and $90°$ changes marginally in the smooth case, a significant difference is evident as roughness configuration changes from R_1 to R_3. It clearly indicates weaker thermal stratification and greater mixing of fluid at these two inclinations in taller roughness configurations, as observed in the flow structures in Sec. 6.6. Contrary to lower *Ra* cases, we observe that $Re(\phi)$ trend does not show notable changes till $\phi = 45°$ for the highest *Ra*. It can be attributed to the similar flow structures that show a greater turbulent intensity at this inclination range for $Ra = 10^9$. On the other hand, evidence of thermally stratified flow at

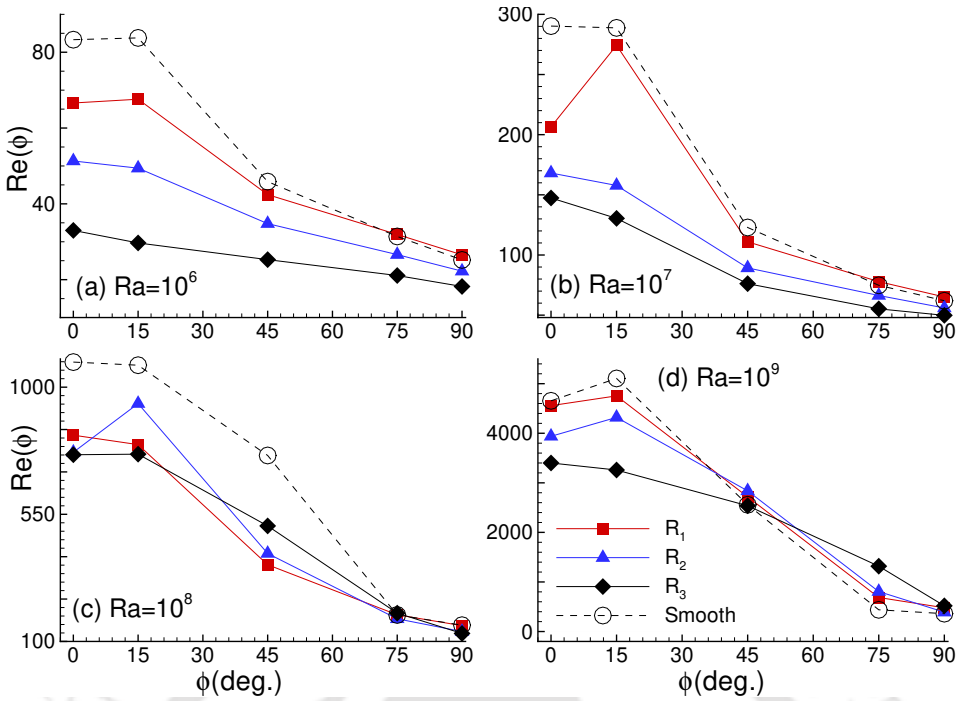

Figure 6.15: $Re - \phi$ dependence for three roughness and smooth case at four Ra = (a) 10^6, (b) 10^7, (c) 10^8, and (d) 10^9. The $Re - \phi$ curves in roughness cases are similar to the smooth case. Note that while Re decreases from R_1 to R_3 at lower Ra, it becomes comparable in all three configurations at the highest Ra.

$\phi = 45^\circ$ for lower Ra cases is responsible for the sudden drop in Re.

We further study the effect of inclination on $Re(Ra)$ dependence for different inclination angles in Fig. 6.16. The least-square fit of $Re(Ra)$ data clearly shows that the scaling law $Re \sim Ra^n$ for $\phi = 0^\circ$ and 15° are nearly same, where the scaling exponents for R_1, R_2, and R_3 are 0.61, 0.64, and 0.68, respectively. The nearly same exponent for $\phi = 0^\circ$ and 15° cases indicates a similar transport mechanism which is also reflected in their flow structures. Note the effect of roughness on the scaling exponent, which is nearly same for the smooth and tiny roughness heights. However, as roughness changes from R_1 to R_3, the exponent increases with respect to the smooth case. For $\phi = 45^\circ$, although turbulent intensity decreases, the scaling exponent remains nearly same as in the two smaller inclinations, which is reflected by the $n(\phi)$ trend in frame (d). However, beyond $\phi = 45^\circ$ the exponent as well as turbulent intensity drops remarkably due to settling down of the cold and hot fluid near the the cold and hot walls of the cell, respectively (see the time-averaged temperature field in Fig. 6.11). For $\phi = 75^\circ$ and 90°, we observe that the exponent in smooth and R_1 case does not change appreciably, which indicates a similar flow state. On the other hand, flow structures in R_2 and R_3 change significantly at these inclinations, which is also reflected in their $n(\phi)$ trend. In R_3, greater turbulent intensity (weaker thermal

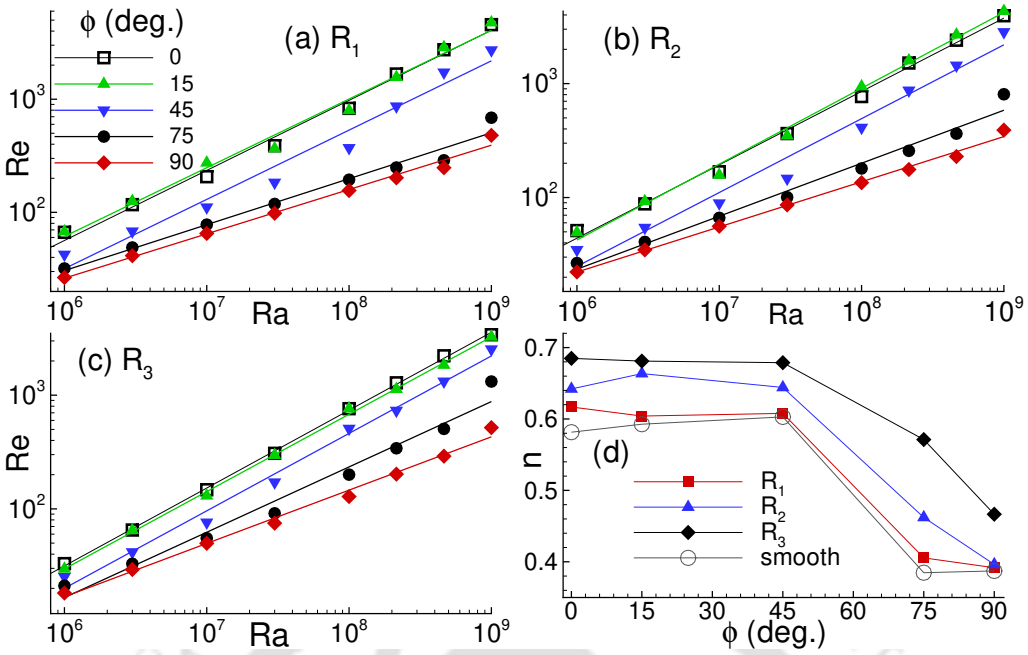

Figure 6.16: For five inclinations, least square fit of *Re* data for (a) R_1, (b) R_2, and (c) R_3. Frame (d) shows $n - \phi$ trend for the three roughness and smooth cases. The scaling exponent remains nearly same till $\phi = 45^\circ$ and drops beyond this range.

stratification) as compared to the other smaller roughness setups at $\phi = 75^\circ$ is responsible for a higher scaling exponent.

6.9 Conclusions

In this chapter, we have investigated the effect of inclination on heat flux in a wide range of *Ra* varying from 10^6 to 10^9 in two-dimensional tilted RBC. The investigation is carried out in a double-aspect-ratio convection cell filled with air ($Pr = 0.71$) for five inclination angles ($\phi = 0^\circ, 15^\circ, 45^\circ, 75^\circ$, and 90°) for both the rough and smooth cases. Shishkina & Horn [70] suggests that $Nu(\phi)$ and $Re(\phi)$ trends are non-monotonic complex functions of *Ra* and *Pr*. In the same line, the present work has addressed one of these complexities, i.e., the effect of *Ra* on $Nu(\phi)$ dependence for a relatively wider cell ($\Gamma = 2$) in $2D$ RBC. We have listed the $Nu(\phi)$ trend observed in the previous studies and current work in Table 6.3. Based upon the analysis, we have made the following observations:

1. In the smooth case, inclined convection can be used to enhance the heat flux below $Ra = 10^8$, whereas, above it, RBC yields the highest heat flux. On the other hand, for the roughness cases, effectiveness of IC (determined by Ra_c) to transport heat shifts to lower *Ra* as characteristic height of the roughness increases due to early onset of turbulence.

Table 6.3: Summary of $Nu(\phi)$ trend in inclined thermal convection. From left to right: references; aspect-ratio (Γ); Prandtl number (Pr); Rayleigh number (Ra); the characteristic of $Nu(\phi)$ trend; and the inclination angle at which maximum heat flux is obtained. Here, unimodal and bimodal in $Nu(\phi)$ trend refer to a single and dual peaks, respectively.

References	Γ	Pr	Ra	$Nu(\phi)$ trend (max. at $\phi =$)
Frick *et al.* [71]	$1/5$	0.0094	$2 \times 10^6 - 10^7$	unimodal $(45°)$
Vasilev *et al.* [72]	$1/20$	0.0094	2.4×10^6	unimodal $(65°)$
Khalilov *et al.* [67]	1	0.0094	1.47×10^7	unimodal $(70°)$
Shishkina & Horn [70]	1	$0.1, 1$	$10^6 - 10^8$	unimodal $(\approx 54°)$
Chilla *et al.* [69]	$1/2$	2	$10^{11} - 10^{12}$	monotonically decreasing $(0°)$
Guo *et al.* [65]	$\Gamma_x(\Gamma_y) = 1(1/4)$	6.3	4.42×10^9	monotonically decreasing $(0°)$
Wang *et al.* [64]	$1/2$	$0.1 - 100$	$10^6 - 10^9$	unimodal for $Pr = 0.71$ $(80°)$
Jiang *et al.* [66]	1	480	$10^8, 5 \times 10^8$	bi-modal $(75°)$
		Present work		
Smooth case	2	0.7	$10^6 - 10^8$	unimodal $(75°)$
			$10^8 < Ra$	monotonically decreasing $(0°)$
Rough cases	2	0.7	10^6	unimodal $(75°)$
			$10^7 \leq Ra \leq 10^8$	complex trend
			10^9	monotonically decreasing $(0°)$

2. In the smooth case, the maximum heat flux is obtained at $\phi = 75°$ for $Ra \leq 10^8$, while for the roughness cases, it depends upon the Ra and roughness setups.

3. For $\phi = 75°$, in the smooth case, a Ra range, $2.15 \times 10^6 \leq Ra \leq 2.15 \times 10^7$, is identified wherein heat flux improves significantly, at least by 15%. In the three roughness configurations, we observed an increment of 18%, 24%, and 25% in Nu for R_1, R_2, and R_3 cases, respectively.

4. For both smooth and roughness cases, with increase in Ra, transition to a single large-scale circulation shift towards a greater tilt angle. Moreover, an increase in roughness height also delays this transition. Contrary to the previous observations [64], a single-roll state is found to diminish heat flux for $Ra \leq 10^7$ at $\phi = 15°$.

5. While increase in *Ra* delays the onset of thermal stratification in the smooth case, increase in the characteristic height of the roughness setups does the same in rough configurations, which indicates early onset of turbulence in greater tilt cases.

6. Similar to the effect of *Ra* on $Nu(\phi)$ dependence, $Re(\phi)$ trend remains nearly same up to $Ra = 10^8$ and changes marginally beyond it. It is also found that *Re* drops faster in the intermediate inclination range than near the VC.

CHAPTER 7

Effect of conical roughness on heat transport properties

In this chapter, we investigate the effect of roughness (conical) on heat flux through coherent structures for a fixed Ra $= 10^8$ *in* $3D$ *cubical cell. We consider two roughness configurations: uniform (U) and irregular (R) cases. In the uniform case, roughness height remains unchanged* $h = 0.1H$*, while in the irregular case, the height varies in the range* $50 - 100\%$ *of the maximum height* $(0.1H)$*. In addition, we have also studied their half-variants (HU and HR), where the rough surface is considered only on the bottom plate. It is observed that heat flux increases significantly in the rough cases, whereas, surface roughness impacts the flow strength relatively weakly. The heat flux increases due to emission of a large number of intense thermal plumes in the rough cases, which is ascertained by an increase in plume volume fraction* V_{pl}*. Larger temperature variance in the rough cases confirms the frequent emission of thermal plumes. A shift in mean temperature in the bulk region is observed for HU and HR cases due to emission of more hot plumes. LSC remains in the diagonal plane in the smooth case, whereas it is aligned along the Cartesian planes* $(x$ *or* $z)$ *in the rough cases. The strength of the LSC is quantified by angular velocity based on Reynolds number, which ascertains the differences in the reorientation of LSC between smooth and rough cases. Greater local heat flux in the rough cases ascertains the intense characteristics of emitted thermal plumes. Second-order structure function of vertical velocity and temperature reveals energetic flow structures in the rough cases, whereas power spectra of temperature fluctuations reveals the existence of* $BO59$ *scaling in the bulk region.*

7.1 Introduction

In the previous chapters, we have studied the effect of roughness on heat transport properties in $2D$ convection cells, where triangular roughness elements were used. In this chapter, we investigate the effect of $3D$ conical roughness elements on heat transport mechanism, transport properties, coherent structures, and small-scale statistics in a cubic cell.

In RBC, there are three coherent structures, i.e., LSC, boundary layer and thermal plumes, which are associated with heat transport mechanism. In what follows, a detailed literature review shows the connection between heat flux and coherent structures in roughness-aided convection. We first describe the role of boundary layer and thermal plumes and then report the impact of roughness on LSC and smaller rolls. In the previous studies [55, 132, 133], it has been well established that surface roughness can augment the heat flux, which depends on geometric parameters of the roughness elements. In an experimental study, Shen *et al.* [54] used pyramidal roughness and observed 20% increment in heat flux and proposed that the increment occurs when the thermal boundary layer thickness (λ_θ) and roughness height are comparable. Later, Ciliberto & Laroche [56] experimented with spherical roughness elements and observed a higher $Nu(Ra)$ scaling exponent, which was again attributed to the relationship between the thermal boundary layer and roughness height. Roche *et al.* [58] also observed greater heat flux and scaling exponents for triangular surface roughness and reported that the roughness is effective when its height becomes 80% of λ_θ.

In a recent $3D$ RBC study, Belkadi *et al.* [79] investigated $Nu(Ra)$ scaling exponent in the presence of surface roughness and observed three heat flux regimes, which are discussed as follows. In the first regime, observed at lower Ra, surface roughness affects the heat flux due to fluid entrapment in the cavities. Here, the roughness elements remain inactive. With further increase in Ra, they observed the second regime, wherein roughness elements perturb the boundary layer due to its diminishing thickness. This perturbation is responsible for frequent emission of thermal plumes, which results in higher heat flux. The enhancement in heat flux occurs mainly because turbulence sets in the boundary layer due to roughness asperities. In the third regime, obtained by increasing Ra beyond the second regime, the turbulence in the boundary layer vanishes due to weakening of the perturbation [1, 2]. The weakening effect can be attributed to the similar flow characteristics inside the cavities and bulk region, which suppresses the effect of roughness on plume dynamics. Thus, in this regime, the flow behaves like that of the smooth surface and heat flux increases due to increase in the heated area. The above-mentioned three regimes were also reported by Xie & Xia [60], wherein pyramid-shaped roughness of four dif-

ferent aspect ratios were used. Apart from the $Nu(Ra)$ regimes, they also found that the aspect ratio of roughness element is directly connected with the increase in scaling exponent.

In the following discussion, we describe the effect of roughness on LSC and its role in heat flux enhancement. For a taller and smaller pyramid roughness geometry, Du & Tong [57] observed that *Nu* increases by 76% and 29%, respectively. They attributed the enhancement to the interaction between the shear flow induced by LSC and the surface roughness, resulting in secondary vortices in the valleys. Both these structures (LSC and secondary vortices) detach more thermal plumes and yield greater heat flux and $Nu(Ra)$ scaling exponent. Later, Qiu *et al.* [134] investigated the effect of pyramidal grooves on the characteristics of LSC in a cylindrical cell of unit aspect ratio. They observed that roughness elements do not impact the LSC, whereas their effect on the velocity boundary layer remains confined to the groove region.

In addition to the global flow structures, Liot *et al.* [135] investigated the flow characteristics in the notch and at the top of the obstacles in a roughness-aided convection cell. They reported that a stratified fluid and slow circulation inside the notch yield low heat flux. On the other hand, incursion of bulk fluid inside the notch results in emission of larger thermal plumes, which yields greater heat flux. Further, Liot *et al.* [136] studied the flow characteristics in a cell facilitated with roughness elements only on the bottom plate. They reported stronger fluctuations in both the horizontal and vertical velocities as compared to the smooth case. Moreover, they observed asymmetry in the vertical profiles, which were attributed to the enhanced plume emission and the emergence of different turbulent structures.

Further, Jiang *et al.* [112] considered a complex roughness configuration (asymmetric ratchet surface) to investigate its effect on LSC and heat transport properties. They observed that heat flux increases significantly when the blunt face of the ratchet interrupts the LSC, which results in the eruption of a larger number of thermal plumes. In another numerical study inside a cylindrical cell over a *Ra* range $10^6 \leq Ra \leq 10^8$, Emran & Shishkina [137] carried out a detailed investigation on the effect of roughness attributes on *Nu* and *Re*. They used concentric circular rings of varying geometric attributes. They reported that both the roughness height and cavity space decide the enhancement of heat flux, and both of them are related to the thermal boundary layer thickness. *Nu* was found to increase linearly with heated surface area. However, the rate at which *Nu* increases with roughness height (h) was found to depend on the width of the cavity. Interestingly, this dependence was found to sustain only up to a critical value. Beyond the critical width, $Nu(h)$ becomes independent of the width.

For understanding the morphological changes in large-scale rolls due to roughness, Tummers

& Steunebrink [62] considered the square-base roughness elements. They studied the effect of roughness on heat flux through LSC. They observed that roughness elements break the LSC, which can be attributed to the injection of thermal plumes directly into the bulk region. The breaking of LSC yields smaller rolls, enhancing the efficiency of evacuating the cavities. The enhanced emission of thermal plumes and efficient evacuation of cavities contribute to augmented heat flux. On the contrary, Foroozani *et al.* [138] observed a slight drop in heat flux for $Ra = 10^8$ in a cubical cell facilitated with pyramid roughness. They considered three roughness cases characterized by their heights: $0.00625H$, $0.0125H$, and $0.025H$. The drop in heat flux was attributed to the entrapped fluid inside the cavities. Owing to the tiny roughness elements, boundary layer perturbation was nearly absent at $Ra = 10^8$ in all three cases. Consequently, the entrapped fluid was observed inside the cavities, which resists convective heat transfer. They also reported that shorter roughness elements (hydrodynamically smooth case) do not alter the orientation of LSC, and it remains in the diagonal plane. However, for hydrodynamically rough cases, the orientation changes from the diagonal plane to the Cartesian plane.

Thus far, it has been observed that geometric attributes of roughness elements control the heat flux. For roughness-aided RBC, the common observations are that the spacing between the roughness elements and their heights, thermal plumes, thickness of boundary layer, and LSC play a crucial role in determining the enhanced heat flux. Therefore, the present work is mainly focussed in studying the effect of roughness on the coherent structures in roughness-aided convection. To the best of our knowledge, in all the previous $3D$ studies [60, 61, 138, 79], uniform (mono-scale) roughness geometries were used. For the first time in a $3D$ cubic cell, we consider multi-scale roughness configurations to investigate their effect on heat transport properties. In particular, the present work focuses on the statistics of coherent structures to study their relationship with enhanced heat flux for both multi-scale and mono-scale roughness arranged in irregular fashion. We use conical roughness elements of mono-scale (uniform case, U) and multi-scale (irregular case, R), as shown in Fig. 7.1. In uniform cases, the roughness height is fixed (10% of the cell height), whereas it varies in the range $5 - 10\%$ of the cell height in the irregular cases. Note that the roughness-aided convection is effective only when the roughness perturbs the boundary layer. For $Ra = 10^8$, the tiny roughness elements (whose height is much smaller than boundary layer thickness) remain buried inside the boundary layer and do not perturb it. On the other hand, boundary layer takes the shape of rough surface for taller configurations, which makes the flow characteristics similar to the smooth case. We have selected the range of roughness heights which can perturb the boundary layer. Further, we also study the asymmetric

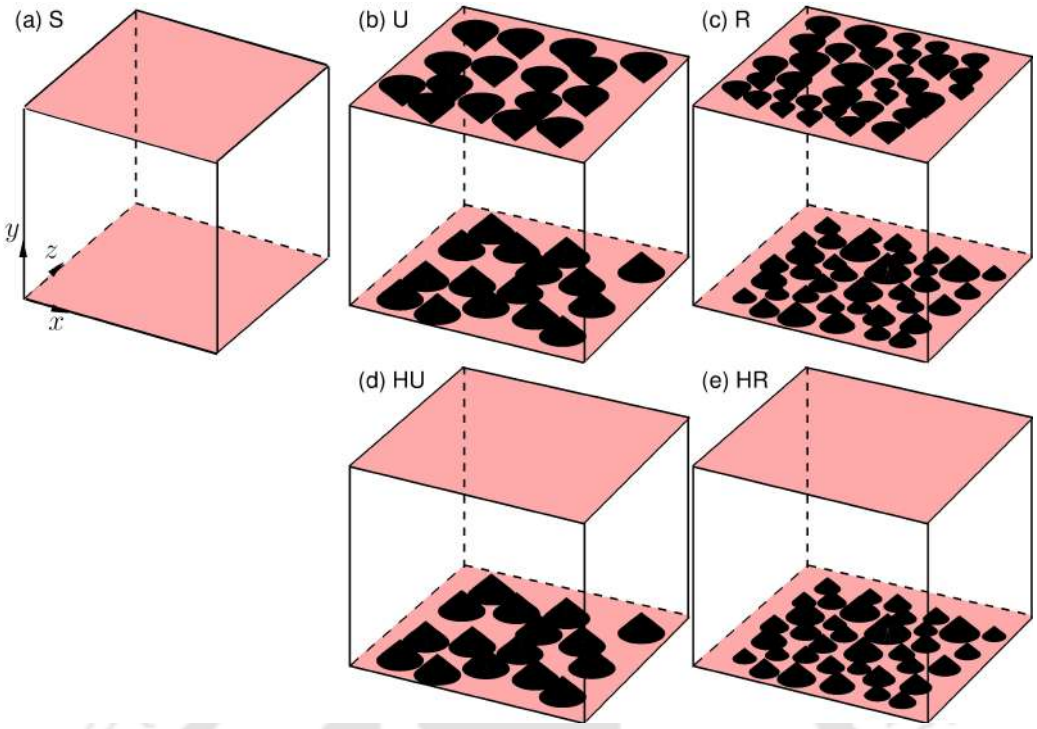

Figure 7.1: Schematic of the (a) smooth, (b) uniform, (c) irregular, (d) half-uniform, and (e) half-irregular cases.

variant of roughness-aided RBC, where the roughness elements are placed only on the bottom plate. These cases are termed as Half-uniform (HU) and Half-irregular (HR). The reason for considering these cases lies in the fact that LSC plays an important role in the interaction of the top and bottom boundary layers, at least for the present Pr case, and helps to comprehend the connection between the two layers. Thus, it would be interesting to investigate the properties of LSC and thermal plumes in the two asymmetric cases.

7.2 Numerical details

The conservation of mass, momentum and energy governs the flow inside a $3D$ Rayleigh-Bénard cell, as described in Sec. 2.1. The flow is simulated inside a cubic cell filled with air $(Pr = 0.7)$ at $Ra = 10^8$. The no-slip velocity boundary condition is used at all the surfaces. While the lateral walls are kept insulated, isothermal condition is used for the top $(\theta = 0)$ and bottom $(\theta = 1)$ walls. Moreover, no-slip velocity boundary and isothermal condition are implemented for all the roughness elements. The temperature of the elements placed on the top and bottom plates are $\theta = 0$ and 1, respectively. Since vertical height between the isothermal surfaces does not remain fixed in the roughness cases, we choose the idea of effective height (h_{eff}) of the cell

and effective *Ra* (Ra_{eff}), which are computed as:

$$h_{\text{eff}} = \frac{V}{Ar} \text{ and } Ra_{\text{eff}} = Ra\left(\frac{h_{\text{eff}}}{H}\right)^3 \tag{7.1}$$

where V is the volume occupied by fluid in the rough cell, and Ar is base area of the smooth isothermal plate. The effective height, actual volume of the cell, and effective *Ra* of all the cases are listed in Table 7.1.

In this study, we use two types of roughness configurations (conical elements), which are classified based on the variation of roughness heights: uniform (U) and irregular (R). In uniform cases, the roughness height remains fixed, i.e., 10% of the cell height $(H/10)$, whereas it varies in the range $50 - 100\%$ of the maximum roughness height $(H/10)$ for the irregular cases. As mentioned in Sec. 7.1, we further use two more cases in which the roughness elements of U and R are considered only on the bottom surface: half-uniform (HU) and half-irregular (HR). The incremental heat transfer area $(\Delta HTA_i = (HTA_i/HTA_S - 1)$ and the number of roughness elements are tabulated in Table 7.1. The increment of 40% (20%) in ΔHTA for U and R (HU and HR) cases yields sufficient roughness elements to perturb the boundary layer.

We have carried out the grid independence study for four progressively refined meshes $(M_i, i = 1, 2, 3, \text{ and } 4)$ as listed in Table 7.2. Note that we have used uniform mesh in the horizontal direction, whereas a non-uniform mesh in the vertical direction. To check the sensitivity of mesh resolution on the results, we have compared global *Nu* and variance of temperature (σ_θ) and observed a maximum deviation of 1.14%, and 5.30%, respectively. With a progressive increase in mesh size, the deviation diminishes to sufficiently small values. Thus, we select a grid size of $N_x \times N_y \times N_z = 300 \times 300 \times 300$ for all the cases. The mesh is refined close to the walls, which serves two purposes. First, the rough geometries are adequately resolved due to sufficient grid cells inside the roughness elements. Second, it satisfies the criterion of a minimum number of grid points required inside the thermal boundary layer [76], which is computed as $\lambda_\theta = H/(2Nu)$.

In the present work, we have selected $Ra = 10^8$ because roughness elements of height $= 0.1H$ are sufficiently tall to perturb the boundary layer whose thickness depends upon *Ra*. Figure 7.2 shows the triangulated uniform and irregular surfaces and their zero-level set representation. The exact representation of the rendered zero-level set function confirms the body resolution. The rendered volume of the object yields a maximum error of 0.085% and 0.4% for uniform and irregular cases, respectively. For all the statistical analysis, we have sampled the data up to 250 free-fall time units after the flow enters a statistical steady state. To show the statistical convergence, we have computed *Nu* in two subsequent equal intervals (Nu_I and Nu_{II}), listed in

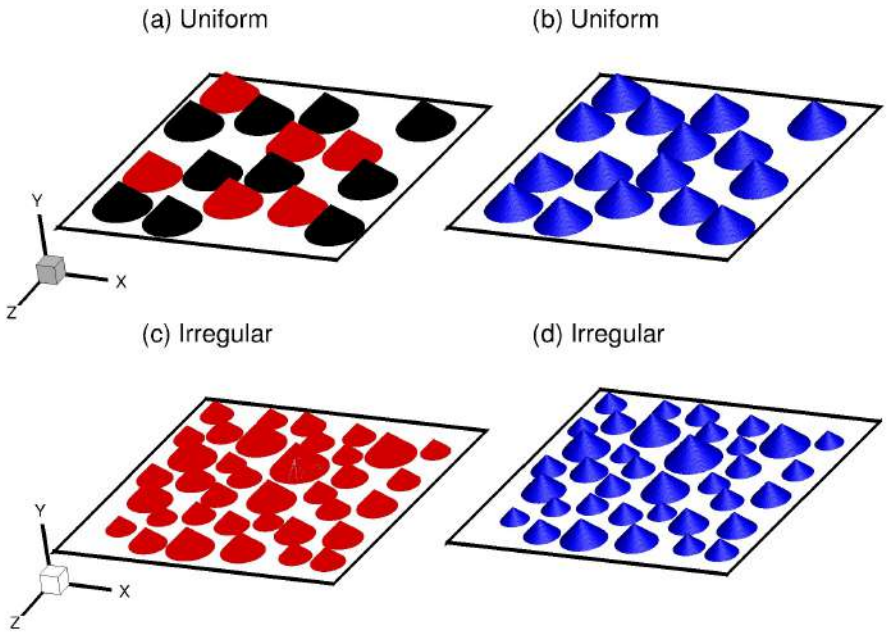

Figure 7.2: Representation of triangulated surface (a and c) and their zero-level set representation (b and d) for uniform (a and b) and irregular (c and d) cases. For better visualization, we show only the bottom surface.

Table 7.1: Geometric attributes (h_{eff}, Vol_{cell}, and number of roughness elements N) and control parameters (Ra_{eff} and ΔHTA) for the five cases.

S. No.	Parameters	Smooth	Uniform	Random	Half uniform	Half random
1	h_{eff}	1	0.966	0.977	0.983	0.989
2	Vol_{cell}	1	0.966	0.977	0.983	0.989
3	$\Delta HTA(\%)$	0	40	40	20	20
4	N	–	32	73	16	37
5	$Ra_{eff}(\times 10^8)$	1	1.10	1.07	1.05	1.035
6	Nu	31.27	46.45	47.71	37.93	38.27

Table 7.3. We further compute the relative difference between the two intervals as

$$Nu_r(\%) = 1 - \frac{Nu_I}{Nu_{II}}. \tag{7.2}$$

Nu_r remains less than 0.5% in the four cases, whereas it is maximum (1.73%) in the uniform case. These trivial differences clearly indicate that the sampling is statistically converged and does not dependent on the sampling length.

Table 7.2: Grid independence study showing the deviation in global *Nu* and variance of temperature (σ_θ) for four progressively refined meshes. The deviation is computed in the progressive sense, i.e., $\Delta Nu_i = (Nu_i - Nu_{i-1})/Nu_i$. Note that *Nu* and σ_θ are volume and time-averaged quantities.

M_i	$N_x \times N_y \times N_z$	*Nu* (ΔNu)	σ_θ ($\Delta\sigma_\theta$)
M_1	$240 \times 240 \times 240$	47.02(0.00)	3.23×10^{-3} (0.00)
M_2	$280 \times 280 \times 280$	47.18(0.33)	3.07×10^{-3} (5.30)
M_3	$300 \times 300 \times 300$	47.71(1.10)	3.16×10^{-3} (2.79)
M_4	$320 \times 320 \times 320$	47.17(1.14)	3.09×10^{-3} (2.27)

Table 7.3: Convergence of statistics for the data sampling of 250 time units computed in two subsequent equal intervals. Here Nu_I, and Nu_{II} represent *Nu* in the first, and second interval, respectively, while Nu_r shows the relative difference in Nu_I and Nu_{II}.

S. No.	Cases	Nu_I	Nu_{II}	$Nu_r(\%) = 1 - Nu_I/Nu_{II}$
1	S	31.35	31.20	0.48
2	U	46.70	45.89	1.73
3	R	47.28	47.14	0.30
4	HU	37.62	37.64	0.05
5	HR	38.07	37.95	0.32

7.3 Global heat transport properties

The two key response parameters in RBC are *Nu* and *Re*, which measure heat flux and flow intensity, respectively [18]. Heat flux increases in the presence of rough surfaces provided the roughness height perturbs the boundary layer [2]. However, the increase in *Nu* depends on the roughness geometry. The arrangement of roughness elements in the present work does not follow a fixed pattern. We first compare heat flux among the five cases in Fig. 7.3 (a). Compared to the smooth case, remarkably higher *Nu* is evident in all the rough cases. While comparing *Nu* between U and R cases, it is observed that both yield nearly the same heat flux. As expected, a similar observation in the comparison of heat flux is noted between HR and HU cases. At moderate *Ra*, thermal boundary layer remains relatively thicker ($\lambda_\theta \propto 1/Ra$), which buries the smaller roughness elements in R and HR cases. The smaller roughness elements buried inside the boundary layer do not contribute in the emission of thermal plumes. Therefore, the trivial

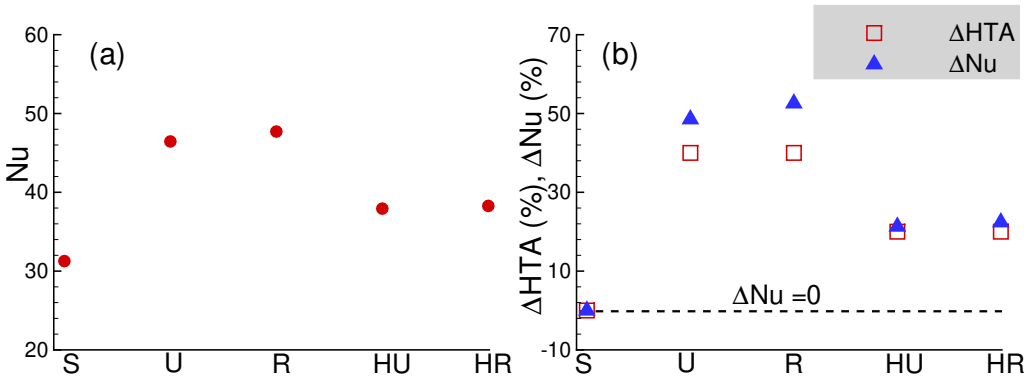

Figure 7.3: Comparison of (a) *Nu* and (b) incremental *Nu* represented by $\Delta Nu = (Nu - Nu_S)/Nu_S)$ among different configurations, where Nu_S is Nusselt number in the smooth case. The red square boxes represent the increment in heat transfer area $(\Delta HTA = (HTA - HTA_S)/HTA_S)$, which is 40% in U and R cases and 20% in HU and HR cases.

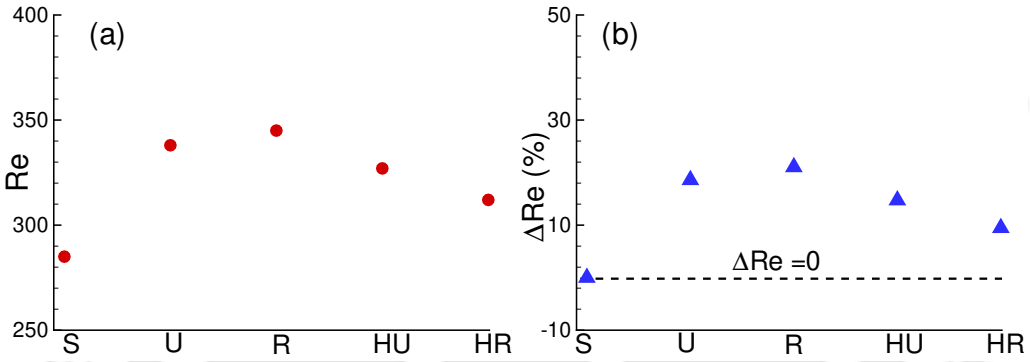

Figure 7.4: Comparison of (a) *Re* and (b) incremental *Re* represented by $\Delta Re = (Re - Re_S)/Re_S)$ among different configurations, where Re_S is Reynolds number in the smooth case.

difference between the uniform and irregular rough cases can be attributed to the nearly same number of active roughness peaks.

In Fig. 7.3(b), we show the increment in heat flux $(\Delta Nu = (Nu - Nu_S)/Nu_S)$ with respect to the increase in heat transfer area (ΔHTA), which is defined as

$$\Delta HTA = \frac{HTA - HTA_S}{HTA_S} \tag{7.3}$$

here S refers to the smooth case. In R and U cases, the conical roughness augments the HTA by 40%, whereas in their half-variants (HR and HU), the increment is barely 20%, see Table 7.4. However, the increment in heat flux (ΔNu) is observed as $48.54, 52.57, 21.30$, and 22.38% in U, R, HU, and HR, respectively. The inconsistency between the increase in ΔHTA and ΔNu suggests that enhancement is not simply because of increase in heat transfer area but due to

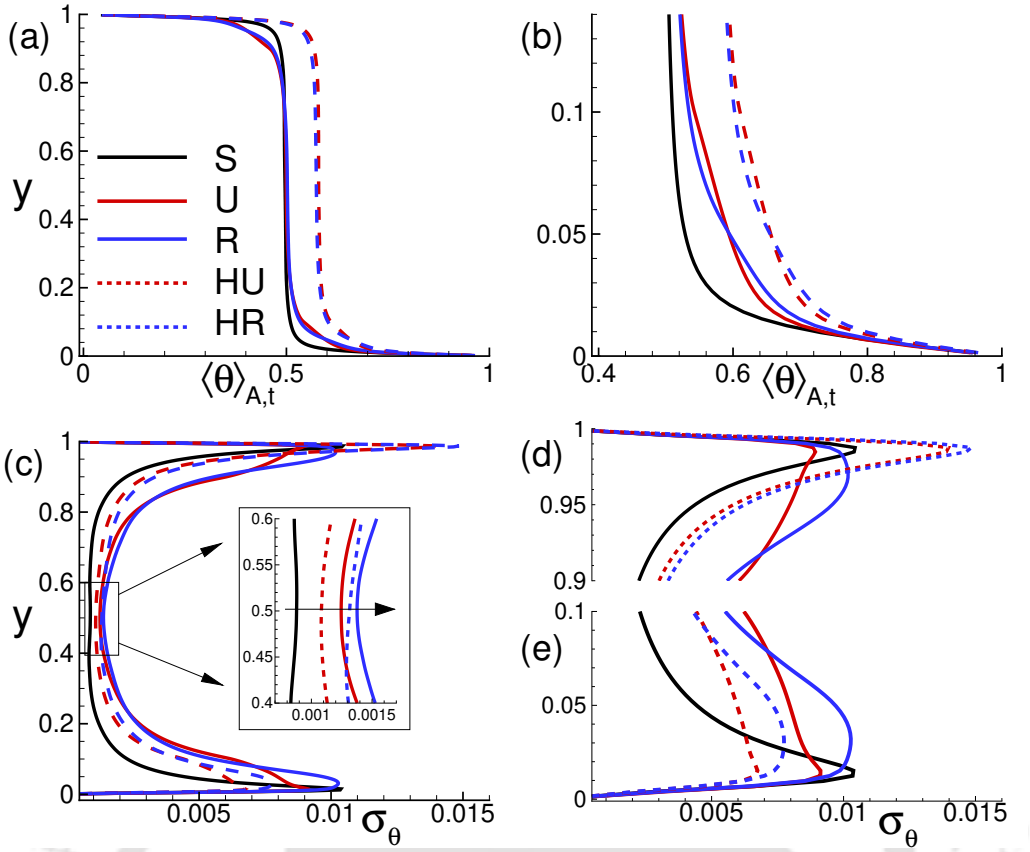

Figure 7.5: Vertical profiles of (a-b) mean $(\langle\theta\rangle_{A,t})$ and (c-e) variance of temperature (σ_θ). While (b) shows the blown-up view of mean temperature near the bottom wall, (d) and (e) show the same for σ_θ near the top and bottom walls, respectively.

frequent emission of plumes, which is discussed in detail in the next section.

Reynolds number *Re* is another heat transport property that measures flow intensity in RBC. Mathematically, it is defined as $Re = \sqrt{Ra/Pr}U_{rms}$, where $U_{rms} = \sqrt{\langle u^2 + v^2 + w^2\rangle_{V,t}}$. In the rough cases, plumes are emitted more frequently as compared to the smooth case [2]. Since the role of thermal plumes is to feed large-scale circulation, at least for lower *Pr*, it is expected that a larger quantity of plumes augments the strength of LSC or in other words flow intensity gets a boost in the rough cases. These observations are evident from Fig. 7.4a, wherein *Re* in all the rough cases is greater than the smooth case. In particular, *Re* increases by 18.60, 21.05, 14.74, and 9.47%, in U, R, HU, and HR cases, respectively, see frame b. Contrary to *Nu*, the effect of roughness on *Re* is relatively weaker.

To study the effect of roughness on temperature statistics, we observe the vertical profiles of mean and variance of temperature in Fig. 7.5. These vertical profiles characterize the entire domain into near-wall and bulk regions. Nearly straight profiles of the mean temperature in the

bulk region signify homogeneity. On the other hand, higher temperature gradients are associated with non-homogeneity in the near-wall regions. In the HU and HR cases, a horizontal shift is observed in the mean bulk temperature, which is due to asymmetricity of the surface roughness (top plate is smooth). This shift shows that the bulk region is flooded with more hot thermal plumes emitted from the localized roughness elements on the bottom plate. Nevertheless, the asymmetricity does not impact the homogeneity of the bulk region. Further, it is evident that the profiles in the near-wall region depend upon the roughness configuration, see frame b. Despite having the same bottom configuration, the profiles for the U and R cases do not match with the HU and HR cases, respectively. This inconsistency shows that the two opposite walls are linked with each other through the LSC which carries thermal plumes emitted from the bottom wall/surface to the top wall/surface. In HU and HR cases, hot thermal plumes are emitted immensely near the bottom rough surface compared to the top smooth surface, resulting in an imbalance between the hot and cold thermal plumes. LSC carries the hot plumes from the bottom surface to the bulk region. Since hot plumes are larger in number, they dissipate mainly in the bulk region and contribute to larger mean bulk temperature. On the other hand, in R and U cases, the hot and cold plumes carried by LSC are in balance and dissipate equally in the bulk region.

Variance is a measure of the intensity of fluctuation, and it is defined as

$$\sigma_\theta = \langle \theta'^2 \rangle_{A,t} \tag{7.4}$$

where the prime denotes the fluctuation, and $\langle \cdot\cdot \rangle_{A,t}$ shows the horizontal area-time averaging. The homogeneous character of the bulk region is also reflected in the temperature variance, see frame (c). The inset shows the blown-up view of the variance in the bulk region, which is higher for the rough cases as compared to the smooth one. It is evident that roughness alters the fluctuations in the bulk by emitting intense thermal plumes more frequently. Also, since HU and HR have higher $\langle \theta \rangle_{A,t}$, σ_θ is lesser as fluctuations are less. Further, we compare σ_θ profiles near the top and bottom walls in frames (d) and (e), respectively. While the S, U, and R cases show symmetric profiles, HR and HU reflect geometric asymmetry. Note the intensity of fluctuation in HU and HR cases near the top (bottom) wall, where it rises (drops) significantly as compared to other cases. This change can be attributed to the interaction of bulk and near-wall regions, which is different for the top and bottom surfaces. In the vicinity of the top (cold) surface, boundary layer flow remains at a higher temperature with respect to the surface, resulting in large thermal gradient which causes greater instability and an intense fluctuating region. On the other hand, in the vicinity of the bottom surface, relatively lower temperature difference between the boundary

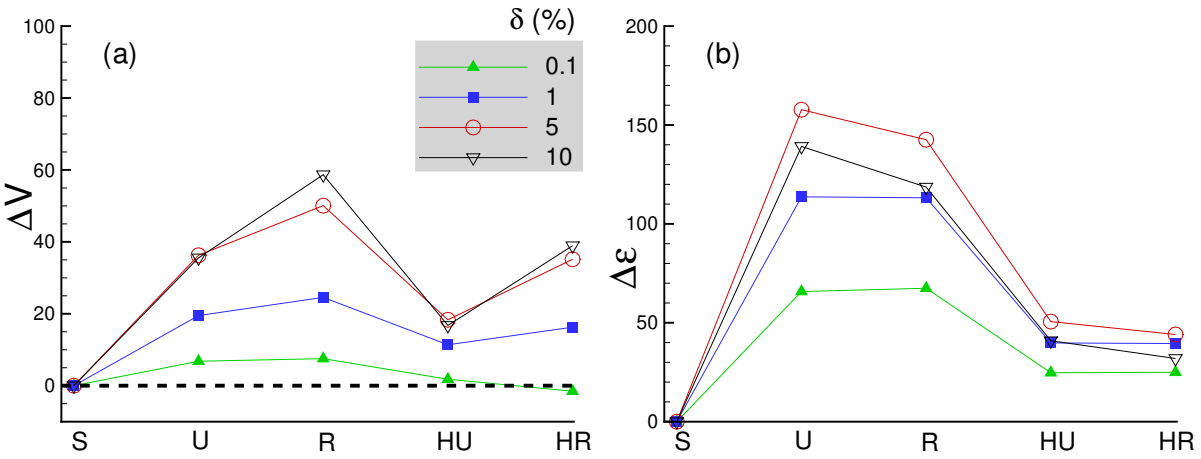

Figure 7.6: For the four different threshold values, increment in (a) volume fraction (ΔV) and (b) thermal dissipation $(\Delta\epsilon)$ of thermal plumes with respect to the smooth case.

layer flow and bottom surface is responsible for the significant drop in fluctuation intensity.

7.4 Statistics of thermal plumes

Thermal plumes are the coherent structures that carry heat from the bottom to the top plate and vice-versa. Emran & Schumacher [89] quantified thermal plumes and background region through a positive correlation between the fluctuation of vertical velocity and temperature. We have followed the same methodology to identify thermal plumes. Mathematically, the plume dominated region is identified using the following expression:

$$V = \{\mathbf{x} \in V : v'\theta'/(v'\theta')_{max} > c\} \tag{7.5}$$

where c and $(v'\theta')_{max}$ represent the threshold and global maximum values, respectively. In the present study, we have taken four threshold values: $0.1, 1, 5$, and 10%. Once the plume dominated regions are identified, their thermal dissipation rate is quantified as

$$\epsilon = \langle \epsilon_\theta \rangle_t = \frac{1}{V_{pl}} \Big\langle \int_{V_{pl}} \epsilon_\theta(\mathbf{x}, t) dV \Big\rangle_t \tag{7.6}$$

In the previous section, we have observed that increase in heat transfer area (ΔHTA) and heat flux (ΔNu) do not follow a linear relationship. In roughness-aided RBC, morphological changes of thermal plumes due to geometrical attributes of roughness elements enhance the heat flux [53, 79]. In this section, we ascertain the role of thermal plumes in enhanced heat flux by quantifying

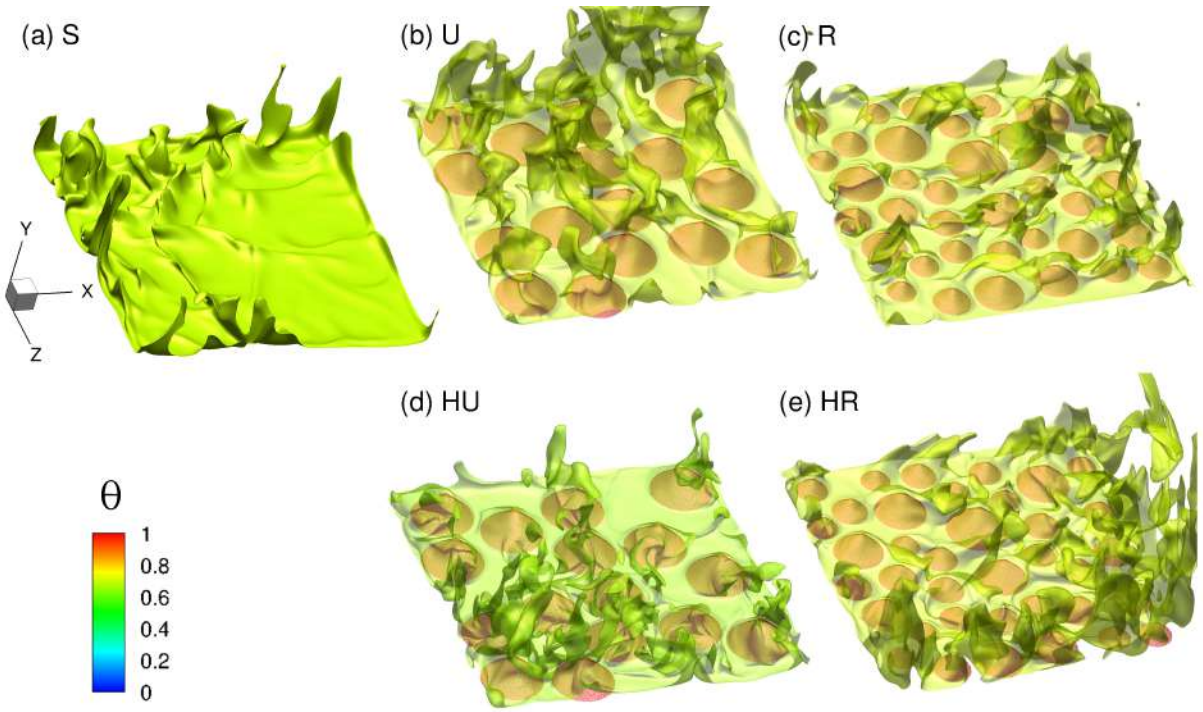

Figure 7.7: Temperature isosurfaces for $\theta = 0.7$ and 1 for the five cases showing the direction of movement of thermal plumes, which indicates the orientation of LSC.

the increment in volume fraction ($\Delta V = (V_{rough} - V_S)/V_S$) and thermal dissipation ($\Delta\epsilon = (\epsilon_{rough} - \epsilon_S)/\epsilon_S$), where V_S and ϵ_S represent quantities for the smooth case.

In Fig. 7.6a, volume fraction of the plumes increases significantly in the rough cases, which directly connects the heat flux enhancement with emission of thermal plumes. This can be understood from the comparison of plume emission mechanism between the rough and smooth cases. In the smooth case, thermal plumes erupt from the boundary layer due to thermal instability. On the other hand, roughness elements act as localized spots of plume emission and emit significantly more plumes, which will be discussed later in this section. Although, irregular case has more (nearly twice) roughness elements as compared to the uniform case, the difference in ΔV (see Fig. 7.6) between them is insignificant except for the $c = 10\%$ case. It can be attributed to the tiny peaks submerged in the boundary layer, which do not emit thermal plumes. We also note that the increase in ΔV remains consistent for all the threshold values.

Thermal dissipation is a measure of heat flux, and they are related as $Nu_{\epsilon_\theta} \propto |\nabla\theta|^2$ [128]. As expected, a significant rise in $\Delta\epsilon$ is observed for the rough cases in Fig. 7.6b. This trend is consistent with the variation of heat flux in Fig. 7.3. This coherence between Nu and ϵ_θ based on thermal plumes signifies their importance in enhancement of heat flux in roughness-aided RBC. Similar to the variation of volume fraction, difference in thermal dissipation rate is also

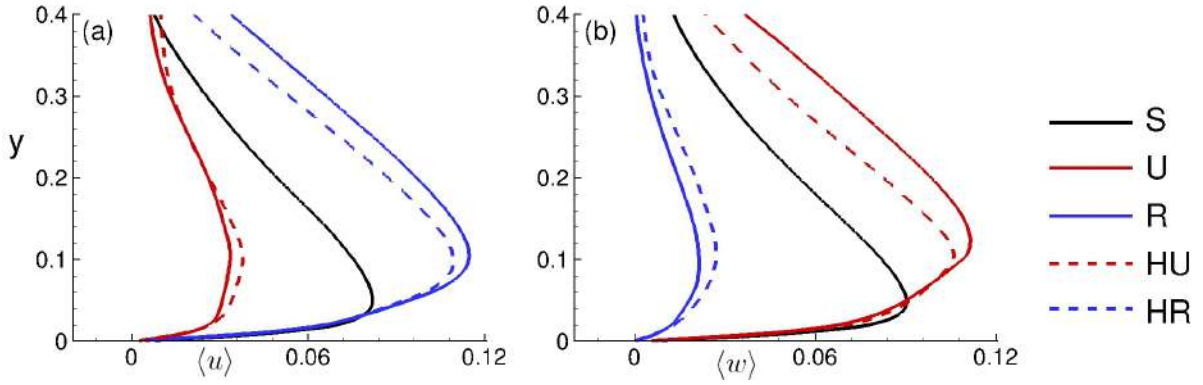

Figure 7.8: Vertical profiles of absolute horizontal area-averaged velocities: (a) $\langle u \rangle$ and (b) $\langle w \rangle$.

found insignificant in the irregular and uniform cases. For both HU and HR cases, dissipation rate drops significantly compared to U and R cases for all thresholds. This can be attributed to the reduced plume emitting peaks. To elucidate it, consider a configuration where both the top and bottom surfaces are rough. In such a case, the plumes emitted from their peaks not only enhance the volume fraction of plume in the bulk, but the plumes tend to destabilize the opposite boundary layer, which results in an even larger number of plumes. On the other hand, owing to a smooth top surface, such coupling of thermal plumes is absent in HU and HR cases, resulting in relatively lesser volume fraction and smaller thermal dissipation.

To further elucidate the significance of enhanced plume emission, we show the instantaneous temperature isosurfaces for the five cases in Fig. 7.7. In the smooth case, eruption of a few thermal plumes due to interaction of LSC and boundary layers along the diagonal plane is observed. On the other hand, a larger number of thermal plumes are clearly evident in the roughness cases. More the number of thermal plumes, greater is their volume fraction and dissipation rates, which enhance the heat flux. Note that the plumes emitted in the smooth case are driven by LSC, whereas, in the rough cases, they can directly enter the bulk region, which is responsible for enhanced heat flux.

7.5 Statistics of large-scale circulation

Large-scale circulation (LSC) is also known as mean wind, and it plays an important role in heat transfer by carrying thermal plumes [41]. In terms of the length scale, it is the largest coherent structure and spans the entire domain. Based on the LSC and nesting of thermal boundary layer inside the viscous one, Shraiman & Siggia [41] reported the $Nu(Ra)$ dependence as $Nu \approx 0.3Ra^{2/7}$, which shows its importance in heat transport theories. The dynamics of LSC unveils

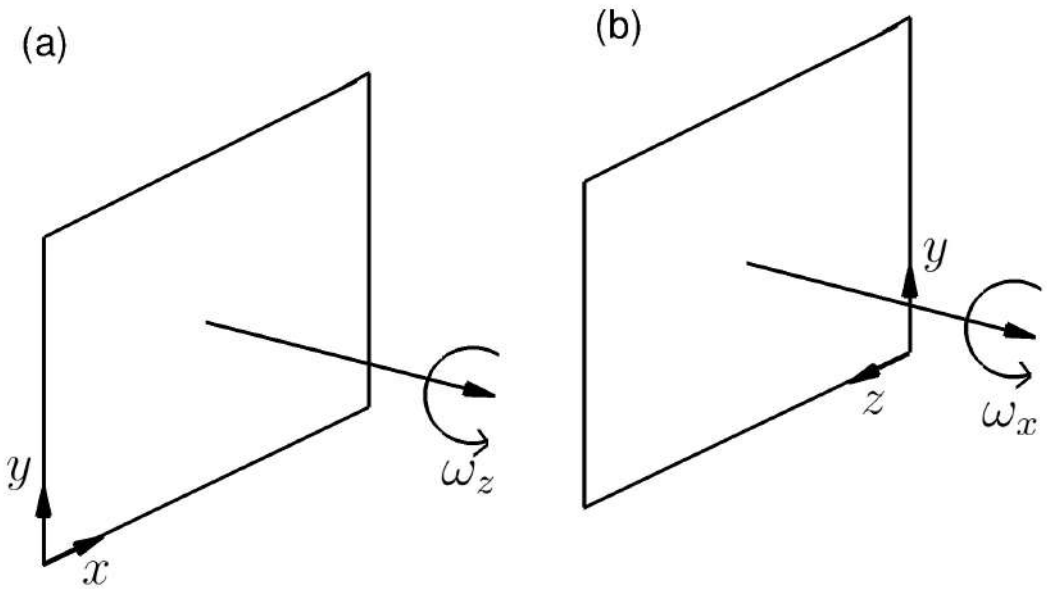

Figure 7.9: Schematic of angular velocities in (a) $x-y$ and (b) $y-z$ planes.

some interesting phenomena such as flow reversal, where the direction of LSC reverses [139, 140]. It was found that the flow reversal influences the heat flux [74]. Orientation of LSC depends upon the geometric configuration [140], and it also couples the top and bottom boundary layers [141]. Growth of corner rolls diminishes the LSC which results in reorientation of LSC, for more details, refer [142, 139]. Note that LSC is responsible for carrying thermal plumes, which plays an important role in heat transfer. In a cubic cell filled with a fluid of $Pr = 0.71$, Vishnu *et al.* [140] reported that LSC is locked in the diagonal plane, which has a connection with the heat flux. Owing to its significance, we explore the connection between LSC and heat transport properties in rough cases.

The present setup consists of rough asperities on the surfaces, which may influence the orientation of LSC. To understand this effect, we first observe the mean vertical profiles of horizontal velocities as ($\langle u \rangle$ and $\langle w \rangle$) close to the bottom surface, see Fig. 7.8. The velocities are computed as

$$\langle u \rangle = |\langle u \rangle_{A,t}| \tag{7.7}$$

$$\langle w \rangle = |\langle w \rangle_{A,t}| \tag{7.8}$$

where A, t represents the horizontal-area time averaging. In the smooth case, it is evident that both u and w have nearly equal strength. However, for the other configurations, horizontal motion appears to be biased towards either Cartesian directions. The flow dominates in the $z(x)$

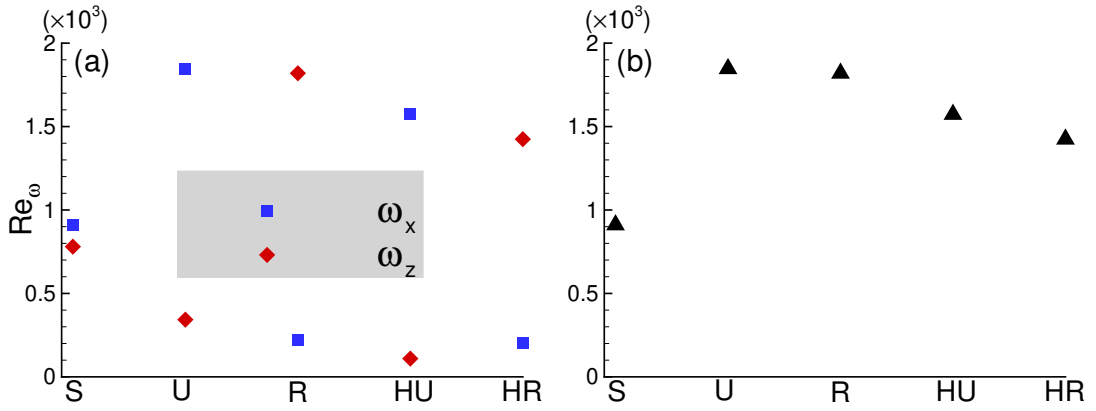

Figure 7.10: (a) Comparison of Reynolds number based on angular velocities (Re_{ω_x} and Re_{ω_z}) among the five cases. (b) The comparison of dominating Re_ω among the five cases.

direction for U and HU (R and HR) cases. This biasing shows the persistent abode of LSC in the horizontal planes as compared to the diagonal plane in the smooth case. The profile signifies that the flow strength increases as y increases from the bottom surface and attains a maximum before plummeting again. Inside the cavities, the protruding surfaces affect the maneuverability of the flow. The peak in the profiles represents the maximum flow intensity of LSC in that particular direction. Note that in all the rough cases, the peak is evident nearly at the maximum roughness height ($h = 0.1$), which shows the location of the maximum strength of LSC. On the other hand, the maximum is observed at $h \approx 0.05$ in the smooth case. Interestingly, the h is of the order of thermal boundary layer thickness ($\lambda_\theta = 0.016$). This consistency between h and λ_θ shows that maximum strength of LSC is observed slightly above the boundary layer. It also implies that LSC interacts with the boundary layer at its periphery, which is physically viable.

Vertical profiles of horizontal velocities have suggested that surface roughness alters the orientation of LSC. To ascertain the effect of roughness on LSC, we quantify the strength of LSC in the horizontal planes by defining Reynolds number based on angular velocity (Re_ω). As shown in Fig. 7.9, angular velocities (ω_x and ω_z) in a plane is defined at its center as

$$\omega_x = \frac{1}{2}\langle \frac{\partial w}{\partial y} - \frac{\partial v}{\partial z} \rangle_{A,t} \qquad \text{and} \qquad \omega_z = \frac{1}{2}\langle \frac{\partial v}{\partial x} - \frac{\partial u}{\partial y} \rangle_{A,t} \tag{7.9}$$

where $\langle \cdot\cdot \rangle_{A,t}$ represents area-time averaging. The Reynolds number ($Re = v^* h^*/\nu$) can be expressed in terms of non-dimensional length ($h = h^*/H_{ref}$) and velocity ($v = v^*/V_{ref}$) scales. Note that h^* and v^* represent the corresponding dimensional scales, while the term "ref" is used

for the reference scales. The expression for *Re* can be written as

$$\begin{aligned} Re &= \frac{v^* h^*}{\nu} \\ &= \frac{v V_{ref} h H_{ref}}{\nu} \\ &= vh\sqrt{\frac{g\beta\Delta T H_{ref}^3}{\nu\alpha}}\sqrt{\frac{\alpha}{\nu}} \\ &= \sqrt{\frac{Ra}{Pr}} vh. \end{aligned}$$

Now, since $h = 1$ in the present case, the expression for Reynolds number becomes

$$Re = \sqrt{\frac{Ra}{Pr}} v. \tag{7.10}$$

where v is a velocity scale and can be described differently depending upon the analysis. For instance, in Sec. 7.3, U_{rms} was used as the velocity scale to quantify the global flow strength. We further define Re_ω from $Re = v^* h^*/\nu$ and by using the following expressions

$$v^* = \omega^* \frac{H_{ref}}{2},\ \omega = \frac{\omega^*}{V_{ref}/H_{ref}} \text{ and } h = h^*/H_{ref}. \tag{7.11}$$

By substituting v^* and h^* in $Re = v^* h^*/\nu$, Re_ω can be written as

$$Re_\omega = \frac{\omega V_{ref} h H_{ref}}{2\nu} \tag{7.12}$$

Using the free-fall velocity scale ($V_{ref} = \sqrt{g\beta\Delta T H_{ref}}$), and $h = 1$, Re_ω can be written as

$$\begin{aligned} &= \frac{\omega}{2}\sqrt{\frac{g\beta\Delta T H_{ref}^3}{\nu\alpha}}\sqrt{\frac{\alpha}{\nu}} \\ &= \frac{\omega}{2}\sqrt{\frac{Ra}{Pr}}. \end{aligned}$$

Figure 7.10a shows comparison between Re_{ω_x} and Re_{ω_z} for the five cases. In the smooth case, Re_{ω_x} and Re_{ω_z} have nearly the same strength, which confirms that the LSC is oriented in the diagonal plane. For R and HR cases, Re_{ω_z} is significantly higher than Re_{ω_x}, showing that the LSC is oriented in the z plane. Similarly, in U and HU cases, Re_{ω_z} dominates to show the orientation of the LSC in the x plane. Note that Fig. 7.8 have already shown the orientation of LSC in diagonal and horizontal planes for smooth and rough cases, respectively. Thus, Re_ω quantitatively ascertains the reorientation of LSC. In Fig. 7.10b, we compare the dominating strength of the LSC among the five cases. Similar to the variation of global *Re* in Fig. 7.4, Re_ω follows the same trend, albeit with a larger strength. It can also be viewed from the instantaneous temperature isosurfaces shown in Fig. 7.7 (b and c), where the plumes are oriented in

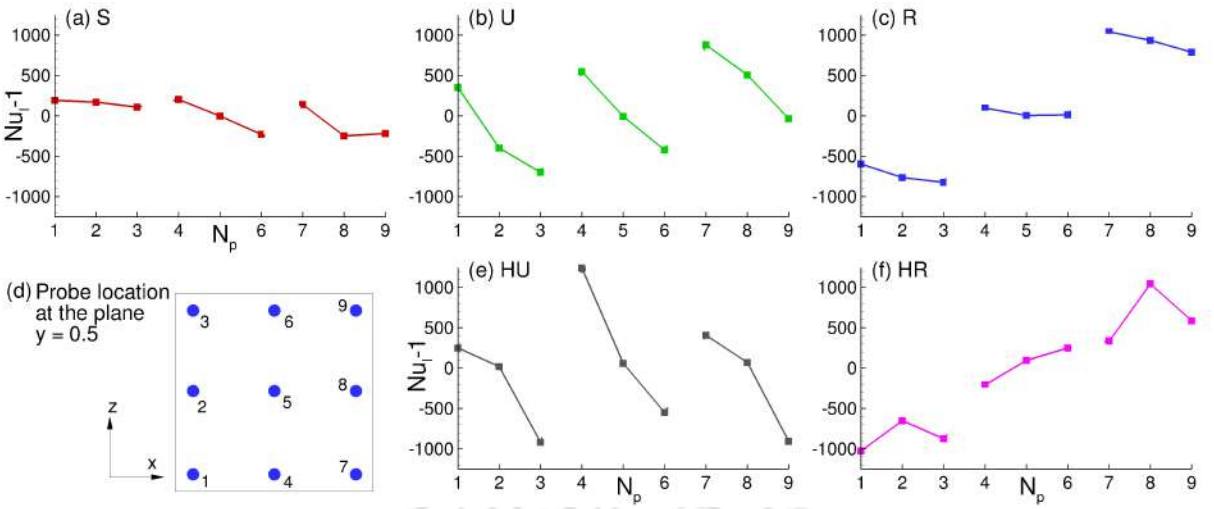

Figure 7.11: Spatial variation of local heat flux obtained from nine probes placed at the mid-height of the cell, shown in frame d. The points are joined with a solid line along the z direction.

the direction of dominating Re_ω, i.e., $y-z$ and $x-y$ planes for uniform and irregular cases, respectively.

Finally, we investigate the connection between LSC and local heat flux. It is well-established that LSC carries intense thermal plumes along its periphery. We have quantified local heat flux ($Nu_l = 1 + \sqrt{RaPr}\langle v\theta\rangle_t$) at 9 different probes placed in the mid-vertical ($y = 0.5$) plane as shown in Fig. 7.11. Note that negative (positive) heat flux shows the downward (upward) movement (v is negative) of thermal plumes. In Fig. 7.11 a, it is observed that the intensity of the local heat flux is significantly lower in the smooth case (see frame a) than in the rough cases (see frames b, c, e and f). It is attributed to the presence of rough surfaces, which emit intense thermal plumes. While the local heat flux varies from positive to negative in the z direction for U and HU cases, Nu_l changes its sign along the x direction in R and HR cases. Interestingly, these trends are consistent with the direction of LSC as observed in Figs. 7.8 and 7.10. Since Nu_l is directly connected with thermal plumes (refer chapter 7.4), higher Nu_l suggests intense thermal plumes in the rough surfaces. Also, the greater intensity of Nu_l observed along the periphery suggests that LSC carries the plumes from the rough surface to the bulk region. Finally, we suggest that intense thermal plumes would result in stronger LSC because it carries the plumes.

7.6 Flow statistics in the bulk region

Based on the nature of fluctuations in RBC, there are primarily two regions, namely, bulk and boundary layer [30, 31]. While meandering along the periphery of LSC, thermal plumes dis-

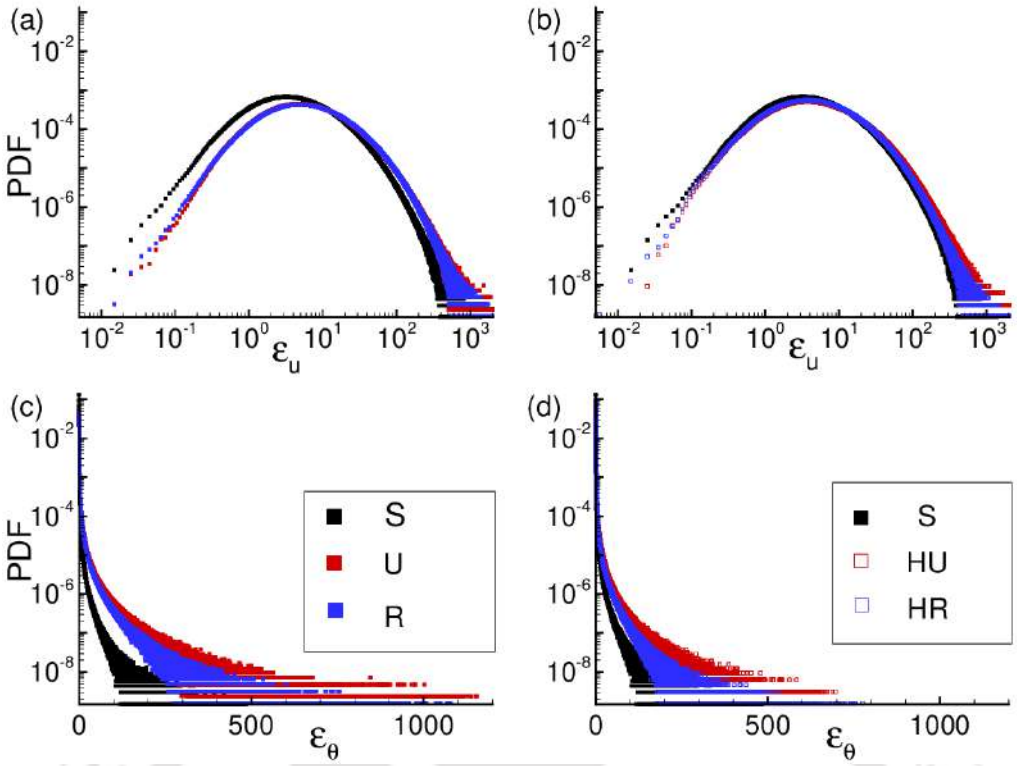

Figure 7.12: PDF of viscous (a-b) and thermal (c-d) dissipation rates showing the nature of fluctuations in the bulk region.

sipate their energy due to which their presence becomes a rare event in the bulk, resulting in the homogeneous temperature statistics. However, the characteristics of the bulk alter in the presence of rough elements due to enhanced emission of thermal plumes as observed in the previous sections. In this section, we investigate the effect of roughness elements on the small-scale statistics in the bulk region, which is defined by excluding the near-wall regions of width $H/4$ from all sides. The resulting computational domain for the bulk region is restricted to a region of dimension $(H/2, H/2, H/2)$ about the geometric center. For this region, we first compare the spatial PDF of thermal and kinetic energy dissipation followed by a second-order longitudinal structure function of vertical velocity and temperature. Finally, by validating Taylor's frozen hypothesis for temperature, we show the existence of $BO59$ scaling and investigate the power spectra of temperature fluctuations. The temperature time series data is obtained by placing a probe at the geometric center of the cell.

Figure 7.12 shows PDF of viscous ($\epsilon_u = \sqrt{Pr/Ra}|\nabla \overline{u}|^2$) and thermal ($\epsilon_\theta = |\nabla\theta|^2/\sqrt{RaPr}$) dissipation rates. In all the cases, PDF of ϵ_u exhibits a normal (Gaussian) distribution, wherein there are two regions of importance: the peak and tail. While the peak signifies the mean value, the tail typifies the extreme events. In RBC, tail of PDF of the dissipation rates becomes thicker,

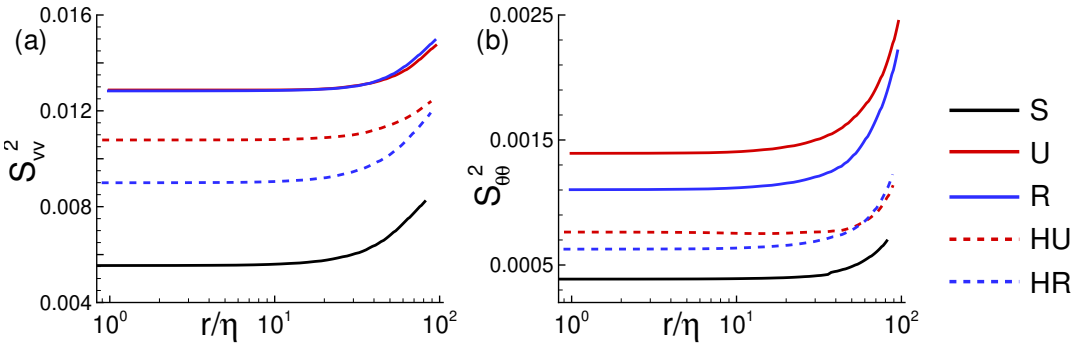

Figure 7.13: Comparison of second order (a) longitudinal velocity (S^2_{vv}) and (b) temperature $(S^2_{\theta\theta})$ structure functions. Note that structure functions are computed in the bulk region.

which shows the intermittency of the extreme and rare events. In frame a, the mean of the distribution shifts to a greater value for U and R cases. The augmented mean ascertains the longevity of plumes emitted from the roughness elements, which sustains in the bulk region and yields greater dissipation. The extreme right tails become thicker in U and R cases, which shows the growing intermittency of intense thermal plumes due to changes in plume morphology. Compared to the U and R cases, the PDFs in HU and HR cases nearly collapse on that of the smooth case, suggesting that asymmetry yields a frivolous effect on the PDF of ϵ_u in the bulk region.

Figure 7.12(c-d) shows PDF of thermal dissipation. Contrary to the viscous dissipation, the distribution follows an exponential tail in all the cases, which is consistent with the previous studies for smooth case [47, 90]. Interestingly, the tail plummets more rapidly in the smooth case, whereas it drops relatively slower in U and R cases. In the HU and HR cases, unlike the U and R cases, the distribution deviates weakly from the smooth case, which is consistent with the PDF of ϵ_u. The deviation shows that intense thermal plumes emitted from the rough surfaces thrive in the bulk region, which in the smooth case dissipate near the walls. Note that the tail becomes thicker for all the rough cases. The bulk region becomes more chaotic with greater thermal gradients in rough cases. The thinner tail in the smooth case signifies a relatively more homogeneous bulk region than that in the rough cases, as seen in Fig. 7.5(c). This study shows that introducing rough surfaces on both the top and bottom walls influences the bulk region by emitting intense thermal plumes that dissipate in the bulk region. However, in the HU and HR cases, the dissipation rates are found to exhibit the characteristics of the smooth case.

Next, we study the second order vertical velocity (S^2_{vv}) and temperature $(S^2_{\theta\theta})$ structure func-

Table 7.4: The ratio of mean ($\langle\theta\rangle$) and variance (σ_θ) of temperature to show the applicability of the ergodicity theorem ($\sigma_\theta/\langle\theta\rangle \ll 1$).

Cases	$\langle\theta\rangle$	σ_θ	$\sigma_\theta/\langle\theta\rangle$
Smooth	0.4956	0.0126	0.0253
Uniform	0.4965	0.0168	0.0338
Random	0.5026	0.0174	0.0345
Half-uniform	0.5797	0.0162	0.0279
Half-random	0.5796	0.0179	0.0309

tions in the bulk region. Mathematically, they are computed as

$$S^2_{vv}(r) = \langle[v(y+r) - v(y)]^2\rangle_{y,t} \tag{7.13}$$

$$S^2_{\theta\theta}(r) = \langle[\theta(y+r) - \theta(y)]^2\rangle_{y,t} \tag{7.14}$$

where r represents the separation distance in y direction [143, 144]. In flows where temperature acts as a passive scalar, energy transfer from large to the small scales can be quantified by a balance between the energy at the large scale and viscous dissipation. On the other hand, in RBC, where temperature is an active scalar, the energy at the large scale is balanced by buoyancy production. Contrary to the former, in RBC, the temperature scale becomes relevant in the inertial subrange, which is represented by Bolgiano length scale [145]. In isothermal flows, Kolmogorov's scaling ($K41$) prevails in the inertial subrange, whereas, in RBC, both $K41$ and Bolgiano scaling ($BO59$) exist [145]. Based on these theories, for a p^{th} order structure function, $S^p_{vv}(r) \sim r^{p/3}$ according to the $K41$ theory, whereas $BO59$ states $S^p_{vv}(r) \sim r^{3p/5}$ [143, 146, 147]. Note that the second-order structure function typifies the cumulative energy [148]. Since roughness elements influence the statistics of bulk region, it would be interesting to study their impact on small-scale statistics.

Figure 7.13 shows a comparison of S^2_{vv} and $S^2_{\theta\theta}$ among the five cases. As compared to the smooth case, energy in all the rough cases is significantly higher. For smaller length scales ($\sim \eta$), it is evident that the variation of structure function with r/η remains unaltered, whereas, it surges for $r/\eta > 20 - 30$. This observation is common in all the cases, irrespective of the presence (or absence) of roughness. However, it is interesting that S^2_{vv} overlaps for U and R cases for the smaller separation distance. As r increases, it appears that the two profiles start separating from each other, which indicates the differences in their kinetic energy influenced by altered plume morphology due to rough surfaces. Similar to $S^2_{vv}(r/\eta)$, $S^2_{\theta\theta}(r/\eta)$ remains unaltered for smaller length scales ($\sim \eta$). However, thermal energy in U is greater than that in R, which remains

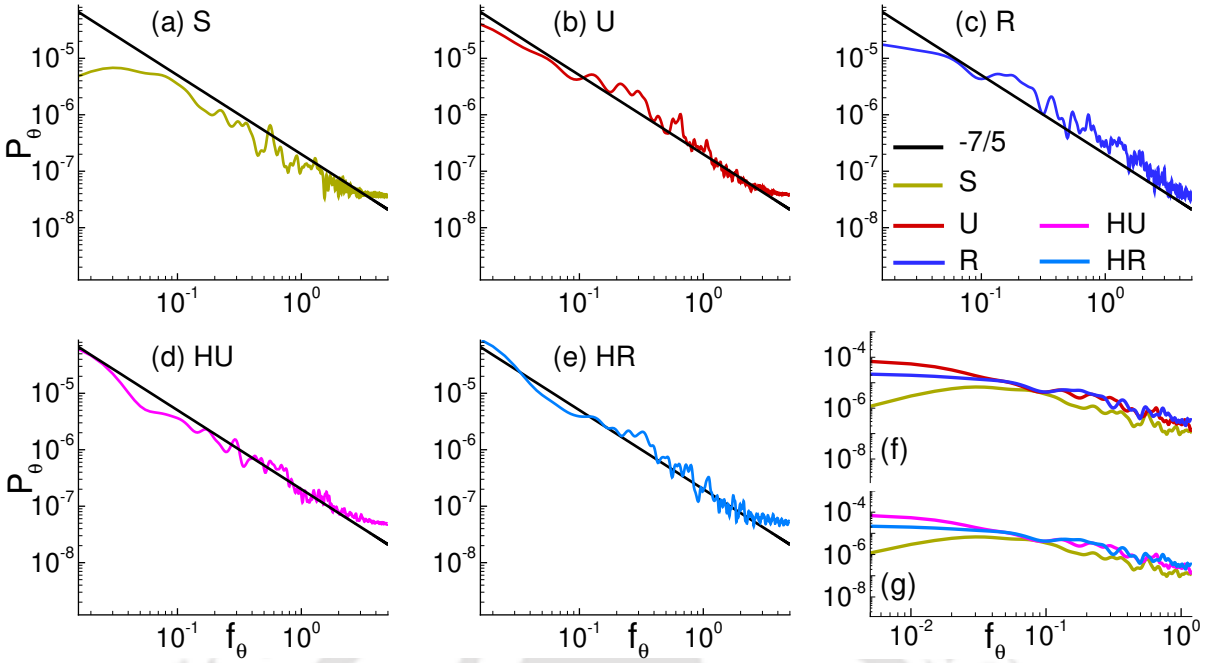

Figure 7.14: Power spectra of temperature P_θ computed at the geometric center of the cell in (a) smooth, (b) uniform, (c) irregular, (d) half-uniform, (e) half-irregular cases. Frame f (g) shows the comparison of U and R (HU and HR) cases with the smooth case, respectively. Note that black line shows the Bolgiano scaling $P_\theta \sim f_\theta^{-7/5}$.

consistent for their respective asymmetric cases. Compared to the R (HR) case, higher energy in U (HU) shows that plumes emitted in the latter are more intense in the bulk region. It may be attributed to the long-lived plumes emitted from the taller peaks $h/H = 0.1$ in the uniform cases.

Finally, we study the temporal statistics of temperature by using time series data obtained from a probe placed at the geometric center to investigate temporal statistics of temperature. We first validate the ergodicity theorem by showing that the measure of fluctuation is negligible as compared to its mean value [149]. Ergodicity theorem or Taylor's frozen hypothesis states that spatial correlation can be approximated by temporal correlations [144]. It is used to understand the spatial characteristics of the flow without resorting to the spatial correlation, as it is not feasible to compute the correlation for every separation distance. This theorem is applicable when the ratio of variance and mean of the quantity is very small. Table 7.12 shows the mean $(\langle\theta\rangle)$, variance (σ_θ), and their ratio $(\sigma_\theta/\langle\theta\rangle)$, which is remarkably less than unity. For temperature at the cell center, $\sigma_\theta/\langle\theta\rangle \ll 1$ shows the homogeneous character of flow in all the cases and validates the applicability of Taylor's frozen hypothesis or ergodicity theorem. We show the temperature power spectra from the temporal data to study the cascade of temperature fluctua-

tions in the bulk region. The main objective of studying the power spectra is to understand the effect of roughness on temperature fluctuation in the bulk region.

Figure 7.14 shows the energy content at different scales. For the inertial subrange ($\eta \ll l \ll H$), Bolgiano-Obukhov ($BO59$) scaling ($P_\theta \propto f_\theta^{-7/5}$) is evident, as shown by black lines in frames (a-e). It appears that roughness does not impact the scaling law, at least the energy decay in the inertial subrange. Further, in frames (f-g), we show the comparison of power spectra. Note that greater energy is evident across all the length scales in all the rough cases compared to the smooth case. This greater energy reflects the stronger temperature fluctuations, which can be attributed to the frequent emission of thermal plumes due to active surface roughness. These results show that roughness influences the temperature fluctuations and augment thermal energy across all the length scales.

7.7 Conclusions

In this chapter, we have investigated the significance of coherent structures in augmented heat flux due to conical surface roughness. We have considered cubical geometries, filled with air, for the investigations at $Ra = 10^8$. In the present work, two types of roughness setups have been used: irregular (R) and uniform (U). While roughness height remains fixed ($h = H/10$) in uniform set-up, it varies from $50 - 100\%$ of the maximum roughness height ($h = H/10$) in the irregular case. In addition, we have also considered their half-variants where only the bottom surface is kept rough while the top one remains smooth, i.e., half-irregular (HR) and half-uniform (HU).

It has been observed that heat flux increases by $48.54, 52.57, 21.30,$ and 22.38% in U, R, HU, and HR cases, respectively. The nearly same heat flux in U (HU) and R (HR) cases has been attributed to the nearly same number of boundary layer penetrating roughness peaks. The same number of effective roughness peaks occurs due to the relatively thicker boundary layer, under which tiny roughness elements in irregular case remain buried. On the other hand, *Re* is found to increase by $18.60, 21.05, 14.74,$ and 9.47%, in the same order, which shows roughness also impacts the flow strength but only weakly. In HU and HR cases, we have reported higher temperature of the bulk region due to the skewness in emission of hot thermal plumes from the bottom (hot) rough surface. This skewness yields significantly higher intensity of fluctuation in HU and HR cases near the top wall because of the strong interaction between bulk ($\theta > 0.5$) and top surface ($\theta = 0$). Further, we have quantified thermal plumes from positive correlation

between the fluctuation of vertical velocity and temperature. The higher fraction of thermal plumes and greater thermal dissipation in the rough cases ascertain that the frequent emission of thermal plumes, due to surface roughness, is responsible for augmented heat flux.

From the perspective of large-scale circulation, it has been observed that surface roughness alters the orientation of LSC. Mean vertical profiles of horizontal velocities have revealed that LSC reorients along the Cartesian plane. While the LSC remains in the diagonal plane in the smooth case, it shows a biasing towards a particular horizontal direction in rough cases. These results are further confirmed by Reynolds number based on angular velocity, which shows greater intensity along the plane of LSC. Also, local heat flux, in the bulk region, is found significantly higher in the plane of LSC, which shows its role in carrying thermal plumes from rough surfaces to the bulk. On the other hand, intensity of local heat flux is found very low in the smooth case.

Spatial PDF of thermal and viscous dissipation rates in the bulk region have revealed that while the former follows an exponential distribution, the latter follows a normal distribution. A shift in the peak and thicker tail of the distributions in the rough cases are found due to altered plume morphology. Second order vertical velocity structure function reveals that flow structures in the rough cases have more turbulent kinetic energy than the smooth case. Interestingly, it is found that the energy of the smaller structures (Kolmogorov scale $(l \lesssim \eta)$) remains the same. However, the energy surges in the inertial range, where $l \gg \eta$. Thermal energy in U (HU) is found greater than in the R (HR) case, which indicates the higher intensity and longevity of thermal plumes emitted in the uniform cases. The validation of the ergodicity theorem for temperature further reveals the existence of $BO59$ scaling $(P_\theta \propto f_\theta^{-7/5})$ in the bulk. The comparison of power spectra has revealed that roughness influences the small-scale statistics by augmenting the energy of flow structures and not by influencing the power-law.

CHAPTER 8

Conclusions and future scope

In this thesis, by using numerical simulations, we have investigated the augmented heat flux in non-standard variants of Rayleigh-Bénard convection in both $2D$ and $3D$ cells. We have used two well-known variants, namely, roughness-aided RBC and tilted RBC. While triangular surface roughness is used in $2D$ RBC, conical roughness elements are used in its $3D$ counterpart. Here, we first summarize each chapter and then provide a brief discussion on the future scope of non-standard variants of RBC.

8.1 Conclusions

In the present work, we have focused on unveiling the heat transport mechanism in the non-standard variants of RBC, which are responsible for augmented heat flux. The two well-known non-standard variants, i.e., roughness-aided RBC and tilted convection, are employed to obtain the higher heat flux. Moreover, their combined effect on global heat transport properties is also investigated. While triangular roughness elements are employed in 2D RBC, conical elements (distributed irregularly) are chosen for their 3D counterpart. Rectangular $(\Gamma = 2)$ and cubical $(\Gamma = 1)$ convection cells are used for $2D$ and $3D$ cases, respectively. While air $(Pr = 0.7)$ is considered as working fluid, a wide *Ra* range (varying from 10^6 to 10^{10}) is explored. The majority of the previous studies dealt only with a limited number of roughness scales (mono-scale [53, 1, 61] and triple-scale [2]), where the scales refer to the geometric attribute of the roughness elements [53, 1, 138]. In the present work, we have incorporated a wide range of

roughness scales, which make the present set-up an improved version of the multi-scale roughness configuration. In addition to the roughness-aided convection, we have disentangled one of the unresolved issues, i.e., dependence of the $Nu - \phi$ trend on Ra in inclined RBC. For the first time, we have reported the combined effect of roughness and tilt on heat flux and flow intensity. In the following, main findings of the current work are highlighted.

We have first investigated the statistics of coherent structures in standard RBC and observed a thermal jet phenomenon, wherein thermal plumes entrapped between the rolls spur out with intense heat. Thermal plumes are responsible for carrying heat, quantified by Nusselt number (Nu) across the two isothermal walls. It is observed that $Nu \sim Ra^{0.285}$, which agrees strongly with 3D data and suggests that the mechanism of formation of plume in $2D$ and $3D$ does not impact the global quantities. It has been found that buoyancy production balances dissipation in the bulk region, whereas transport and dissipation balance each other in the boundary layers. Based on the threshold criterion [89], thermal plumes are characterized by a positive correlation between the fluctuations of vertical velocity and temperature. For any threshold, volume share of plumes drops with increasing Ra, which is compensated by a rise in the background's share. While smaller threshold produces uncertain data that reflects a nearly similar contribution in dissipation, the background share of dissipation far exceeds that of the plume only at larger thresholds. Both these regions asymptotically produce same dissipation at higher Ra. It has also been found that the coherent movement of thermal plumes forms convection rolls, which carry the plumes from the boundary layer to the bulk. The interaction between boundary layer and the convection rolls determines the structure of the boundary layers, whose thickness (λ) is computed using the slope and 99% methods. Further, it has been observed that boundary layer thickness and Ra follows a power-law scaling, $\lambda_\theta = 2.93Ra^{-0.27}$, which agrees well with the theoretical estimate.

For three roughness setups (R_1, R_2 and R_3) marked by their maximum roughness height in the increasing order, we have identified the onset of enhanced heat flux regimes. The onset is in terms of critical Rayleigh number (Ra_c), beyond which heat flux surges as compared to the smooth case. Such onset is also reflected in the transformation of PDF of temperature fluctuation from a double to a single peak in the bulk region. Interestingly, Ra_c decreases as the roughness configuration becomes taller. In the enhanced heat flux regime, near-wall and global estimates of thermal dissipation rates become invariant of thermal forcing. It is observed that in R_2 and R_3 configurations, the double-roll state transforms into a multiple roll state. These rolls have a greater tendency to evacuate the entrapped fluid in the valley regions, which is responsible for

enhanced heat flux. These observations are ascertained by greater buoyancy production near the taller roughness heights.

Further, we explore the significance of near-wall dynamics in enhanced heat flux. We have quantified the thermal boundary layer penetrating peaks (N_p) and observed that for $N_p \leq 50\%$ (peaks are submerged inside the boundary layer), heat flux drops, whereas for $\%50 \leq N_p \leq 65\%$, heat flux remains unaffected. For $N_p \geq 65\%$, a sudden rise in *Nu* is observed. In addition, $69.08\%, 84.51\%$, and 83.33% of the peaks are required to penetrate the boundary layer to obtain the enhanced heat flux regime for R_1, R_2, and R_3, respectively. A detailed investigation of the throat and peak revealed that the latter has a higher tendency to emit thermal plumes. The strong secondary vortices in the two taller roughness cases are found responsible for enhanced heat flux. In the two taller cases, we have observed a cascade of secondary vortices inside the throat region, which is absent in the R_1 case. Thinning of thermal boundary layer in the throat region confirms the cascade effect and evacuation of the throat. In addition, it has been observed that the mean vertical temperature profiles show evidence of multi-layer flow characteristics. While the weakly non-linear profile closest to the wall represents the conduction of heat, a greater resemblance of intermediate layer to the bulk results in heat transfer enhancement.

To understand the effect of inclination on heat transport properties, we have chosen five inclination angles ($\phi = 0^\circ, 15^\circ, 45^\circ, 75^\circ$, and 90°). In the smooth case, it is observed that inclined convection is effective only below $Ra \leq 10^8$, where $Nu - \phi$ follows a unimodal behavior with a peak at $\phi = 75^\circ$. On the other hand, monotonically decreasing trend is observed for $Ra > 10^8$ and RBC turns out to be the most efficient heat transport system. We identify $Ra = 10^8$ as the critical *Ra* in the present study. Further, in the roughness cases, we have observed that the critical *Ra* drops with increasing roughness height. It has been found that heat flux increases by $18\%, 24\%$, and 25% in R_1, R_2, and R_3 cases, respectively. It is unveiled that roughness elements onset the turbulence at lower *Ra* because of which effectiveness of the roughness-aided tilted convection is restricted to relatively lower *Ra* range.

Finally, we have investigated the effect of four different conical roughness setups on heat flux through coherent structures at $Ra = 10^8$. Heat flux increases by $48.54, 52.57, 21.30$, and 22.38% in U, R, HU, and HR cases, respectively. The nearly same heat flux in U (HU) and R (HR) cases is attributed to the nearly same number of boundary layer penetrating roughness peaks at moderate $Ra = 10^8$. On the other hand, in the same order, *Re* is found to increase by $18.60, 21.05, 14.74$, and 9.47%, which shows roughness impacts the flow strength weakly. We further quantify thermal plumes and found their higher fraction in the rough cases, which ascer-

tains that the intense thermal plumes are responsible for higher heat flux. In HU and HR cases, temperature of the bulk region increases owing to the non-uniformity in emission of thermal plumes (more hot plumes) due to roughness elements placed only at the hot (bottom) surface. A significantly higher intensity of fluctuation is observed in HU and HR cases because of the strong interaction between the bulk ($\theta > 0.5$) and top surface ($\theta = 0$). Finally, we explore the effect of roughness on the bulk statistics through second-order structure functions and power spectra. The second-order vertical velocity structure function reveals that rough cases have more turbulent kinetic energy than the smooth case. Thermal energy in U (HU) is found to be greater than in the R (HR) case, indicating the higher intensity and longer life of thermal plumes emitted in the uniform cases. The comparison of power spectra shows that roughness influences the small-scale statistics by augmenting the energy contained in all the length scales and not by impacting the energy decay law.

8.2 Future scope

Non-standard variants of RBC, particularly the roughness cases, have revealed interesting heat transfer phenomena. However, the variants are not limited to alteration in the topology of isothermal walls but could go beyond it. One such example is the introduction of magnetic field in RBC, as it plays an essential role inside the earth, which is already being explored [150]. Therefore, we list down some of the ideas that can be explored in the future as follows:

1. Vibration-induced instability: in this case, the isothermal surfaces are provided with a controlled vibration to disturb the boundary layers. In the classical regime, boundary layer remains laminar, whereas it becomes turbulent in the ultimate regime. One possibility to perturb the boundary layer is to introduce surface roughness, which has already been explored in chapters 4-7. Another possibility is to vibrate the isothermal surfaces upon which the boundary layer is attached. This would result in boundary layer transition from a laminar flow state to a turbulent one, which can result in a surge in *Nu*. One such study has been reported in the literature but did not get much attention [151].

2. Combined effect of roughness and vibration-induced instability: in chapter 4, we have shown that the roughness aided RBC results in a drop in heat flux as compared to the smooth case at lower *Ra*. The entrapment of fluid in the cavity region due to a weak thermal forcing was attributed to the reduced *Nu*. However, suppose the same convection cell is facilitated with vibration. In that case, the entrapped fluid could tend to come out of

the cavities, and the roughness aided RBC can become useful in enhancing the heat flux even at the smaller *Ra*. Thus, combining the roughness and vibration on the isothermal surfaces can have a brighter prospects for obtaining higher heat flux at lower *Ra*.

References

[1] Zhu X., Mathai V., Stevens R. J. A. M., Verzicco R., & Lohse D. Transition to the ultimate regime in two-dimensional Rayleigh-Bénard convection. *Phys. Rev. Lett.*, **120**:144502, April 2018.

[2] Zhu X., Stevens R. J. A. M., Shishkina O., Verzicco R., & Lohse D. $Nu \sim Ra^{1/2}$ scaling enabled by multiscale wall roughness in Rayleigh-Bénard turbulence. *J. Fluid Mech.*, **869**:R4, March 2019.

[3] Bejan Adrian. *Convection Heat Transfer*. John Wiley and Sons, 2013.

[4] Ingersoll A. P. Atmosphere dynamics of the outer planets. *Science*, **248**:2308–315, 1990.

[5] Morgan W. J. Deep mantle convection plumes and plate motions. *AAPG Bull.*, **56**: 203–213, 1972.

[6] Davies G. F. Whole-mantle convection and plate tectonics. *Geophys. J. Int.*, **49**:459–486, 1977.

[7] Cattaneo Fausto, Emonet Thierry, & Weiss Nigel. On the interaction between convection and magnetic fields. *The Astrophysical Journal*, **588**(2):1183–1198, may 2003. doi: 10.1086/374313. URL https://doi.org/10.1086/374313.

[8] Wissen van R., Golombok M., & Brouwers J. J. H. Gas centrifugation with wall condensation. *AIChE Journal*, **52**:1271–1274, 2006.

[9] Incropera F.P. *Liquid Cooling of Electronic Devices by Single-phase Convection*. John Wiley & Sons, 1999.

[10] Hunt G.R. & Linden P.P. The fluid mechanics of natural ventilation—displacement ventilation by buoyancy-driven flows assisted by wind. *Building and Environment*, **34**(6):707–720, 1999. ISSN 0360-1323. doi: https://doi.org/10.1016/S0360-1323(98)00053-5. URL https://www.sciencedirect.com/science/article/pii/S0360132398000535.

[11] Flow of warm and cold winds in the atmosphere of the earth. URL https://www.pinterest.com/pin/210261876328880724/.

[12] Thermal convection in the mantle of the earth. URL https://kaiserscience.files.wordpress.com/2014/08/earth-science-volcanoes-339345-1280x1024.jpg.

[13] Thermal convection inside the sun. URL http://khadley.com/Courses/Astronomy/ph_206/topics/sun/images/slide10.png?crc=4144629964.

[14] Bénard H. Les tourbillons cellulaires dans une nappe liquide. -Méthodes optiques d'observation et d'enregistrement. *Journal de Physique Théorique*, **10**:254–266, 1901.

[15] Rayleigh Lord. On convection currents in a horizontal layer of fluid, when the higher temperature is on the under side. *Philosophical Magazine and Journal of Science: Series 6*, **32**:529–546, 1916.

[16] Low A. R. On the criterion for stability of a layer of viscous fluid heated from below. *Proc. Royal Soc. Lond. A*, **125**:180–195, 1929.

[17] Schmidt R. J. & Milverton S. W. On the instability of a fluid when heated from below. *Proc. Royal Soc. Lond. A*, **152**:586–594, 1935.

[18] Ahlers G., Grossmann S., & Lohse D. Heat transfer and large scale dynamics in turbulent Rayleigh-Bénard convection. *Rev. Mod. Phys.*, **81**:503–537, June 2009.

[19] Verzicco R. & Camussi R. Prandtl number effects in convective turbulence. *Journal of Fluid Mechanics*, **383**:55–73, 1999. doi: 10.1017/S0022112098003619.

[20] Krishnamurthi R. & Howard L. N. Large-scale flow generation in turbulent convection. *Proc. Natl Acad. Sci. USA*, **107**:1981–1985, 1981.

[21] Mutabazi Innocent, Wesfreid J. E., & Guyon Etienne. Dynamics of spatio-temporal cellular structures. 2006.

[22] Jeffreys H. The stability of a layer of fluid heated from below. *Philosophical Magazine and Journal of Science: Series 7*, **2**:833–844, 1926.

[23] Jeffreys H. Some cases of instability in fluid motion. *Proc. Royal Soc. Lond. A*, **118**: 195–208, 1928.

[24] Malkus W. V. R. The heat transport and spectrum of thermal turbulence. *Proc. R. Soc. Lond. A*, **225**(1161):196–212, 1954. doi: 10.1098/rspa.1954.0197.

[25] Priestley C. H. B. Convection from a large horizontal surface. *Australian Journal of Physics*, **7**(1):176–201, 1954. doi: https://doi.org/10.1071/PH540176.

[26] Howard L. N. Heat transport by turbulent convection. *Journal of Fluid Mechanics*, **17** (3):405–432, 1963. doi: 10.1017/S0022112063001427.

[27] Spiegel E. A. A generalization of the mixing-length theory of turbulent convection. *Astrophysical Journal*, **138**:216, July 1963. doi: 10.1086/147628.

[28] Kraichnan R. H. Turbulent thermal convection at arbitrary prandtl number. *Phys. Fluids*, **5**:1374, November 1962.

[29] Castaing B., Gunaratne G., Heslot F., Kadanoff L., Libchaber A., Thomae S., Wu X., & Zanetti S. Scaling of hard thermal turbulence in Rayleigh-Bénard convection. *J. Fluid Mech.*, **204**:1–30, August 1989.

[30] Grossmann S. & Lohse D. Scaling in thermal convection: a unifing theory. *J. Fluid Mech.*, **407**:27–56, November 2000.

[31] Grossmann S. & Lohse D. Fluctuations in turbulent Rayleigh-Bénard convection: The role of plumes. *Phys. Fluids*, **16**:4462–4472, August 2004.

[32] Bodenschatz E., Pesch W., & Ahlers G. Recent developments in Rayleigh-Bénard convection. *Annu. Rev. Fluid Mech.*, **32**:709–778, November 2000.

[33] Chilla F. & Schumacher J. New perspectives in turbulent Rayleigh-Bénard convection. *Eur. Phys. J. E.*, **35**:58, July 2012.

[34] Gastine T., Wicht J., & Aurnou J. M. Turbulent Rayleigh-bénard convection in spherical shells. *J. Fluid Mech.*, **778**:721–764, July 2015.

[35] Prandtl L. Meteorologische anwendungen der stromungslehre. *Beitr. Phys. Atmos.*, **19** (3):188–202, 1932.

[36] Herring J. R. Investigation of problems in thermal convection: Rigid boundaries. *Journal of Atmospheric Sciences*, **21**(3):277 – 290, 1964. URL https://journals.ametsoc.org/view/journals/atsc/21/3/1520-0469_1964_021_0277_iopitc_2_0_co_2.xml.

[37] Gough D. O., Spiegel E. A., & Toomre Juri. Modal equations for cellular convection. *Journal of Fluid Mechanics*, **68**(4):695–719, 1975. doi: 10.1017/S0022112075001188.

[38] Toomre Juri, Gough D. O., & Spiegel E. A. Numerical solutions of single-mode convection equations. *Journal of Fluid Mechanics*, **79**(1):1–31, 1977. doi: 10.1017/S0022112077000019.

[39] Toomre Juri, Gough D. O., & Spiegel E. A. Time-dependent solutions of multimode convection equations. *Journal of Fluid Mechanics*, **125**:99–122, 1982. doi: 10.1017/S0022112082003279.

[40] Chilla F., Rastello M., Chaumat S., & Castaing B. Ultimate regime in Rayleigh-Bénard convection: The role of plates. *Phys. Fluids*, **16**:2452–2456, July 2004.

[41] Shraiman B. I. & Siggia E. D. Heat transport in high-Rayleigh-number convection. *Phys. Rev. A.*, **42**:3650, March 1990.

[42] Stevens Richard J. A. M., Poel van der Erwin P., Grossmann Siegfried, & Lohse Detlef. The unifying theory of scaling in thermal convection: the updated prefactors. *Journal of Fluid Mechanics*, **730**:295–308, 2013. doi: 10.1017/jfm.2013.298.

[43] Doering C. R., Toppaladoddi S., & Wettlaufer J. S. Absence of evidence for the ultimate regime in two-dimensional rayleigh-bénard convection. *Phys. Rev. Lett.*, **123**:259401, Dec 2019. doi: 10.1103/PhysRevLett.123.259401. URL https://link.aps.org/doi/10.1103/PhysRevLett.123.259401.

[44] Zhu Xiaojue, Mathai Varghese, Stevens Richard J. A. M., Verzicco Roberto, & Lohse Detlef. Zhu et al. reply:. *Phys. Rev. Lett.*, **123**:259402, Dec 2019. doi: 10.1103/PhysRevLett.123.259402. URL https://link.aps.org/doi/10.1103/PhysRevLett.123.259402.

[45] Grossmann S. & Lohse D. On geometry effects in Rayleigh-Bénard convection. *J. Fluid Mech.*, **486**:105–114, February 2003.

[46] Zhou Q., Sugiyama K., Stevens R. J. A. M., Grossmann S., Lohse D., & Xia K. Horizontal structures of velocity and temperature boundary layers in two-dimensional numerical turbulent Rayleigh-Bénard convection. *Phys. Fluids*, **23**:125104, December 2011.

[47] Emran M. S. & Schumacher J. Fine-scale statistics of temperature and its derivatives in convective turbulence. *J. Fluid Mech.*, **611**:13–34, June 2008.

[48] Zhang Y., Zhou Q., & Sun C. Statistics of kinetic and thermal energy dissipation rates in two-dimensional turbulent Rayleigh-Bénard convection. *J. Fluid Mech.*, **814**:165–184, February 2017.

[49] Heslot F., Castaing B., & Libchaber A. Transitions to turbulence in helium gas. *Phys. Rev. A*, **36**:5870–5873, Dec 1987. doi: 10.1103/PhysRevA.36.5870.

[50] Sano M., Wu X. Z., & Libchaber A. Turbulence in helium gas free convection. *Phys. Rev. A.*, **40**:6421–6430, March 1989.

[51] Wu X. Z., Kadanoff L., Libchaber A., & M.Sano . Frequency power spectrum of temperature fluctuations in free convection. *Phys. Rev. Lett.*, **64**:2140–43, April 1990.

[52] Mandelbrot Benoit. How long is the coast of britain? statistical self-similarity and fractional dimension. *Science*, **156**(3775):636–638, 1967. ISSN 0036-8075. doi: 10.1126/science.156.3775.636. URL https://science.sciencemag.org/content/156/3775/636.

[53] Toppaladoddi S., Succi S., & Wettlaufer J. S. Roughness as a route to the ultimate regime of thermal convection. *Phys. Rev. Lett.*, **118**:074503, February 2017.

[54] Shen Y., Tong P., & Xia K.-Q. Turbulent convection over rough surfaces. *Phys. Rev. Lett.*, **76**:908–911, Feb 1996. doi: 10.1103/PhysRevLett.76.908. URL https://link.aps.org/doi/10.1103/PhysRevLett.76.908.

[55] Villermaux Emmanuel. Transfer at rough sheared interfaces. *Phys. Rev. Lett.*, **81**:4859–4862, Nov 1998. doi: 10.1103/PhysRevLett.81.4859. URL https://link.aps.org/doi/10.1103/PhysRevLett.81.4859.

[56] Ciliberto S. & Laroche C. Random roughness of boundary increases the turbulent convection scaling exponent. *Phys. Rev. Lett.*, **82**:3998–4001, May 1999. doi: 10.1103/PhysRevLett.82.3998. URL https://link.aps.org/doi/10.1103/PhysRevLett.82.3998.

[57] Du Y.-B. & Tong P. Turbulent thermal convection in a cell with ordered rough boundaries. *Journal of Fluid Mechanics*, **407**:57–84, 2000. doi: 10.1017/S0022112099007624.

[58] Roche P.-E., Castaing B., Chabaud B., & Hébral B. Observation of the $\frac{1}{2}$ power law in Rayleigh-Bénard convection. *Phys. Rev. E*, **63**:045303, Mar 2001. doi: 10.1103/PhysRevE.63.045303. URL https://link.aps.org/doi/10.1103/PhysRevE.63.045303.

[59] Zhu X., Stevens R. J. A. M., Verzicco R., & Lohse D. Roughness facilitated local 1/2 scaling does not imply the onset of the ultimate regime of thermal convection. *Phys. Rev. Lett.*, **119**:154501, October 2017.

[60] Xie Yi-Chao & Xia Ke-Qing. Turbulent thermal convection over rough plates with varying roughness geometries. *Journal of Fluid Mechanics*, **825**:573–599, 2017. doi: 10.1017/jfm.2017.397.

[61] Zhang Y., Sun C., Bao Y., & Zhou Q. How surface roughness reduces heat transport for small roughness heights in turbulent Rayleigh-Bénard convection. *J. Fluid Mech.*, **836**: R2, December 2018.

[62] Tummers Mark J. & Steunebrink Martin. Effect of surface roughness on heat transfer in Rayleigh-Bénard convection. *International Journal of Heat and Mass Transfer*, **139**:1056 – 1064, 2019. ISSN 0017-9310. doi: https://doi.org/10.1016/j.ijheatmasstransfer.2019.05.066. URL http://www.sciencedirect.com/science/article/pii/S0017931019300201.

[63] Lülff J., Wilczek M., Stevens R. J. A. M., Friedrich R., & Lohse D. Turbulent Rayleigh-Bénard convection described by projected dynamics in phase space. *J. Fluid Mech.*, **781**: 276–297, August 2015.

[64] Wang Q., Wan Z.-H., Yan R., & Sun D.-J. Flow organization and heat transfer in two-dimensional tilted convection with aspect ratio 0.5. *Physics of Fluids*, **31**(2):025102, 2019. doi: 10.1063/1.5070132. URL https://doi.org/10.1063/1.5070132.

[65] Guo S., Zhou S., Cen X., Qu L., Lu Y., Sun L., & Shang X. The effect of cell tilting on turbulent thermal convection in a rectangular cell. *J. Fluid Mech.*, **762**:273–287, December 2015.

[66] Jiang L., Sun C., & Calzavarini E. Robustness of heat transfer in confined inclined convection at high prandtl number. *Phys. Rev. E*, **99**:013108, Jan 2019. doi: 10.1103/PhysRevE.99.013108. URL https://link.aps.org/doi/10.1103/PhysRevE.99.013108.

[67] Khalilov R., Kolesnichenko I., Pavlinov A., Mamykin A., Shestakov A., & Frick P. Thermal convection of liquid sodium in inclined cylinders. *Phys. Rev. Fluids*, **3**:043503, Apr 2018. doi: 10.1103/PhysRevFluids.3.043503. URL https://link.aps.org/doi/10.1103/PhysRevFluids.3.043503.

[68] Guo S., Zhou S., Qu L., Cen X., & Lu Y. Evolution and statistics of thermal plumes in tilted turbulent convection. *European Journal of mechanics B/Fluids*, **111**:933–942, April 2017.

[69] Chilla F., Rastello M., Chaumat S., & Castaing B. Long relaxation times and tilt sensitivity in Rayleigh-Bénard turbulence. *Euro. Phys. J. B*, **40**:223–227, May 2004.

[70] Shishkina O. & Horn S. Thermal convection in inclined cylindrical containers. *J. Fluid Mech.*, **790**:R3, January 2016a.

[71] Frick P., Khalilov R., Kolesnichenko I., Mamykin A., Pakholkov V., Pavlinov A., & Rogozhkin S. Turbulent convective heat transfer in a long cylinder with liquid sodium. *EPL (Europhysics Letters)*, **109**(1):14002, jan 2015. doi: 10.1209/0295-5075/109/14002. URL https://doi.org/10.1209%2F0295-5075%2F109%2F14002.

[72] Vasilev A. Yu., Kolesnichenko I. V., Mamykin A. D., Frick R. I., P. G. and. Khalilov, Rogozhkin S. A., & Pakholkov V. V. Turbulent convective heat transfer in an inclined tube filled with sodium. *Technical Physics*, **60**:1305–1309, 01 2015. doi: 10.1134/S1063784215090236.

[73] Niemela J. J & Sreenivasan K. R. Rayleigh-number evolution of large-scale coherent motion in turbulent convection. *Europhysics Letters (EPL)*, **62**(6):829–833, jun 2003. doi: 10.1209/epl/i2003-00447-3. URL https://doi.org/10.1209%2Fepl%2Fi2003-00447-3.

[74] Wang Q., Xia S., Wang B., Sun D., Zhou Q., & Wan Z. Flow reversals in two-dimensional thermal convection in tilted cells. *J. Fluid Mech.*, **849**:355–372, May 2018a.

[75] Toppaladoddi S., Wells A. J., Doering C. R., & Wettlaufer J. S. Thermal convection over fractal surfaces. *Journal of Fluid Mechanics*, **907**:A12, 2021. doi: 10.1017/jfm.2020.826.

[76] Shishkina O., Stevens R. J. A. M., Grossmann S., & Lohse D. Boundary layer structure in turbulent thermal convection and its consequences for the required numerical resolution. *New Journal of Physics*, **12**(7):075022, jul 2010. doi: 10.1088/1367-2630/12/7/075022.

[77] Anderson Tannehill J.C., D. & Pletcher R.H. *Computational Fluid Mechanics and Heat Transfer*. John Wiley and Sons, 2012. URL https://doi.org/10.1201/b12884.

[78] Grötzbach Günther. Spatial resolution requirements for direct numerical simulation of the Rayleigh-Bénard convection. *Journal of Computational Physics*, **49**(2):241–264, 1983. ISSN 0021-9991. doi: https://doi.org/10.1016/0021-9991(83)90125-0. URL https://www.sciencedirect.com/science/article/pii/0021999183901250.

[79] Belkadi Mebarek, Sergent Anne, Fraigneau Yann, & Podvin Bérengère. On the role of roughness valleys in turbulent Rayleigh-Bénard convection. *Journal of Fluid Mechanics*, **923**:A6, 2021. doi: 10.1017/jfm.2021.583.

[80] Belkadi M., Guislain L., Sergent A., Podvin B., Chillà F., & Salort J. Experimental and numerical shadowgraph in turbulent Rayleigh-Bénard convection with a rough boundary: investigation of plumes. *Journal of Fluid Mechanics*, **895**:A7, 2020. doi: 10.1017/jfm.2020.296.

[81] King E. M., Stellmach S., & Buffett B. Scaling behaviour in Rayleigh-Bénard convection with and without rotation convection. *J. Fluid Mech.*, **717**:449–471, February 2013.

[82] De A.K. A diffuse interface immersed boundary method for convective heat and fluid flow. *International Journal of Heat and Mass Transfer*, **92**:957 – 969, 2016. ISSN 0017-9310. doi: https://doi.org/10.1016/j.ijheatmasstransfer.2015.09.022.

[83] De A. K. A diffuse interface immersed boundary method for complex moving boundary problems. *Journal of Computational Physics*, **366**:226–251, 2018. ISSN 0021-9991. doi: https://doi.org/10.1016/j.jcp.2018.04.008. URL https://www.sciencedirect.com/science/article/pii/S0021999118302225.

[84] De A. K. & Sarkar S. Three-dimensional wake dynamics behind a tapered cylinder with large taper ratio. *Phys. Fluids*, **32**:063604, 2020.

[85] De A. K. & Sarkar S. Dependence of wake structure on pitching frequency behind a thin panel at $re = 1000$. *J. Fluid Mech.*, **924**:A33, 2021.

[86] De A. K. & Sarkar S. Spatial wake transition past a thin pitching plate. *Phys. Rev. E*, **104**:025106, 2021.

[87] Kushwaha V. K. & De A. K. Aerodynamics of multiple freely falling plates. *Physics of Fluids*, **32**(10):103603, 2020. doi: 10.1063/5.0021794.

[88] Spiegel E. A. Convection in stars. *Annu. Rev. Astron. Astrophys.*, **9**:323–352, 1971.

[89] Emran M. S. & Schumacher J. Conditional statistics of thermal dissipation rate in turbulent Rayleigh-Bénard convection. *Eur. Phys. J. E.*, **35**:108, September 2012.

[90] Vishnu V. T., De A. K., & Mishra P. K. Dynamics and statistics of reorientations of large-scale circulation in turbulent rotating Rayleigh-Bénard convection. *Phys. Fluids*, **31**(5):055112, 2019. doi: 10.1063/1.5093948. URL https://doi.org/10.1063/1.5093948.

[91] Stevens R. J. A. M., Verzicco R., & Lohse D. Radial boundary layer structure and nusselt number in Rayleigh-Bénard convection. *J. Fluid Mech.*, **643**:495–507, 2010.

[92] De A. K., Eswaran V., & Mishra P. K. Scaling of heat transport and energy spectra of turbulent Rayleigh-Bénard convection in a large-aspect-ratio box. *Int. j. Heat Fluid Flow*, **67**:111–124, August 2017.

[93] Zhou Q. & Xia K. Physical and geometrical properties of thermal plumes in turbulent Rayleigh-Bénard convection. *New J. Phys.*, **12**:075006, July 2010.

[94] King E. M., Stellmach S., & Aurnou J. M. Heat transfer by rapidly rotating Rayleigh-Bénard convection. *J. Fluid Mech.*, **691**:568–582, November 2012.

[95] Xin Y.-B., Xia K.-Q., & Tong P. Measured velocity boundary layers in turbulent convection. *Phys. Rev. Lett.*, **77**:1266–1269, Aug 1996. doi: 10.1103/PhysRevLett.77.1266. URL https://link.aps.org/doi/10.1103/PhysRevLett.77.1266.

[96] Xin Y. B. & Xia K. Q. Boundary layer length scales in convective turbulence. *PRE*, **56** (3):3010–3015, Sep 1997. doi: 10.1103/PhysRevE.56.3010.

[97] Sun Chao, Cheung Yin-Har, & Xia Ke-Qing. Experimental studies of the viscous boundary layer properties in turbulent Rayleigh-Bénard convection. *Journal of Fluid Mechanics*, **605**:79–113, 2008. doi: 10.1017/S0022112008001365.

[98] Kolmogorov A. N. A refinement of previous hypotheses concerning the local structure of turbulence in a viscous incompressible fluid at high Reynolds number. *J. Fluid Mech.*, **13**:82–85, May 1962.

[99] Wyngaard J. C. & Weil J. C. Transport asymmetry in skewed turbulence. *Phys. Fluids*, **3**:155–162, 1991.

[100] Verzicco R. & Camussi R. Numerical experiments on strongly turbulent thermal convection in a slender cylindrical cell. *J. Fluid Mech.*, **477**:19–49, september 2003.

[101] Verzicco R. & Sreenivasan K. R. A comparison of turbulent thermal convection between conditions of constant temperature and constant heat flux. *J. Fluid Mech.*, **595**:203–219, June 2008.

[102] Kerr R. M. Rayleigh number scaling in natural convection. *J. Fluid Mech.*, **310**:139–179, September 1996.

[103] Chand K., Sharma M., Venugopal V. T., & De A. K. Statistics of coherent structures in two-dimensional turbulent Rayleigh-Bénard convection. *Physics of Fluids*, **31** (11):115112, 2019. doi: 10.1063/1.5125758. URL https://doi.org/10.1063/1.5125758.

[104] Salort J., Liot O., Rusaouen E., Seychelles F., Tisserand J.-C., Creyssels M., Castaing B., & Chillà F. Thermal boundary layer near roughnesses in turbulent Rayleigh-Bénard convection: Flow structure and multistability. *Physics of Fluids*, **26**(1):015112, 2014. doi: 10.1063/1.4862487. URL https://doi.org/10.1063/1.4862487.

[105] Stringano G., Pascazio G., & Verzicco R. Turbulent thermal convection over grooved plates. *Journal of Fluid Mechanics*, **557**:307–336, 2006. doi: 10.1017/S0022112006009785.

[106] Wagner Sebastian & Shishkina Olga. Heat flux enhancement by regular surface roughness in turbulent thermal convection. *Journal of Fluid Mechanics*, **763**:109–135, 2015. doi: 10.1017/jfm.2014.665.

[107] Shishkina O. & Wagner C. Analysis of thermal dissipation rates in turbulent Rayleigh-Bénard convection. *Journal of Fluid Mechanics*, **546**:51–60, 2006. doi: 10.1017/S0022112005007408.

[108] NIEMELA J. J., SKRBEK L., SREENIVASAN K. R., & DONNELLY R. J. The wind in confined thermal convection. *Journal of Fluid Mechanics*, **449**:169–178, 2001. doi: 10.1017/S0022112001006310.

[109] Qiu X.-L. & Tong P. Large-scale velocity structures in turbulent thermal convection. *Phys. Rev. E*, **64**:036304, Aug 2001. doi: 10.1103/PhysRevE.64.036304. URL https://link.aps.org/doi/10.1103/PhysRevE.64.036304.

[110] Brown Eric, Funfschilling Denis, & Ahlers Guenter. Anomalous reynolds-number scaling in turbulent rayleigh–bénard convection. *Journal of Statistical Mechanics: Theory and Experiment*, **2007**(10):P10005–P10005, oct 2007. doi: 10.1088/1742-5468/2007/10/p10005. URL https://doi.org/10.1088/1742-5468/2007/10/p10005.

[111] Wang Q., Verzicco R., Lohse D., & Shishkina O. Multiple states in turbulent large-aspect-ratio thermal convection: What determines the number of convection rolls? *Phys. Rev. Lett.*, **125**:074501, Aug 2020. doi: 10.1103/PhysRevLett.125.074501. URL https://link.aps.org/doi/10.1103/PhysRevLett.125.074501.

[112] Jiang Hechuan, Zhu Xiaojue, Mathai Varghese, Verzicco Roberto, Lohse Detlef, & Sun Chao. Controlling heat transport and flow structures in thermal turbulence using ratchet surfaces. *Phys. Rev. Lett.*, **120**:044501, Jan 2018. doi: 10.1103/PhysRevLett.120.044501. URL https://link.aps.org/doi/10.1103/PhysRevLett.120.044501.

[113] Dong Dao-Liang, Wang Bo-Fu, Dong Yu-Hong, Huang Yong-Xiang, Jiang Nan, Liu Yu-Lu, Lu Zhi-Ming, Qiu Xiang, Tang Zhan-Qi, & Zhou Quan. Influence of spatial arrangements of roughness elements on turbulent Rayleigh-Bénard convection. *Physics of Fluids*, **32**(4):045114, 2020. doi: 10.1063/1.5143465. URL https://doi.org/10.1063/1.5143465.

[114] Du Y.-B. & Tong P. Temperature fluctuations in a convection cell with rough upper and lower surfaces. *Phys. Rev. E*, **63**:046303, Mar 2001. doi: 10.1103/PhysRevE.63.046303. URL https://link.aps.org/doi/10.1103/PhysRevE.63.046303.

[115] Dropkin D. & Somerscales E. Heat transfer by natural convection in liquids confined by two parallel plates which are inclined at various angles with respect to the horizontal. *Trans. ASME J. Heat Transfer*, **87 (1)**:77–82, 1965.

[116] Langebach R. & Haberstroh Ch. Natural convection in inclined pipes - a new correlation for heat transfer estimations. *AIP Conference Proceedings*, **1573**(1):1504–1511, 2014. doi: 10.1063/1.4860885.

[117] Xin S. & Le Quere P. Direct numerical simulations of two-dimensional chaotic natural convection in a differentially heated cavity of aspect ratio 4. *Journal of Fluid Mechanics*, **304**:87–118, 1995. doi: 10.1017/S0022112095004356.

[118] Zwirner L. & Shishkina O. Confined inclined thermal convection in low-prandtl-number fluids. *Journal of Fluid Mechanics*, **850**:984–1008, 2018. doi: 10.1017/jfm.2018.477.

[119] Zhang S., Chen X., Xia Z., Xi H.-D., Zhou Q., & Chen S. Stabilizing/destabilizing the large-scale circulation in turbulent Rayleigh-Bénard convection with sidewall temperature control. *Journal of Fluid Mechanics*, **915**:A14, 2021. doi: 10.1017/jfm.2021.58.

[120] Ahlers G., Brown E., & Nikolaenko A. The search for slow transients, and the effect of imperfect vertical alignment, in turbulent Rayleigh-Bénard convection. *Journal of Fluid Mechanics*, **557**:347–367, 2006. doi: 10.1017/S0022112006009888.

[121] Wang Q., Wan Z.-H., Yan R., & Sun D.-J. Multiple states and heat transfer in two-dimensional tilted convection with large aspect ratios. *Phys. Rev. Fluids*, **3**:113503, Nov 2018b. doi: 10.1103/PhysRevFluids.3.113503. URL https://link.aps.org/doi/10.1103/PhysRevFluids.3.113503.

[122] Saunders O. A. & Tizard Henry Thomas. Natural convection in liquids. *Proceedings of the Royal Society of London. Series A. Mathematical and Physical Sciences*, **172**(948):55–71, 1939. doi: 10.1098/rspa.1939.0089. URL https://royalsocietypublishing.org/doi/abs/10.1098/rspa.1939.0089.

[123] Churchill S. W. & Chu H. H. S. Correlating equations for laminar and turbulent free convection from a vertical plate. *International Journal of Heat and Mass Transfer*, **18**(11):1323–1329, 1975. ISSN 0017-9310. doi: https://doi.org/10.1016/0017-9310(75)90243-4. URL https://www.sciencedirect.com/science/article/pii/0017931075902434.

[124] Shishkina O. Momentum and heat transport scalings in laminar vertical convection. *Phys. Rev. E*, **93**:051102, May 2016b. doi: 10.1103/PhysRevE.93.051102. URL https://link.aps.org/doi/10.1103/PhysRevE.93.051102.

[125] Chand K., De A. K., & Mishra P. K. Enhanced heat flux and flow structures in turbulent Rayleigh-Bénard convection with rough boundaries. *Phys. Rev. Fluids*, **6**:124605, Dec 2021b. doi: 10.1103/PhysRevFluids.6.124605. URL https://link.aps.org/doi/10.1103/PhysRevFluids.6.124605.

[126] Sun C., Xi H.-D., & Xia K.-Q. Azimuthal symmetry, flow dynamics, and heat transport in turbulent thermal convection in a cylinder with an aspect ratio of 0.5. *Phys. Rev. Lett.*, **95**: 074502, Aug 2005. doi: 10.1103/PhysRevLett.95.074502. URL https://link.aps.org/doi/10.1103/PhysRevLett.95.074502.

[127] Weiss S. & Ahlers G. Effect of tilting on turbulent convection: cylindrical samples with aspect ratio $\gamma = 0.50$. *Journal of Fluid Mechanics*, **715**:314–334, 2013. doi: 10.1017/jfm.2012.520.

[128] Goluskin D. & Doering C. R. Bounds for convection between rough boundaries. *Journal of Fluid Mechanics*, **804**:370–386, 2016. doi: 10.1017/jfm.2016.528.

[129] Sugiyama K., Calzavarini E., Grossmann S., & Lohse D. Flow organization in two-dimensional non-oberbeck-boussinesq Rayleigh-Bénard convection in water. *Journal of Fluid Mechanics*, **637**:105–135, 2009. doi: 10.1017/S0022112009008027.

[130] Yang H., Wei Y., Zhu Z., Dou H., & Qian Y. Statistics of heat transfer in two-dimensional turbulent Rayleigh-Bénard convection at various prandtl number. *Entropy*, **20**(8), 2018. ISSN 1099-4300. doi: 10.3390/e20080582. URL https://www.mdpi.com/1099-4300/20/8/582.

[131] Chand K., Sharma M., & De A. K. Significance of near-wall dynamics in enhancement of heat flux for roughness aided turbulent Rayleigh-Bénard convection. *Physics of Fluids*, **33**(6):065114, 2021a. doi: 10.1063/5.0053522. URL https://doi.org/10.1063/5.0053522.

[132] Shishkina O. & Wagner C. Modelling the influence of wall roughness on heat transfer in thermal convection. *J. Fluid Mech.*, **686**:568–582, September 2011.

[133] Tisserand J.-C., Creyssels M., Gasteuil Y., Pabiou H., Gibert M., Castaing B., & Chillà F. Comparison between rough and smooth plates within the same Rayleigh-Bénard cell. *Physics of Fluids*, **23**(1):015105, 2011. doi: 10.1063/1.3540665. URL https://doi.org/10.1063/1.3540665.

[134] Qiu X.-L., Xia K.-Q., & Tong P. Experimental study of velocity boundary layer near a rough conducting surface in turbulent natural convection. *Journal of Turbulence*, **6**: N30, 2005. doi: 10.1080/14685240500460733. URL https://doi.org/10.1080/14685240500460733.

[135] Liot O., Salort J., Kaiser R., Puits du R., & Chillà F. Boundary layer structure in a rough Rayleigh-Bénard cell filled with air. *Journal of Fluid Mechanics*, **786**:275–293, 2016. doi: 10.1017/jfm.2015.649.

[136] Liot O., Ehlinger Q., Rusaouen E., Salort J., Coudarchet T., & Chillà F. Velocity fluctuations and boundary layer structure in a rough Rayleigh-Bénard cell filled with water. *Phys. Rev. Fluids*, **2**:044605, Apr 2017. doi: 10.1103/PhysRevFluids.2.044605. URL https://link.aps.org/doi/10.1103/PhysRevFluids.2.044605.

[137] Emran Mohammad S. & Shishkina Olga. Natural convection in cylindrical containers with isothermal ring-shaped obstacles. *Journal of Fluid Mechanics*, **882**:A3, 2020. doi: 10.1017/jfm.2019.797.

[138] Foroozani N., Niemela J. J., Armenio V., & Sreenivasan K. R. Turbulent convection and large scale circulation in a cube with rough horizontal surfaces. *Phys. Rev. E*, **99**: 033116, Mar 2019. doi: 10.1103/PhysRevE.99.033116. URL https://link.aps.org/doi/10.1103/PhysRevE.99.033116.

[139] Mishra P. K., De A. K., Verma M. K., & Eswaran V. Dynamics of reorientations and reversals of large-scale flow in Rayleigh-Bénard convection. *J. Fluid Mech.*, **668**:480–499, September 2011.

[140] Vishnu V. T., De A. K., & Mishra P. K. Dynamics of large-scale circulation and energy transfer mechanism in turbulent Rayleigh-Bénard convection in a cubic cell. *Physics of Fluids*, **32**(9):095115, 2020. doi: 10.1063/5.0021667. URL https://doi.org/10.1063/5.0021667.

[141] Ciliberto S., Cioni S., & Laroche C. Large-scale flow properties of turbulent thermal convection. *Phys. Rev. E*, **54**:R5901–R5904, Dec 1996. doi: 10.1103/PhysRevE.54.R5901. URL https://link.aps.org/doi/10.1103/PhysRevE.54.R5901.

[142] Siggia E D. High Rayleigh number convection. *Annual Review of Fluid Mechanics*, **26**(1):137–168, 1994. doi: 10.1146/annurev.fl.26.010194.001033. URL https://doi.org/10.1146/annurev.fl.26.010194.001033.

[143] Kunnen R. P. J., Clercx H. J. H., Geurts B. J., Bokhoven van L. J. A., Akkermans R. A. D., & Verzicco R. Numerical and experimental investigation of structure-function scaling in turbulent rayleigh-bénard convection. *Phys. Rev. E*, **77**:016302, Jan 2008. doi: 10.1103/PhysRevE.77.016302. URL https://link.aps.org/doi/10.1103/PhysRevE.77.016302.

[144] Pope S. B. *Turbulent Flows*. Cambridge University Press, 2000.

[145] Bolgiano Jr. R. Turbulent spectra in a stably stratified atmosphere. *Journal of Geophysical Research (1896-1977)*, **64**(12):2226–2229, 1959. doi: 10.1029/JZ064i012p02226.

[146] Wang Dongpu, Liu Shuang, Zhou Quan, & Sun Chao. Spectra and structure functions of the temperature and velocity fields in supergravitational thermal turbulence. *Physics of Fluids*, **34**(5):055108, 2022. doi: 10.1063/5.0091012. URL https://doi.org/10.1063/5.0091012.

[147] Lohse Detlef & Xia Ke-Qing. Small-scale properties of turbulent Rayleigh-Bénard convection. *Annual Review of Fluid Mechanics*, **42**(1):335–364, 2010. doi: 10.1146/annurev.fluid.010908.165152. URL https://doi.org/10.1146/annurev.fluid.010908.165152.

[148] Davidson P.A. & Davidson R.F.M.P.A. *Turbulence: An Introduction for Scientists and Engineers*. Oxford University Press, 2004. ISBN 9780198529491. URL https://books.google.co.in/books?id=V3TvAAAAMAAJ.

[149] Frisch Uriel. *Turbulence: The Legacy of A. N. Kolmogorov*. Cambridge University Press, 1995. doi: 10.1017/CBO9781139170666.

[150] Naffouti Awatef, Ben-Beya Brahim, & Lili Taieb. Three-dimensional rayleigh–bénard magnetoconvection: Effect of the direction of the magnetic field on heat transfer and

flow patterns. *Comptes Rendus Mécanique*, **342**(12):714–725, 2014. ISSN 1631-0721. doi: https://doi.org/10.1016/j.crme.2014.09.001. URL https://www.sciencedirect.com/science/article/pii/S1631072114001740.

[151] Cisse I., Bardan G., & Mojtabi A. Rayleigh bénard convective instability of a fluid under high-frequency vibration. *International Journal of Heat and Mass Transfer*, **47**(19):4101–4112, 2004. ISSN 0017-9310. doi: https://doi.org/10.1016/j.ijheatmasstransfer.2004.05.002. URL https://www.sciencedirect.com/science/article/pii/S0017931004001796.

Publications

Journals

1. Statistics of coherent structures in two-dimensional turbulent Rayleigh-Bénard convection, **K. Chand**, M. Sharma, T. Vishnu, and A. K. De, *Phys. Fluids*, 31 (2019), 115112.

2. Significance of near-wall dynamics in enhancement of heat flux for roughness aided turbulent Rayleigh-Bénard convection, **K. Chand**, M. Sharma, and A. K. De, *Phys. Fluids*, 33 (2021), 065114.

3. Enhanced heat flux and flow structures in turbulent Rayleigh-Bénard convection with rough boundaries, **K. Chand**, A. K. De, and P. K. Mishra, *Phys. Rev. Fluids*, 6 (2021), 124605.

4. Effect of inclination angle on heat transport properties in two-dimensional turbulent Rayleigh-Bénard convection with smooth and rough boundaries, **K. Chand**, M. Sharma, and A. K. De, *J. Fluid Mech.* 950 (2022), A16.

5. Investigation of flow dynamics and heat transfer mechanism in turbulent Rayleigh-Bénard convection over multi-scale rough surfaces, M. Sharma, **K. Chand**, and A. K. De, *J. Fluid Mech.*, 941 (2022), A20.

6. Influence of Prandtl number in turbulent Rayleigh-Bénard convection over rough surfaces, M. Sharma, **K. Chand**, and A. K. De, *Phys. Rev. Fluids*, 7 (2022), 104609.

7. Understanding the enhanced heat flux through coherent structures in three-dimensional turbulent Rayleigh-Bénard convection with rough boundaries, **K. Chand**, M. Sharma, and A. K. De, (under preparation).

8. Effect of rough boundaries on the statistics of velocity and temperature fluctuations in $2D$ turbulent Rayleigh-Bénard convection, **K. Chand**, D. N. Laskar, M. Sharma, and A. K. De, (under preparation).

9. Heat transfer mechanism in a cubic box facilitated with conical roughness in turbulent Rayleigh-Bénard convection, M. Sharma, **K. Chand**, and A. K. De, (under preparation).

Conference proceedings

1. Effect of random roughness on heat flux in turbulent Rayleigh-Bénard convection, **K. Chand**, M. Sharma, and A. K. De, *The* 7^{th} *International and* 45^{th} *National Conference on Fluid Mechanics and Fluid Power*, IIT Guwahati, (2020).

2. Role of near-wall dynamics in roughness aided turbulent Rayleigh-Bénard convection, **K. Chand**, and A. K. De, *Proceedings of the* 26^{th} *National and* 4^{th} *International ISHMT-ASTFE Heat and Mass Transfer Conference*, IIT Madras, (2021).

3. Extending the range of local $1/2$ scaling regime in Rayleigh-Bénard convection using multi-scale random roughness, M. Sharma, **K. Chand** and A. K. De, *The* 26^{th} *National and* 4^{th} *International ISHMT-ASTFE Heat and Mass Transfer Conference*, IIT Madras, 2021.

4. Heat transfer mechanism in roughness aided tilted Rayleigh-Bénard convection, **K. Chand**, M. Sharma, and A. K. De, *The* 9^{th} *International and* 49^{th} *National Conference on Fluid Mechanics and Fluid Power*, IIT Roorkee, (2022).

5. $Pr-$effect on flow structures and heat transport in turbulent Rayleigh-Bénard convection from rough surfaces, M. Sharma, **K. Chand** and A. K. De, *The* 9^{th} *International and* 49^{th} *National Conference on Fluid Mechanics and Fluid Power*, IIT Roorkee, (2022).